

Spin-wave measurements  
of sodium cobaltate and linarite  
using inelastic neutron scattering

**Eron Cemal**

ROYAL HOLLOWAY  
UNIVERSITY OF LONDON

A DISSERTATION SUBMITTED TO THE UNIVERSITY OF LONDON  
FOR THE DEGREE OF DOCTOR OF PHILOSOPHY

August 2016

### Declaration of Authorship

I, Eron Cemal, hereby declare that this thesis and the work presented in it is entirely my own. Where I have consulted the work of others, this is always clearly stated.

Signed: \_\_\_\_\_

Date: \_\_\_\_\_

# Abstract

In this thesis work, the magnetic excitations of two different materials,  $\text{Na}_x\text{CoO}_2$  and linarite ( $\text{PbCuSO}_4(\text{OH})_2$ ) have been explored using inelastic neutron scattering. The study of these materials improves our understanding of quantum theory and paves the way for new technologies.

In  $\text{Na}_x\text{CoO}_2$ , for certain values of  $x$ , long-ranged Na-vacancy superstructures can occur. It has been shown that these superstructures have anharmonic lattice vibration modes which drastically reduces thermal transport in  $\text{Na}_x\text{CoO}_2$ . It is believed that the superstructures have an effect on the magnetism as well; however, this has not been proven so far. In this thesis work, the spin-wave spectrum is measured for two different superstructures. An anomalous magnetic waterfall effect is observed in the spin-wave dispersion for one sample which is interpreted as magnon-phonon coupling.

Linarite ( $\text{PbCuSO}_4(\text{OH})_2$ ) is a naturally occurring mineral. At low temperatures, it creates a quasi low-dimensional system which is of theoretical interest. Such a system has very strong magnetic interactions along one particular direction, but rather weak interactions along other directions. Based on some physical-properties measurements, it has been suggested that linarite could sustain an exotic new quantum phase. In this novel phase it is suggested the spins do not have any transverse long range order but instead they have quasi-long-range spin-multipolar order. In this thesis work, the measured magnetic excitations indicate that linarite could be in

the correct parameter region for displaying the novel quantum phase. Diffraction experiments were carried out to try and find direct experimental evidence of the suggested spin-multipolar phase. Additionally, the rich magnetic phase diagram of linarite was explored by various magnetisation and diffraction experiments.



# Acknowledgements

There are many people who have helped me achieve the completion of this thesis. Primarily, my supervisors Jon Goff and Mechthild Enderle, who have been very kind and patient with me.

Most of my work at Royal Holloway would not be possible without the support of our group. Without the wonderful crystals that Sivaperumal Uthayakumar had grown, there most likely would be no sodium cobaltate project. On the  $\text{Na}_x\text{CoO}_2$  project, I worked closely with Dan Porter and David Voneshen. I truly enjoyed my time in the experimental cabins with them. I had great support from Toby Willis, David Bowman, Gabriele Sala, and other members of the group.

For the neutron experiments on linarite, Mechthild and I closely worked with Bjorn Fåk. This project was a close collaboration with Reinhart Kremer from the Max Planck Institute, Stuttgart. He was the owner of the crystals used and was a perfect host when I came over to Stuttgart to use their MPMS.

The majority of my experiments were performed at the Institut Laue Langevin. The help of the instrument scientists gave here was invaluable. Martin Boehm (IN3, IN14, ThALES), Paul Steffens (IN14, ThALES), Karin Schmalzl (IN12), and many others, were all very helpful. At IN20 Mechthild was the instrument scientist, and she was present in all of the other experiments. The data analysis was much swifter thanks to Pauls “nplot” code. Special thanks goes to Jiri Kulda for very interesting discussions during TAS outings.

The people who inspired me to study solid state research in the first place were my lecturers at St Andrews: Chris Hooley and Andy Mackenzie. They made it look like great fun, and it truly has been!

My girlfriend, her family, and my family have been incredibly supporting throughout this PhD thesis. I am especially thankful to my parents İsmail and Lois. I hope to have made them proud.

I am lucky to have found some great friends at the ILL and RHUL. I will treasure our time together.

# Contents

<b>1</b>	<b>Introduction</b>	<b>11</b>
1.1	Brief Introduction for $\text{Na}_x\text{CoO}_2$ . . . . .	11
1.2	Brief Introduction for linarite . . . . .	14
1.3	Theory . . . . .	18
1.3.1	Crystal Structures . . . . .	18
1.3.2	Diffraction . . . . .	20
1.3.3	Magnetic Structures . . . . .	22
1.3.4	Linear Spin-Wave Theory . . . . .	24
<b>2</b>	<b>Experimental Methods</b>	<b>29</b>
2.1	Neutron Scattering Theory . . . . .	29
2.1.1	Scattering from a Single Nucleus . . . . .	29
2.1.2	Scattering from a Crystal . . . . .	33
2.1.3	Polarisation Analysis . . . . .	41
2.2	Neutron Instrumentation . . . . .	45
2.2.1	Neutron Sources . . . . .	45
2.2.2	Three-Axis Spectrometers . . . . .	47
2.2.3	XYZ Polarisation Analysis . . . . .	51
2.2.4	Neutron Instruments . . . . .	54
2.3	Magnetometry . . . . .	58

2.3.1	SQUID Magnetometry . . . . .	58
2.3.2	Magnetometry Instrumentation . . . . .	60
<b>3</b>	<b>Na<sub>x</sub>CoO<sub>2</sub></b>	<b>62</b>
3.1	Introduction . . . . .	62
3.1.1	Phase Diagram . . . . .	63
3.1.2	Crystal Structure . . . . .	64
3.1.3	Thermoelectric Properties . . . . .	68
3.1.4	Magnetism . . . . .	70
3.2	Experimental Set-Up . . . . .	78
3.2.1	Crystal Superstructures . . . . .	81
3.3	Experimental Results . . . . .	86
3.3.1	Inelastic Neutron Scattering Results . . . . .	86
3.3.2	Polarised Inelastic Neutron Scattering Measurements for Square Phase Na <sub>0.8</sub> CoO <sub>2</sub> . . . . .	91
3.4	Analysis . . . . .	97
3.4.1	Fitting the Spin Waves . . . . .	97
3.4.2	Waterfall Features . . . . .	104
3.4.3	Comparison to Phonon calculations . . . . .	106
3.4.4	Magnetic Superstructure Model . . . . .	109
3.4.5	Spin-Orbital Polaron Model . . . . .	113
3.5	Discussion . . . . .	116
3.6	Conclusion . . . . .	121
<b>4</b>	<b>Linarite (PbCuSO<sub>4</sub>(OH)<sub>2</sub>)</b>	<b>123</b>
4.1	Introduction . . . . .	123
4.1.1	Classical $J_1$ - $J_2$ Chain . . . . .	124
4.1.2	Heisenberg $J_1$ - $J_2$ Chain . . . . .	128

4.1.3	Crystal Structure . . . . .	136
4.1.4	Magnetic Structure . . . . .	140
4.1.5	Magnetic and Thermodynamic Properties . . . . .	142
4.1.6	Phase Diagram and Neutron Diffraction . . . . .	147
4.1.7	Review of Cuprate $J_1 - J_2$ Chains . . . . .	152
4.2	Crystals and Orientation . . . . .	162
4.3	Spin-wave Measurements Above Saturation Field . . . . .	178
4.3.1	Experimental Set-Up . . . . .	179
4.3.2	Data Reduction . . . . .	181
4.3.3	Experimental Results . . . . .	184
4.3.4	Analysis . . . . .	191
4.4	Spin-wave Measurements at Zero Field . . . . .	213
4.4.1	Experimental Set-up . . . . .	213
4.4.2	Data Reduction . . . . .	214
4.4.3	Experimental Results . . . . .	215
4.4.4	Analysis . . . . .	218
4.5	Diffraction Measurements with an Applied Field . . . . .	231
4.5.1	Experimental Set-up . . . . .	232
4.5.2	Experimental Results . . . . .	233
4.5.3	Analysis . . . . .	241
4.6	Magnetisation Measurements . . . . .	247
4.7	Discussion . . . . .	258
4.8	Conclusion . . . . .	267
<b>5</b>	<b>Summary and Outlook</b>	<b>271</b>
5.1	$\text{Na}_{0.8}\text{CoO}_2$ . . . . .	271
5.1.1	Summary . . . . .	271
5.1.2	Outlook . . . . .	273

5.2	Linarite . . . . .	274
5.2.1	Summary . . . . .	274
5.2.2	Outlook . . . . .	276

# Chapter 1

## Introduction

In this thesis work, experimental results from two different compounds are presented. These are  $\text{Na}_{0.8}\text{CoO}_2$  and linarite ( $\text{PbCuSO}_4(\text{OH})_2$ ). Inelastic neutron scattering (INS) is used to study the magnetic excitations in these two very different materials. A detailed review of the scientific background of these materials will follow in later chapters. In the first two sections of this chapter, the general interest in these materials will be described. In the last section of this chapter, some of the common theory for both compounds will be introduced. This will include some fundamental solid state concepts, such as crystal structures and reciprocal space, as well as some more advanced concepts, such as the derivation of the magnon dispersion for a ferromagnet.

### 1.1 Brief Introduction for $\text{Na}_x\text{CoO}_2$

$\text{Na}_x\text{CoO}_2$  has attracted interest over the years for three main reasons. These are for its relatively high thermopower [1], its battery electrode capabilities [2], and its superconductivity under hydration [3].

$\text{Na}_x\text{CoO}_2$  became the first Co based superconductor via its hydrated version

$\text{Na}_x\text{CoO}_2 \cdot y(\text{H}_2\text{O})$  with  $x=0.35$ ,  $y=1.3$  [3]. There are similarities between this compound and the well studied Cu based superconductors, the cuprates. Both the cuprates and  $\text{Na}_x\text{CoO}_2$  share a layered crystal structure and are considered electronically two dimensional. The non-hydrated version may be considered magnetically three dimensional [4, 5]; however, the hydration massively increases the separation between the layers, making it more two dimensional [3]. The most important difference between cuprates and  $\text{Na}_x\text{CoO}_2 \cdot y(\text{H}_2\text{O})$  is that they are on square and hexagonal lattices respectively. Elemental superconductors are well understood using Bardeen-Cooper-Schrieffer theory of superconductivity [6, 7] and they exhibit s-wave pairing. However, “unconventional superconductors” can exhibit p-, d-, or f-wave pairing. The cuprate high-temperature superconductors exhibit d-wave pairing [8]. The pairing symmetry in  $\text{Na}_x\text{CoO}_2$  is controversial and it has been attributed to s-waves [9], f-waves [10] and anisotropic chiral  $d+id$  waves [11].

$\text{Na}_x\text{CoO}_2$  is also one of the good candidates for Na-based batteries [2]. There are many possible advantages for using a Na based battery over the widely used Li based battery. The primary reason is economic. Na is much more abundant, it costs roughly six times less to obtain compared to Li [12]. Also Na-based batteries are less toxic [12] and can be transported more safely. A Li based battery has to be transported with a certain amount of charge, which can cause it to short circuit and catch fire [13]. Because Na is three times heavier, it was thought that a Na-based battery could not achieve the same energy density as a Li-based batteries. However, this has since been disproved. Some Na-based batteries have shown to have large capacities and the ability to sustain many cycles. This would make it suitable for supporting grid networks [14].

$\text{Na}_x\text{CoO}_2$  has also been proposed as a good thermoelectric material [1]. Thermoelectricity is the capability to convert a temperature gradient across a material into a voltage difference (or vice versa). Thermopower can be explained with the



help of figure 1.1. In the hot region of the material, the electrons are faster compared to the cold region. This allows them to diffuse into the cold region, creating a current. In order to have a high thermopower, good electrical conductivity but bad thermal conductivity is required. Thermoelectric materials are of high technological importance. They can be used to convert “wasted heat” into electricity. This can be the waste heat from a cars exhaust, power plants, or even someone’s body. Alternatively, thermoelectrics can be used to cool computer components, since the dissipation of heat can be the limiting factor for processing speed.

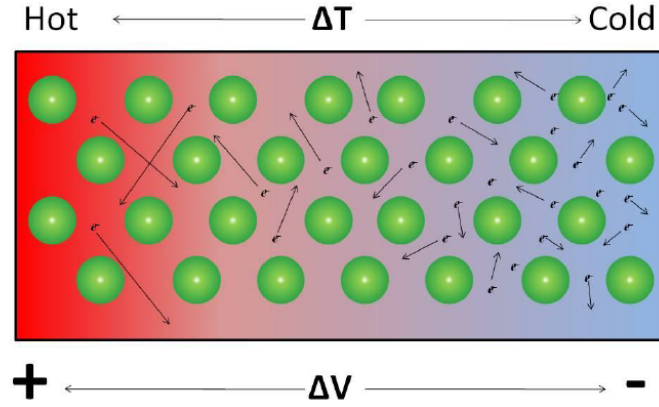


**Figure 1.1: The Thermoelectric effect.** Electrons on the hotter side diffuse into the colder side creating a voltage difference. Image from Ref. [15].

There have been two major discoveries regarding the large thermopower of  $\text{Na}_x\text{CoO}_2$ . The first is that the thermopower can be suppressed with a magnetic field [16]. To understand this, people have considered the degeneracy of the  $\text{Co}^{4+}$  and  $\text{Co}^{3+}$  spin states. However, there is no consensus on the spin states or their distribution throughout the material. There have been models which consider electrons as localised [4, 5, 17], or a mixture of localised and itinerant [18, 19]. More experiments might be necessary to fully explain this magnetic field dependence of the thermo-

power. The second major discovery was the effect of the Na superstructures on the thermal transport.  $\text{Na}_x\text{CoO}_2$  produces long ranged superstructures from Na vacancies [17, 20]. It was shown that the Na sites near the vacancies are in anharmonic potentials. At these sites the Na “rattles” which disturbs the flow of phonons. It was shown that for a particular superstructure, the existence of such rattling modes can reduce the thermal transport by a factor of six [21]. Additional to this, it is believed superstructure must affect the electronic and magnetic order in the Co layers [17].

INS experiments have measured the spin waves of two  $\text{Na}_x\text{CoO}_2$  samples with very similar concentrations,  $x=0.75, 0.82$  [4, 5]. It was found that between the two samples, the out-of-plane coupling differs by a factor of two. It is known that in this concentration range there are three possible superstructures. It is possible that this factor of two difference can be attributed to the differences in superstructures. The initial aim of this thesis work was to perform inelastic neutron experiments on  $\text{Na}_x\text{CoO}_2$  samples with known superstructures and highlight any possible difference. After all, in the initial inelastic neutron experiments the superstructures of the samples were not known.

## 1.2 Brief Introduction for linarite

Linarite is a naturally occurring, relatively rare mineral [22]. Linarite has attracted interest because it has been proposed that it might be able to sustain novel quantum phases. This originates from the special magnetic conditions of linarite: its low dimensionality, and low spin. Linarite is composed of chains of  $\text{CuO}_2$  plates which propagate along the  $\mathbf{b}$  axis [23]. At low temperatures spin moments of  $S=1/2$  localise at the Cu sites creating a spin chain. These Cu sites are magnetically strongly interacting along the chain but the interactions between the chains are rather weak. This makes it a quasi-one-dimensional system [24–26].

The low spin ( $S=1/2$ ) of linarite is important. It is known that for simple quantum mechanical systems that as  $S \rightarrow \infty$ , the system behaves more classically [27]. The importance of dimensionality can be seen for an electron gas with electron-electron interactions. For a three dimensional system, it has been shown by Landau that such a system behaves very similarly to a free electron gas. The excitations of the system are quasiparticles which behave very similarly to electrons, with a different effective mass and a reduced lifetime. In one dimension, the interacting electron cloud behaves very differently to the free electron cloud [28]. The reason for this can be illustrated in figure 1.2. Here it can be seen that for a higher dimensional system, the electron can still move about even though it feels some force from its neighbouring electrons. However, in the one dimensional case, an electron cannot pass beyond its neighbouring electrons. This causes the excitations of the system to become collective excitations. This one dimensional interacting electron system is referred to as the Luttinger-Tomaga liquid [29, 30]. In this system, the principal excitations of the system are the spinon and chargon quasi-particles, which carry the spin and charge of the electron respectively. This is known as spin-charge separation [28].



**Figure 1.2: Effects of dimensionality on electron movement.**

(a) For a multi-dimensional system the electron can move about. (b) However, for a one-dimensional system, the electrons cannot move freely as they cannot pass through their neighbours. This forces the system to have collective excitations [28]. Image from Ref. [28].

In linarite one can also observe geometrical frustration. The concept of geometrical frustration in magnetism can be visualised in figure 1.3 on page 17. Here three spins are to be placed on the corners of a triangle. The three spins are expected to satisfy an anti-ferromagnetic bond, which causes them to be anti-parallel. The first two spins can be placed easily; however, the third spin cannot be anti-parallel to both the spins. The energy of an up spin and a down spin are the same. This degeneracy is the basis of the frustrated magnetism. This degeneracy can be removed with quantum or thermal fluctuations [31]. At finite temperature not all of the degenerate ground states have the same excitations. Some of these ground states might have higher entropy. This higher entropy case can lift the degeneracy, stabilising the ground state. This interesting phenomena is known as order-from-disorder [32]. One of the most famous frustrated systems are the “spin-ice” compounds [33]. These systems reside on a pyrochlore lattice and have been observed in compounds of the type  $A_2Ti_2O_7$  where  $A=Dy, Ho$ . At the vertices of the pyrochlore lattice reside Ising moments which either point towards or away from the centre of each corner-sharing tetrahedron. The ground state is macroscopically degenerate, with two spins pointing in and two spins pointing out of the tetrahedron. If one of these moments is flipped, it creates two entities which locally act like a north or south monopole. There is no energy cost to separate these entities, therefore they act as deconfined magnetic monopoles [31, 34]. This discovery of such monopole-like particles created large interest in the field of frustrated magnets.

In linarite the frustration comes from competing nearest- and next-nearest-neighbour interactions along the spin chain. The nearest-neighbour interaction is ferromagnetic, whilst the next-nearest-neighbour interaction is antiferromagnetic. For linarite this results in a cycloidal magnetic structure at low temperatures [25, 26]. These cycloidal magnetic structures are of much interest for multiferroics. Multiferroic materials exhibit coupling between magnetic field, electric field, or stress.

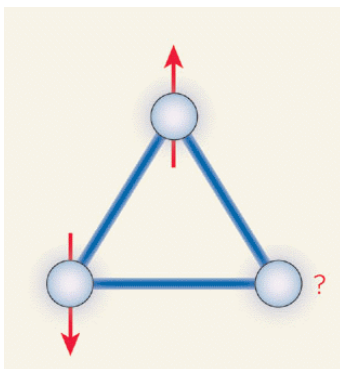


**Figure 1.3: Geometric frustration on a triangular lattice.** The spins on each site try to align antiferromagnetically with respect to each other. The first two spins can satisfy this easily; however, the third spin cannot satisfy this for both bonds. Image sourced from Ref. [35].

Cycloidal magnetic structures are of interest because they directly create an electric polarisation within the material. This type of materials is known as ferroelectric materials [36,37].

Currently, linarite is attracting interest due to its possibility of supporting a novel quantum phase. This phase arises from condensation of multiple magnons and it has no long-range dipolar order but instead has quasi-long range spin-multipolar order [38–42]. These phases are also referred to as spin-nematics and are related to the classical nematics such as seen with liquid crystals [43]. Another Cu based spin chain compound,  $\text{LiCuVO}_4$ , has already shown some strong evidence of such a novel phase [44, 45]. However, the saturation field for this compound is  $\sim 50\text{T}$  [44]. This does not allow the measurement of this phase with neutron scattering methods. Magnetic susceptibility and specific heat measurements suggest that linarite could be in the right parameter region to support a spin-multipolar phase [24–26]. Unlike  $\text{LiCuVO}_4$ , linarite has a saturation field of  $\sim 10\text{T}$  [26]. This allows one to perform neutron scattering experiments on linarite up to and above saturation. The thesis

work aimed at finding if linarite is in the right parameter region to sustain the spin-multipolar phase and, if possible, measure it directly.

## 1.3 Theory

In this section important theoretical concepts used in this thesis work are introduced. Some of these are fundamental solid-state physics concepts which are covered in detail in various introductory textbooks [6, 7]. Also covered in this section is the Heisenberg Hamiltonian and linear spin-wave theory. These concepts create a theoretical basis for modelling spin-wave dispersions.

### 1.3.1 Crystal Structures

A crystal is a solid structure where atoms are ordered in a periodic lattice structure and they can contain  $\sim 10^{23}$  atoms. Because of this periodicity, the whole crystal can be represented by a very small unit cell composed of few atoms. A typical unit cell can be seen in figure 1.4 on page 19. Such a unit cell is called a primitive lattice because it has only one atom per unit cell. Here  $\mathbf{a}$ ,  $\mathbf{b}$ , and  $\mathbf{c}$  are lattice vectors, defining the size of the unit cell, and the atoms are given in black circles. The three angles  $\alpha$ ,  $\beta$ , and  $\gamma$  are the angles between the lattice vectors. Real crystal-line materials might have different domains where the unit cell is the same, but the orientations are different. The term “single crystal” refers to samples in which the unit cell and the orientation is the same throughout the whole crystal [6, 7].

A position in real space with respect to an arbitrary origin is stated as:

$$\mathbf{R} = (n_1\mathbf{a} + n_2\mathbf{b} + n_3\mathbf{c}) + \mathbf{r}, \quad (1.1)$$

where  $n_1$ ,  $n_2$ , and  $n_3$  are all integers. The term within the brackets indicates the origin of the closest unit cell. The position with respect to the origin of this unit

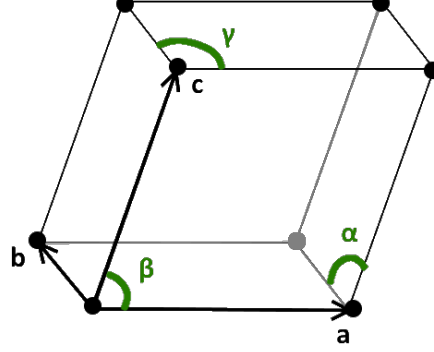


**Figure 1.4: An example of a unit cell of a crystal.** Here,  $\mathbf{a}$ ,  $\mathbf{b}$ , and  $\mathbf{c}$  are lattice vectors and the black points represent atomic positions.

cell is given by the vector  $\mathbf{r}$ :

$$\mathbf{r} = x\mathbf{a} + y\mathbf{b} + z\mathbf{c}. \quad (1.2)$$

For scattering experiments, it is useful to define a reciprocal lattice defined by:

$$\mathbf{a}^* = \frac{2\pi\mathbf{b} \times \mathbf{c}}{\mathbf{a} \cdot (\mathbf{b} \times \mathbf{c})}, \mathbf{b}^* = \frac{2\pi\mathbf{c} \times \mathbf{a}}{\mathbf{a} \cdot (\mathbf{b} \times \mathbf{c})}, \mathbf{c}^* = \frac{2\pi\mathbf{a} \times \mathbf{b}}{\mathbf{a} \cdot (\mathbf{a} \times \mathbf{b})} \quad (1.3)$$

A vector along reciprocal space can be represented in units of the reciprocal lattice in the following form:

$$\boldsymbol{\tau} = h\mathbf{a}^* + k\mathbf{b}^* + l\mathbf{c}^* \quad (1.4)$$

The reciprocal lattice is useful for defining lattice planes within the crystal. These planes can be denoted by integer values of  $(hkl)$  which are called Miller indices. The vector  $\boldsymbol{\tau}_{(hkl)}$  would be normal to the plane and the distance between the planes would be given by [6]:

$$d_{(hkl)} = \frac{2\pi}{|\boldsymbol{\tau}_{(hkl)}|} \quad (1.5)$$

Points in the reciprocal lattice are often described relative to the Brillouin zone. The Brillouin zone is centred at a reciprocal lattice point and contains all of the points closest to that lattice point [7, 46]. An example of a Brillouin zone for two-dimensional cubic and hexagonal lattices can be seen in figure 1.5 [7]. The centre of Brillouin zones is referred to as the  $\Gamma$  point [47].

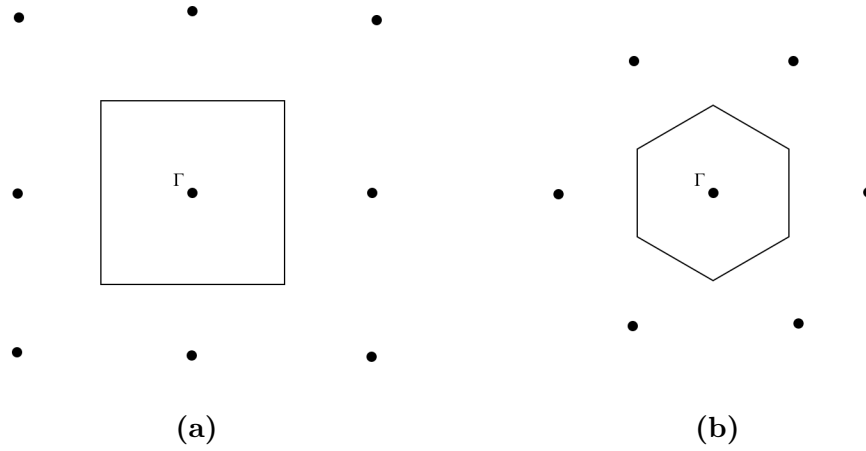


**Figure 1.5: Brillouin zone examples in two dimensions.** Here, the zones for (a) cubic or (b) hexagonal lattices can be seen.

### 1.3.2 Diffraction

One way to obtain information about the crystal structure is to shine x-rays through it. This will result in a diffraction pattern composed of intense spots in a symmetric pattern. By measuring the position and intensity of these spots, it is possible to obtain information about crystal structure, such as lattice spacing and the occupation of sites within the unit cell [7, 48].

One way of thinking about the diffraction event is by considering x-rays scattering from lattice planes which is visualised in figure 1.6 on page 22. Here the blue



and red lines represent two parallel beams of light which have the same phase before they reach the crystal. Both beams hit the crystal plane at an angle  $\theta$ ; however, the red beam scatters from the second layer instead of the first layer. The two beams exit the sample with the same angle but, because they have travelled different paths, there could be a phase difference between the two. If there is no phase difference, there is constructive interference, i.e. a peak in intensity. The condition for constructive interference can be deduced from the geometry of the situation and can be simply stated in the following equation [6]:

$$n\lambda = 2d\sin(\theta) \quad (1.6)$$

Here,  $n$  is an integer,  $\lambda$  is the wavelength of the light,  $d$  is the distance between two crystal planes, and  $\theta$  is the angle between the incident light wave and the crystal plane, also referred to as the scattering angle. This equation is referred to as Bragg's Law [49]. The peaks in intensity observed at these positions are referred to as a Bragg peaks [6, 7].

Using Bragg's law one can successfully reproduce the positions of the observed diffraction patterns. However, Laue [50] has shown that the diffraction conditions can also be stated in terms of the reciprocal lattice. The initial and final wavevectors of the scattered beam are given as  $\mathbf{k}_i$  and  $\mathbf{k}_f$ . The scattering vector is defined as:

$$\mathbf{Q} = \mathbf{k}_f - \mathbf{k}_i. \quad (1.7)$$

Diffraction is an elastic scattering event and, therefore,  $|\mathbf{k}_f| = |\mathbf{k}_i|$ . The Laue condition of diffraction states that diffraction will occur if the scattering vector is at a reciprocal lattice point. Therefore, diffraction occurs for integer values of  $hkl$  in the following equation [6, 7]:

$$\mathbf{Q} = \boldsymbol{\tau}_{hkl}. \quad (1.8)$$

For non-primitive crystals, where there are more than one atom in the unit cell, some integer  $hkl$  values may correspond to extinctions, where there is no intensity. The reason for this will be explained in section 2.1.2.

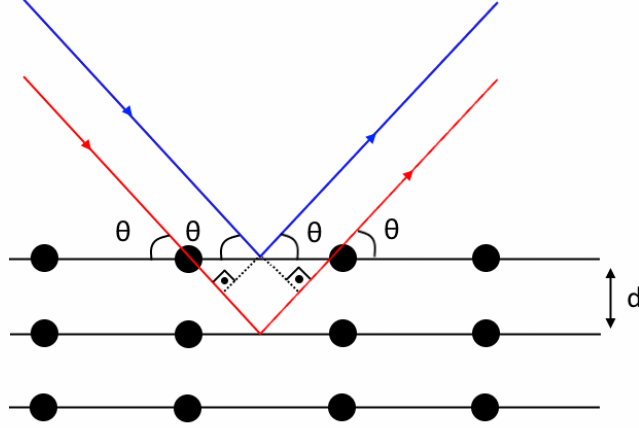


**Figure 1.6: Scattering from lattice planes.** Two parallel beams of light scatter from the first and second layers of a crystal. The two beams have travelled different paths and there could be a phase difference between them. The highest intensity is when there is no phase difference between the two beams and the condition for this is given in Bragg's Law in equation 1.6 [6, 7, 49].

### 1.3.3 Magnetic Structures

An electron localised at an atomic site can produce a net magnetic moment at this site. This magnetic moment has two contributions. The first is due to the internal magnetic moment of the electron of size  $\sim 1\mu_B$ , where  $\mu_B$  is the Bohr magneton. The second contribution is due to its charge and its orbital motion. The filled electron shells do not contribute to the magnetic moment, therefore one only considers the electrons in the unfilled electron shells [6].

In a crystal, electrons localised at atomic sites can align their magnetic moments in such a way to create long-ranged magnetic structures. Some examples of magnetic structures can be seen in figure 1.7(a,b). Here only one-dimensional cases are shown, but these examples can be extended into three dimensions. In figure 1.7(a) a ferromagnetic (FM) structure can be seen, where all the moments prefer to be parallel along a given direction. In figure 1.7(b) an antiferromagnetic (AFM) structure can be seen. It is important to note that for the AFM the magnetic unit cell is not the same size as the nuclear unit cell, but instead it is twice as large. In figure 1.7(c) a phase with no long-range order, a paramagnet, can be seen. For this structure the orientations of the moments are completely random [6].

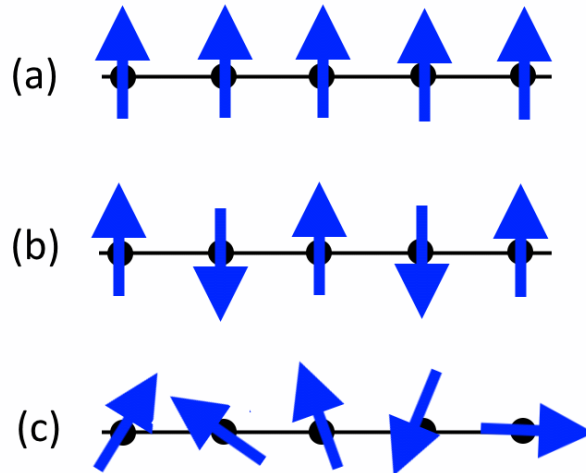


**Figure 1.7: Examples of magnetic structures.** Here one dimensional analogues of (a) FM, (b) AFM, and (c) paramagnetic structures can be seen.

The formation of magnetic structures in crystals is dependent on the quantum nature of electrons. Typically, the magnetic dipole of the electron is too weak to create any alignment [6]. Instead, the process called the “exchange interaction” as

suggested by Heisenberg [51] and Dirac [52] is responsible for creation of magnetic structures. Electrons are fermions and, therefore, two electrons with the same spin cannot be at the same position. This introduces a spin component of the energetics of the electrons. The additional energy the electrons gain due to their spin is stated by the Heisenberg Hamiltonian as:

$$\mathcal{H} = - \sum_{ij} J_{ij} \mathbf{S}_i \cdot \mathbf{S}_j. \quad (1.9)$$

Here  $\hbar \mathbf{S}_i$  is the total angular momentum of the electrons at site  $i$  and  $J_{ij}$  is referred to as the exchange integral or the exchange energy [6]. If only nearest-neighbour interactions are considered, a positive  $J_{ij}$  will mean that spins  $\mathbf{S}_i$  and  $\mathbf{S}_j$  will align parallel in order to minimise energy; thus forming a FM structure. However, if  $J_{ij}$  is negative, they will align anti-parallel forming an AFM magnetic structure. There are different types of exchange processes. If there is overlap of electron wavefunctions between two magnetically ordered sites, this is called direct exchange. However there is also the case of indirect exchange where two magnetically ordered sites interact via the conduction electrons instead [6]. Two magnetic sites can also interact each other via a non-magnetic atom between them. This process is called superexchange and the value of  $J_{ij}$  is dependent on the relative positions of the three sites and their orbital's orientations [53–57].

### 1.3.4 Linear Spin-Wave Theory

Aside from the static magnetic structure, there are also magnetic excitations which can be measured directly via neutron scattering methods. In a classical system, the spins are treated as vectors with a given magnitude  $|\mathbf{S}|$  which can point along any direction. At finite temperature these spins rotate about an axis. By considering the phase difference in such a rotation for neighbouring spins, it is pos-

sible to construct a magnetic excitation with a certain wavelength. This excitation is called a spin wave and is illustrated in figure 1.8 [6].

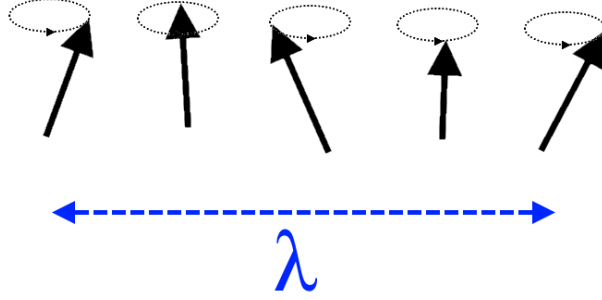


**Figure 1.8: Illustration of a spin wave.** All spins precess about the same axis. The relative phase difference between neighbouring spins creates an excitation with a given wavelength.

In a quantum mechanical treatment of the spins, the spin excitations are represented by magnons. Magnons are quasi-particles which represent a total spin change of  $\Delta S=1$  [6, 7]. The energy-momentum relation of the magnons (i.e. its dispersion) can be solved for the Heisenberg Hamiltonian. This is done via linear spin-wave theory (LSWT). In this section the derivation of the magnon dispersion for a FM will be shown. The derivation stated here follows the work of Squires [58]

In the Heisenberg model, spins with value  $S$  are localised at the nuclear position. At this site the angular momentum of any spin component is  $\hbar M$  where  $M = S, S-1, \dots, -S+1, -S$ . At zero field, all the spins will have  $M=S$  for the same component. The Heisenberg Hamiltonian can be written as:

$$\mathcal{H} = - \sum_{\mathbf{l}\mathbf{l}'} J(\mathbf{l} - \mathbf{l}') \mathbf{S}_{\mathbf{l}} \cdot \mathbf{S}_{\mathbf{l}'} \quad (1.10)$$

Here  $\mathcal{H}$  is the Hamiltonian,  $J(\mathbf{l} - \mathbf{l}')$  is the exchange energy between spins at positions  $\mathbf{l}$  and  $\mathbf{l}'$ , and  $\mathbf{S}_{\mathbf{l}}$  is the spin operator for the site at position  $\mathbf{l}$ . Note that from

symmetry arguments  $J(\mathbf{l} - \mathbf{l}') = J(\mathbf{l}' - \mathbf{l})$  must hold. The aim is to transform the operators in the Hamiltonian in equation 1.10 into raising and lowering operators. The starting point is to separate the operator  $\mathbf{S}_l$  into three operators  $S_l^x$ ,  $S_l^y$ , and  $S_l^z$  which correspond to spin angular momentum along the x, y, and z directions. The eigenstate of  $S_l^z$ , is presented as  $|M\rangle$ , with eigenvalue  $M$ . This eigenvalue is the  $z$  component of angular momentum in units of  $\hbar$ . The  $S_l^x$ ,  $S_l^y$  operators are written in terms of operators  $S_l^+$ ,  $S_l^-$  which are defined by the following equations:

$$S_l^+ = S_l^x + iS_l^y \quad (1.11)$$

$$S_l^- = S_l^x - iS_l^y \quad (1.12)$$

The  $S_l^+$  and  $S_l^-$  operators act similar to raising and lowering operators. When acting upon the wavefunction  $|M\rangle$ , they give the following result:

$$S^+|M\rangle = [(S - M)(S + M + 1)]^{1/2}|M + 1\rangle \quad (1.13)$$

$$S^-|M\rangle = [(S + M)(S - M + 1)]^{1/2}|M - 1\rangle \quad (1.14)$$

Here the subscript  $l$  has been dropped for convenience. Taking  $n = S - M$ , this can be re-written as the following:

$$S^+|n\rangle = (2Sn)^{1/2} \left[ 1 - \frac{n-1}{2S} \right]^{1/2} |n-1\rangle \quad (1.15)$$

$$S^-|n\rangle = (2S(n+1))^{1/2} \left[ 1 - \frac{n}{2S} \right]^{1/2} |n+1\rangle \quad (1.16)$$

Note that if the second terms inside the square brackets in equations 1.15-1.16 were neglected, one would have raising and lowering operators. This is the approach followed by the linear approximation. It sets the components in the square brackets to one. This allows one to define  $S^+$  and  $S^-$  in terms of raising and lowering

operators with  $S^+ = (2S)^{1/2}a$  and  $S^- = (2S)^{1/2}a^+$ . The term  $S^z$  can also be expressed in terms of these operators via  $S^z = S - a^+a$ . The next step is to Fourier transform the ladder operators which will result in:

$$b_{\mathbf{q}} = N^{-1/2} \sum_{\mathbf{l}} \exp(-i\mathbf{q} \cdot \mathbf{l}) a_{\mathbf{l}}, \quad (1.17)$$

$$b_{\mathbf{q}}^+ = N^{-1/2} \sum_{\mathbf{l}} \exp(i\mathbf{q} \cdot \mathbf{l}) a_{\mathbf{l}}^+, \quad (1.18)$$

where  $N$  is the number of atoms in the crystal. These operators have the commutation relation  $[b_{\mathbf{q}}, b_{\mathbf{q}'}^+] = \delta_{\mathbf{q}\mathbf{q}'}$ . Substituting  $\mathbf{S}_{\mathbf{l}} \cdot \mathbf{S}_{\mathbf{l}'} = 1/2(S_{\mathbf{l}}^+ S_{\mathbf{l}'}^- + S_{\mathbf{l}}^- S_{\mathbf{l}'}^+) + S_{\mathbf{l}}^z S_{\mathbf{l}'}^z$  into the Hamiltonian in equation 1.10, one obtains:

$$\mathcal{H} = - \sum_{\mathbf{l}\mathbf{l}'} J(\mathbf{l} - \mathbf{l}') (S_{\mathbf{l}}^+ S_{\mathbf{l}'}^- + S_{\mathbf{l}}^z S_{\mathbf{l}'}^z) \quad (1.19)$$

Here the fact that  $\mathbf{l} \neq \mathbf{l}'$  S operators commute has been used. Using  $\boldsymbol{\rho} = \mathbf{l} - \mathbf{l}'$ , the Fourier transform of the exchange energy can be stated as:

$$\mathcal{J}(\mathbf{q}) = \sum_{\boldsymbol{\rho}} J(\boldsymbol{\rho}) \exp(i\boldsymbol{\rho} \cdot \mathbf{q}) \quad (1.20)$$

With this definition, the Hamiltonian can be written in units of  $b_{\mathbf{q}}$  and  $b_{\mathbf{q}}^+$  operators. The resulting Hamiltonian will have the form:

$$\mathcal{H} = \mathcal{H}^0 + \sum_{\mathbf{q}} \hbar\omega_{\mathbf{q}} b_{\mathbf{q}}^+ b_{\mathbf{q}}, \quad (1.21)$$

$$\mathcal{H}^0 = -S^2 N \mathcal{J}(0), \quad (1.22)$$

$$\hbar\omega_{\mathbf{q}} = 2S[\mathcal{J}(0) - \mathcal{J}(\mathbf{q})] \quad (1.23)$$

Here the  $\hbar\omega_{\mathbf{q}}$  term gives the dispersion relation of the magnons. One can consider the scenario with only the nearest-neighbour exchange energy,  $J_{FM}$ . For simplicity,

one can consider a cubic primitive lattice where there is only one magnetic atom per unit cell. There will be a total of six nearest-neighbours to consider. The term  $\mathcal{J}(\mathbf{q})$  can be written as:

$$\mathcal{J}(\mathbf{q}) = J_{FM} [\exp(i\mathbf{a}\cdot\mathbf{q}) + \exp(-i\mathbf{a}\cdot\mathbf{q}) + \exp(i\mathbf{b}\cdot\mathbf{q}) - \exp(-i\mathbf{b}\cdot\mathbf{q}) + \exp(i\mathbf{c}\cdot\mathbf{q}) - \exp(-i\mathbf{c}\cdot\mathbf{q})] \quad (1.24)$$

After some transformation this reduces to:

$$\mathcal{J}(\mathbf{q}) = J_{FM} [\cos(2\pi h) + \cos(2\pi k) + \cos(2\pi l)] \quad (1.25)$$

Therefore, the magnon dispersion is given by:

$$\hbar\omega = 2SJ_{FM}[3 - \cos(2\pi h) - \cos(2\pi k) - \cos(2\pi l)] \quad (1.26)$$

The minimum of the dispersion is  $\hbar\omega_{(000)} = 0$  and the maximum is  $\hbar\omega_{(1/2,1/2,1/2)} = 6SJ_{FM}$ . It is important to note that this result is unique to the FM state. For the AFM state the magnon dispersion will have a different result.



# Chapter 2

## Experimental Methods

In this chapter, the experimental methods used in the thesis will be introduced. The majority of the data presented in this thesis is obtained via neutron scattering experiments. Therefore, the first two sections will go into neutron scattering theory and instrumentation respectively. In the neutron instrumentation section, the operation of the instrument will be discussed as well as the configuration of the particular instruments used. Some small amount of data was obtained via magnetometry measurements. For this reason the final section will focus on the operation and set-up of the magnetometer used for this thesis.

### 2.1 Neutron Scattering Theory

In this section the relevant neutron scattering theory will be established. The work in this section will closely follow the work of Squires [58].

#### 2.1.1 Scattering from a Single Nucleus

A good place to start with neutron scattering theory is to consider neutron scattering from a single nucleus, as shown in figure 2.1. The neutrons originate from

the source and propagate towards the nucleus. The source is placed sufficiently far away from the nucleus that the neutron waves arriving at the nucleus can be treated as plane waves. This incoming plane wave has wavevector  $\mathbf{k}_i$ , momentum  $\hbar\mathbf{k}_i$ , and energy  $E_i = \hbar^2 k_i^2 / (2m_n)$ , where  $m_n$  is the neutron mass. After scattering from the nucleus, the neutron wave has wavevector  $\mathbf{k}_f$ , and propagates radially outwards. At a large distance away, the detector counts the number of neutrons. At the detector the neutron wave can also be treated as plane waves.

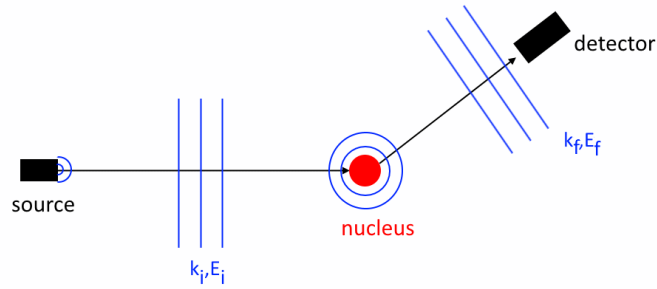


**Figure 2.1: Scattering from a nucleus.** A plane wave of neutrons with wavevector  $\mathbf{k}_i$  and energy  $E_i$  interacts with the nucleus. After the interaction with the nucleus, the neutron scatters isotropically. At a large distance away the detector measures the scattered neutrons which can also be treated as plane waves. The scattered neutrons have wavevector  $\mathbf{k}_f$  and energy  $E_f$ .

The detector will count the number of particles that scatter into a specific solid angle  $d\Omega$ , which is defined by the size of the detector. This quantity, normalised to the flux of oncoming neutrons  $\Phi$ , is defined as the differential cross-section. For the system depicted in figure 2.1, the differential cross-section will have the form:

$$\left(\frac{d\sigma}{d\Omega}\right)_{\lambda_i \rightarrow \lambda_f} = \frac{1}{\Phi} \frac{1}{d\Omega} \sum_{\mathbf{k}_f \text{ in } d\Omega} W_{\mathbf{k}_i, \lambda_i \rightarrow \mathbf{k}_f, \lambda_f}, \quad (2.1)$$

where  $\lambda_i$  and  $\lambda_f$  are initial and final quantum states of the nucleus, and  $W_{\mathbf{k}_i, \lambda_i \rightarrow \mathbf{k}_f, \lambda_f}$  is the transition rate from  $k_i, \lambda_i$  into  $k_f, \lambda_f$  per second. In order to determine the transition rate, Fermi's Golden rule [27, 59] is used. This results in a differential cross-section of the form:

$$\left(\frac{d\sigma}{d\Omega}\right)_{\lambda_i \rightarrow \lambda_f} = \frac{k_f}{k_i} \left(\frac{m}{2\pi\hbar^2}\right)^2 |\langle \mathbf{k}_f \lambda_f | V | \mathbf{k}_i \lambda_i \rangle|^2. \quad (2.2)$$

Here,  $V$  is the potential that the neutron feels from the nucleus. Another important quantity is the partial differential cross-section which is given by:

$$\left(\frac{d^2\sigma}{d\Omega dE_f}\right)_{\lambda_i \rightarrow \lambda_f} = \frac{k_f}{k_i} \left(\frac{m}{2\pi\hbar^2}\right)^2 |\langle \mathbf{k}_f \lambda_f | V | \mathbf{k}_i \lambda_i \rangle|^2 \delta(E_{\lambda_i} - E_{\lambda_f} + E_i - E_f). \quad (2.3)$$

$E_{\lambda_i}$  and  $E_{\lambda_f}$  are the energies of states  $\lambda_i$  and  $\lambda_f$  respectively and  $E_i$  and  $E_f$  are initial and final energies of the scattered particle. In order to get to this equation the conservation of energy has been applied. If the particle has lost energy due to scattering, the state  $\lambda_f$  must have a higher energy state than  $\lambda_i$ . It is known that the neutron interacts with the nucleus via the strong and weak forces which are very short ranged. For simplicity, the potential  $V$  can be treated as a Dirac delta function:

$$V(\mathbf{r}) = \frac{2\pi\hbar^2}{m} b \delta(\mathbf{r}). \quad (2.4)$$

This potential is referred to as the Fermi pseudo-potential. Here,  $b$  is defined as the scattering length of the object and it can be negative or positive. Its value is dependent on the element, its particular isotope, and its nuclear spin. For an elastic scattering event, which is defined as  $E_i = E_f$ , the differential cross-section achieves the desirable result of

$$\frac{d\sigma}{d\Omega} = b^2. \quad (2.5)$$

This result is desirable because isotropic scattering is achieved. Basic diffraction theory states that if the stationary object is much smaller than the wavelength of the scattered object, the scattering must be isotropic. The nuclear potential has a range of  $\sim 10^{-14}\text{m}$  which is very small compared to the typical neutron wavelength of  $\sim 10^{-10}\text{m}$  used in neutron scattering experiments.

In order to get isotropic scattering from a nucleus Fermi's Golden rule has been used. This is equivalent to the Born approximation as they are both based on first order perturbation theory [58]. A derivation of the differential cross-section with a more quantum mechanical approach can be found in Ref. [27]. It is important to note that the use of Fermi's Golden rule (or Born approximation) is not always valid for neutron scattering. However, it is used regardless because it results in the desired isotropic scattering from a nucleus [58].

### Coherent vs Incoherent Scattering

One can consider scattering from a system composed of many different nuclei, where not all nuclei have the same scattering length. If the number of atoms is large enough, the measured cross-section is approximately the average of all the individual cross-sections. This is certainly valid for most crystal samples used in neutron scattering where the number of nuclei is of the order of  $\sim 10^{23}$ . The partial differential cross-section is given by:

$$\frac{d^2\sigma}{d\Omega dE_f} = \frac{k_f}{k_i} \frac{1}{2\pi\hbar} \sum_{jj'} \overline{b_j b_{j'}} \int \langle j', j \rangle e^{-i\omega t} dt, \quad (2.6)$$

where  $\omega$  is the angular frequency,  $t$  is time, and the overline in the term  $\overline{b_j b_{j'}}$  represents an average of  $(b_j b_{j'})$ . Here  $\langle j, j' \rangle$  is defined as:

$$\langle j', j \rangle = \langle e^{-i\mathbf{Q} \cdot \mathbf{R}_j(0)} e^{i\mathbf{Q} \cdot \mathbf{R}_{j'}(t)} \rangle. \quad (2.7)$$

$\mathbf{Q}$  is the scattering vector and  $\mathbf{R}_j$  is the position of atom  $j$  in real space. One can re-write equation 2.6 in two different parts:

$$\begin{aligned} \frac{d^2\sigma}{d\Omega dE_f} = & \frac{k_f}{k_i} \frac{1}{2\pi\hbar} (\bar{b})^2 \sum_{jj'} \int \langle j', j \rangle e^{-i\omega t} dt \\ & + \frac{k_f}{k_i} \frac{1}{2\pi\hbar} \{\bar{b}^2 - (\bar{b})^2\} \sum_j \int \langle j, j \rangle e^{-i\omega t} dt. \end{aligned} \quad (2.8)$$

Here,  $\bar{b}$  and  $\bar{b}^2$  are the averages of  $b_i$  and  $b_i^2$  respectively. The first term in equation 2.8 is known as the coherent cross-section and the second term is known as the incoherent cross-section. Physically, the coherent cross-section looks into the correlation between two atoms at different times as if they both had the same scattering length  $\bar{b}$ . The incoherent cross-section looks into the correlation between the same atom at different times [58].

For this thesis work, the desired information is in the coherent signal, and the incoherent scattering signal is treated as a background. This is because the coherent part of the signal contains information about the structure and the collective excitations. For single crystal scattering, the most discernible difference between the two signals is that incoherent scattering is approximately isotropic whilst coherent scattering changes rapidly with changes in the scattering vector.

### 2.1.2 Scattering from a Crystal

The neutron scattering from a crystal can be separated into two main components. These are nuclear scattering and magnetic scattering which respectively represent interactions with the nuclei or with the electrons of the crystal. A scattering event can also be elastic ( $E_i = E_f$ ) or inelastic ( $E_i \neq E_f$ ). From nuclear elastic

scattering, one can obtain information regarding to the crystal structure such as atom positions and lattice parameters. From magnetic elastic scattering, one can obtain information about the magnetic structure, such as the orientations of the moments and average moment size. With inelastic scattering events, one can observe nuclear or magnetic excitations within the crystal.

## Nuclear Scattering

When neutrons scatter from a nucleus within a crystal, it can displace it from its equilibrium position,  $\mathbf{R}_i$  by a small amount  $\mathbf{u}_i$ . The nucleus will feel a force pulling it towards the equilibrium position, similar to a classical spring-mass system. These displacements in the crystal are treated via a quantum harmonic oscillator model first developed by Bloch [58,60]. For elastic scattering from a primitive crystal, the coherent part of the differential cross-section has a relatively simple form given by:

$$\left(\frac{d\sigma}{d\Omega}\right)_{coh. \ el.} = N(\bar{b})^2 \frac{(2\pi)^3}{v_o} e^{-2W} \sum_{\boldsymbol{\tau}} \delta(\mathbf{Q} - \boldsymbol{\tau}_{(hkl)}). \quad (2.9)$$

Here,  $N$  is the number of unit cells in the crystal,  $v_o$  is the volume of the unit cell,  $W$  is the Debye-Waller factor. The sum is performed for integer values of  $(hkl)$ . The exponential with the Debye-Waller factor originates from considerations of atom vibrations. For isotropic displacements the Debye-Waller factor is proportional to the mean of the atom displacement squared,  $W \propto \langle u^2 \rangle$ . The most important result from equation 2.9 is that it will only be non-zero for integer values of  $(hkl)$ . This is in fact the Laue condition for diffraction as discussed in section 1.3.2. Therefore, with elastic neutron scattering, the real space lattice parameters of the crystal can be determined.

For non-primitive crystals, there is not necessarily intensity for all integer values of  $(hkl)$ . This is dependent on the nuclear structure factor  $F_N(Q)$ . For a non-primitive crystal the differential cross-section becomes:

$$\left(\frac{d\sigma}{d\Omega}\right)_{coh. el.} = N \frac{(2\pi)^3}{v_o} \sum_{\boldsymbol{\tau}} \delta(\boldsymbol{Q} - \boldsymbol{\tau}) |F_N(\boldsymbol{Q})|^2, \quad (2.10)$$

where  $F_N(Q)$  is defined as:

$$F_N(\boldsymbol{Q}) = \sum_{\boldsymbol{r}} \bar{b}_{\boldsymbol{r}} e^{\boldsymbol{Q} \cdot \boldsymbol{r}} e^{-W_{\boldsymbol{r}}}. \quad (2.11)$$

Note that the small  $\boldsymbol{r}$  refers to the position of the atom within the unit cell and the summation is performed only within the unit cell.  $W_{\boldsymbol{r}}$  and  $b_{\boldsymbol{r}}$  represent the Debye-Waller factor and scattering length of the atoms at position  $\boldsymbol{r}$  respectively. The structure factor is important because it contains information about atomic positions and also the elements at these positions (due to scattering length). By measuring many neutron Bragg peak intensities, and comparing their intensities, it is possible to solve the chemical composition and structure of a crystal [61, 62].

## Magnetic scattering

Aside from scattering from the nucleus of an atom, the neutron can also scatter from the electrons of the atom. The neutron has a magnetic moment which interacts with the magnetic field generated by the electrons. Only the unfilled electron shells contribute to the magnetic field, therefore only the unfilled electrons interact with the neutrons. The partial differential cross-section for magnetic scattering is slightly different to the nuclear one. It is necessary to consider the spin state of the neutron  $\sigma$  in the differential cross-section:

$$\left(\frac{d^2\sigma}{d\Omega dE_f}\right)_{\sigma_i \lambda_i \rightarrow \sigma_f \lambda_f} = \frac{k_f}{k_i} \left(\frac{m}{2\pi\hbar^2}\right)^2 |\langle \boldsymbol{k}_f \sigma_f \lambda_f | V_m | \boldsymbol{k}_i \sigma_i \lambda_i \rangle|^2 \delta(E_{\lambda_i} - E_{\lambda_f} + \hbar\omega). \quad (2.12)$$

Here,  $V_m$  is the magnetic potential,  $\sigma_i$  and  $\sigma_f$  are the initial and final spin states of the neutron, and  $\hbar\omega$  is defined as  $\hbar\omega = E_i - E_f$ . The electrons contribute to the

magnetic potential in two ways. The first is simply due to an electron's internal magnetic moment, and the second is due to its orbital motion, which creates a magnetic field. The partial differential cross-section for magnetic scattering can be stated as:

$$\left( \frac{d^2\sigma}{d\Omega dE_f} \right)_{\sigma_i \lambda_i \rightarrow \sigma_f \lambda_f} = (\gamma r_0)^2 \frac{k_f}{k_i} |\langle \sigma_f \lambda_f | \boldsymbol{\sigma} \cdot \boldsymbol{\mathcal{M}}_{\perp} | \sigma_i \lambda_i \rangle|^2 \delta(E_{\lambda_i} - E_{\lambda_f} + \hbar\omega). \quad (2.13)$$

$\gamma$  is a constant with  $\gamma=1.913$ ,  $r_0$  is the classical electron radius with  $r_0 \sim 10^{-15}\text{m}$ .  $\boldsymbol{\sigma}$  is the Pauli spin operator and it is related to the spin of the neutron via  $\boldsymbol{\sigma} = 2\mathbf{S}/\hbar$ .  $\boldsymbol{\mathcal{M}}_{\perp}$  is defined as:

$$\boldsymbol{\mathcal{M}}_{\perp} = \sum_i e^{i\mathbf{Q} \cdot \mathbf{r}_i} \left[ \hat{\mathbf{Q}} \times (\mathbf{s}_i \times \hat{\mathbf{Q}} + \frac{i}{\hbar Q} (\mathbf{p}_i \times \hat{\mathbf{Q}})) \right]. \quad (2.14)$$

Here, the two terms in the square brackets represent magnetic fields due to spin and orbital motion respectively. The operator  $\boldsymbol{\mathcal{M}}_{\perp}$  is related to the magnetisation of the system. The term  $\boldsymbol{\mathcal{M}}$  corresponds to the Fourier transform of  $\mathbf{M}(\mathbf{R})$ , the operator for magnetisation at point  $\mathbf{R}$  in real space. The operator  $\boldsymbol{\mathcal{M}}_{\perp}$  is simply the component of  $\boldsymbol{\mathcal{M}}$  perpendicular to the scattering vector  $\mathbf{Q}$ . This is an important result for neutron scattering. The neutron can only probe magnetisation perpendicular to the scattering vector [58, 63].

Elastic magnetic scattering can be useful for determining the magnetic structure of a crystal. For an arbitrary magnetic structure the coherent part of the differential cross-section has the form:

$$\left( \frac{d\sigma}{d\Omega} \right)_{coh.el.} = (\gamma r_0)^2 N \frac{1}{4} F(Q)^2 e^{-2W} \sum_{\alpha, \beta} \left( \delta_{\alpha, \beta} - \hat{Q}_{\alpha} \hat{Q}_{\beta} \right) \sum_{\mathbf{l}} e^{i\mathbf{Q} \cdot \mathbf{l}} \langle S_0^{\alpha} \rangle \langle S_{\mathbf{l}}^{\beta} \rangle. \quad (2.15)$$

$\alpha$  and  $\beta$  can be x, y, or z, and  $F(\mathbf{Q})$  is the magnetic form factor. The vector  $\mathbf{l}$  is the position of the spin and  $\langle \dots \rangle$  denotes a thermal average of the operator.



The magnetic form factor is a Fourier transform of the unpaired electron density. For nuclear scattering, the nucleus can be treated as a Dirac delta function. The Fourier transformation of this would give a constant as a function of  $|\mathbf{Q}|$ . However, the electrons are spread across a much larger space and the magnetic forces have a longer range compared to nuclear forces. For these reasons,  $F(\mathbf{Q})$  is not constant with  $|\mathbf{Q}|$ , and instead it decreases rapidly with increasing  $|\mathbf{Q}|$ . The magnetic form factors for various ions have been obtained experimentally and they are tabulated in Ref. [63]. Note that the magnetic form factor also applies to inelastic magnetic signals.

The elastic magnetic scattering from an FM holds important insight into magnetic scattering. The coherent part of the elastic magnetic scattering differential cross-section has a very simple form for a FM:

$$\left(\frac{d\sigma}{d\Omega}\right)_{coh.el.} = (\gamma r_0)^2 N \frac{(2\pi)^3}{v_0} \langle S^z \rangle^2 \sum_{\boldsymbol{\tau}} \frac{1}{4} g^2 F(\boldsymbol{\tau})^2 e^{-2W} [1 - (\hat{\boldsymbol{\tau}} \cdot \hat{\mathbf{z}})^2] \delta(\mathbf{Q} - \boldsymbol{\tau}) \quad (2.16)$$

Here it has been assumed that there is only one ferromagnetic domain and the spins are oriented along the  $\hat{\mathbf{z}}$  direction. It can be seen that there will only be intensity when  $\mathbf{Q}$  is at a reciprocal lattice point. The intensity will be proportional to the square of average component of the spin along  $\hat{\mathbf{z}}$  direction. Here it can also be seen that when  $\mathbf{Q} // \hat{\mathbf{z}}$ , there will be no intensity, which was the general result obtained for magnetic scattering from equation 2.13. Equation 2.16 can be re-written in the form:

$$\left(\frac{d\sigma}{d\Omega}\right)_{coh.el.} = (\gamma r_0)^2 \frac{(2\pi)^3}{v_0} \langle S^z \rangle^2 \sum_{\boldsymbol{\tau}} e^{-2W} \delta(\mathbf{Q} - \boldsymbol{\tau}) |\hat{\boldsymbol{\tau}} \times \{\mathcal{F}(\boldsymbol{\tau}) \times \hat{\boldsymbol{\tau}}\}|^2 \quad (2.17)$$

Here  $\mathcal{F}(\mathbf{Q})$  is the Fourier transform of the average magnetisation  $\langle \mathbf{M}(\mathbf{r}) \rangle$ . Therefore, by measuring the magnetic intensity of Bragg peaks for a FM, it is possible to

obtain the average magnetisation  $\langle \mathbf{M}(\mathbf{r}) \rangle$ . This result can be extended to any FM component of a magnetic structure. For example a paramagnet will scatter isotropically; however, with a field applied along the  $\hat{z}$  direction, a net FM component will appear. By measuring the change in intensity at FM Bragg peak positions, one can establish the change in the average magnetisation  $\langle \mathbf{M}(\mathbf{r}) \rangle$  [58].

## Inelastic Neutron Scattering

So far it has been shown that with elastic neutron scattering events, information about the nuclear and magnetic structures of the crystal can be obtained. These are the static properties of the crystal. One can also look at inelastic neutron scattering processes where  $E_i \neq E_f$ . Inelastic scattering experiments provide a way to study the excitations within the crystal. Typically, the excitations are treated as purely structural or purely magnetic in origin, similar to the elastic case.

The excitations of the magnetic system are spin waves. In section 1.3.4, the spin-wave dispersion,  $\hbar\omega_{\mathbf{q}}$ , was derived for a FM system. When the neutron interacts with the magnetic system inelastically, it can create or destroy one magnon. The partial-differential cross-section for such a process is:

$$\begin{aligned} \left( \frac{d^2\sigma}{d\Omega dE_f} \right)_{\sigma_i \lambda_i \rightarrow \sigma_f \lambda_f} &= (\gamma r_0)^2 \frac{k_f}{k_i} \frac{1}{4\pi\hbar} S(1 + \hat{Q}_z^2) \left[ \frac{1}{2} g F(\mathbf{Q}) \right]^2 e^{-2W} \\ &\times \sum_{\tau, \mathbf{q}} [\langle n_{\mathbf{q}} + 1 \rangle \delta(\hbar\omega_{\mathbf{q}} - \hbar\omega) \delta(\mathbf{Q} - \mathbf{q} - \boldsymbol{\tau}) \\ &\quad + \langle n_{\mathbf{q}} \rangle \delta(\hbar\omega_{\mathbf{q}} + \hbar\omega) \delta(\mathbf{Q} + \mathbf{q} - \boldsymbol{\tau})]. \end{aligned} \quad (2.18)$$

Note only in this equation,  $g$  is not the  $g$  factor, instead it is the Landé splitting factor. The value of this factor only depends on the spin and total angular quantum numbers  $S$  and  $J$  respectively. In equation 2.18, the  $\langle n_{\mathbf{q}} + 1 \rangle$  and  $\langle n_{\mathbf{q}} \rangle$  terms represent magnon creation and annihilation terms respectively. The term  $\langle n_{\mathbf{q}} \rangle$  is the thermal

average of magnon density at  $\mathbf{q}$ . Its value is given by Bose-Einstein statistics:

$$\langle n_{\mathbf{q}} \rangle = 1/(e^{\hbar\omega_{\mathbf{q}}/(k_B T)} - 1), \quad (2.19)$$

where  $k_B$  is the Boltzmann constant and  $T$  is the temperature.

The excitations of the nuclear lattice are collective lattice vibrations. These excitations can be represented by the quasi particle phonon. For systems with many atoms in a unit cell the calculation of the phonon dispersions can become complicated. For this reason phonon dispersions are often calculated using software algorithms such as CASTEP [64] which rely on first-principles density-functional theory (DFT). DFT is based on using approximate functions (i.e. functionals) for the electron density in order to find the minimum energy, therefore the ground state of the system [65,66]. The one phonon partial differential cross-section can be stated as:

$$\begin{aligned} \left( \frac{d^2\sigma}{d\Omega dE} \right)_{coh.} = & \frac{k_f}{k_i} \frac{(2\pi)^3}{2v_0} \sum_s \sum_{\boldsymbol{\tau}} \frac{1}{\omega_s} \left| \sum_{\mathbf{r}} \frac{\overline{b_{\mathbf{r}}}}{\sqrt{M_{\mathbf{r}}}} e^{-W_{\mathbf{r}}} e^{-i\mathbf{Q} \cdot \mathbf{r}} (\mathbf{q} \cdot \mathbf{e}_{s,\mathbf{r}}) \right|^2 \\ & \times [\langle n_s + 1 \rangle \delta(\omega - \omega_s) \delta(\mathbf{Q} - \mathbf{q} - \boldsymbol{\tau}) \\ & + \langle n_s \rangle \delta(\omega + \omega_s) \delta(\mathbf{Q} + \mathbf{q} - \boldsymbol{\tau})]. \end{aligned} \quad (2.20)$$

The phonon energy is given by  $\hbar\omega_s$ . The index  $s$  represents two different indices  $\mathbf{q}$  and  $j$ . The index  $j$  has value 1,2,3 and they refer to the different polarisations of the displacement which is labelled by the unit vector  $e_j$ . The term  $\mathbf{e}_{s,\mathbf{r}}$  refers to the polarisation vector of mode  $s$  for the atom with equilibrium position  $\mathbf{r}$ .  $M_{\mathbf{r}}$  is the mass of the atom with equilibrium position  $\mathbf{r}$ . The  $\langle n_s \rangle$  and  $\langle n_s + 1 \rangle$  terms correspond to the one phonon destruction and creation terms respectively, similar to that for the magnon cross-section equation 2.18.

The phonon or spin-wave excitations can have multiple branches in the Brillouin zone. The lowest energy branch is referred as the acoustic branch whereas the higher

energy branches are called the optic branches. The observed neutron intensity along these branches often varies in  $\mathbf{Q}$ -energy space. Part of this dependence can be derived from the respective Hamiltonian of the system. The intensity also depends on the type of inelastic scattering event that has occurred. In the scattering event the neutron can gain energy or lose energy. A neutron energy loss ( $E_i > E_f$ ) event will correspond to the neutron creating a phonon or magnon with momentum given by the scattering vector  $\mathbf{Q}$  and energy  $\hbar\omega = E_i - E_f$ . A neutron energy gain ( $E_f > E_i$ ) corresponds to an annihilation of a phonon or magnon with momentum  $\mathbf{Q}$  and energy  $\hbar\omega = E_f - E_i$ . These two processes are similar; however, they are dependent on the energy population of the magnons and phonons. At low temperatures, the higher energy excitations will not be populated. Therefore, a neutron energy gain event will have a much lower intensity compared to the equivalent neutron energy loss event [58]. To understand this one must look at the coherent scattering function  $S(\mathbf{Q}, \omega)$  defined as:

$$\left( \frac{d^2\sigma}{d\Omega dE_f} \right)_{coh} = A \frac{k_f}{k_i} S(\mathbf{Q}, \omega), \quad (2.21)$$

where  $A$  is an arbitrary constant. The scattering function is a function of the scattering wavevector  $\mathbf{Q}$  and energy  $\hbar\omega$ . The difference between neutron energy gain and neutron energy loss is stated as:

$$S(\mathbf{Q}, \omega) = e^{\hbar\omega/(k_B T)} S(-\mathbf{Q}, -\omega). \quad (2.22)$$

This equation is known as the principle of detailed balance. As the temperature is increased, more higher energy states are populated and the difference between neutron energy loss and energy gain events decreases.

Aside from the detailed balance, the intensity of phonons and magnons also have their own temperature dependence. This dependence is generally different for phonons and magnons. In order to determine if an unknown excitation is from a

phonon or magnon, one could look at the temperature dependence of the excitation. For magnons, one might expect the intensity to fall to zero at temperatures above the ordering temperature, whereas for phonons, one might expect the intensity to increase due to the population factor. Another method to differentiate between a phonon and magnon branch is to look at its  $|\mathbf{Q}|$  dependence. As discussed before the average magnon intensity falls with  $|\mathbf{Q}|$  as determined by the magnetic form factor. On the contrary, the intensity of a single phonon cross-section, on average, increases with a  $Q^2$  dependence [58]. Differentiating between magnon and phonon branches can become quite difficult in some circumstances. Even though the temperature and  $|\mathbf{Q}|$  dependence provides some insight to the origin of an excitation, it is not sufficient on its own. The most rigorous way to differentiate between magnons and phonons is to perform a polarised neutron experiment, the details which will be explained in the following section.

### 2.1.3 Polarisation Analysis

The initial and final spin states of the neutron hold important knowledge about the scattering system. So far, the spin state of the neutron has been ignored for simplicity. The spin of the neutron can be denoted in the vectorial operator  $\mathbf{S}$ , with components  $S_x, S_y, S_z$ . The eigenvalues of  $S_z$  are  $\pm 1/2\hbar$ ; therefore, a neutron is either “up” or “down” with respect to an arbitrary direction. Instead of the  $\mathbf{S}$  operator, it is more convenient to use the Pauli spin operator  $\boldsymbol{\sigma} = 2\mathbf{S}/\hbar$ . Its components are the Pauli matrices [67]:

$$\sigma_x = \begin{pmatrix} 0 & 1 \\ 1 & 0 \end{pmatrix}, \sigma_y = \begin{pmatrix} 0 & -i \\ i & 0 \end{pmatrix}, \sigma_z = \begin{pmatrix} 1 & 0 \\ 0 & -1 \end{pmatrix}. \quad (2.23)$$

The operator  $\sigma_z$  has eigenvalues  $\pm 1$  and does not change the eigenstate. The operators  $\sigma_x$  and  $\sigma_y$  operators change the eigenstates from  $\sigma_z = +1$  to  $\sigma_z = -1$  and

vice versa [68].

The polarisation of a the  $j$ -th neutron in a neutron beam is defined as  $\mathbf{p}_j = \langle \boldsymbol{\sigma} \rangle$ . The polarisation of a neutron beam for an arbitrary direction,  $P_\alpha$ , is defined as:

$$P_\alpha = \frac{1}{N} \sum_j \mathbf{p}_j = \frac{n_\uparrow - n_\downarrow}{n_\uparrow + n_\downarrow} \quad (2.24)$$

Here  $N$  is the total number of neutrons, whereas  $n_\uparrow$  and  $n_\downarrow$  are the number of neutrons which are in the spin up and spin down states respectively. Using this definition,  $P=0$  refers to the unpolarised case, whilst  $P=-1$  or  $P=1$  refer to perfect polarisation [67]. Another commonly used value to define the polarisation is the flipping ratio  $F = n_\uparrow/n_\downarrow$  [63, 69].

The partial differential cross-section for a polarised scattering event starts of similar to the unpolarised case shown in equation 2.3.

$$\left( \frac{d^2\sigma}{d\Omega dE_f} \right)_{\sigma_i \rightarrow \sigma_f} = \frac{k_f}{k_i} |\langle \mathbf{k}_f \sigma_f | \tilde{V}(Q) | \mathbf{k}_i \sigma_i \rangle|^2 \delta(E_{\lambda_i} - E_{\lambda_f} + E_i - E_f), \quad (2.25)$$

Here the neutrons spin is going from  $\sigma_i$  to  $\sigma_f$ . The potential  $\tilde{V}(Q)$  has the form:

$$\tilde{V}(Q) = \sum_n e^{i\mathbf{Q}\mathbf{R}_n} b_n - \gamma r_0 \boldsymbol{\sigma} \mathbf{M}_\perp(\mathbf{Q}). \quad (2.26)$$

The first and second terms of equation 2.26 represent scattering from the nucleus and the unfilled electron shell respectively [68]. However, unlike the unpolarised case, the nuclear scattering length  $b_n$  is now dependent on the neutron polarisation in the following way:

$$b_n = A_n + B_n \boldsymbol{\sigma} \mathbf{I}, \quad (2.27)$$

where  $A_n$ ,  $B_n$  are constants and  $\mathbf{I}$  is the spin of the nucleus. It is typically assumed that the nuclear spin direction or the isotope distribution does not have any correlation in the system. This assumption will be used in this thesis also. Therefore,

scattering from the nuclear spin will only contribute to incoherent scattering [68]. The coherent part of the nuclear scattering can be given by the operator:

$$N(\mathbf{Q}) = \sum_n e^{i\mathbf{Q}\mathbf{R}_n} \bar{b}_n, \quad (2.28)$$

where  $\bar{b}_n = \overline{A}_n$ . It is important to note that this operator does not depend on the neutron spin. Therefore, coherent nuclear scattering events does not have any effect on the neutron spin. However, the neutrons spin direction does factor into magnetic scattering. Ignoring nuclear spin scattering, the magnetic scattering cross-section will have a component of the form:

$$\langle \mathbf{k}_f \sigma_f | \boldsymbol{\sigma} \mathbf{M}_\perp | \mathbf{k}_i \sigma_i \rangle \approx \sum_\alpha \langle \sigma_f | \sigma_\alpha | \sigma_i \rangle \langle \mathbf{k}_f | M_\perp^\alpha | \mathbf{k}_i \rangle. \quad (2.29)$$

Here, the neutron spin element is separated from the sample. In this form, some important observations can be made. For fields parallel or antiparallel to the neutron spin, the neutron spin is left unchanged. However, for fields orthogonal to the initial neutron spin, a spin flip will occur, i.e. neutron spin will go from spin “up” to spin “down” or vice versa [68].

The elastic-scattering partial-differential cross-section for polarised neutrons is given by the Blume-Maleyev equations [68, 70–72] :

$$\begin{aligned} \frac{d^2\sigma}{d\Omega dE_f} = & \langle N^* N \rangle_{T,\omega} + \langle \mathbf{M}_\perp^* \mathbf{M}_\perp \rangle_{T,\omega} + \langle N^* [\mathbf{P}_i \mathbf{M}_\perp] \rangle_{T,\omega} + \langle N [\mathbf{P}_i \mathbf{M}_\perp^*] \rangle_{T,\omega} \\ & + i \mathbf{P}_i \langle \mathbf{M}_\perp^* \times \mathbf{M}_\perp \rangle_{T,\omega} + \langle \nu_i \rangle_T + \langle \sigma_{nsi} \rangle_T. \end{aligned} \quad (2.30)$$

The terms  $N$  and  $\mathbf{M}_\perp$  represents the coherent nuclear scattering and coherent magnetic scattering at  $\mathbf{Q}$ . The initial polarisation of the neutron beam is given by  $\mathbf{P}_i$ . The terms,  $\nu_i$  and  $\sigma_{nsi}$  represent the nuclear isotope incoherent and nuclear spin incoherent signals respectively. The subscript  $T$  and  $\omega$  represent a thermal average

and a time Fourier transform respectively [68]. The inelastic scattering version of this equation can be found in Ref. [72].

### XYZ Polarisation Analysis

XYZ polarisation analysis is one of the ways of using polarised neutrons to study magnetic and nuclear excitations in crystals. A coordinate system is created such that  $\hat{\mathbf{x}} // -\mathbf{Q}$ ,  $\hat{\mathbf{y}}$  is perpendicular but in the scattering plane, and  $\hat{\mathbf{z}}$  is perpendicular to the scattering plane. The initial and final polarisations of the neutron are measured along these directions. For example, consider a neutron with initial spin along  $\hat{\mathbf{z}}$  but after a spin-flip the final spin is along  $-\hat{\mathbf{z}}$ . This would be denoted by the partial differential cross-section  $\left(\frac{d^2\sigma}{d\Omega dE_f}\right)_{z\bar{z}}$  or for simplicity, by  $\sigma_{z\bar{z}}$ . The different elastic-scattering cross-sections and their contributions can be seen in table 2.1 [73]. Here, only scattering processes in which initial and final polarisation are parallel or anti-parallel have been considered. Thermal averages and time Fourier transforms such as shown in equation 2.30 is omitted in this table for sake of clarity. For the inelastic scattering case, the results in table 2.1 should be scaled by  $k_f/k_i(1/e^{-\omega/T})^{-1}$ , where  $\omega$  is the change in neutron energy and  $T$  is temperature.



$$\begin{aligned}
\sigma_{xx} &= NN^* + \nu_i + \frac{1}{3}\sigma_{nsi} \\
\sigma_{\bar{x}\bar{x}} &= NN^* + \nu_i + \frac{1}{3}\sigma_{nsi} \\
\sigma_{x\bar{x}} &= \mathbf{M}_\perp^* \mathbf{M}_\perp + i\hat{\mathbf{x}} \cdot (\mathbf{M}_\perp^* \times \mathbf{M}_\perp) + \frac{2}{3}\sigma_{nsi} \\
\sigma_{\bar{x}x} &= \mathbf{M}_\perp^* \mathbf{M}_\perp - i\hat{\mathbf{x}} \cdot (\mathbf{M}_\perp^* \times \mathbf{M}_\perp) + \frac{2}{3}\sigma_{nsi} \\
\hline
\sigma_{yy} &= NN^* + (\mathbf{M}_\perp \hat{\mathbf{y}})(\mathbf{M}_\perp^* \hat{\mathbf{y}}) + \hat{\mathbf{y}} \cdot (\mathbf{M}_\perp N^* + \mathbf{M}_\perp^* N) + \nu_i + \frac{1}{3}\sigma_{nsi} \\
\sigma_{\bar{y}\bar{y}} &= NN^* - (\mathbf{M}_\perp \hat{\mathbf{y}})(\mathbf{M}_\perp^* \hat{\mathbf{y}}) + \hat{\mathbf{y}} \cdot (\mathbf{M}_\perp N^* + \mathbf{M}_\perp^* N) + \nu_i + \frac{1}{3}\sigma_{nsi} \\
\sigma_{y\bar{y}} &= (\mathbf{M}_\perp \hat{\mathbf{z}})(\mathbf{M}_\perp^* \hat{\mathbf{z}}) + \frac{2}{3}\sigma_{nsi} \\
\sigma_{\bar{y}y} &= (\mathbf{M}_\perp \hat{\mathbf{z}})(\mathbf{M}_\perp^* \hat{\mathbf{z}}) + \frac{2}{3}\sigma_{nsi} \\
\hline
\sigma_{zz} &= NN^* + (\mathbf{M}_\perp \hat{\mathbf{z}})(\mathbf{M}_\perp^* \hat{\mathbf{z}}) + \hat{\mathbf{z}} \cdot (\mathbf{M}_\perp N^* + \mathbf{M}_\perp^* N) + \nu_i + \frac{1}{3}\sigma_{nsi} \\
\sigma_{\bar{z}\bar{z}} &= NN^* - (\mathbf{M}_\perp \hat{\mathbf{z}})(\mathbf{M}_\perp^* \hat{\mathbf{z}}) + \hat{\mathbf{z}} \cdot (\mathbf{M}_\perp N^* + \mathbf{M}_\perp^* N) + \nu_i + \frac{1}{3}\sigma_{nsi} \\
\sigma_{z\bar{z}} &= (\mathbf{M}_\perp \hat{\mathbf{y}})(\mathbf{M}_\perp^* \hat{\mathbf{y}}) + \frac{2}{3}\sigma_{nsi} \\
\sigma_{\bar{z}z} &= (\mathbf{M}_\perp \hat{\mathbf{y}})(\mathbf{M}_\perp^* \hat{\mathbf{y}}) + \frac{2}{3}\sigma_{nsi}
\end{aligned}$$

**Table 2.1: XYZ polarisation cross-sections.** [73]

From table 2.1, important insights can be made. For example,  $\sigma_{xx}$  has no magnetic component  $\mathbf{M}_\perp$ , whilst  $\sigma_{y\bar{y}}$  and  $\sigma_{z\bar{z}}$  have no structural component  $N$ .

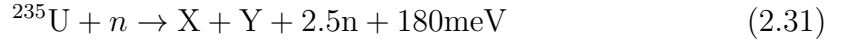
It is important to note that XYZ polarisation analysis cannot be used to study FM samples. The different magnetic domains create different internal magnetic fields which destroy the polarisation of the neutron beam [63].

## 2.2 Neutron Instrumentation

### 2.2.1 Neutron Sources

There are two different ways to obtain a flux of neutrons, through spallation or reactor sources. Spallation sources use particle accelerators to accelerate protons to high speeds before crashing them into a target material which will then

release neutrons in turn. The target material is often made from Tungsten or Lead. Spallation sources are often not continuous sources. The protons are accelerated in pulses milliseconds apart. This provides a pulsed profile to the neutron flux [63]. The exception is the SINQ spallation source [74], which provides a quasi continuous beam of neutrons. Another reliable way of obtaining neutrons is via nuclear reactors. These reactors are optimised for neutron generation and, therefore, have some differences to the typical power generating reactor. The most notable difference is that the reactors for neutron sources have a much higher concentration of  $^{235}\text{U}$  in the fuel rods, up to 93%. From fission an average of 2.5 neutrons and 180meV energy is produced [63]:



Here X and Y are the fission fragments such as  $^{141}\text{Ba}$  and  $^{92}\text{Kr}$ . When the neutrons are produced they are very fast with energies of  $\sim 1\text{MeV}$ . Their energies are lowered by collisions with the moderator, such as water or heavy water, which surrounds the fuel rods. The neutrons and the moderator come closer to a thermal equilibrium and the neutrons gain an energy profile described as Maxwell-Boltzmann distribution [75]. The highest flux is observed at the energy corresponding to the moderator temperature. For a room temperature moderator, this will result in highest flux for  $\sim 25\text{meV}$  neutrons. These are referred to as thermal neutrons. However, it is possible to pass the neutrons through materials with different temperatures to change the energy profile of the neutrons. One can pass neutrons through  $^4\text{He}$  at 20K to obtain cold neutrons, which have a highest flux at  $\sim 5\text{meV}$  or through graphite at 2700K to obtain hot neutrons, which have a highest flux at  $\sim 200\text{meV}$  [63].

The neutron experiments carried out in this thesis were performed at the high-flux reactor Institut Laue Langevin (ILL) in Grenoble, France. In the experiments either thermal or cold neutrons were used.

### 2.2.2 Three-Axis Spectrometers

Three-axis spectrometer (TAS) instruments, also called triple-axis spectrometers, get their name for the three axes of rotation which are located at the monochromator, sample, and analyser positions. A typical set up of a TAS instrument can be seen in figure 2.2 on page 48. Here the path that the neutrons follow are given in black arrows and in blue arrows, the relevant directions of  $\mathbf{Q}$ ,  $\mathbf{k}_i$ , and  $\mathbf{k}_f$  are shown. TAS instruments require a constant stream of neutrons therefore they are predominantly used at reactors neutron sources. The neutrons originating from the reactor will contain a distribution of energies. This beam is directed to the monochromator which will filter out only one energy. The sample is often surrounded by environment control apparatus which can change the temperature, pressure, magnetic or electric field strength at the sample position. In general, the neutron will scatter in every direction from the sample position; however, the analyser will only be subjected to neutrons leaving the sample in a particular direction. Out of the many different energy neutrons scattered into this direction, the analyser will filter out a specific energy which it will direct towards the detector.

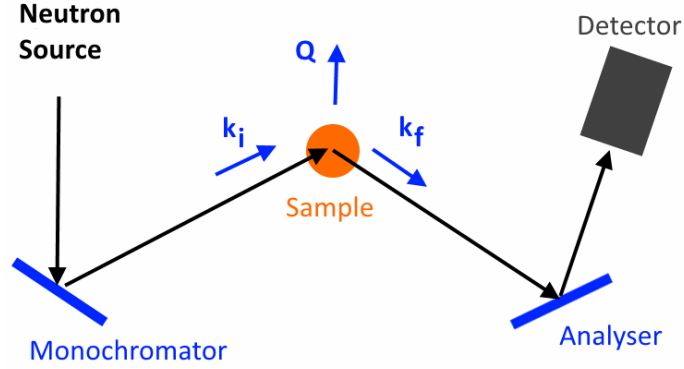


**Figure 2.2: Three-axis spectrometer.** The neutron beam direction is given in black arrows. The relative directions of  $\mathbf{Q}$ ,  $\mathbf{k}_i$ , and  $\mathbf{k}_f$  are shown in blue.

Monochromators and analysers are multi-crystal arrays, where many single crystals are glued to a flat surface. To first approximation, these arrays act like one large single crystal. The desired wavelength is picked by going to the necessary angular orientation as defined by Bragg's law (see equation 1.6). The crystals and orientations used for the monochromator and analysers are Cu(111), Si(111) or pyrolytic graphite(PG) (002). Some monochromators and analysers have vertical or horizontal bending which allows focusing of neutrons at the sample position, because the sample size is typically much smaller than the width of the beam [63].

In TAS instruments, there will always be a certain amount of higher order neutrons coming through with wavelengths  $2k_i$ ,  $3k_i$ ,...etc. For example, the Si (111) plane is used to obtain  $k_i = 2.36\text{\AA}^{-1}$ . However, at this same configuration the neutrons with  $k = 2k_i$  and  $k = 3k_i$  can also scatter from the (222) and (333) planes respectively. There are a few different ways of removing such higher order neutrons. One is to use a velocity selector between the source and the monochromator. Velocity selectors are rotating cylinders with grooves as seen in figure 2.3. They are

designed so that a neutron with a specific speed will pass through the grooves of the velocity selector without ever touching it. On the contrary neutrons too slow or too fast will touch the neutron absorbent walls and stop. The other way to remove higher order neutrons is to use filters. Filters can be from single crystals or from powders and the chemistry of the crystal is chosen to match the specific  $k_i$  used. For thermal TAS instruments a thick piece of graphite is used; however for cold TAS instruments Beryllium powder at liquid nitrogen temperatures is used instead. The cooling of the Beryllium powder improves its efficiency [63].

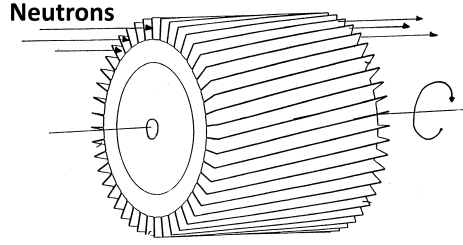


**Figure 2.3: Neutron velocity selector.** Image sourced from Ref. [76].

An example of an energy scan in reciprocal space can be seen in figure 2.4 on page 50. Here, as with most TAS experiments, the length of  $\mathbf{k}_f$  is fixed and measurements are made at various scattering angles. The energy is calculated from  $\hbar\omega = \hbar^2(k_i^2 - k_f^2)/2m_n$ . Here, as usual, one is working in the “neutron energy loss” mode.

A measurement with a TAS instrument at a given  $\mathbf{Q}, \omega$  is not a point like measurement. Instead, the measurement is of a certain volume in  $\mathbf{Q}, \omega$  defined by the instrumental resolution. The resolution of a TAS instrument can be best described as an ellipsoid in  $\mathbf{Q}, \omega$  space and is dependent on the geometry of the instrument. A TAS measurement at  $\mathbf{Q}, \omega$  corresponds to the actual signal from the signal at  $\mathbf{Q}, \omega$  convolved with the crystal mosaic and the instrumental resolution [63]. For

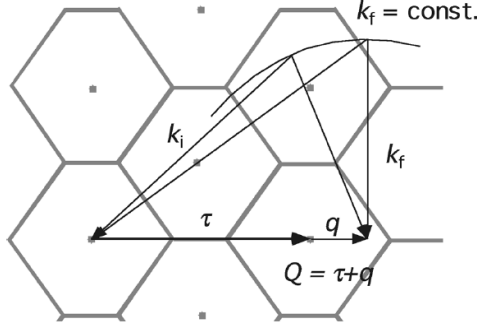


**Figure 2.4: TAS energy scan at fixed  $Q$ .** Image from Ref. [63].

inelastic neutron scattering experiments it is important to consider the tilting of the resolution ellipsoid with respect to the slope of the excitation branch measured. An example of an TAS measurement on an acoustic excitation can be seen in figure 2.5 on page 51. Here the resolution ellipsoid is given in red and the acoustic branch is given in blue. Keeping the energy,  $\hbar\omega$ , fixed, a  $q$  scan is performed where  $q = Q - \tau$ , so that the zero point is the centre of a Brillouin zone. On the lower panel, the resulting intensity from such a  $q$  scan is shown. The convolution of the resolution ellipsoid with the excitation branch results in a much broader signal on the left hand side compared to the right hand side. In such a case, one should perform most measurements of the excitation on the right hand side, as its position can be obtained much more accurately.

There are two main theoretical methods for obtaining the resolution of a TAS instrument. These are the Cooper-Nathans method [77], and the Popovici method [78]. Various resolution calculation software has been established such as ResLibCal [79] and Restrax [80]. These softwares require the physical geometry of the experimental set up to determine the size and tilt of the resolution ellipsoid. This can be particularly helpful in the planning stages of an experiment.

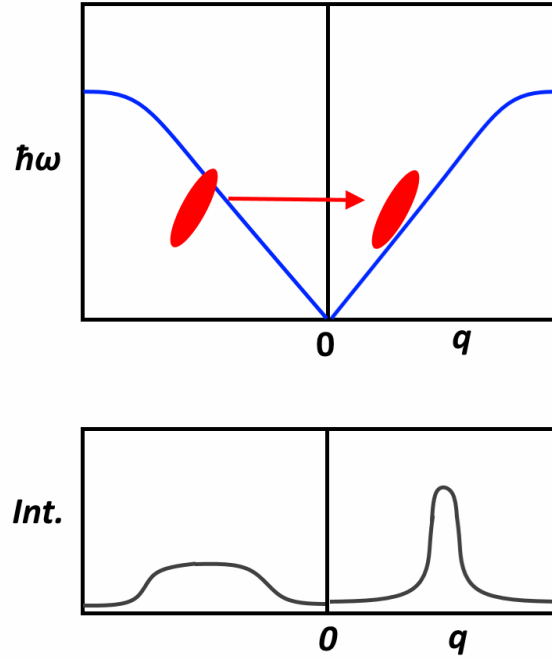


**Figure 2.5: TAS resolution ellipsoid.** Here it can be seen that due to the tilting of the resolution ellipsoid (red), the position of the excitation (blue) can be much better observed on the right hand side. The expected intensity from such a constant energy  $q$  scan can be seen in the lower panel in grey.

### 2.2.3 XYZ Polarisation Analysis

TAS instruments can be adapted to perform XYZ polarisation analysis. A typical set up of such a polarised TAS experiment can be seen in figure 2.6 on page 52. In contrast to a typical TAS experiment, three different components have been introduced. These are the flippers, the Helmholtz coil and the Heusler alloy crystals used in the monochromator and the analyser. The neutrons which originate from the reactor are unpolarised. The Heusler monochromator only reflects neutrons with the spins along the  $\hat{z}$  direction. The polarised neutron beam passes through

the first flipper which if turned on, will flip the neutron spin into  $-\hat{z}$  direction. The Helmholtz coil supplies a magnetic field around the sample so that the incoming neutron is parallel along any arbitrary direction at the sample direction. Once the neutron exits the coil, it returns to being parallel (or anti-parallel) to  $\hat{z}$  direction. The neutron passes through the second flipper where its spin can be flipped if the flipper is on. At the Heusler analyser, only neutrons with spin  $\hat{z}$  direction are reflected.

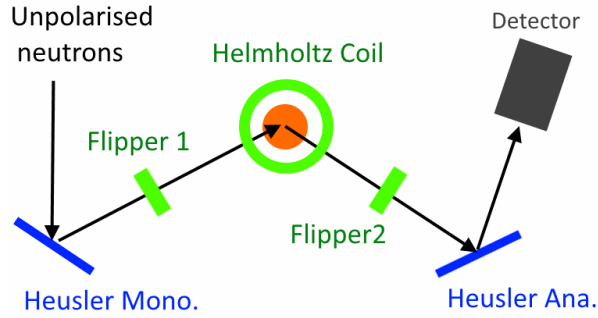


**Figure 2.6: TAS with XYZ polarisation analysis capability.**

A Heusler alloy is a ferromagnetic metal alloy. The crystals chosen for monochromators have an  $(hkl)$  reflection where the nuclear structure factor  $F_N(\mathbf{Q})$  and magnetic structure factor  $F_M(\mathbf{Q})$  are roughly the same size. The scattered intensity for a spin parallel to the internal magnetic moment is proportional to  $I \propto (F_N(\mathbf{Q})^2 + F_M(\mathbf{Q})^2)$ . For a spin anti-parallel to the internal magnetic moment the intensity is proportional to  $I \propto (F_N(\mathbf{Q})^2 - F_M(\mathbf{Q})^2)$ . This allows one to obtain a polarised beam via scattering from a crystal [63].

The flippers used in XYZ analysis are also called  $\pi$  flippers because they rotate the spin direction from  $\hat{z}$  direction to  $-\hat{z}$  direction or vice versa. This is done using coils to create a field perpendicular to  $\hat{z}$  [63, 81]. Similarly, the Helmholtz coil uses a number of coils to produce a magnetic field in any given direction. The coil set



up used on IN20 can be seen in figure 2.7(a). In figure 2.7(b), the magnetic field created from each one of the coloured coils can be seen. The magnetic field in the Helmholtz coil ensures an adiabatic rotation of the neutron polarisation axis. This way the exact polarisation at the sample position can be controlled. Once the neutron is leaving the sample, the neutron adiabatically reverts to its original polarisation axis [82].

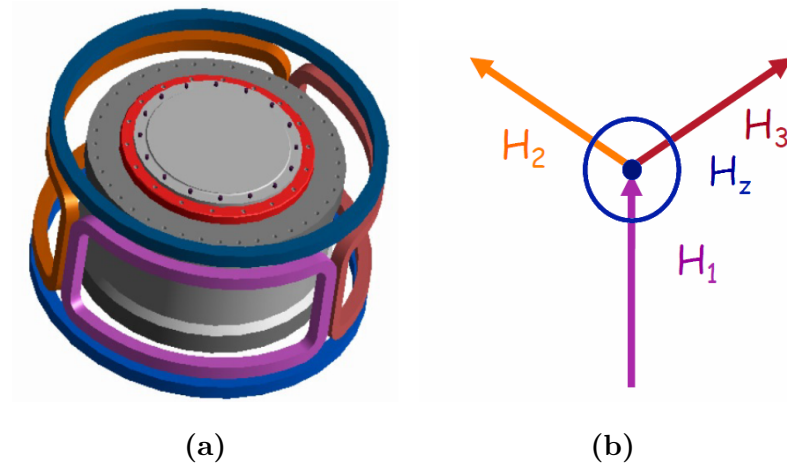


**Figure 2.7: Helmholtz coil used on IN20.** (a) The Helmholtz coils are composed of five different coils. (b) The direction of the field for each one of the coils is represented in the same colour. Image sourced from Ref. [82].

In a real experiment, there are some imperfections in the polarisation. Part of this is the inefficiencies of the flippers. One way to quantify this is to look at the flipping ratios. The direct beam or a non-magnetic sample can be used to measure the flipping ratios. For a nuclear scattering event, there should be no spin flip. If the flippers were fully efficient and the beam were fully polarised, one would expect no signal in the spin flip channels. The flipping ratios for the two flippers are defined as:

$$F_1 = \frac{I_{zz}}{I_{\bar{z}z}}, F_2 = \frac{I_{z\bar{z}}}{I_{\bar{z}\bar{z}}}. \quad (2.32)$$

Here  $I_{zz}$  refers to intensity when both flippers are off, a line on first or second term means that the respective flipper was on. An acceptable flipping ratio is 40 [63].

## 2.2.4 Neutron Instruments

### TAS instruments

For this thesis work, experiments were carried out on thermal TAS instrument IN20 and cold TAS instruments IN12, IN14, and ThALES. These instruments were based at the Institut Laue Langevin, Grenoble, France. On a thermal TAS instrument a typical energy range of 5-60meV can be expected with a resolution of 0.8-4meV. For a cold TAS instrument the typical energy range which can be explored is much lower at 0.1-10 meV with a resolution of 0.05-0.5 meV [63].

The experimental set-up for IN20 can be seen in figure 2.8 on page 55. IN20 is positioned very close to the reactor which provides it with a large neutron flux. In its polarised setting it can achieve 90% polarisation [83]. The principles of operation for most of the components have already been discussed in earlier sections. The most important components not yet discussed are the two monitors and diaphragms. The monitors are a very inefficient neutron detector (typically  $10^{-4}$ ). Monitor 1 is used as a measurement of the incoming neutron flux. This measurement is important as there can be fluctuations in the reactor power which in turn result in changes in the neutron flux. However, if one normalises the counts in the detectors to the flux as measured by Monitor 1, this will not be a problem. The second monitor is useful for troubleshooting spurious signals [63]. The diaphragms are made of neutron absorbent materials and are used to reduce the size of the neutron beam. It is common in TAS experiment to use a sample which is many times smaller than

the width and height of the beam at sample position. The neutrons which do not scatter from the sample can end up in the detector and cause an increase in the background. For this reason, the two diaphragms are closed as much as possible. Various Bragg peaks are checked as the diaphragms are closed to make sure there is no signal being lost from the sample.

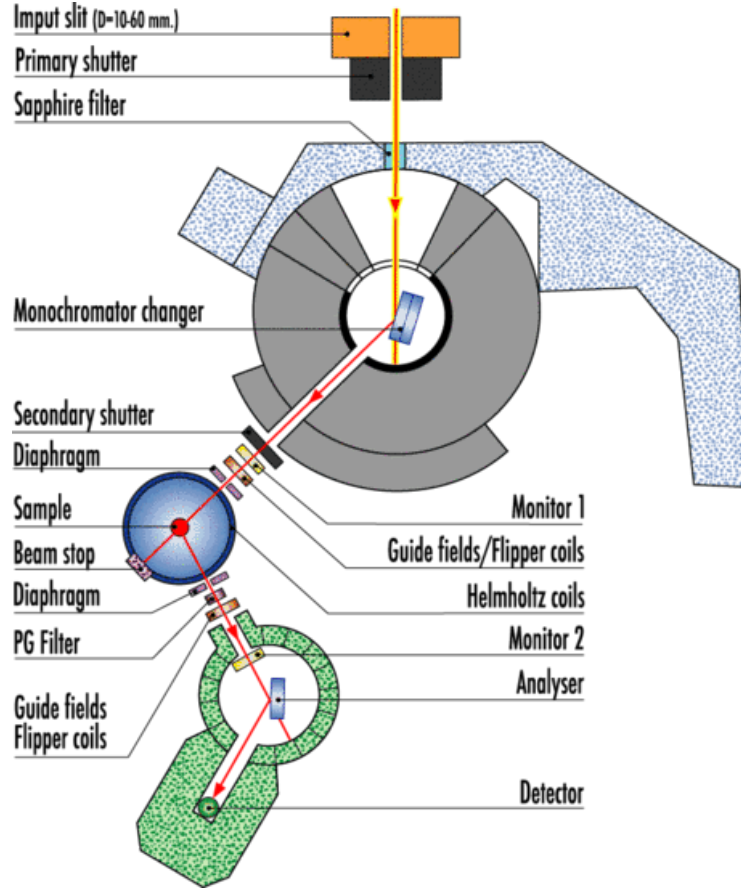


**Figure 2.8: IN20 Three-axis spectrometer.** Image from Ref. [83].

The experimental set-up of cold TAS instruments ThALES and IN12 are very similar. The set-up of IN12 can be seen in figure 2.9 on page 56, but this set up is also representative of ThALES. The main difference between IN12 and IN20's set up is that IN12 has a velocity selector placed before the monochromator. This reduces

the number of second and third order neutrons the sample will be subjected to. The cold TAS IN14 is now a decommissioned instrument which has been replaced by ThALES. The experimental set up of IN14 was similar to that of IN12, with the main difference that there was no velocity selector. For this reason a beryllium filter was used instead to filter out the second and third order neutrons. A photograph of the IN14 instrument can be seen in figure 2.10 on page 57. Here the monochromator is positioned behind the circular shielding. The sample is surrounded by environment control unit. Between the sample and the analyser is the beryllium filter which is cooled down by liquid nitrogen. Finally past the analyser the detector can be seen.

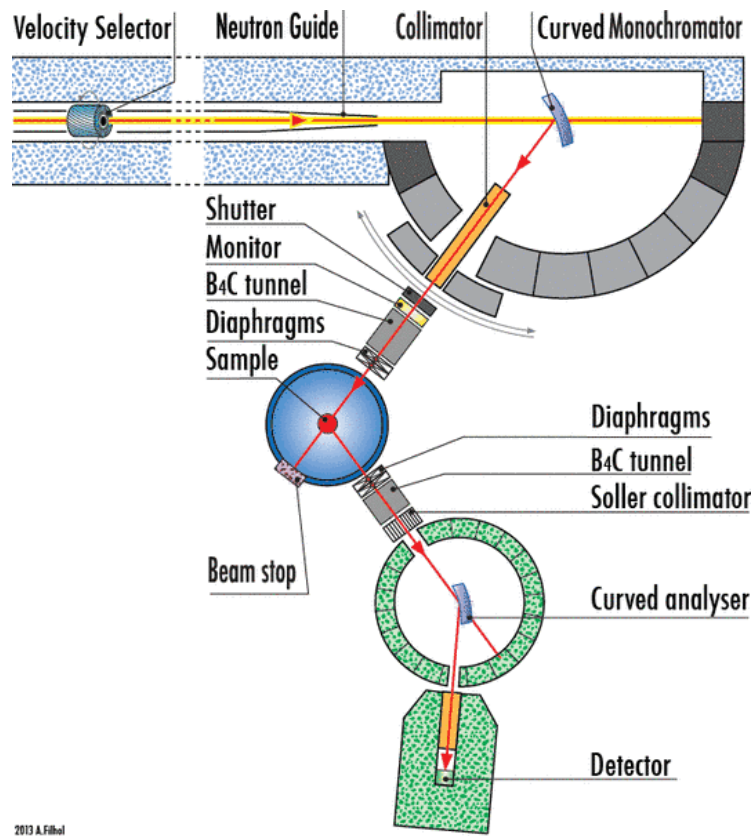


**Figure 2.9: IN12 Three-axis spectrometer.** Image from Ref. [83].



**Figure 2.10: IN14 Three-axis spectrometer.** Image from Ref. [83].

### Neutron diffractometer

Also used in this thesis work is the diffractometer D23 based at the Institut Laue Langevin, Grenoble, France. Its principle is very similar to that of the TAS instrument; however, it does not have an analyser. The set up of D23 can be seen in figure 2.11 on page 58. Here it can be seen that the detector is placed directly after the sample. The detector can tilt out of the horizontal plane to explore different scattering planes. It can accommodate complex sample environments in order to supply large magnetic fields, low temperatures, or high pressures. It is used for magnetic structure and magnetic phase diagram determination [83].

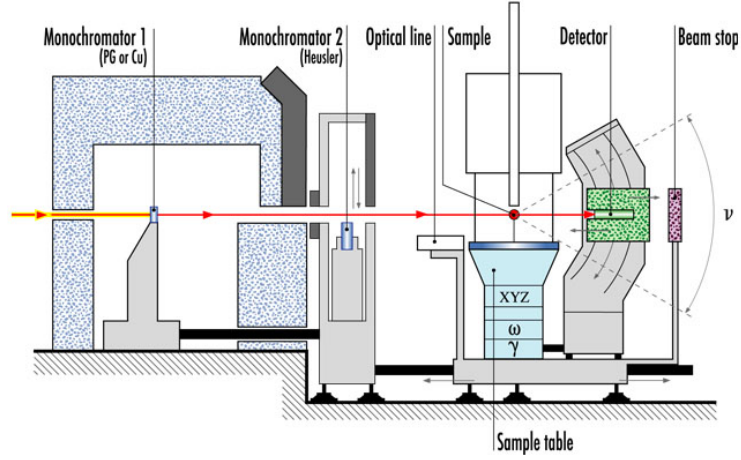


Figure 2.11: D23 diffractometer. Image from Ref. [83].

## 2.3 Magnetometry

Magnetometry is the experimental method of measuring the magnetic response of a sample for changing environmental conditions such as temperature or applied field. For crystals with net magnetic moments, the measurement of magnetic moment can be very useful. Most importantly it can be used as a tool to identify magnetic phase transitions. A discontinuity in magnetisation or its derivatives can indicate a phase transition in the system. Aside from identifying phase transitions, the magnetisation measurements can provide information with regards to the nature of the magnetic phase. This can be through the phase transition, or through comparing the temperature or field dependence to other known systems [84].

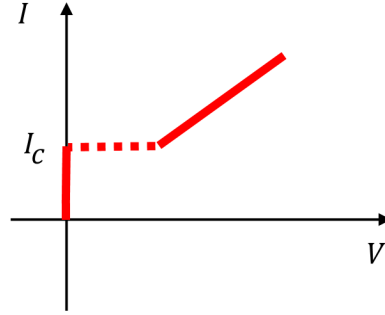
### 2.3.1 SQUID Magnetometry

One of the most sensitive methods for measuring magnetic field is through a device called SQUID, which stands for “superconducting quantum interference

device”. They make use of interference effects between two superconductors to detect very small changes in magnetic field. They act as devices that convert magnetic flux into voltage and they are the most sensitive detectors of their kind [85].

The operation of SQUIDs are based on two important phenomena regarding superconductivity: the quantisation of flux and Josephson junctions. The flux inside a superconducting ring will always be quantised in units of flux quantum  $\Phi_0 = h/2e$  where  $h$  is the Planck’s constant and  $e$  is the electric charge. The Josephson junction is composed of two superconducting materials separated by a thin non-superconducting material. Josephson suggested that the Cooper pairs would be able to tunnel through the non-superconducting material [86]. Starting from zero, an increase in current ( $I$ ) will not result in an increase in potential ( $V$ ) because at low currents, the Cooper pairs can tunnel through the non-superconducting material. This is known as the DC (direct current) Josephson effect. However, past a critical current  $I_c$ , the junction no longer acts like a superconductor and potential difference is created across the junction. The IV behaviour for increasing current can be seen in figure 2.12 on page 60 [85]. The critical current  $I_c$  is dependent on the phase difference of the two superconductors. This phase difference between the two superconductors oscillates as a function of time in the non-zero-voltage region. This is known as the AC Josephson effect.

The SQUID is composed of a superconducting ring which has one or two Josephson junctions on it. The version with two junctions is called the DC SQUID and the version with one junction is called the rf SQUID. These SQUIDs rely on the DC and AC Josephson effects respectively to operate. Here rf stands for radio frequency, as the electronics in a rf SQUID requires an oscillating current in the radio-frequency range.



(a)

**Figure 2.12: IV curve for a Josephson junction.** Starting from zero current, the system acts like a superconductor until it reaches a critical current  $I_c$ , after which it has a non-zero potential difference across it [85].

### 2.3.2 Magnetometry Instrumentation

The magnetometer used in this thesis is the Quantum Design Magnetic Properties Measurement System (MPMS). The MPMS is capable of reaching temperatures as low as 1.8K and field strengths of 7 Tesla. The set up of the instrument can be seen in figure 2.13 on page 61 [87].

The sample is temperature controlled by  $^4\text{He}$  based cryogenics and the applied magnetic field is controlled by a superconducting magnet. The magnetic moment at the sample position is not measured directly by the SQUID. Instead a superconducting coil is used to pick up the signal, which is referred to as the detection coil. As seen in figure 2.14 on page 61, this coil has two positive and two negative turns. This configuration is helpful for minimising signals originating from the fluctuations in the applied magnetic field. A measurement is taken by moving the sample through the coils. The samples magnetic field will cause a current change in the detection coil which will be then sent to a rf SQUID. The detection coil and the rf SQUID are not wired together, instead they are connected inductively [87].



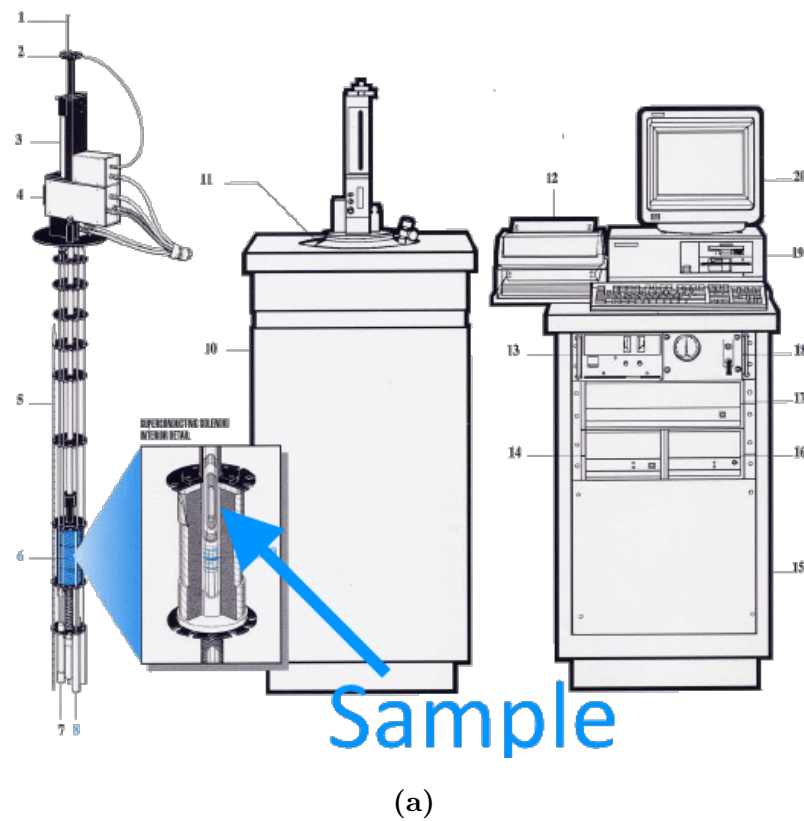


**Figure 2.13: Quantum Design MPMS.** Image sourced from Ref. [87].

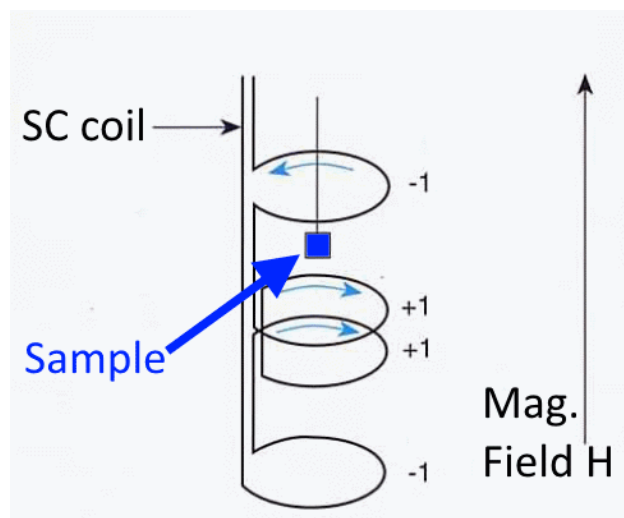


**Figure 2.14: Detection coil in the MPMS.** A measurement is taken by moving the sample through the coils. This creates an electric signal which is sent to the SQUID. Image sourced from Ref. [87].

# Chapter 3

## $\text{Na}_x\text{CoO}_2$

### 3.1 Introduction

$\text{Na}_x\text{CoO}_2$  has received attention for a wide range of properties. It has been considered as a battery electrode material [2], a model thermoelectric [1], and also it is the first Co based superconductor to be discovered [3]. For  $x > 0.65$  small magnetic moments appear at  $T_N \sim 22\text{K}$  [88, 89]. The suggested magnetic structure is an A-type AFM structure with spins along the  $\mathbf{c}$  axis. However, there are large number of anomalies below  $T_N$  which requires a more complex magnetic structure [4, 88–92]. Some of these models suggest a magnetic patterning influenced by the long range Na superstructures known to exist in  $\text{Na}_x\text{CoO}_2$  [17, 19]. Inelastic neutron scattering experiments show a large difference of out-of-plane exchange interaction  $J_c$  for samples of very similar concentrations ( $x=0.75, x=0.82$ ) but on samples of unknown superstructures [4, 5]. There are three different superstructures possible in this concentration range which might be responsible for the large discrepancy observed for  $J_c$ .

In this thesis work, inelastic neutron scattering data is presented for  $\text{Na}_{0.8}\text{CoO}_2$  crystals for which the superstructures are known. The possible relationship between

the superstructures and the observed novel magnetic behaviour is considered.

### 3.1.1 Phase Diagram

The concentration of Na in  $\text{Na}_x\text{CoO}_2$  directly controls the hole concentration in the  $\text{CoO}_2$  layer. By varying  $x$ , a rich phase diagram of electronic ground states appears which can be seen in detail in figure 3.1 on page 64 [93]. In the low concentration range  $1/4 < x < 1/3$  under hydration superconductivity is achieved. The superconducting region has an optimum  $T_c \sim 4.5\text{K}$  with the composition  $\text{Na}_{0.35}\text{CoO}_2(\text{H}_2\text{O})_{1.3}$  [3]. This compound was the first Co-based superconductor to be discovered. Similar to the cuprate superconductors it has a layered structure, but unlike the cuprates it sits on a triangular lattice, not on a square one. The superconductivity in  $\text{Na}_x\text{CoO}_2$  is not very well understood, however, there are some experimental indications that the superconductivity in  $\text{Na}_x\text{CoO}_2$  might be unconventional [94, 95]. The system is insulating at  $x=1/2$  but metallic on either side. The  $x > 1/2$  side is called a “Curie-Weiss metal”, since it surprisingly shows linear conductivity and a Curie-Weiss type susceptibility. In the regime  $x > 0.65$  long-range magnetic ordering occurs below  $T_N \sim 23\text{K}$  [88–90]. At  $x=1$ , this magnetic phase disappears and the system becomes insulating [96, 97]. The nature of the magnetically ordered phase is not completely clear, and it will be discussed in detail in section 3.1.4. The dotted line at  $T \sim 5\text{K}$  highlight some anomalous physical-properties measurements [89, 98] which some has interpreted as another phase transition [98]. The phase diagram shown in figure 3.1 has been obtained from Ref. [93]; however, it has been modified to highlight some of the features of other published phase diagrams, namely those of Refs. [99] and [98]. The work in this thesis will investigate the magnetism for the concentration  $x=0.8$ .

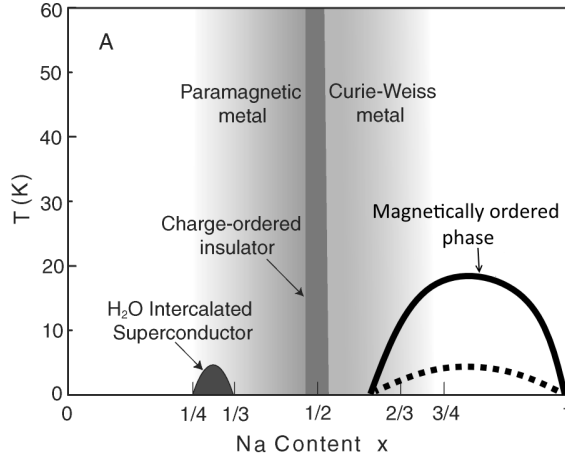


**Figure 3.1: Phase diagram of  $\text{Na}_x\text{CoO}_2$ .** There is a hydrated superconductor phase at  $x \sim 0.35$ , an insulating phase at  $x=0.5$  and a SDW phase for  $x > 0.65$ . Image has been obtained from Ref. [93]; however, changes have been made in order to represent some features of phase diagrams in Refs. [99] and [98].

### 3.1.2 Crystal Structure

The parent structure of  $\text{Na}_x\text{CoO}_2$  ( $x > 0.65$ ) has hexagonal symmetry, space group  $P6_3/\text{mmm}$  with  $a=b=2.85\text{\AA}$ ,  $c=10.8\text{\AA}$ ,  $\beta = 120^\circ$  which can be seen in figure 3.2 on page 65. Here the Co and O atoms are given in black and white respectively. Red and Blue colours represent the two possible sites for a Na atom. The red sites, Na1, cost more energy because they sit right on top of the Co atoms compared to the blue sites, Na2, which sit at the centre of the Co triangles [17].

Aside from controlling the hole concentration, the Na concentration also plays an important role in creating long-range superstructures in the system. Across a wide ranges of Na concentrations various superstructures were found to exist [2, 17, 100–104]. The mechanism for the superstructure formation at high concentrations was successfully explained by Roger et al. [17] by using a pure electrostatic model.

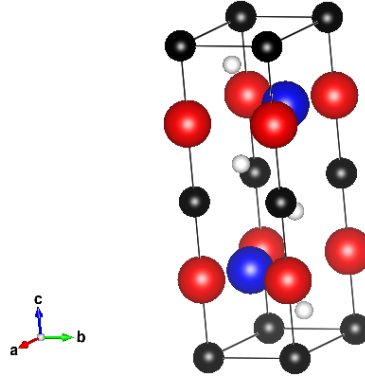


**Figure 3.2: Parent structure of  $\text{Na}_x\text{CoO}_2$ .** There are two possible Na sites Na1 (red) and Na2 (blue) which correspond to high and low energy sites respectively [17]. The Co (black) and O (white) layers reside between the Na layers.

In  $\text{Na}_x\text{CoO}_2$ , there are two possible sites for the Na atoms in the ***ab*** plane. If viewed along the *c* axis, the Na1 positions sit directly above a Co site whilst the Na2 positions are in the centre of the triangle made by the Co atoms. The Na1 site has a higher energy cost and, therefore, one would not expect it to be filled. However, it can be calculated that the lowest energy configuration is clusters of Na vacancies where at the centre of the cluster the Na atoms are in the Na1 position. This can be seen in detail in figure 3.3(a). This di-vacancy cluster model can be extended for a tri- vacancy model where there are three atoms in Na1 sites. The di-vacancy model is lowest energy in the  $0.5 < x < 0.71$  regime whilst tri-vacancy model is more favourable in the  $0.75 < x < 0.8$  regime. The energy of different cluster sizes can be seen in figure 3.3(b) for mono (black), di (red), tri (blue), and quadri (green) vacancy clusters. The clustering creates a Coulomb landscape on the Co-O layers where there are higher potentials above and below the clusters. It is expected that such an effect will have consequences on the electronic and magnetic properties of the system [17].

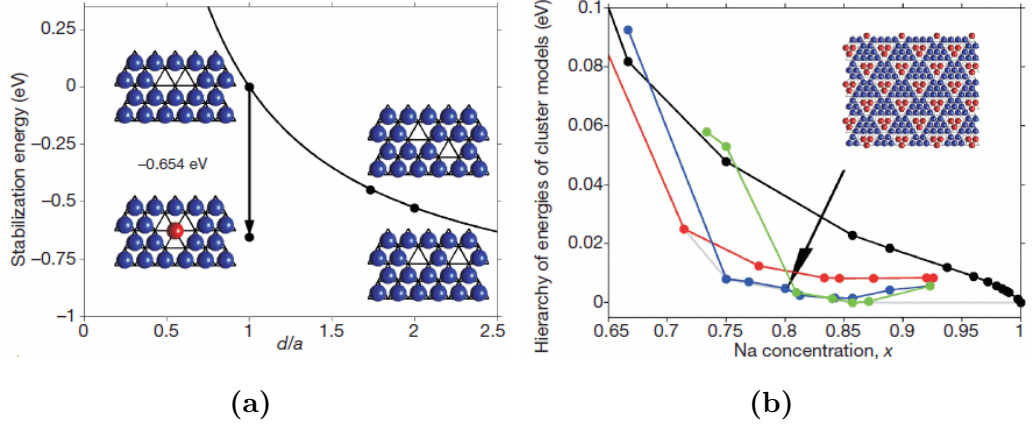


**Figure 3.3: Na vacancy superstructures.** (a) For large Na concentrations, it is energetically more favourable to have the vacancies around a Na1 site rather than have all Na on Na2 sites. (b) At even higher concentrations, different Na1 cluster size becomes possible. Here the energy of mono (black), di (red), tri (blue), and quadri (green) vacancy clusters are shown. Images from Ref. [17].

In the concentration range  $0.75 < x < 0.85$ , there are three possible superstructures which can form. These are the square ( $x=0.8$ ), stripe ( $x=0.8$ ), and 1/13th ( $x=0.77$ ) phases and can be seen in figure 3.4 on page 67. The square and stripe phases both have the same concentration and appear only below  $\sim 285\text{K}$  [102]. The 1/13th has a lowest concentration of the three phases with  $x \cong 0.77$ , and will often coexist with the stripe or square phase. The samples will gradually lose Na if left in contact with the atmosphere and the concentration of 1/13th phase will increase [105]. All three phases are easy to distinguish using single crystal diffraction methods. A calculated intensity of square, stripe, and 1/13th phase for neutron diffraction can be seen in figure 3.5 on page 67. The superstructure of a sample can be identified easily by checking the positions of the superstructure Bragg peaks.

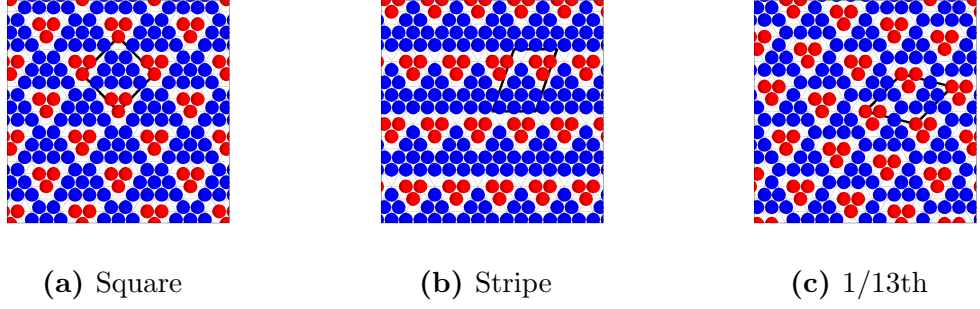


**Figure 3.4: Na layer of three possible superstructures for concentration range  $x \sim 0.77-0.8$ .** Here, the Na layers of (a) square, (b) stripe, and (c) 1/13th phases can be seen. Images from work of Ref. [15].

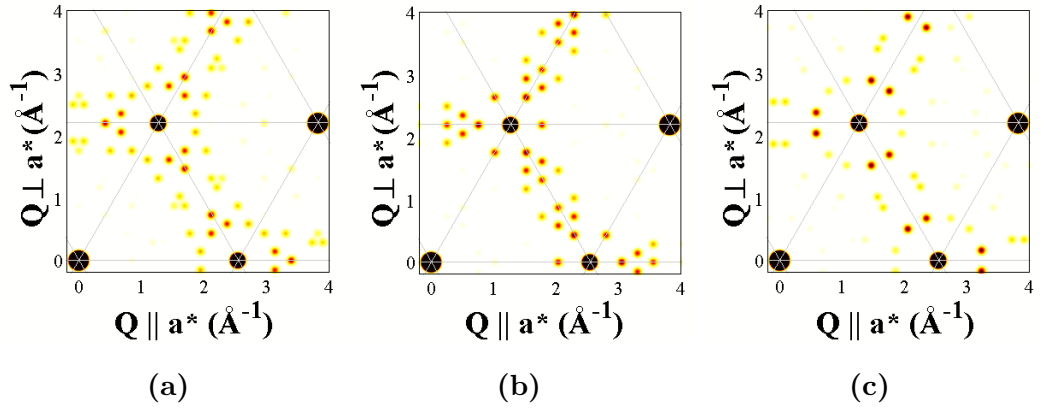


**Figure 3.5: Calculated neutron diffraction pattern for different superstructures.** Here, the calculated diffraction pattern of the  $(hk0)$  plane for the (a) square, (b) stripe, and (c) 1/13th phase can be seen. Images from work of Ref. [15].

The  $c$  lattice parameter has also been found to be closely correlated with the Na concentration in the sample [105–107]. This correlation can be clearly seen in figure 3.6, where with increasing  $x$ , the  $c$  lattice parameter becomes smaller. For the square and stripe phase samples where  $x = 0.8$ , a  $c$  lattice of  $\sim 10.7\text{\AA}$  is expected.

For the 1/13th phase, where  $x = 0.77$ , a  $c$  lattice of  $\sim 10.8\text{\AA}$  is expected. The data points in figure 3.6 agree with this linear trend within  $\sim 0.1\text{\AA}$  [107].

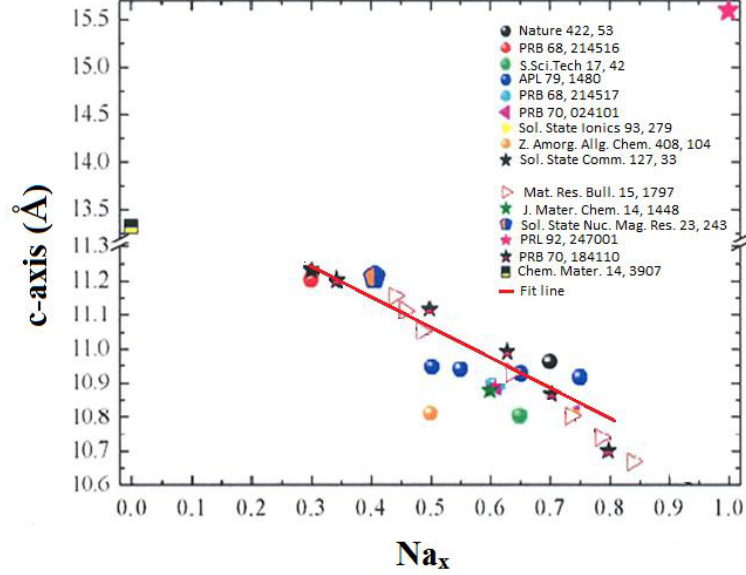


**Figure 3.6: Correlation between  $c$  lattice and Na concentration.**

This image was obtained from Ref. [105]; however, the original source is Ref. [107].

### 3.1.3 Thermoelectric Properties

Thermopower is the ability of a material to create a voltage difference from a temperature difference. A high thermopower material would have great technological applications such as turning waste heat into electricity.  $\text{Na}_x\text{CoO}_2$  started receiving interest as a thermoelectric after it was discovered that  $\text{Na}_x\text{CoO}_2$  has a roughly ten times higher thermopower compared to similar materials [1]. The thermopower of  $\text{Na}_x\text{CoO}_2$  increases with  $x$  until  $x=1$  where an insulating phase is formed [96, 97]. Surprisingly, it was discovered that an applied magnetic field can suppress the thermopower in  $\text{Na}_x\text{CoO}_2$ , which can be seen in figure 3.7. Because of



this field dependence, it is believed that the thermopower is of magnetic origin, i.e. due to spin entropy.

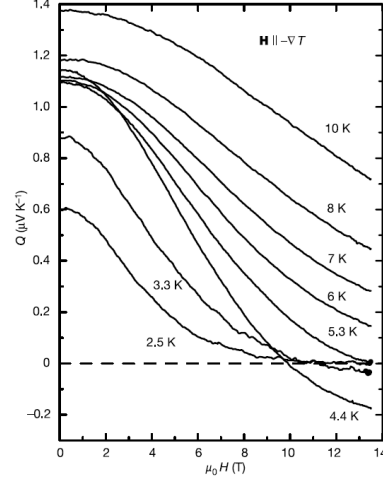


**Figure 3.7: Suppression of the thermopower with applied magnetic field.** This is an indication that the thermopower is of magnetic origin. Image from Ref. [16].

There have been models which try to explain this by considering the degeneracy in the  $\text{Co}^{3+}$  and  $\text{Co}^{4+}$  sites. For a Na concentration of  $x$ , it is expected that  $x$  sites would have  $\text{Co}^{3+}$  and  $1-x$  sites would have  $\text{Co}^{4+}$ . It is expected that the  $\text{Co}^{3+}$  and  $\text{Co}^{4+}$  sites are in the low spin configurations of  $S=0$  and  $S=1/2$  which would result in degeneracies of one and six respectively. Therefore, a hole jumping away from a  $\text{Co}^{4+}$  to a  $\text{Co}^{3+}$  site will transfer not only charge of  $+1e$  but also a finite amount of entropy [16, 108]. A better understanding of the magnetic structure and excitations in  $\text{Na}_x\text{CoO}_2$  would result in a better understanding of its unusual thermopower.

It has also been shown that the Na superstructures play a very important role in the thermoelectric properties of  $\text{Na}_x\text{CoO}_2$ . In the square phase of  $\text{Na}_{0.8}\text{CoO}_2$ , the large distance between the tri-vacancy Na1 clusters and the surrounding Na2 atoms create an anharmonic potential in which the Na atoms can “rattle”. It has been

shown that such rattling modes disturb the flow of heat throughout the material. First-principles DFT calculations using the square phase superstructure were able to successfully predict the existence of such flat rattling phonon mode at  $\sim 13\text{meV}$ . This rattling mode causes a reduction in the thermal transport by six times compared to the  $x=1$  version. This can be seen in figure 3.8 where physical-property measurements (black) agree with measured phonon lifetimes from inelastic neutron scattering (red) and x-ray (yellow) measurements. The calculated thermal transport for  $x=1$  (blue) is considerably larger [21].

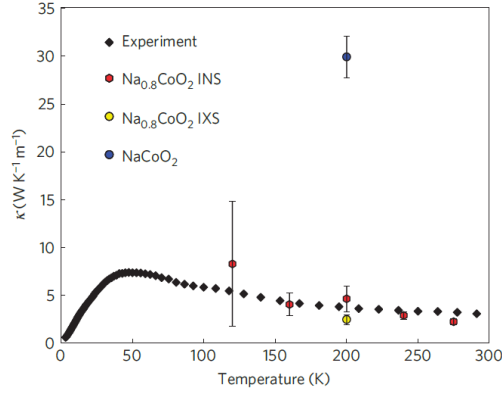


**Figure 3.8: Thermal transport of square phase  $\text{Na}_{0.8}\text{CoO}_2$ .** The thermal transport for  $\text{NaCoO}_2$  (given in blue), which has no superstructure, is much higher than the thermal transport of the square phase  $\text{Na}_{0.8}\text{CoO}_2$ . This shows that the Na superstructure can have very important consequences for the physical properties. Image from Ref. [21].

### 3.1.4 Magnetism

$\text{Na}_x\text{CoO}_2$  shows a magnetic transition in susceptibility measurements for  $x=0.65$ - $0.95$  at  $T_N \sim 22\text{K}$  [88, 89]. The most agreed upon magnetic structure is  $S=1/2$ , A-type AFM structure which can be seen in figure 3.9(a) on page 73 and is in agreement with neutron [4, 5], muon [91, 109], and physical-property measurements [88–90].

However, the magnetism below  $T_N$  has many anomalous features which suggests the existence of a more complex magnetic structure. Many different models have been suggested to try and account for these anomalies and they include charge ordered structures [17,110], magnetic clusters [111], and a mixture of localised and itinerant states [18,19]. INS experiments can be an important tool for distinguishing between such models.

The interaction scheme of  $\text{Na}_x\text{CoO}_2$  can be seen in figure 3.9(a) [5] where  $J_{ab}$  and  $J_c$  are the nearest-neighbour exchange interactions in the  $ab$  plane or along the  $c$  axis respectively. INS measurements were performed on single crystals of  $\text{Na}_x\text{CoO}_2$  with concentrations  $x=0.75$  [5] and  $x=0.82$  [4]. Linear spin-wave theory fits to the spectrum gave a result of  $J_{ab}=-6(2)\text{meV}$  and  $J_c=12.2(5)\text{meV}$  for  $x=0.75$  [5] and  $J_{ab}=-9.0(6)\text{meV}$  and  $J_c=6.6(6)\text{meV}$  for  $x=0.82$  [4]. Two important observations can be made from these findings. The first is that  $J_{ab}$  and  $J_c$  are of similar magnitude. This is surprising since the structure is two dimensional in nature and therefore a relatively smaller  $J_c$  would be expected. The second observation is that even though  $J_{ab}$  is similar for both compositions,  $J_c$  is different by a factor of two. One possible explanation for this could be the different superstructures which form in this concentration range. The 1/13th phase  $\text{Na}_{0.77}\text{CoO}_2$  has already been measured and produced  $J_c \sim 12\text{meV}$  and  $J_{ab} \sim -6\text{meV}$  [69]. Therefore, it is possible that the stripe or square phase might be responsible for the observed  $J_c \sim 6\text{meV}$ .

The apparent three dimensionality of the magnetism was explained qualitatively by first-principles DFT calculations. It was shown that a diagonal interaction  $J'_c$  as seen in figure 3.9(a) with its 12 next-nearest neighbours can be strong enough to contribute significantly to the out-of-plane excitations. In particular for  $x=0.82$  a ratio of  $J_c/J'_c = 9$  is expected which would result in  $J_c=3.96\text{meV}$  and  $J'_c=0.44\text{meV}$ , thus making it less magnetically isotropic. In the DFT calculations a varying atomic number of  $Z=10+x$  was used for Na which in principle would consider the effects

of Na concentration. Using such a model it is possible to extrapolate the exchange interactions of  $x=0.75$  by using the exchange interactions of  $x=0.82$  as a starting point. Such an extrapolation has worked well for  $J_{ab}$  but it does not work well for  $J_c$ . In fact the model suggests that  $J_c$  should decrease with concentration, not increase. This is summarised in figure 3.9(b) where the calculated spin-waves along  $(hh0)$  and  $(00l)$  can be seen for the  $x=0.82$  sample (dark green), the  $x=0.75$  sample (light green), and the  $x=0.82 \rightarrow 0.75$  extrapolation attempt (blue). Thus a  $Z=10+x$  DFT model was incapable of explaining the factor of two discrepancy in  $J_c$  between  $x=0.75$  and  $x=0.82$  results [112].

The spin waves along  $(hh3)$  direction showed two minor anomalies. Firstly, the spin-wave intensity dropped much faster than expected with a drop of factor of two from 6.5 to 14meV [5, 113]. Secondly, the excitations became broader in  $Q$  at larger energies [4, 5]. This could be indicative of short range correlation within the  $ab$  plane or a Landau damping by charged quasiparticles [4]. Additionally, cold neutron measurements showed that there are two gaps at  $(003)$ . These were explained as an easy-axis anisotropy along  $c$  axis and a twofold easy-plane anisotropy within the  $ab$  plane. The easy-plane anisotropy would have to be twofold because a threefold anisotropy would not result in two gaps [92].

The physical-property measurements also show various anomalous behaviours for  $\text{Na}_x\text{CoO}_2$ . In fact the observed behaviour is not compatible with a purely local moment interpretation. These anomalous behaviours are the entropy jump, the large positive magnetoresistance, and thermomagnetic irreversibility which all occur below  $T_N$  [88–90]. This is an indication that the magnetic structure of  $\text{Na}_x\text{CoO}_2$  is more complex than the  $S=1/2$  A-type AFM structure. The small moment size of  $\sim 0.13\mu_B$  per Co as obtained by neutron and muon measurements is another indicator of the complexity [4, 91, 92]. Surprisingly the magnetisation measurements predict a much smaller moment size of  $1.2 \times 10^{-4}\mu_B$  per Co [88]. There is another

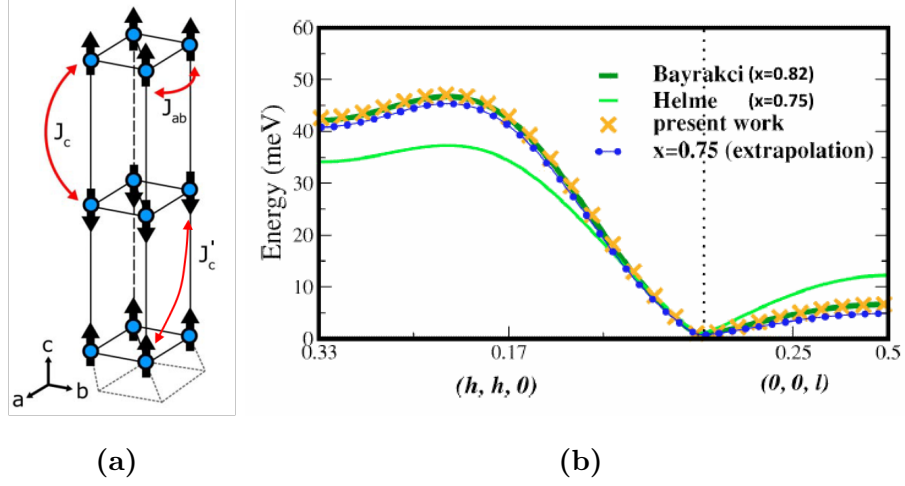


**Figure 3.9:  $\text{Na}_x\text{CoO}_2$  magnetic structure, interaction scheme, and spin waves.** (a)  $\text{Na}_x\text{CoO}_2$  ( $x > 0.65$ ) has an A-type AFM structure [4]. Initial interaction models only considered  $J_{ab}$  and  $J_c$  but DFT calculations show that the diagonal interaction  $J'_c$  can be important as well [112]. (b) The spin waves along  $(hh0)$  and  $(00l)$  are calculated using  $J$  parameters obtained from samples with  $x=0.75$  (Helme et al. [5]) and  $x=0.82$  (Bayrakci et al. [4]). The  $J$  parameters are fixed to reproduce the dispersion for  $x=0.82$  (yellow crosses). The extrapolation to  $x=0.75$  is shown by the blue line. This attempt fails to explain the factor of two difference observed along  $(00l)$  for the two different concentrations. Images (a) and (b) from Refs. [4] and [112] respectively.

discrepancy between the neutron and physical-property measurements. The fits to susceptibility produce a negative Curie-Weiss constant which would indicate that AFM correlations should be dominant; however, such a result is not compatible with strong FM in-plane coupling observed for  $\text{Na}_x\text{CoO}_2$  by neutrons [16, 113, 114].

There are quite a few different magnetic models that one can use to explain the various anomalies in the magnetism of  $\text{Na}_x\text{CoO}_2$ . The main factor for most of

these models is the idea that not all Co sites are the same. In  $\text{Na}_x\text{CoO}_2$  ( $x > 0.65$ ) the sodium concentration  $x$  also controls the electron doping and as a result the  $\text{Co}^{3+}/\text{Co}^{4+}$  ratio. For  $\text{Na}_x\text{CoO}_2$ ,  $x$  sites will be  $\text{Co}^{3+}$  and  $1-x$  sites will be  $\text{Co}^{4+}$ . Assuming low spin configuration,  $S=0$  and  $S=1/2$  is expected from  $\text{Co}^{3+}$  and  $\text{Co}^{4+}$  respectively. Herein lies a problem: for  $\text{Na}_x\text{CoO}_2$  ( $x > 0.65$ ) only 10% – 35% of the sites can have  $S=1/2$ . It is not possible to have large clusters of  $S=1/2$   $\text{Co}^{4+}$  because the Coulomb cost would be too large [5]. So far this is assuming a completely localised  $\text{Co}^{3+}$  and  $\text{Co}^{4+}$  picture. In reality, all or part of the electrons from the Co sites could be delocalised, i.e. itinerant. Initial nuclear-magnetic resonance (NMR) and susceptibility measurements were interpreted as evidence that  $\text{Co}^{3+}$  and  $\text{Co}^{4+}$  are both in their low spin state [115]. More recent NMR measurements on  $\text{Na}_x\text{CoO}_2$ ,  $x = 0.65 - 0.8$ , have been interpreted as  $\sim 23\%$  localised  $\text{Co}^{3+}$  with  $S=0$ , and an itinerant band with an average charge  $\text{Co}^{3.5+}$  which is responsible for the conductivity and the magnetism [19]. It is expected that the Na superstructures control the electronic patterning directly. The  $\text{Co}^{3+}$   $S=0$  sites should localise under the Na1 sites [106]. Such a prediction was previously made for the square phase superstructure. The Na layer of the square phase superstructure can be seen in figure 3.10(a) on page 75. From this Na layer, a specific Coulomb potential is created on the Co layer which is shown in figure 3.10(b). The Co sites (green) feel the largest potential when they are directly under or above a Na1 site. The minimum is surrounded by a potential well much larger than the hopping integral of  $t \sim 10\text{meV}$  [17, 116]. Therefore, it might be possible to localise a  $\text{Co}^{4+}$  at the potential minima [17].

An itinerant and localised magnetic model has been tested for  $\text{Na}_x\text{CoO}_2$ . Such a model predicts FM order appearing above  $x < 0.67$  [18]. This is consistent with the susceptibility experiments which find magnetic transitions for concentrations  $x = 0.65 - 0.95$  [88, 89]. In contrast to the NMR results previously discussed, this itin-

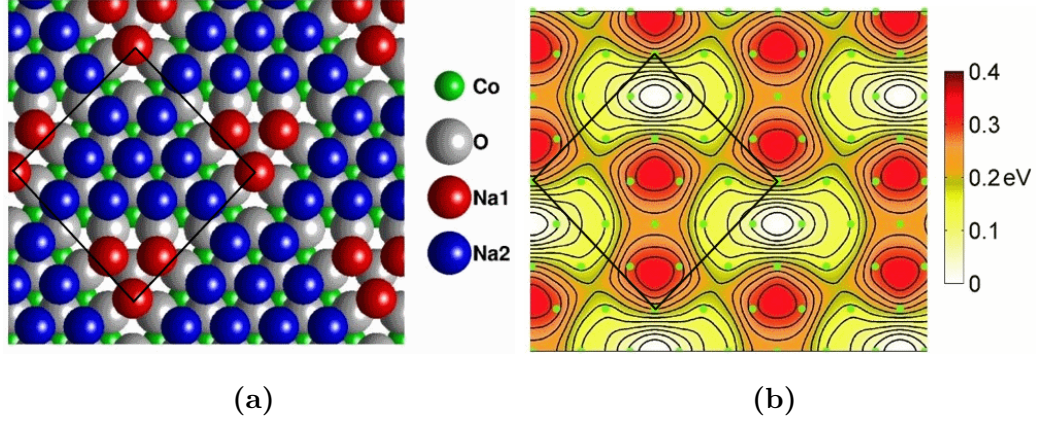


**Figure 3.10: Coulomb potential on the Co layer in square phase superstructure.** Na superstructure calculations suggest that there must be some Co charge patterning. Here, **(a)** the square phase  $\text{Na}_{0.8}\text{CoO}_2$  structure and **(b)** its corresponding Coulomb potential landscape in the Co layer can be seen. The Co sites (green) situated below or above an occupied Na1 site have the largest Coulomb potential and are therefore expected to have  $S=0$   $\text{Co}^{3+}$ . At the sites which correspond to a potential minimum,  $\text{Co}^{4+}$  with  $S=1/2$  are expected [17]. Image from Ref. [17].

erant model uses a randomly placed, localised  $\text{Co}^{4+}$   $S=1/2$  within a sea of  $\text{Co}^{3+}$ . It is assumed that the localised  $\text{Co}^{4+}$  will break the symmetry of the surrounding  $\text{Co}^{3+}$  and drive it into the intermediate spin state of  $S=1$ . The  $\text{Co}^{3+}$  further away from the  $\text{Co}^{4+}$  will remain in low spin  $S=0$  state. The physical picture of such a model can be seen in figure 3.11 on page 76. Here the localised  $\text{Co}^{4+}$   $S=1/2$  are given in white and the surrounding cluster of  $\text{Co}^{3+}$   $S=1$  are given in black. It is these ferromagnetically correlated  $\text{Co}^{3+}$   $S=1$  clusters which connect and provide conduction pathways. The non-magnetic  $\text{Co}^{3+}$  is represented by the white background [18]. The idea of such FM clusters have also been suggested by muon [111] and physical-property

measurements [98]. Muon measurements have been interpreted as nm size magnetic clusters separated nm apart [111]. Similar to the previous model,  $\text{Co}^{4+}$  surrounded by intermediate spin  $\text{Co}^{3+}$  is expected. The dominant interactions are expected to be AFM, with a small FM interaction to cause a structure similar to A-type AFM structure suggested before. As concentration is lowered, the clusters extend into each other and become continuous at  $x < 0.78$ . A tentative phase diagram for such a cluster models suggests that the FM ordering does not occur until  $\sim 8\text{K}$  [98]. It is important to note that magnetisation measurements report an unexpected upturn in magnetisation below 8K and similarly in the region 5-8K there is also a change from  $M_{ab} > M_c$  to  $M_c > M_{ab}$  [89].

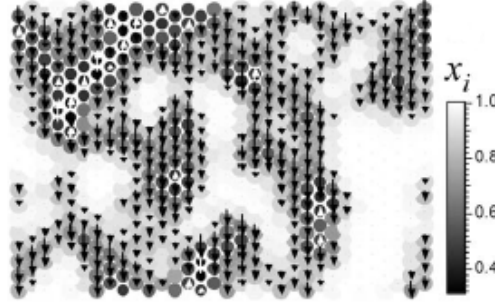


**Figure 3.11: Random  $\text{Co}^{4+}$  spin distributions for  $\text{Na}_{0.8}\text{CoO}_2$ .** In the randomised model the  $S=1/2$   $\text{Co}^{4+}$  (white arrows) are surrounded by  $S=1$   $\text{Co}^{3+}$  (black arrows) in intermediate spin configuration. Further out the  $\text{Co}^{3+}$  is in the non magnetic,  $S=0$  state (white background). Image from Ref. [18].

The physical picture of a localised  $\text{Co}^{4+}$   $S=1/2$  creating an intermediate spin  $\text{Co}^{3+}$   $S=1$  around itself can be considered as a spin-orbital polaron and can be seen in figure 3.12(a) on page 78. Here, the exchange interactions  $J$ ,  $J'$  and  $J_{diag}$  can be seen. Based on comparisons to susceptibility measurements and some assumptions about the energetics within the Co layer, a rough estimate of these exchange parameters



can be made. The  $J$  exchange constant between the  $\text{Co}^{3+}$   $S=1$  is AFM with  $|J| \sim 10\text{-}20\text{meV}$ . The diagonal interaction  $J_{diag}$  is also AFM with  $|J_{diag}| \lesssim |J|$ . As for the interaction between the central  $\text{Co}^{4+}$  and its surrounding  $\text{Co}^{3+}$ ,  $J'$ , the interaction could be AFM or FM. However, susceptibility measurements are indicative of  $|J'| \lesssim |J|$  and the existence of spin waves at low energies rule out the possibility of a large AFM  $J'$ . Two polarons can also create a bipolaron as seen in figure 3.12(b). Here the two  $\text{Co}^{4+}$ ,  $S=1/2$  sites interact ferromagnetically with  $J_{ab}$ , where  $J_{ab} \sim -J$  is expected [117, 118]. A spin-orbital polaron model like this is capable of explaining three major problems regarding the magnetism in  $\text{Na}_x\text{CoO}_2$ . Firstly, it can explain the large susceptibility of  $\text{Na}_x\text{CoO}_2$  which cannot be explained using only non-magnetic  $\text{Co}^{3+}$  [118]. Secondly, it can explain the negative Curie Weiss constant despite the strong in-plane FM coupling observed in INS experiments [118]. Thirdly, it predicts a dampening of spin waves between 10-20meV [117] which has been observed in INS experiments [4, 5]. In the polaron picture, the spin-waves originate from itinerant ferromagnetism within the  $\text{CoO}_2$  planes. The polarons have internal excitations which correspond to higher order spin states. These states should show in INS as broad non-dispersive excitations [118].

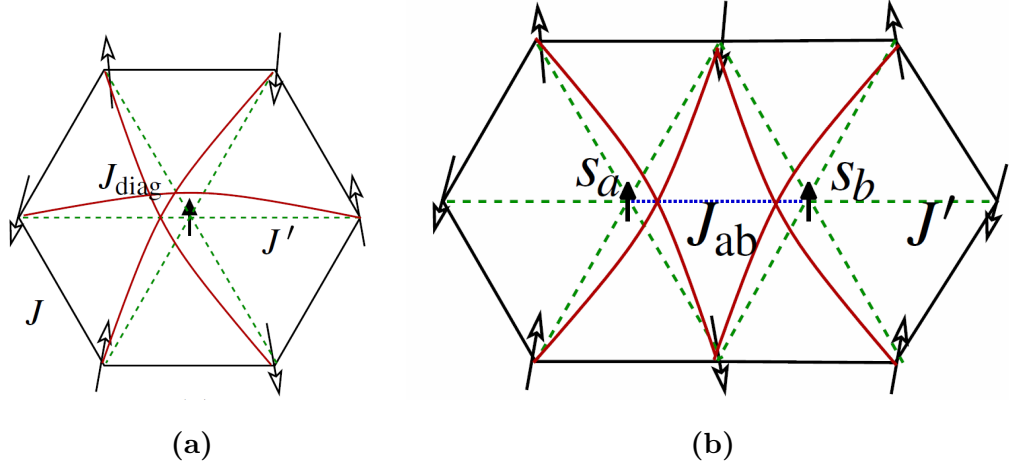


**Figure 3.12: Spin-orbital polaron model for  $\text{Na}_x\text{CoO}_2$ .** (a) A localised  $\text{Co}^{4+}$   $S=1/2$  surrounded by  $\text{Co}^{3+}$  with  $S=1$ . (b) In a bipolaron there are two  $\text{Co}^{4+}$   $S=1/2$  sites surrounded by  $\text{Co}^{3+}$   $S=1$ . Images from Ref. [117].

## 3.2 Experimental Set-Up

Spin-wave dispersion were measured for two different  $\text{Na}_x\text{CoO}_2$  samples, each with a different Na superstructure. The samples were grown using the floating zone method by Sivaperumal Uthayakumar at Royal Holloway, University of London. Each sample was measured on SXD, ISIS, UK and the dominant superstructure was established. The list of samples, their superstructures, and the experiments they were used in can be seen in table 3.1 on page 79. The dominant superstructure of each sample is also shown here. It is important to note that in each sample a small amount of  $1/13$ th phase superstructure has been observed. In subsection 3.2.1, the superstructure determination for the samples will be discussed in greater detail. The majority of the neutron experiments were carried out on the triple-axis spectrometer IN20 at the ILL, Grenoble, France. This instrument was used with

and without polarisation analysis on the square and stripe phase samples.

Sample	Phase	Neutron Experiments
Sample 1	stripe	IN20 (unpol.)
Sample 2	square	IN20 (pol. and unpol.)

**Table 3.1:  $\text{Na}_x\text{CoO}_2$  samples used for neutron experiments.**

Here the sample name, dominant superstructure, and the experiments the samples were used in can be seen.

The  $\text{Na}_x\text{CoO}_2$  samples will gradually lose Na if it comes into contact with air. It has been observed that a sample in the square or the stripe phase will gradually decay into the  $1/13$ th phase. In order to prevent this, samples were kept in desiccators. For the square and stripe phase samples used in IN20 experiments, special aluminium canisters were built at the ILL. The canisters and the samples can be seen in figure 3.13 on page 80. Once inside, the samples were sealed inside a helium atmosphere with an indium seal. During each experiment, the dominant superstructure was checked by going to some of the large superlattice reflections unique to that superstructure. For the alignment of the samples, neutron instruments such as IN3 (ILL), ALF (ISIS), SXD (ISIS), and a laboratory x-ray diffractometer were used.

Before displaying any results, it is important to state the experimental set-up for each experiment. On IN20 four different experiments were carried out.

In the December 2012 IN20 experiment the spin-wave dispersions of the stripe phase sample (Sample 1) along  $(hh3)$  and  $(00l)$  directions were measured. A fixed wave vector of  $k_f = 2.662\text{\AA}^{-1}$  was used. For the monochromator and analyser, Si(111) and PG(002) crystals were used respectively. Horizontal and vertical focusing was used on both the monochromator and the analyser. An orange cryostat was used to keep the sample temperature at  $\sim 1.6\text{K}$  during the experiment. Vertical and horizontal slits were used before and after the cryostat in order to reduce

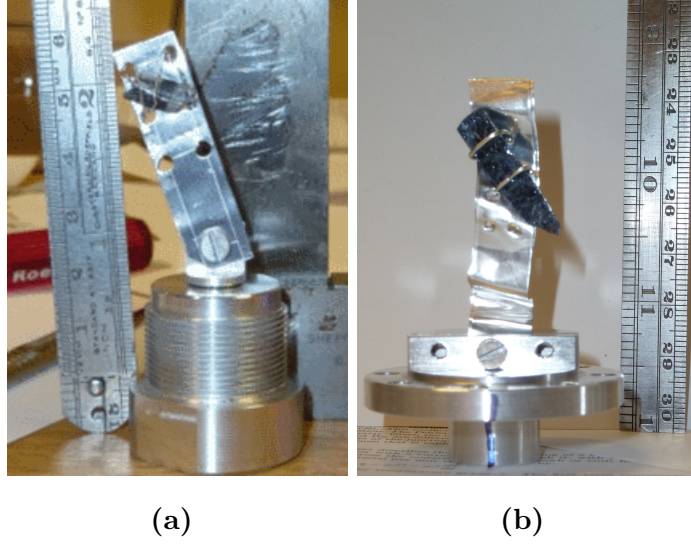


**Figure 3.13: Photographs of the  $\text{Na}_x\text{CoO}_2$  samples.** Here, (a) Sample 1 (stripe phase) and (b) Sample 2 (square phase) can be seen. Both samples are aligned so that  $(hhl)$  scattering plane is vertical. The samples are attached to an aluminium mount with aluminium wire. Once alignment was complete, the samples were sealed in their aluminium canisters with an helium atmosphere with an indium seal.

background.

In the April 2013 IN20 experiment the spin-wave dispersions of the square phase sample (Sample 2) were measured along  $(hh3)$ ,  $(hh5)$  and  $(00l)$  directions. The experimental conditions were the same as that of the December 2012 experiment.

In the May 2013 IN20 experiment, polarisation analysis was used to measure the spin-wave dispersions of the square phase sample (Sample 2). Measurements were performed along  $(hh3)$  and  $(00l)$  directions. Heusler(111) monochromator and analyser was used in fixed  $k_f = 2.662\text{\AA}^{-1}$ . Horizontal focusing was used on the analyser. Flippers were placed before and after the sample; however, only the flipper after the sample was used. At the  $(-1,-1,0)$  Bragg peak a flipping ratio of  $\sim 22$  was

obtained which corresponds to  $\sim 91.5\%$  polarisation. An orange cryostat was used to supply a base temperature of  $\sim 1.8\text{K}$  throughout the experiment. The orange cryostat was situated at the centre of a Helmholtz coil. On either sides of the coil, vertical and horizontal slits were used to reduce background. The slits before the sample had an opening of  $\sim 21\text{mm}$  and  $\sim 13\text{mm}$  vertically and horizontally. The slits after sample had an opening of  $\sim 46\text{mm}$  and  $\sim 24\text{mm}$  vertically and horizontally.

In the June 2013 IN20 experiment the spin-wave dispersions of the square phase sample (Sample 2) were measured along  $(h03)$ , and  $(h, 0, 2.5)$  directions. Before the experiment, the sample was re-oriented to the  $(h0l)$  scattering plane on IN3 and re-sealed in its aluminium canister. The experimental set up was the same as that of the December 2012 experiment.

### 3.2.1 Crystal Superstructures

The superstructures of each sample was determined on SXD. The resulting diffraction pattern was compared to the expected diffraction patterns of 1/13th, square and stripe phase calculations (see figure 3.5). Each superstructure has a unique set of superlattice Bragg-peaks such as the  $(0.8, 0.8, 0)$  for the square phase and the  $(0.6, 0.4, 0)$  for the stripe phase. By searching for intensity at these unique positions, it is possible to determine if a certain phase is present in the material. Once the samples arrived at the ILL, their superstructures were checked on IN3. Many different superstructure positions were measured for each sample. Some of the peaks were close to aluminium powder lines, therefore, scans in  $h$ ,  $k$  and  $l$  directions were performed at each point. For sample 1, very clear stripe phase superlattice peaks were measured at four unique  $\mathbf{Q}$  positions:  $(-0.867, -0.667, 0)$ ,  $(-1, -0.6, 0)$ ,  $(-0.6, -0.4, 0)$ ,  $(-0.467, -0.667, 0)$ . No clear square phase signal could be found; however, some 1/13th signal could be found at  $(-0.769, -0.923, -0.25)$  and  $(-0.462, -0.385, 0.25)$ . Some examples of these scans from the IN20 Dec 2012 experiment can be seen in figure 3.14.

For sample 2, Bragg peaks at four unique square phase superlattice positions were observed:  $(-1, -0.667, 0)$ ,  $(-0.8, -0.8, 0)$ ,  $(-0.6, -0.533, 0)$ ,  $(-0.667, -0.333, 0)$ . No signature of a stripe phase was found. Two clear  $1/13$ th phase superlattice Bragg peaks were measured:  $(-0.462, -0.385, -0.25)$ ,  $(-0.923, -0.769, -0.25)$ . Some examples of these from IN3 March 2013 can be seen in figure 3.15.

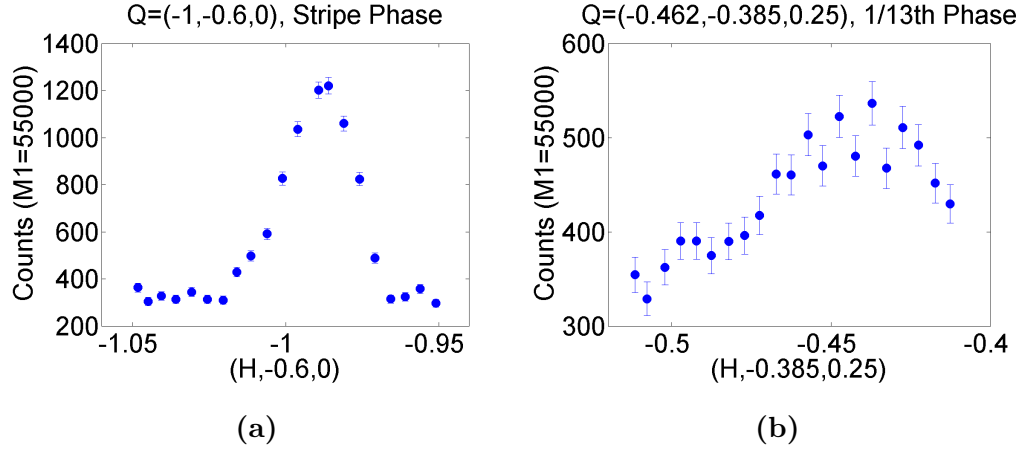


**Figure 3.14: Sample 1, example of superlattice peaks.** Intensities were measured at (a) stripe and (b)  $1/13$ th superlattice Bragg peak positions.

Both sample 1 and sample 2 had some quantity of the  $1/13$ th phase. It is of interest to quantify the volume fractions of the  $1/13$ th phase to the other phase in the sample; however, this is no simple task. For a simple unit cell, the structure of a material can be solved by comparing the calculated intensities with measured Bragg peak intensities. For the Na superstructures, the unit cell contains  $\sim 100$ s of atoms. This creates too many free parameters, and therefore a direct structure determination becomes very difficult. In this thesis, two different methods were used in an effort to quantify the amount of each superstructure in the  $\text{Na}_x\text{CoO}_2$  samples.

For the first method, the intensities were calculated for the square, stripe, and stripe superstructures. These intensities were calculated using software of D.G.

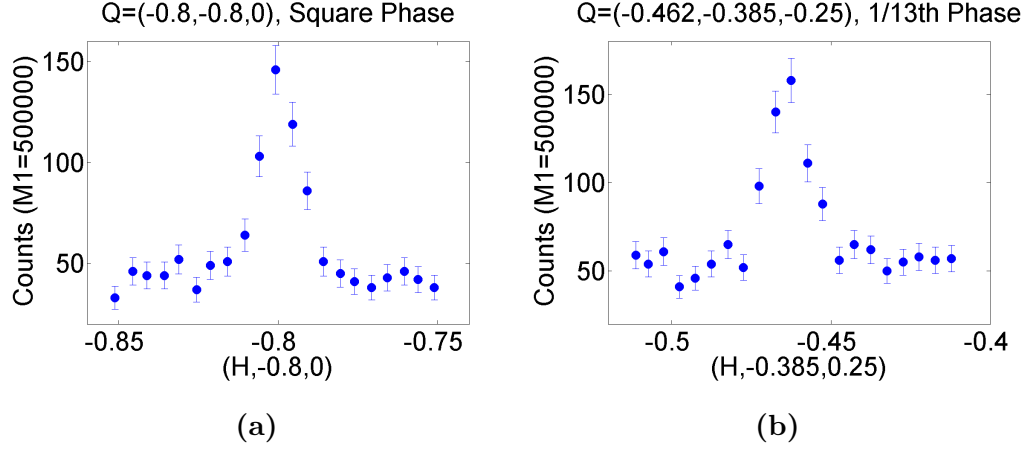


**Figure 3.15: Sample 2, example of superlattice peaks.** Intensities were measured at (a) square and (b) 1/13th superlattice Bragg peak positions.

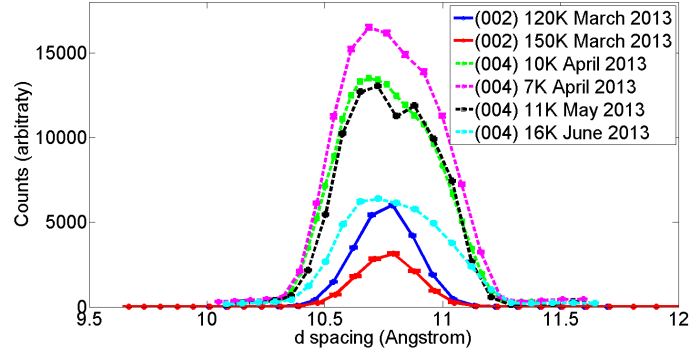
Porter [15]. In these calculations, no atom displacement or variance in site occupation was considered. These calculated intensities were used as reference point to compare measured intensities of parent structure Bragg peaks and superlattice Bragg peaks. For both samples, the calculations and measured intensities, were within the same order of magnitude. For sample 2, the intensities of the square phase superlattice Bragg-peaks were compared to that of the 1/13th phase. From the data available, it was not possible to obtain a definitive answer. However, from this data one could speculate that the volume ratio of 1/13th phase to square phase is similar within a factor of ten. A similar result was found for sample 1 for a comparison between stripe and 1/13th phase peaks.

The second method for determining the superstructure volumes relied on measuring the  $c$  lattice parameter for each sample. It has already been stated that the Na concentration  $x$  is closely related to the  $c$  lattice parameter. The square and stripe phases ( $x=0.8$ ) are expected to have a smaller  $c$  lattice parameter compared to the 1/13th phase ( $x=0.77$ ). These two slightly different  $c$  lattice parameters

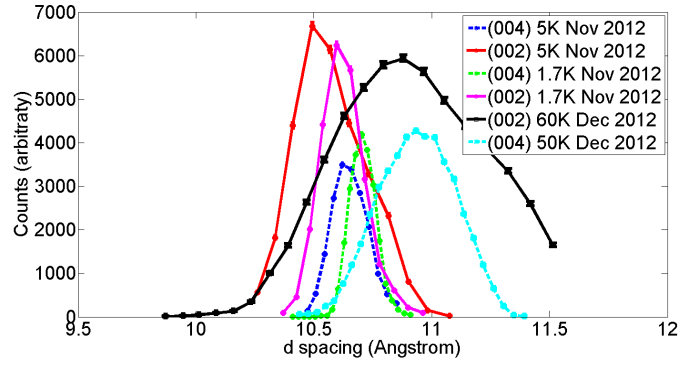
should be observable at  $(00l)$  type Bragg peaks, assuming sample quality and instrumental resolution are sufficiently good. In all of the TAS experiments,  $|Q|$  scans were performed centred at Bragg peaks (002) and (004). In figure 3.16, this data is presented in terms of  $d$ -spacing as given by the Bragg equation,  $d = l\lambda/(2\sin(\theta))$ . In the legends, temperature and the date of the experiment are presented. Sample 2's results can be seen in figure 3.16(a). Some of the scans show a double peak structure which could represent the two different phases. In the 11K, May 2013 data, which is presented in black, the two peaks are positioned at  $\sim 10.7$  and  $\sim 10.9\text{\AA}$ . These two peaks could represent the square and  $1/13$ th phases respectively. If this is the case, the volume fraction of the  $1/13$ th phase is slightly less than that of the square phase. The dataset is limited and therefore it is not possible to come to a definite conclusion. A better resolution and more scans at different temperatures might be necessary. In figure 3.16(b), sample 1's data can be seen. Here the  $c$  lattice parameter determination is less consistent between different experiments. The reason for this is not clear, but it could have to do with temperature history of the sample. In these scans, the two-peak feature is not as clear either. The 5K November 2012 (002) and the 60K Dec 2012 (002) scans show the signatures of a secondary peak on the right hand side. If one assumes that this smaller contribution corresponds to the  $1/13$ th phase, the  $1/13$ th phase's volume fraction must be roughly half of that of the stripe phase.

To summarise, both samples have some amount of  $1/13$ th phase. Even though it is not possible to determine with certainty the volume fraction of the  $1/13$ th phase from the data available, the  $1/13$ th phase does appear to be the minority phase. The stripe and square phases appear to be dominant in samples 1 and 2 respectively.





(a)



(b)

**Figure 3.16:**  $d$  spacing from (002) and (004)  $|Q|$  scans. These scans can be used to determine the  $c$  lattice parameter and possibly the volume fractions of certain superstructures. **(a)** For sample 2, the (004) 11K May 2013 scan shows a clear two-peak signature with both peaks with similar intensities. **(b)** For sample 1, the 60K Dec 2012 scan shows some evidence of two-peak feature with a factor of two difference in their relative intensities.

## 3.3 Experimental Results

### 3.3.1 Inelastic Neutron Scattering Results

The INS spectrum of  $\text{Na}_x\text{CoO}_2$  samples in the square and stripe phase were measured at IN20, ILL at a base temperature of  $\sim 1.8\text{K}$ . For  $\text{Na}_x\text{CoO}_2$ , there is a structural extinction at odd  $(00l)$ . This is favourably positioned with respect to the magnetic signals which is strongest at odd  $(00l)$ . At IN20, with  $k_f = 2.662\text{\AA}$ , one can only reach low energy excitations at  $(001)$  due to its small  $|Q|$ . For this reason, the measurements were performed in the vicinity of  $(003)$ . For both the square and the stripe phase spin-wave like signal is measured along  $(hh3)$  and  $(00l)$ . Surprisingly, both phases have a very similar spin-wave spectrum. Additionally the in-plane excitations of the square phase show some kind of anomaly.

The spin-wave spectrum for the stripe and square phase along the  $(00l)$  direction can be visualised in figure 3.17(a) and (b) respectively on page 87. Here a number of energy scans have been represented as a colour map where the colour of each pixel corresponds to counts from a monitor of  $M1=2000000$  ( $\sim 200$  seconds). This same monitor will be used for all the colour maps from IN20 for consistency. Here it can be seen that there is very little difference between the two INS spectra. They both go to a maximum of  $\sim 12\text{meV}$  at  $l=2.5$ . The square phase sample has a better signal which is due to its larger crystal size.

The  $(hh3)$  direction spin waves have been measured for both of the phases as well. In figure 3.18(a) and (b) on page 88, the INS spectra for the stripe and square phases can be seen respectively. These colour maps were from  $Q$  scans with a monitor of  $M1=2000000$ . For both samples there is a similarity below  $\sim 12\text{meV}$ : there is excitation at roughly  $h=0.08$  and  $10\text{meV}$  and it seems to go to  $h=0$  linearly. For the stripe phase sample, above  $12\text{meV}$  the signal fades away and there is no clear excitation branch. However, for the square phase sample there is

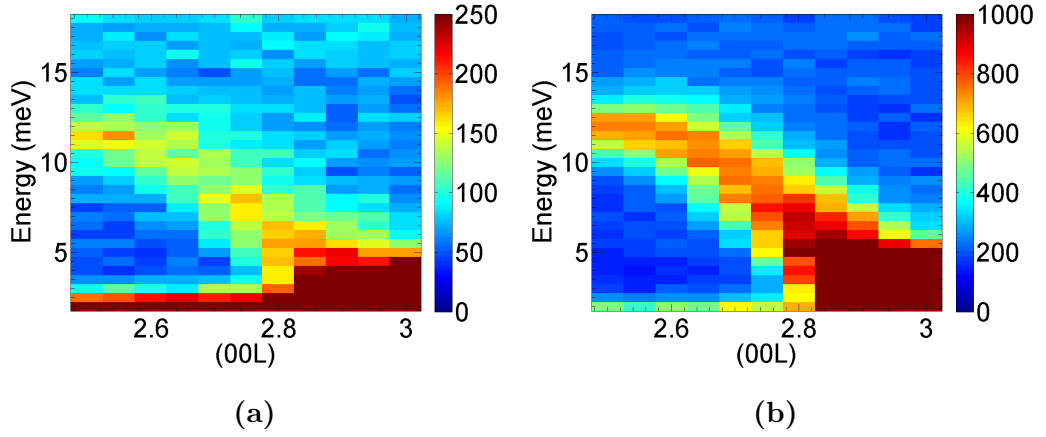


**Figure 3.17: INS spectrum along  $(00l)$ .** The observed spectrum is very similar for both the (a) stripe and (b) square phase samples. The spin-wave spectrum reaches a maximum of  $\sim 12$  meV at  $(0,0,2.5)$  for both phases.

slight dip in intensity at  $\sim 13$  meV but the intensity is regained at higher energies and a clear excitation branch still remains. Surprisingly the dispersion remains at  $h \sim 0.08$  between 13 meV and 21 meV. This kind of anomalous behaviour is referred to as a “waterfall effect” in the literature due the dispersion’s visual similarity to a waterfall [119]. At 23 meV there is a strong optic excitation which means that the waterfall feature cannot be followed any further in energy. This 23 meV feature is likely to be the optic phonon mode reported in literature [4, 5].

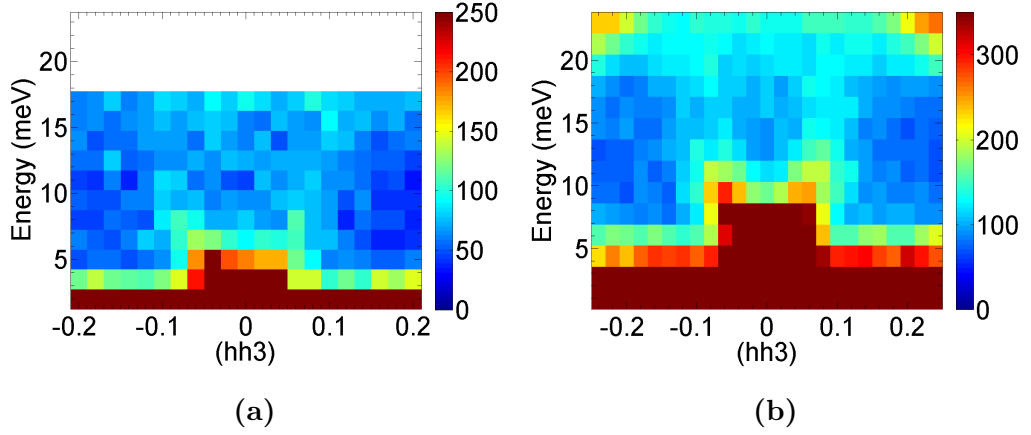


**Figure 3.18: INS spectrum along  $(hh3)$ .** For both the (a) stripe (b) square phase samples spin waves can be seen originating from  $(003)$ . For the square phase sample, the dispersion is fixed at  $h \sim 0.08$  between 13meV and 21meV. Such a feature is called the “waterfall effect” [119].

For the stripe phase sample, due to limited signal, measurements were only made along  $(00l)$  and  $(hh3)$ . However, for the square phase sample, measurements were also made along  $(hh5)$ ,  $(h03)$ , and  $(h,0,2.5)$ . These measurements were performed to shed more light on the nature of the observed “waterfall effect”. The square phase INS data along  $(hh3)$  can be seen in more detail in figure 3.19(a) on page 89. Here, there is an optic branch which starts at  $h = 0.5$ , 20meV and moves towards higher energies as  $h$  goes to zero. In figure 3.19(b) the square-phase  $(hh5)$  Q-scans are collated in an colour map. At this Q, it is possible to go to higher energies compared to  $(hh3)$  scans. The  $(hh5)$  scans do not reveal any clear continuation of a waterfall but it does reveal multiple optical branches. It is possible that these branches are of non-magnetic origin since they are considerably more intense than the  $(hh3)$  spin-wave dispersion. One would expect the spin-wave intensity to drop with increasing Q due to the magnetic form factor. Note that the large diagonal intensity on the left hand side of the  $(hh5)$  colour map is a spurious signal, most likely

originating from a higher order Bragg reflection. Its spurious nature is obvious from two of its main properties. It is not symmetric about  $h = 0$ , and it is considerably more intense than its surrounding excitations.

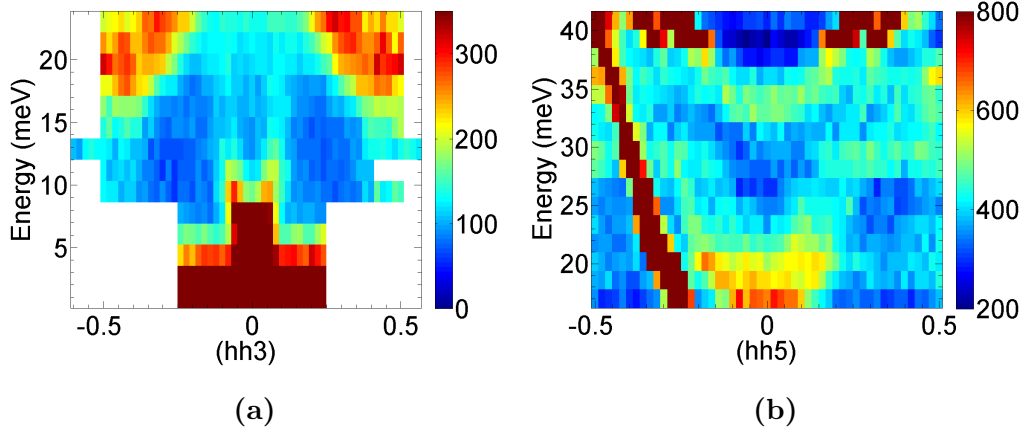


**Figure 3.19: Optic branches in square phase.** Optic branches are present along (a)  $(hh3)$  and (b)  $(hh5)$  directions. Part of an optic branch is visible in the upper corners of the  $(hh3)$  colour map. In the  $(hh5)$  colour map multiple optic branches are present. The large diagonal signal on the left hand side of the  $(hh5)$  colour map is likely of spurious origin.

Measurements performed along  $(h03)$  direction also show a waterfall feature which can be seen in figure 3.20(a). Different to the  $(hh3)$  direction a smaller energy step was used between Q scans. This has given a clearer picture of the waterfall effect. Additionally, measurements were performed along  $(h,0,2.5)$  which can be seen in figure 3.20(b). Here at 12meV the signal is most intense and there appears to be some excitations above 12meV; however, these excitations are rather diffuse and it is difficult to identify any particular spin-wave branch. It is important to note that the large intensity at  $h=0$  at 19meV may not be due to spin waves. This is the position where the scattering angle of the sample (A4 angle on triple-axis spectrometers) is

at its lowest. As this angle approaches zero, the sample approaches the direct beam and the background increases.

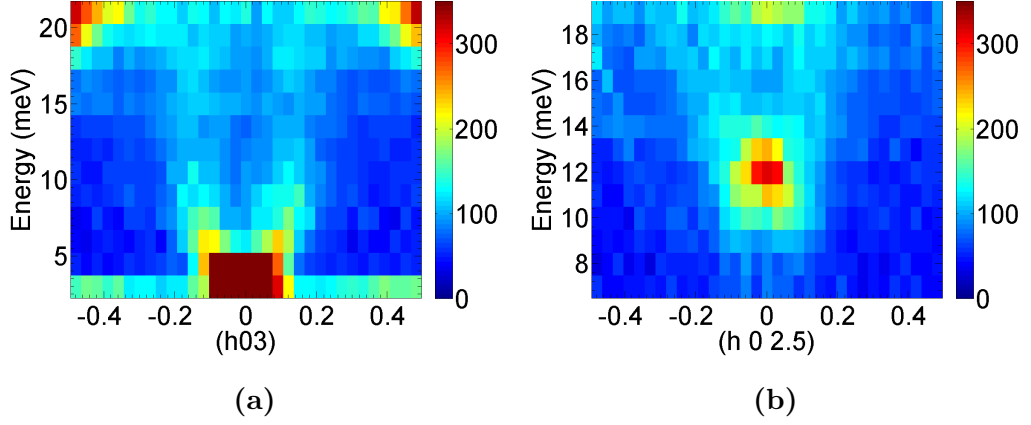


**Figure 3.20: INS spectrum of square phase along  $(h03)$  and  $(h,0,2.5)$  directions.** (a) For the  $(h03)$  dispersion there appears to be waterfall-like feature, similar to  $(hh3)$  dispersion. (b) Along  $(h,0,2.5)$  direction there is not a well defined excitation branch. Part of the large intensity at  $h=0$ , 19meV could be due to high background at low scattering angles.

There are some unexpected spin-wave excitations in the 9meV and 10meV Q scans performed along  $(h,0,2.5)$  direction which can be seen in figures 3.21(a) and (b) respectively. At 9meV, there appears to be two excitations at roughly  $|h| \sim 0.8$ . At 10meV, even though they are more difficult to resolve, the excitations have moved closer together to  $|h| \sim 0.65$ . For this direction, one wouldn't expect any spin-wave signal below  $\sim 12$ meV.

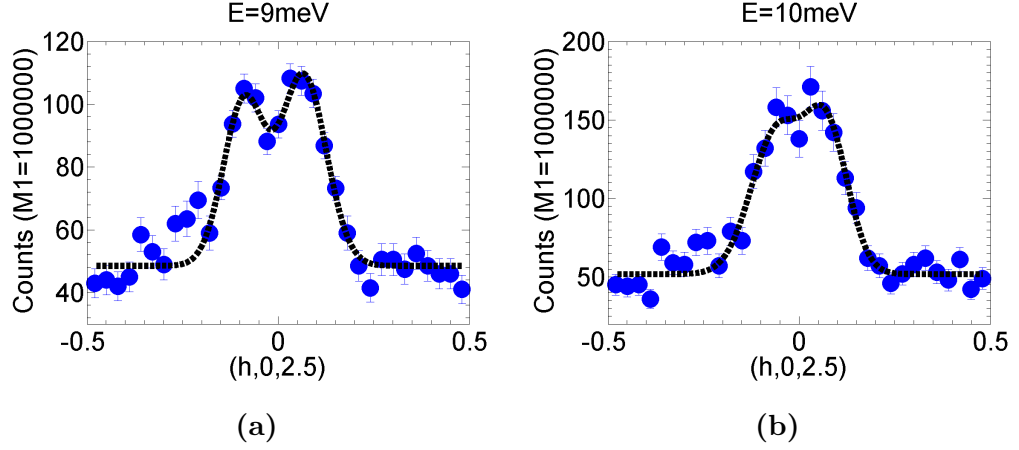


**Figure 3.21: Unexpected spin-wave signal for  $(h, 0, 2.5)$  direction.** Below  $\sim 12\text{meV}$  no spin-wave signal is expected; however, (a) at  $9\text{meV}$  and (b) at  $10\text{meV}$  there are excitations at  $|h| \sim 0.8$  and  $|h| \sim 0.65$  respectively.

### 3.3.2 Polarised Inelastic Neutron Scattering Measurements for Square Phase $\text{Na}_{0.8}\text{CoO}_2$

It is highly likely that the acoustic modes emerging from (003) are magnetic in origin. However, in the region of most interest above  $12\text{meV}$  where there are rattling modes, and up to  $20\text{meV}$  where there are optical phonon modes, it is not clear whether the observed excitations are structural or magnetic. In order to find out the true nature of the waterfall feature, polarised INS measurements were performed on the square phase sample at IN20, ILL, Grenoble, France. With the use of Helmholtz coils and a spin flipper, a total of six different polarisation channels were explored. These channels were the non spin-flip channels  $\sigma_{xx}, \sigma_{yy}, \sigma_{zz}$ , and the three spin-flip channels  $\sigma_{x\bar{x}}, \sigma_{y\bar{y}}, \sigma_{z\bar{z}}$ . Notice that all the spin-flip channels are obtained from flipping with flipper 2, which is situated between the sample and the analyser.

Energy scans were performed at (003) and (0,0,2.5) to establish that the observed

signal in the previous INS measurements was of magnetic nature. A polarised measurement at the magnetic Bragg peak (003) is additionally useful as it will show if the magnetic excitations are gapped. The (003) energy scans in the four different polarisation channels can be seen in figure 3.22(a). The pure magnetic signal can be obtained from a linear combination of the three spin flip channels via  $2\sigma_{xx} - \sigma_{yy} - \sigma_{zz}$  which can be seen in figure 3.22(b). Here it can be seen that the magnetic excitation is indeed gapped. In fact it is better explained by two different gaps centred at 1.6(1)meV and 2.8(6)meV. In figure 3.23 on page 93, the (0,0,2.5) polarised energy scans can be seen. This scan confirms that the excitation centred at  $\sim 12$ meV is indeed magnetic.

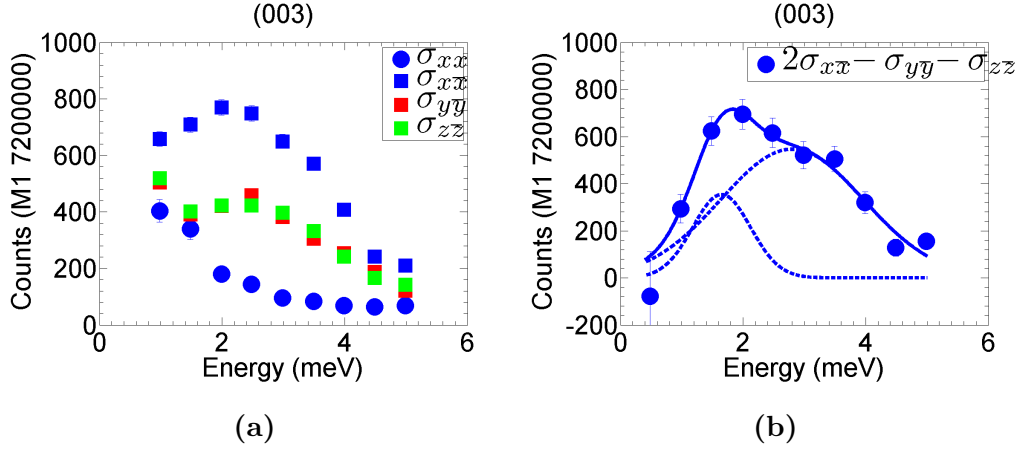


**Figure 3.22: Polarised energy scans at (003).** From the (a) polarisation channels measured it is possible to obtain the (b) pure magnetic signal. This magnetic signal is fitted with two Gaussians centred at 1.6(1)meV and 2.8(6)meV.

The remainder of the experiment was focused on measuring the waterfall feature along ( $hh3$ ) direction and determining if it was of magnetic nature. Q-scans were made at fixed energy transfers 11meV, 17meV, and 21meV. The 11meV scan is just before the waterfall feature whilst 17meV and 21meV scans are at different parts



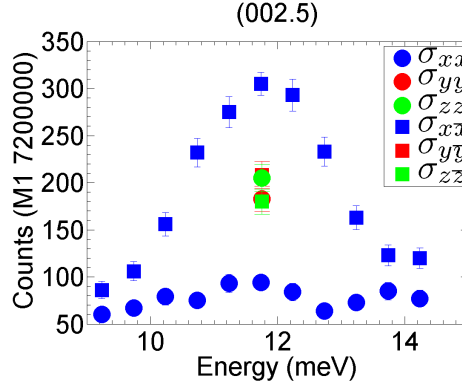


**Figure 3.23: Polarised energy scans at (0,0,2.5).** These scans show that the  $\sim 12\text{meV}$  excitation is of magnetic origin.

of the waterfall feature. The individual scans with all six polarisation channels can be seen in plots on the left hand side of figures 3.24 and 3.25 on pages 95 and 96 respectively. These scans are not that useful in themselves, as often the important information is in their linear combinations. The pure magnetic signal  $M_{\perp}$  for each Q scan is plotted on the right hand side of figures 3.24 and 3.25. Here for the 17meV signal only one Gaussian was fitted as the statistics on the negative  $h$  side was not of sufficient statistics. Due to time constraints measurements were focused on the positive  $h$  side. For these plots  $M_{\perp}$  was obtained using both the spin-flip and non spin-flip equations  $2\sigma_{x\bar{x}} - \sigma_{y\bar{y}} - \sigma_{z\bar{z}}$  and  $\sigma_{yy} + \sigma_{zz} - 2\sigma_{xx}$ . Technically these linear combinations do not give the same thing. Even though they both get rid of the incoherent and direct nuclear contributions, some other contributions remain. The difference between them can be seen in the equations below.

$$\sigma_{yy} + \sigma_{zz} - 2\sigma_{xx} = M_{\perp}^* M_{\perp} + (M_{\perp} N^* + M_{\perp}^* N) \quad (3.1)$$

$$2\sigma_{x\bar{x}} - \sigma_{y\bar{y}} - \sigma_{z\bar{z}} = M_{\perp}^* M_{\perp} - i\hat{x} \cdot (M_{\perp}^* \times M_{\perp}) \quad (3.2)$$

Here  $i\hat{x} \cdot (M_{\perp}^* \times M_{\perp})$  is the chiral term and should be zero if there is no chirality

in the structure. For the A-type AFM expected for  $\text{Na}_{0.8}\text{CoO}_2$ , this should be the case. The  $(M_\perp N^* + M_\perp^* N)$  term is a mixing term between structural and magnetic signals. This second term must be very close to zero. If  $(M_\perp N^* + M_\perp^* N)$  was non-zero a large difference between the  $\sigma_{yy} + \sigma_{zz} - 2\sigma_{xx}$  and  $2\sigma_{x\bar{x}} - \sigma_{y\bar{y}} - \sigma_{z\bar{z}}$  signals would be expected. No such difference was observed for these measurements.

It is important to note that it is possible to obtain the purely magnetic signal via the linear combination  $M_\perp^* M_\perp = (\sigma_{x\bar{x}} + \sigma_{\bar{x}x}) - (\sigma_{y\bar{y}} + \sigma_{\bar{y}y} + \sigma_{z\bar{z}} + \sigma_{\bar{z}z})/2$ . This requires the spin-flip channels from flipper 1. This method was not used for two main reasons. The first reason is that the chiral and nuclear-magnetic signals were considered to be negligible. The second reason is the fact that with flipper two, one could obtain a better flipping ratio.

The pure magnetic signals from the Q scans in figures 3.24 and 3.25 can be summarised in figure 3.26(a) on page 96. Here it can be seen that the centre of the magnetic waterfall moves very little. The pure structural contribution can be inferred from the  $\sigma_{xx}$  channel alone. The contributions to the  $\sigma_{xx}$  channel can be seen below.

$$\sigma_{xx} = NN^* + \nu_i + \frac{1}{3}\sigma_i \quad (3.3)$$

Here  $\nu_i$  is the isotope-incoherent signal and  $\sigma_i$  is the spin-incoherent signal. Neither of these should be Q dependent. Therefore, any features seen in the Q scans can be attributed to the structural component  $NN^*$ , i.e., phonons. The plot of the  $\sigma_{xx}$  channels can be seen in figure 3.26(b). Here it can be seen that both 11meV and 21meV have clear peaks. At 17meV however, there is a really broad peak centred around zero. Since 11meV and 21meV have a clear phonon branch, it is likely that at 17meV there is also a branch roughly at  $h \sim 0.08$ .

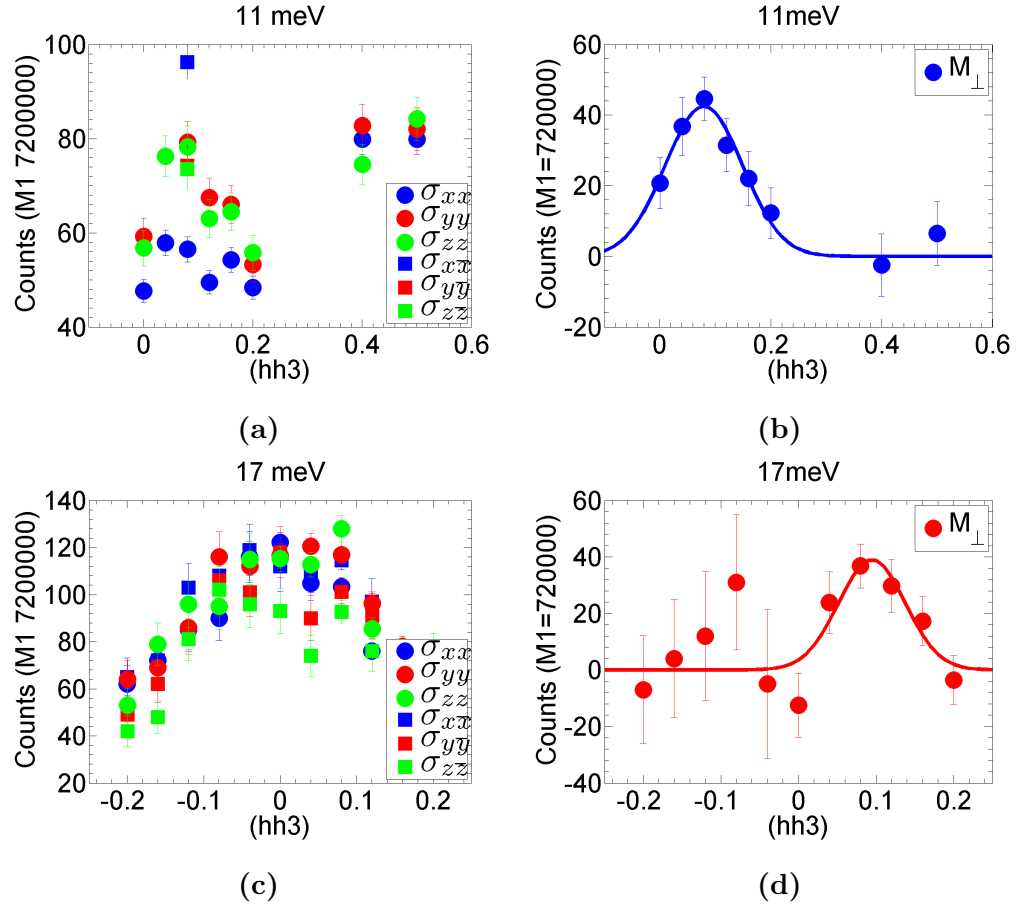


**Figure 3.24: Polarised Q scans along  $(hh3)$  for 11meV and 17meV.** The individual polarisation channels can be seen on the left hand side (a,c), whilst the pure magnetic contribution can be seen on the right hand side (b,d).

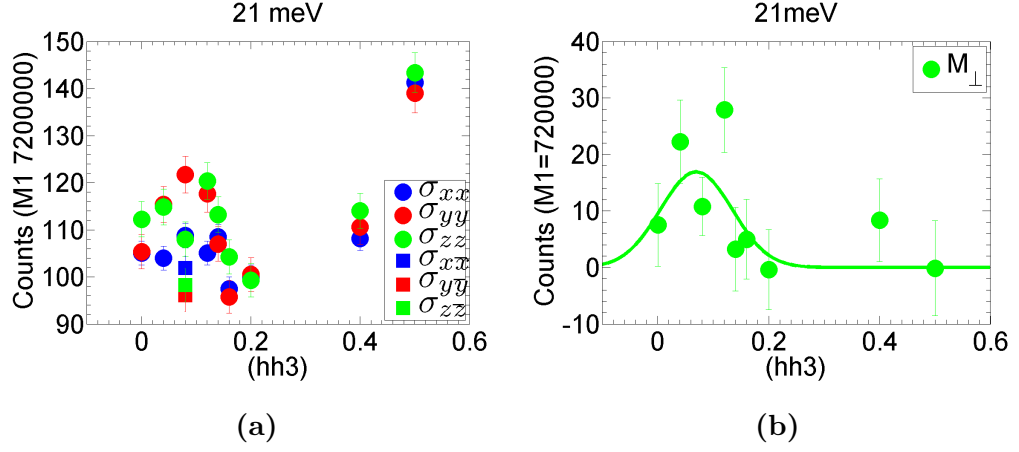


**Figure 3.25: Polarised Q scans along  $(hh3)$  for 21meV.** (a) The individual polarisation channels, (b) and the pure magnetic contribution can be seen.

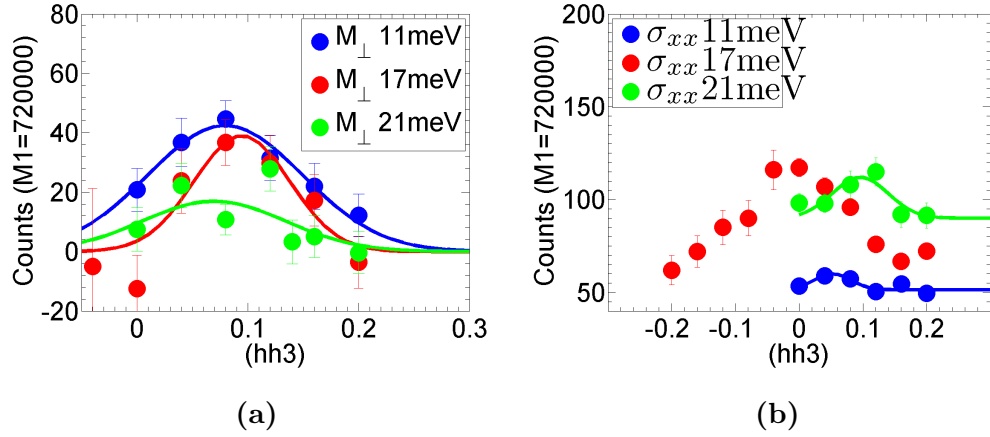


**Figure 3.26: Summary of the polarised Q scans.** Here, (a) the pure magnetic component  $M_{\perp}$  and the (b) the pure structural component as inferred from the  $\sigma_{xx}$  channel can be seen.

## 3.4 Analysis

In this section the INS spectrum will be studied in further detail. Background will be removed and magnetic signal will be modelled using linear spin-wave theory. Various magnetic superstructure models will be discussed as a means to explain the waterfall feature. Finally, the INS spectrum will be compared to the expected phonon spectrum from first-principles DFT calculations [21].

### 3.4.1 Fitting the Spin Waves

The interaction model for  $\text{Na}_x\text{CoO}_2$  is shown in figure 3.9(a). The interactions consist of  $J_{ab}$  and  $J_c$  and  $J'_c$  which correspond to nearest-neighbour interactions in the  $ab$  plane, nearest-neighbour interactions along the  $c$  axis, and a diagonal interaction between cobalt layers respectively. However, the dataset is not of high enough quality to distinguish between different  $J'_c$  models. One could use a fixed ratio of  $J'_c/J_c$  as used in Ref. [112]. For simplicity, in this thesis work  $J'_c$  will be set to zero and will not be considered in the calculations. Also, at (003) the polarised energy scan revealed two separate gaps. The spin-wave model used must replicate this double gap feature. Such a spin-wave model can be obtained from Ref. [92]. The Hamiltonian is given as:

$$H = -J_{ab} \sum_{\langle ii' \rangle} S_i S_{i'} - J_c \sum_{\langle ij \rangle} S_i S_j - D \sum_i (S_i^z)^2 - E \sum_i [(S_i^x)^2 - (S_i^y)^2] \quad (3.4)$$

Here  $D$  is the easy axis anisotropy along the  $c$  axis and  $E$  is a two-fold easy plane anisotropy. Such a Hamiltonian will result in a spin-wave of the following form given below in equations 3.5-3.7 [92]. Note that  $E=0$  produces a single gap and will be assumed for the stripe case.

$$\hbar\omega = \sqrt{(A_Q + D)^2 - (C_Q \pm E)^2} \quad (3.5)$$

$$A_Q = -J_{ab} [\cos(2\pi h) + \cos(2\pi k) + \cos(2\pi(h+k)) - 3] - J_c \quad (3.6)$$

$$C_Q = -J_c \cos(\pi l) \quad (3.7)$$

With the theoretical spin-wave model defined, the next step is to obtain fits to the spin waves from the INS data. For the Q scans the spin-wave positions can be obtained easily with a Gaussian function and a constant background. For the  $(hh3)$  and  $(h03)$  directions, an additional constraint was placed so that the positions of the two Gaussian functions were symmetric with respect to  $h = 0$ . For the  $(h, 0, 2.5)$  direction additional background subtraction was required to obtain the spin-wave positions. In the 19meV  $h = 0$  region the scattering angle (A4 angle on triple axis spectrometers) is at it lowest and is subject to a higher background. The  $(h, 0, 2.5)$  low scattering angle (A4) background can be seen in further detail in figure 3.27 on page 99. An energy scan was performed at  $(0.4, 0, 0.5)$  in order to determine low A4 background. At  $h = 0.4$ , the energy scan should be sufficiently far away from the excitations observed along  $(h, 0, 2.5)$  direction. This energy scan plotted as a function of A4 can be seen in figure 3.27 in black. A Gaussian centred at zero is fitted to this data which is presented in the black dashed line. For comparison, all the Q scans performed along  $(h, 0, 2.5)$  direction are plotted as a function of A4 in colours ranging from red to purple. It is important to note that in the  $(0.4, 0, 0.5)$  energy scan there was a very high point at  $A4=7^\circ$  with 1400 counts. This point was discarded because including it results in an unrealistic, large A4 background. It is possible that at this high point, which corresponds to  $(0.4, 0, 0.5)$ , 13meV, there is an excitation. The full background removed  $(h, 0, 2.5)$  spectrum can be seen in figure 3.28 on page 99. Here the white circles are the fits to the Q scans. Note that the spin-wave signal below 12meV can be seen also. The origin of this lower energy signal is not clear. Also, after the A4 background removal, there is hardly any signal left at  $(0, 0, 2.5)$  at 19meV.

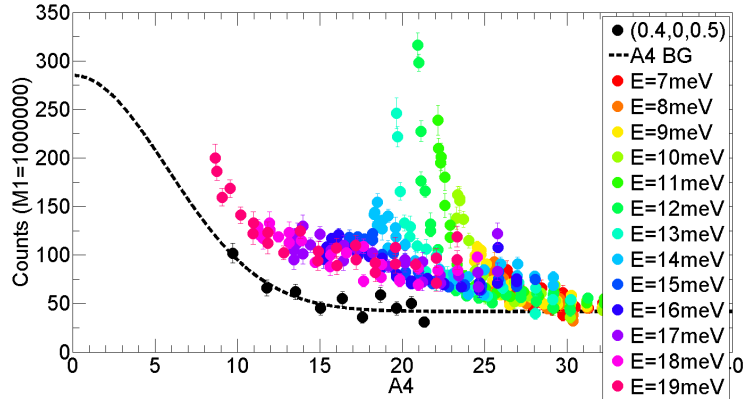


**Figure 3.27: Removal of low scattering angle background.** An  $(0.4,0,0.5)$  energy scan is plotted as a function of the scattering angle ( $A4$ ) and shown in black. This scan is used to fit the low  $A4$  background (black dashed lines). Here the  $(h,0,2.5)$  Q scans are presented as a function of  $A4$  as well (coloured circles).

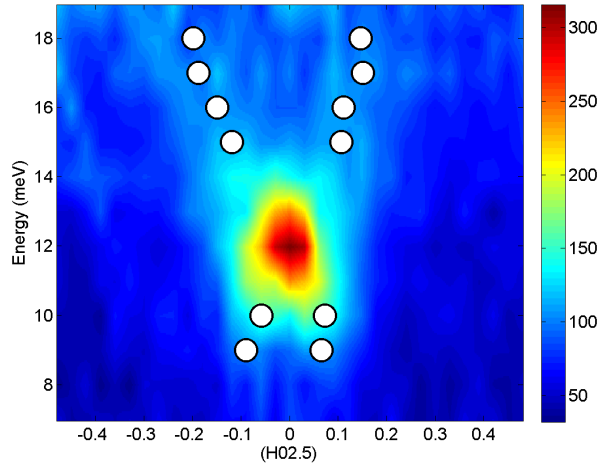


**Figure 3.28: The background removed INS spin-wave spectrum along  $(h,0,2.5)$ .** The white circles are fits to the Q scans after the background subtraction.

In the  $(00l)$  direction, the data is obtained via energy scans. In these scans, the elastic incoherent signal was modelled with a Gaussian centred at zero energy. The remainder background showed a slight linear dependence, with slightly higher intensities at higher energies. A linear function was used to fit this dependence. For both the square and the stripe phase INS data, the background was obtained by fitting  $l = 2.5, 2.55, 2.6$  and  $2.65$  scans. For these energy scans, the background signal and the spin-wave excitation is clearly distinguishable from one other. From these fits an average background is obtained for the  $(00l)$  energy scans. From the obtained spin-wave positions after background subtraction, only the energy scans close to  $l = 2.5$  could be used. Due to resolution effects any other energy scan fit underestimated the spin-wave energy whilst a Q-scan-type fit overestimated the spin-wave Q position. It is possible to overcome this problem by considering the resolution of the instrument. However, it was found that, knowing the position of the spin-wave in the vicinity of  $l = 2.5$  is sufficient information to qualitatively reproduce the observed INS features.

The obtained spin-wave positions were used with a  $\chi^2$  minimisation routine in order to establish a best fit to the theoretical spin-wave parameters. For the minimisation of  $\chi^2$  the MINUIT [120] software package was used through its MATLAB interface fminuit [121]. The parameter values for the best fit can be seen in table 3.2 on page 101 for the square and stripe phase samples. It is important to note that not all measured spin-wave positions were used to obtain this fit. For the  $(hh3)$  and  $(h03)$  directions, only data points below 12meV were used, i.e. the square phase waterfall feature was not considered in the spin-wave fit. The  $(h, 0, 2.5)$  direction is not considered in the spin-wave fit either. This is because the position of the spin wave is dependent on the background correction. An incorrect background subtraction could result in incorrect spin-wave positions.



Sample Phase	$J_{ab}$ (meV)	$J_c$ (meV)	$D$ (meV)	$E$ (meV)
<b>Stripe</b>	5.7(4)	-11.35(8)	-0.09(4)	-
<b>Square</b>	5.5(2)	-11.64(3)	-0.18(3)	0.07(3)

**Table 3.2: Spin-wave fit to stripe and square phase samples.**

These fits to the spin-waves can be seen in figures 3.29 and 3.30 for the stripe and square phase samples respectively. In these figures the left hand side colour map shows the experimental data after the removal of elastic incoherent background and a two dimensional interpolation of the data. The fits obtained from unpolarised scans are given as white circles and the black line is the fit to the dispersion. On the right hand side the colour map is given by the expected neutron intensity as calculated using SpinW programme [122]. For these intensity calculations an arbitrary resolution and intensity scale has been used. The arbitrary resolution used is sufficient for a qualitative comparison between calculated and measured spin-wave dispersions. Therefore, more detailed resolution calculations were deemed unnecessary. For the square phase, the two different dispersions are represented by solid and dashed lines. Additionally the fits to the polarised scans are given in black circles.

The stripe phase spin-wave fit can be seen in figure 3.29 on page 102 for the  $(00l)$  and  $(hh3)$  directions. For the  $(00l)$  direction, very good agreement between the measured and calculated INS spectrum can be seen. In figure 3.29(b), the elastic incoherent background was modelled by collecting all the data performed at  $(-0.2, -0.2, 3)$  and fitting it with a Gaussian centred at zero. For the  $(hh3)$  direction, there is a slight disagreement between measurement and calculations. The measured spin-wave intensity disappears rapidly above  $\sim 11$  meV which is not expected in the calculations.

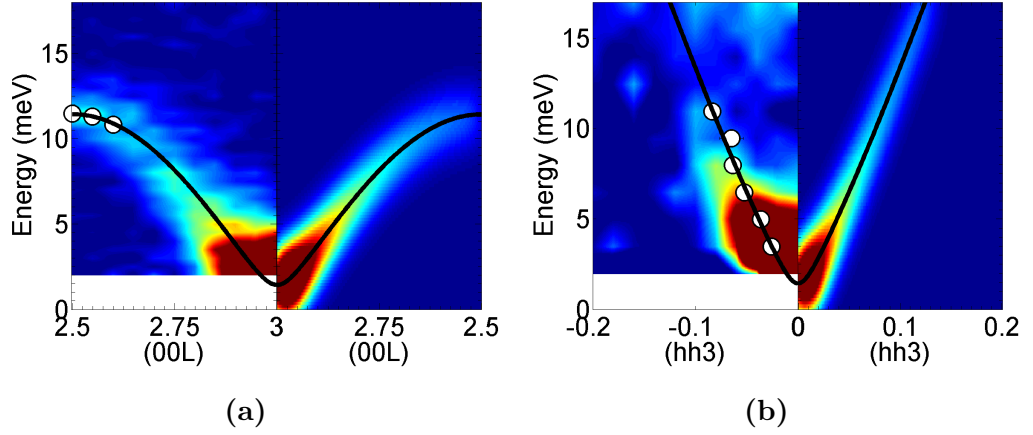


**Figure 3.29: Spin-wave fit to stripe phase sample** shows good agreement along (a)  $(00l)$  direction. For the (b)  $(hh3)$  direction the spin-intensity does die down rather rapidly.

For the square phase, the measurements along the  $(00l)$  direction can be modelled more accurately than the stripe phase, as the location of the gaps are known. As seen from figure 3.30(a) on page 103, there is very good agreement along this direction. For the  $(hh3)$  and  $(h03)$  directions, which can be seen in figures 3.30(b) and (c) respectively, there is disagreement between the measurement and calculations above 12meV. The largest difference is the waterfall feature where the dispersion becomes infinitely dispersive above  $\sim 12$ meV. There is also a difference in the rate of change of intensity with increasing energy. For the calculation a steady decrease of intensity with energy is expected, instead in the measurements there is a rapid decrease of intensity up to  $\sim 12$ meV, after which there is an increase in intensity which remains roughly constant at higher energies. For the square phase, the measurements along the  $(h,0,2.5)$  direction can be seen in figure 3.30(d). Here, the high background from the low scattering angle has been removed. The white circles are the fits to Q scans. These spin-wave positions have not been used in the theoretical spin-wave fit. Despite this, the INS spectrum observed along  $(h,0,2.5)$  above 12meV does agree

with the theoretical spin-wave dispersion. However, the observed spin-wave signal below 12meV is not predicted in this theoretical spin-wave model.

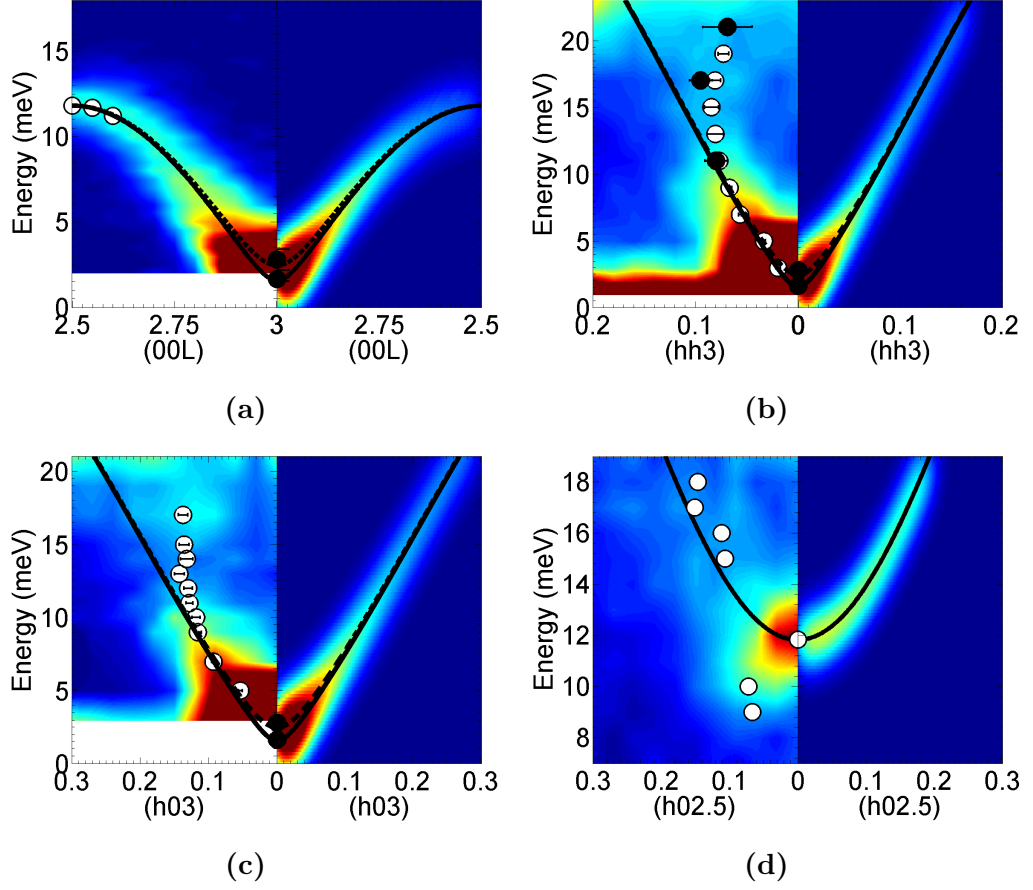


**Figure 3.30: Spin-wave fit to square phase sample.** There is good agreement between the measured and the calculated spin-wave spectrum for **(a)** (00 $l$ ) direction and partial agreement for **(b)** ( $hh3$ ), **(c)** ( $h03$ ), and **(d)** ( $h02.5$ ) directions. The theoretical spin-wave model cannot replicate the waterfall feature observed along the ( $hh3$ ) and ( $h03$ ) directions. For the ( $h,0,2.5$ ) direction there is good agreement above 12meV; however, below 12meV there are some signals unaccounted by the theoretical model.

### 3.4.2 Waterfall Features

It is of interest to quantify the properties of the waterfall. This can be done by looking at the fitted amplitude, area and full-width at half-maximum (FWHM) of the  $(hh3)$  and  $(h03)$  Q scans which can be seen in figure 3.31 on page 105. Here, the fitted amplitude and area are plotted in log scale on the y axis in order to emphasize the change upon entering the waterfall. It can be seen that both the area and the amplitude decrease exponentially until it reaches  $\sim 14\text{meV}$  after which, there is a slight increase. This trend is the same for both  $(hh3)$  and  $(h03)$  directions as shown in blue and red points respectively. The fitted FWHM for  $(hh3)$  and  $(h03)$  are roughly the same in units of  $\text{\AA}^{-1}$ . The overall trend for both dispersions is a broadening with increasing energy.

The increase in FWHM with increasing energy can either originate from the sample or the instrument. If it is originating from the sample, this indicates that the excitations have a shorter correlation length at higher energies. The alternative is simply that the instrumental Q resolution becomes broader with increasing energy. For these experiments it is not possible to distinguish between these two cases. The experiments were not optimised for accurate measurements of FWHM and the true instrumental resolutions are unknown. However it is possible to perform simple calculations of the resolution using ResLibCal software [79] in order to gain some understanding as to how the resolution should change with increasing energy. ResLibCal can calculate the resolution ellipsoid for triple axis instruments given the instrument geometry and sample mosaic. The calculations can be performed using two different methods, the Cooper-Nathans method or the Popovici method. The Popovici method considers the effect of focusing the monochromators and analysers whilst Cooper-Nathans method does not. For the data displayed in figure 3.31, focusing was used on the monochromator and the analyser. Therefore, one might expect the Popovici method to give better results. Both methods were tested on

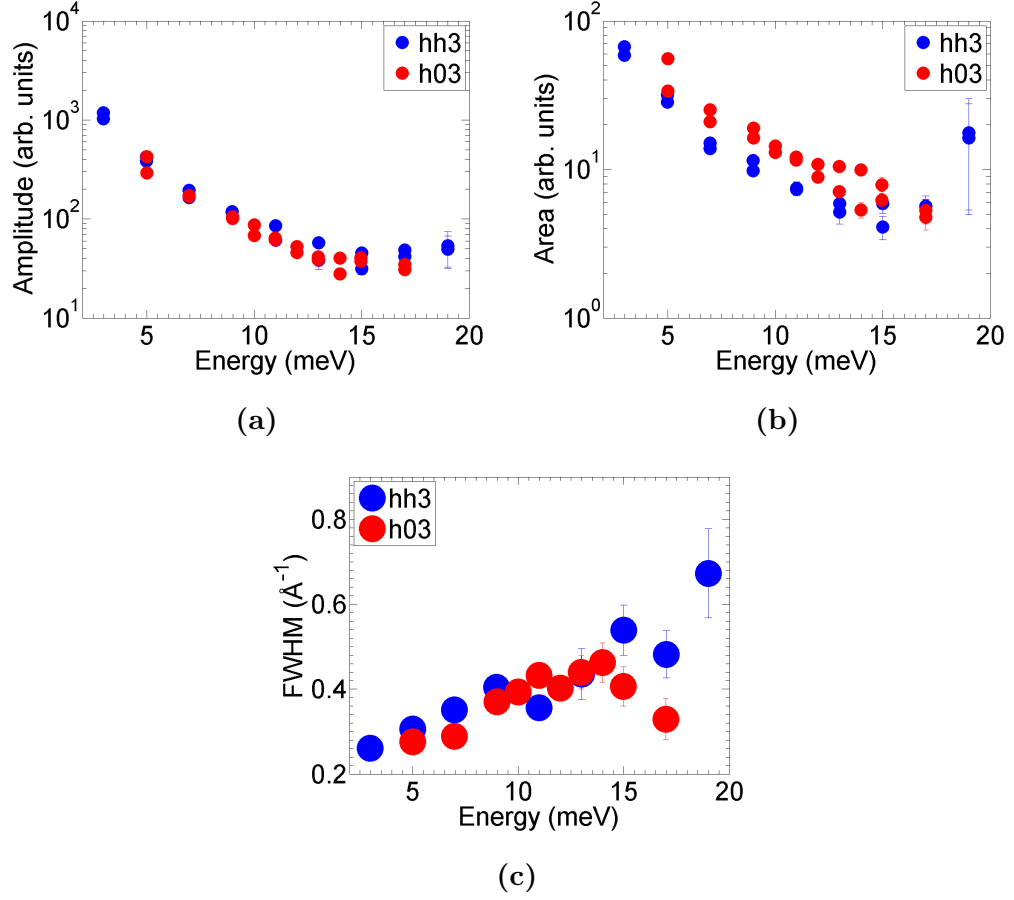


**Figure 3.31: Fitted spin-wave area and FWHM for square phase.** (a) The fitted amplitude and (b) area for ( $hh3$ ) and ( $h03$ ) Q scans decrease exponentially, show a minimum at  $\sim 14$  meV, and then start increasing again. (c) The FWHM of the ( $hh3$ ) and ( $h03$ ) dispersions increase at roughly the same rate. Such an increase is not predicted by resolution calculations which indicates that the spin-waves could have less correlation at higher energies.

(004) and (0.8,0.8,0) Bragg peak widths and showed reasonable agreement. The resolution FWHM was calculated along the ( $hh3$ ) dispersion using both methods. The Cooper-Nathan method gave  $\sim 0.6 \text{ \AA}^{-1}$  at lower energies and  $\sim 0.4 \text{ \AA}^{-1}$  at higher

energies whilst the Popovici method gave a constant of  $\sim 0.14 \text{ \AA}^{-1}$  for all energies. Despite poor agreement with the data, an important insight can be achieved from these calculations. Neither method predicts a broadening at higher energies along the dispersion, in fact Cooper-Nathans method predicts the contrary. This would mean that the broadening seen in figure 3.31(b) must be due to a loss of correlation in the spin-waves. It is very important to note that these resolution calculations are not conclusive and in order to make any strong statements concerning broadening it is necessary to carry out another set of INS experiments.

Another important parameter is the waterfall wave vector,  $Q_{wf}$ . The position of the waterfall is at  $h = 0.085$  and  $h = 0.14$  for  $(hh3)$  and  $(h03)$  dispersions respectively. For both directions, this corresponds to the same  $Q$  length of  $|Q_{wf}| = 0.37(2) \text{ \AA}^{-1}$  and distance  $d_{wf} = 17(1) \text{ \AA}$ . If the out of plane component of the wave vector is considered, the waterfall  $Q$  length becomes  $|Q_{wf}| \sim 1.78 \text{ \AA}^{-1}$  and distance of  $d_{wf} \sim 3.5 \text{ \AA}$ . These distances could potentially be a measure of the magnetic nano-clusters or relate to the Coulomb landscape of  $\text{Na}_{0.8}\text{CoO}_2$ .

### 3.4.3 Comparison to Phonon calculations

The structural excitations for the square phase  $\text{Na}_{0.8}\text{CoO}_2$  has been studied extensively by DJ Voneshen et al. [21]. They have used a first-principles DFT model to calculate the phonon spectrum which was later verified by inelastic neutron and x-ray scattering methods. Using this DFT model it was possible to calculate neutron intensity of the phonons in the regions of interest. This is extremely useful for  $\text{Na}_{0.8}\text{CoO}_2$  where it can be hard to say where the spin-wave branch ends and the phonon branch begins. The results of the phonon calculations as obtained from DJ Voneshen [123] compared to the INS measurements from this thesis work can be seen in figure 3.32. Here, for each subfigure, the left hand side represents the INS measurements and the right hand side represents the calculated neutron intensity

of the phonons. The white data points are fits to unpolarised Q scan and the black data points are the fits to the pure magnetic signal. The black lines represent the theoretical spin-wave dispersion calculated using the parameters in table 3.2. In figure 3.32(a) the  $(hh3)$  comparison can be seen. Here the red points are fits to the structural part of the polarised measurements, i.e. the  $\sigma_{xx}$  channel. These red points agree very well with the expected phonon intensities. In addition, the 17meV  $\sigma_{xx}$  measurement in figure 3.26(b) is also in great agreement with the phonon calculations. In figure 3.32(b) the phonon comparison can be seen for the  $(h03)$  direction. The phonon spectrum here is not too different to that observed along  $(hh3)$  direction. In both cases the spin waves are measured accurately up to the acoustic-like phonon branch after which it becomes difficult to fit the dispersion. It is not clear if the spin waves cross this branch or not. In figure 3.32(c) the  $(h,0,2.5)$  phonon comparison can be seen. Only a small presence of phonons are expected in this direction which is consistent with the polarised measurement made at  $(0,0,2.5)$  12meV as seen in figure 3.23. It is noteworthy that both the nuclear and magnetic signal happen to be at the same energy at  $(0,0,2.5)$ . In figure 3.32(d) the  $(hh5)$  direction comparison can be made. There are two main areas where there is disagreement between neutron measurements and phonon calculations. The first is the 17meV signal in the region  $h = 0.25-0.5$  and the second is 40meV signal in the region  $h = 0.2-0.4$ . The 17meV signal could be of magnetic origin but it is less likely that the 40meV signal is magnetic due to its quite large intensity. The magnetic form factor is expected to reduce the spin-wave intensity by roughly factor of two going from  $(003)$  to  $(005)$ . The 40meV is much stronger than the  $(003)$  spin-waves which would mean it is not of magnetic origin.

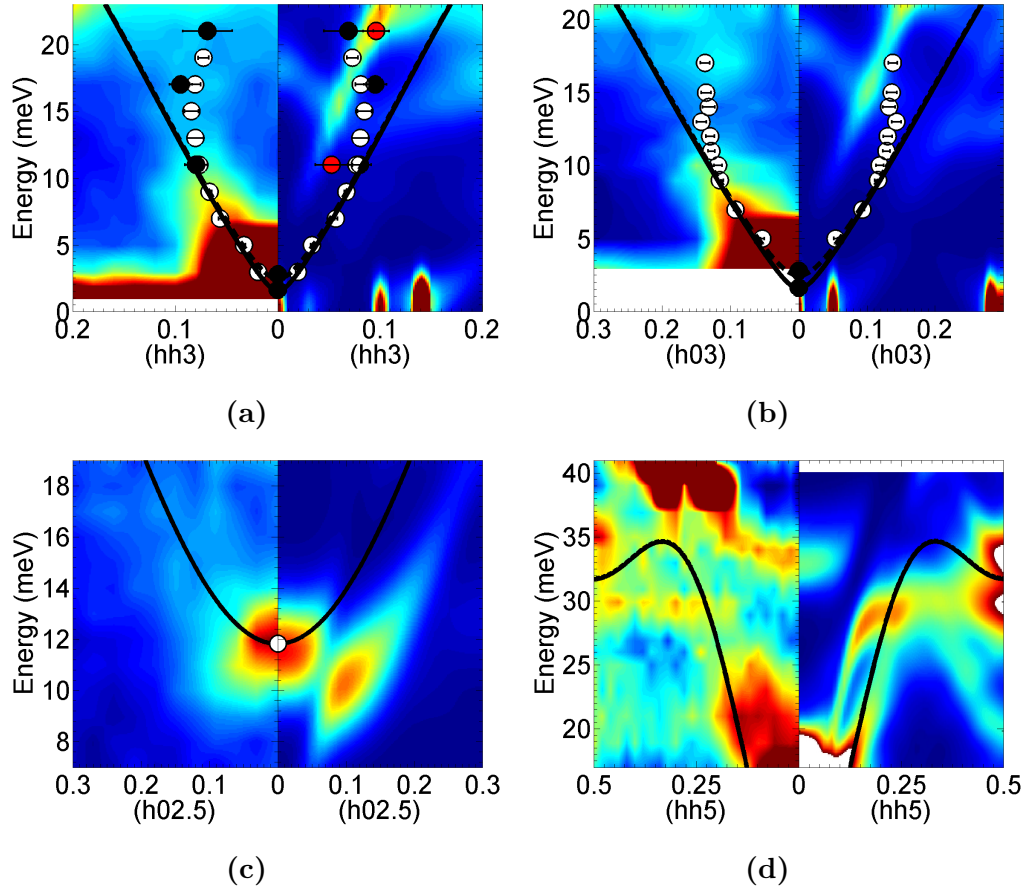


**Figure 3.32: Comparison between measured INS spectrum and calculated phonon intensities.** Here in each subfigure the INS data are presented on the left hand side and the phonon calculations are shown on the right hand side. Fits to unpolarised data are given in white circles. Pure magnetic or nuclear signals are given in black or red circles respectively. The calculated spin-wave dispersion is given in black. Phonon calculations by Ref. [123].



### 3.4.4 Magnetic Superstructure Model

It was already mentioned in the introduction that for the square phase  $\text{Na}_{0.8}\text{CoO}_2$  charge ordering might occur as a direct result of the Na ordering. It would be expected that directly under the Na tri-cluster sites, there would be  $\text{Co}^{3+}$  with  $S=0$  and Co sites far away from Na tri-clusters could be potential places for  $\text{Co}^{4+}$  with  $S=1/2$  to localise. This was established from calculations of the Coulomb potential within the Co layer which can be seen in figure 3.10(b) [17]. The DFT calculations for the square phase  $\text{Na}_{0.8}\text{CoO}_2$  also predict some level of magnetic patterning within the Co layer. In the DFT model, each Co site has a moment size between  $0.07\mu_B$  and  $0.11\mu_B$ , distributed in such a way that there is a smaller moment size below or above the Na tri-clusters. This can be seen in detail in figure 3.33 on page 110. Here the size of the circles represents the moment size ( $0.07\text{-}0.11\mu_B$ ), and the colour represents the position with respect to the Na tri-cluster. The red Co sites sit directly above or under a Na tri-vacancy cluster and the blue sites do not [21, 123]. Such a model is qualitatively in agreement with the Coulomb potential calculations [17].

In this section the aim will be to try out some fully localised models with the help of the SpinW software [122]. The easy to use interface of SpinW allowed the test of many different superstructures rapidly. Once a superstructure was established, the spin-wave spectrum along  $(hh3)$  or  $(h03)$  was calculated and compared to the neutron results. None of the tested magnetic superstructure models were able to produce something similar to the magnetic waterfall observed. However there were some models which shared some of the features of the  $(hh3)$  or  $(h03)$  dispersions. Here two superstructure models will be discussed which individually can explain the gap in intensity at  $\sim 15\text{meV}$ , or the rapid drop in intensity.

The first magnetic superstructure model is very similar to the A-type AFM structure proposed for the parent structure (see figure 3.9) but with one modification: the spins were placed only on the blue sites and not on the red sites. The spin-wave

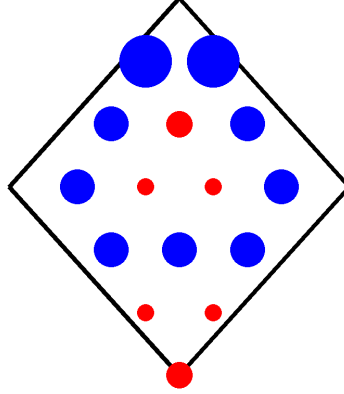


**Figure 3.33: Magnetic moment distribution for the square phase as calculated by DFT.** Here the size of the circles represents the Co moment size and the colour represents different types of Co sites. The red Co sites have a Na immediately above or below them, whilst the blue Co sites do not. DFT calculation of moment sizes from Ref. [123].

dispersion from such a magnetic superstructure can be seen in figure 3.34(a). Here the in plane exchange interaction  $J_{ab}$  was scaled to  $J_{ab}=12\text{meV}$  in order to match the observed neutron results. The spin-wave dispersions as calculated from equations 3.5-3.7 and parameters 3.2 are given by the black lines. The white and black circles are the fits to the unpolarised and polarised scans respectively. It can be seen that such a model does produce a gap in the spin-wave dispersion similar to the INS results. However, such a model does not have the rapid intensity drop and it has additional spectral signatures which are not present in the INS data.

The second model approaches the same problem in a different way. In this model, there is no spin removal. The magnetic structure is identical to the A-type AFM structure. The superstructure is introduced by having different in plane exchange interactions  $J_{ab}$  between different sites. The out of plane interaction  $J_c$  is assumed identical. There are too many non-equivalent sites therefore a major simplification

was put in. It was assumed that all couplings between two blue sites will be identical and similarly all red-red and blue-red couplings will be equivalent. This reduced the system to three in plane interactions. By setting all red-blue and red-red interactions close to zero, and by setting the blue-blue interactions to 12meV, a spectrum with a rapid intensity decrease was observed which can be seen in figure 3.34(b). Such a model predicts very faint features at higher energies which are not waterfall-like. There is also a very low lying interaction which could technically also exist in the neutron data. However, it would be very difficult to observe such a signal as it would be overpowered by the incoherent signal.

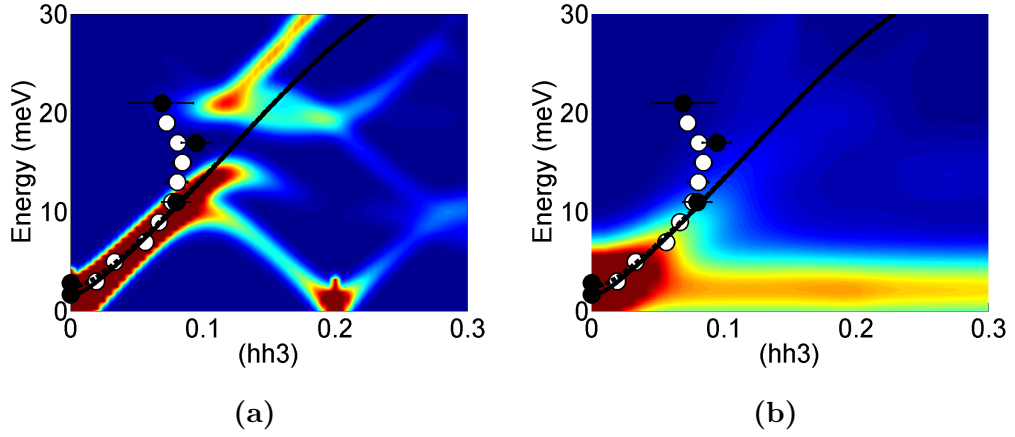


**Figure 3.34: Comparisons of magnetic superstructure calculations with INS data.** Two different superstructure models have been tested which present a qualitative description of the data. For both structures, the square phase supercell is used. **(a)** If spins are removed from under and above the Na1 sites, and  $J_{ab}$  is increased to 12meV, a gap forms at  $\sim 18$ meV. However, there are many spectral signatures which are not compatible with neutron measurements. **(b)** In a different model no spins are removed but different  $J_{ab}$  interactions are used in plane. If any interaction between two red sites or one blue and one red site is set to zero, it is possible to obtain a dispersion which loses intensity rapidly. Additionally, a very low level excitation is formed which could be lost in the neutron incoherent signal. These two models are not successful in reproducing the waterfall feature but can qualitatively account for the dip in intensity at  $\sim 12$ meV and the rapid drop in intensity as we approach 12meV.

### 3.4.5 Spin-Orbital Polaron Model

The spin-orbital polaron model for  $\text{Na}_x\text{CoO}_2$  has been used to explain the existence of negative Curie-Weiss constant and the drop in intensity of the  $(hh3)$  spin-wave dispersion around  $\sim 12\text{meV}$  [117]. It is possible to use the polaron model to create a magnetic superstructure for the square phase. In the Coulomb landscape calculations, there are two sites at the minimum of the potential where  $\text{Co}^{4+}$   $S=1/2$  moments are expected to localise [17]. Following the polaron-type scenario, the surrounding eight nearest-neighbour sites would be  $\text{Co}^{3+}$   $S=1$ , and  $\text{Co}^{3+}$  sites further away would be in the low spin state of  $S=0$ . The resulting magnetic superstructure of such a scenario can be seen in figure 3.35(a). Here the  $\text{Co}^{4+}$   $S=1/2$  sites are shown in green, the  $\text{Co}^{3+}$   $S=1$  are shown in blue and the  $\text{Co}^{3+}$   $S=0$  sites are not shown since they are non-magnetic. The AFM orientations between neighbouring  $S=1$  sites are taken from, Daghofer et al. [117]. This configuration is referred to as the bipolaron, because it is composed of two  $\text{Co}^{4+}$   $S=1/2$  sites. The magnetic superstructure, and its different type of next-nearest bonds can be seen in figure 3.35(b). Here, magnetic unit cell is related to the square phase unit cell after an origin shift of  $\mathbf{a}+\mathbf{b}$ , where  $\mathbf{a}$  and  $\mathbf{b}$  are the principle axes of the parent compound. Along the  $\mathbf{c}$  axis, the bipolarons reside directly above each other and are stacked in AFM order. In total four different nearest neighbour interactions are considered within the Co layer. These are  $J_{ab}$  which is between two  $S=1/2$  sites,  $J$  which is between two  $S=1$  sites,  $J'$  which is between  $S=1$  and  $S=1/2$  sites, and finally,  $J_{bipol}$  which is the coupling between two neighbouring bipolarons. In literature there are estimates of the strength of the exchange parameters. It is expected that  $J \sim -10-20\text{meV}$ (AFM),  $J_{ab} \sim -J$ , and  $|J'| \lesssim |J|$ . The exchange coupling  $J'$  can either be FM or weakly AFM. In figure 3.12(b), it can be seen that there is also a AFM second-nearest neighbour interaction (given in red) between the  $S=1$  sites for which AFM  $|J_{diag}| \leq |J|$  is expected. This interaction  $J_{diag}$  is also introduced in the

magnetic superstructure model considered below. In this model  $J_{diag}$  is used only within the bipolaron as shown in figure 3.12(b) and is not used between two different bipolarons.

The spin-wave dispersion of this magnetic superstructure was calculated along ( $hh3$ ) using SpinW Matlab code [122]. The exchange interactions  $J_{ab}$  and  $J'$  were taken to be FM. The resulting spectrum for  $J=-10$  (AFM),  $J_{ab} = J' = J_{bipol} = -J$ , and  $J_{diag} = J$  can be seen in the colour map in figure 3.36 on page 116. The presented spin-wave spectrum is an average of the different symmetry directions and is presented in units of the parent structure. The fits to the spin-wave data are given in black and white circles. The black lines are the calculated spin-wave from equations 3.5-3.7 and parameters 3.2. This magnetic superstructure calculation is incompatible with the INS observations. In the calculated spectrum, there are many features which aren't observed in experiments, such as the strong spin-wave branch originating from (0.2,0.2,3).

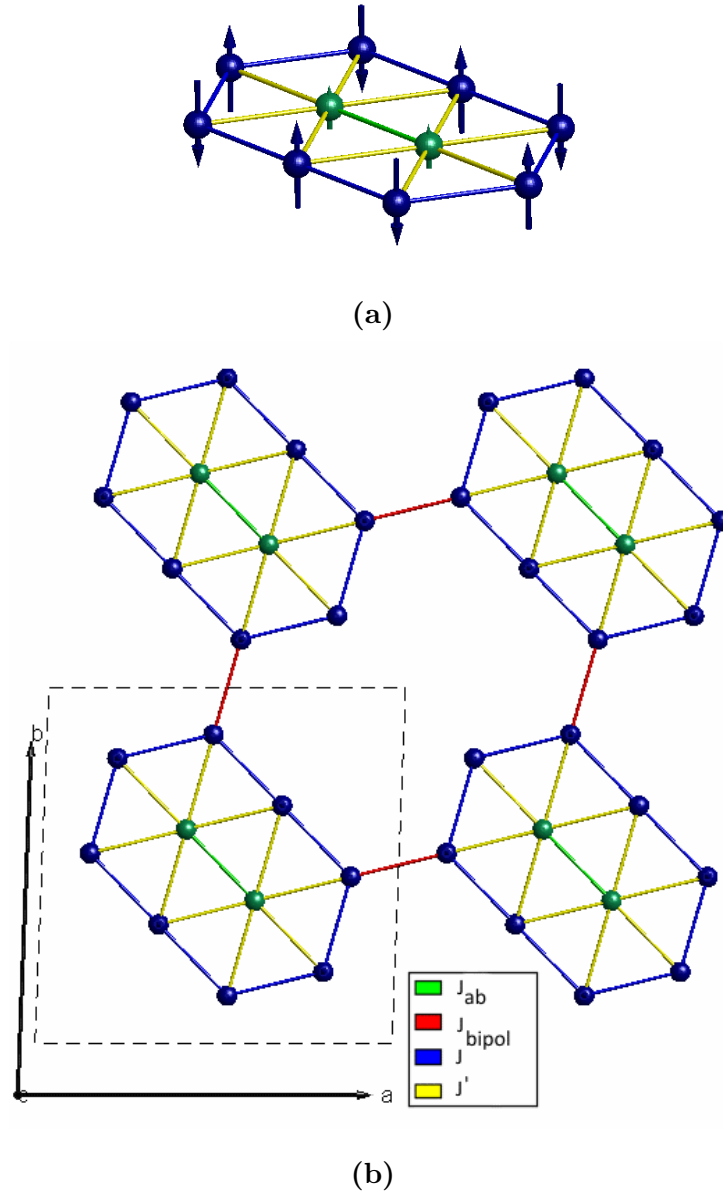


**Figure 3.35: Bipolaron based magnetic superstructure model.** (a) The bipolaron can be visualised as two  $\text{Co}^{4+}$   $S=1/2$  sites (green) surrounded by eight  $\text{Co}^{3+}$   $S=1$  sites (blue). (b) The unit cell of the magnetic superstructure is the same size as that of the square phase superstructure. Here the different possible exchange paths are highlighted in different colours.

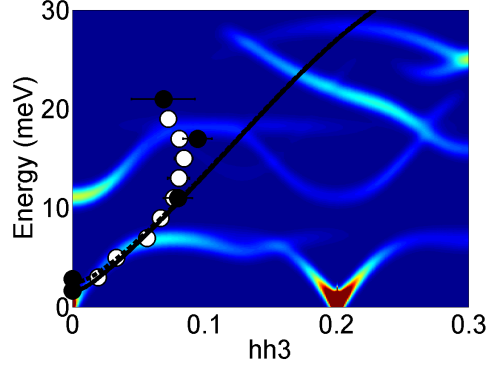


**Figure 3.36: Comparisons of bipolaron based magnetic superstructure and INS data.** The spectrum was calculated for  $J=10$ ,  $J_{ab} = J' = J_{bipol} = -J$ , and  $J_{diag} = J$ . The resulting spectrum is incompatible with INS experimental observations.

### 3.5 Discussion

One of the main motivations of the thesis work was to explain the large difference in  $J_c$  for two samples with very similar concentrations,  $x=0.75$  and  $x=0.82$ . It was known that within this concentration range there are three possible superstructures: the square, stripe, and the 1/13th phase. It was plausible that the different superstructures resulted in different exchange parameters. However, the measurements of square and stripe phase  $\text{Na}_{0.8}\text{CoO}_2$  in this thesis and measurement of 1/13th phase from Ref. [69] all show very similar interaction scheme of  $J_{ab} \sim -6\text{meV}$  and  $J_c \sim 12\text{meV}$ . This interaction scheme agrees with the previous measurements of  $\text{Na}_{0.75}\text{CoO}_2$  [5] but not of  $\text{Na}_{0.82}\text{CoO}_2$  [4]. This is a very surprising result considering the square and the stripe phase are closer in concentration to  $\text{Na}_{0.82}\text{CoO}_2$ . Therefore, the factor of two smaller  $J_c$  observed in  $\text{Na}_{0.82}\text{CoO}_2$  remains unexplained.

The double spin-wave gap feature at (003), which was previously measured for  $x=0.75$  [92], was confirmed using polarised neutrons for square phase  $\text{Na}_{0.8}\text{CoO}_2$ .



Both the square and the stripe phase samples had the same spin-wave anomalies already reported in literature: at higher energies, the intensity drops rapidly and excitations broaden in  $Q$  [4, 5]. However, additional to these measurements, the square phase sample showed a waterfall dispersion. Polarised measurements confirmed that this waterfall is of magnetic origin, which makes this the first observation of a magnon waterfall. The explanation of the waterfall effect is no simple task considering the fact that the true magnetic nature of  $\text{Na}_x\text{CoO}_2$  is not fully understood. Before considering how different magnetic models might reproduce such a dispersion it is important to discuss the previous observations of the waterfall effect.

The waterfall effect has been observed in a wide range of relaxor materials of type  $\text{Pb}(\text{A}_{1/3}\text{Nb}_{2/3})\text{O}_3$  where  $\text{A}=\text{Mg}, \text{Zn}$ , with or without certain levels of  $\text{PbTiO}_3$ . Unlike  $\text{Na}_x\text{CoO}_2$ , in these compounds the waterfall is of pure structural origin. It was initially thought that the waterfalls at  $q_{wf} = 0.2\text{\AA}^{-1}$  could indicate the size of the polar nano regions within the sample. However, detailed INS measurements showed that  $q_{wf}$  changed in different Brillouin zones. This can be seen in figure 3.37(a). This indicates that the waterfall cannot be due to the polar nano regions. Instead, it was possible to explain the waterfall feature through a coupling between the transverse acoustic and transverse optic branches. Such a coupling creates apparent dispersion which connects the two branches without changing the position of the original branches [119]. A more recent discovery of a phonon waterfall was observed in popular thermoelectric material  $\text{PbTeO}_3$  at the  $\Gamma$  point as seen in figure 3.37(b). The mechanism behind this is believed to be identical to those of the relaxor materials. Different to the relaxor materials, the coupling is between a transverse optic and longitudinal acoustic mode. This transverse optic mode acts like a rattling mode due to its anharmonic coupling [124]. This makes it possible to draw many parallels between  $\text{PbTeO}_3$  and square phase  $\text{Na}_{0.8}\text{CoO}_2$ . They are both good thermoelectrics, they both have a waterfall feature, and they both have rattling like

behaviour due to anharmonicity [21].

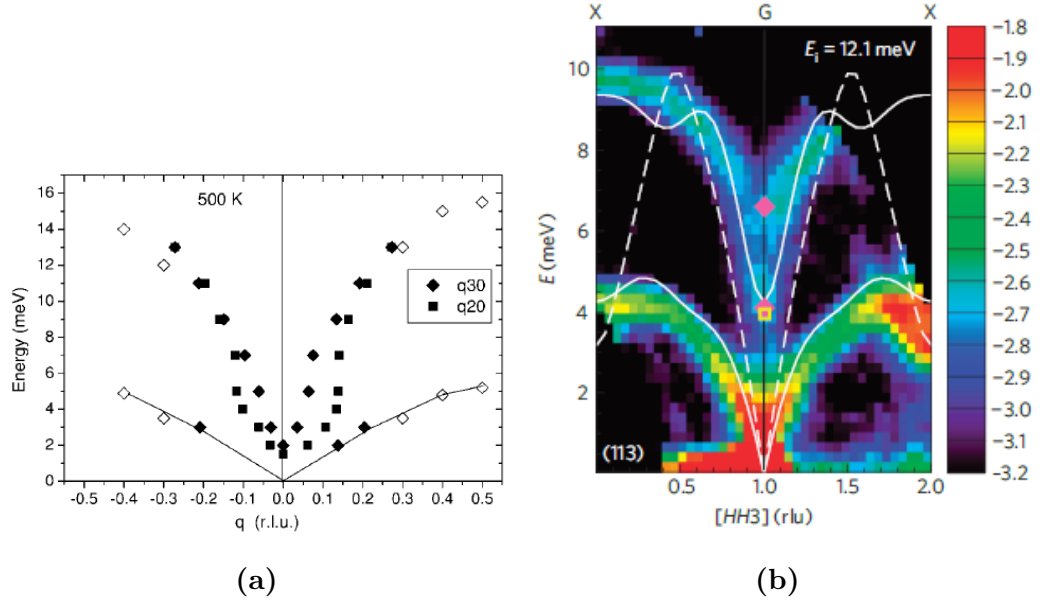


**Figure 3.37: Phonon waterfalls observed in literature.** (a) In Pb(Zn<sub>1/3</sub>Nb<sub>2/3</sub>)O<sub>3</sub> based relaxor material, the waterfalls occurred in different places for different Brillouin zones. (b) For the thermoelectric material PbTeO<sub>3</sub> the waterfall is observed at the zone centre, between the two purple diamond symbols. Images (a) and (b) from [119] and [124] respectively.

The similarities between PbTeO<sub>3</sub> and square phase Na<sub>0.8</sub>CoO<sub>2</sub> give an indication that the magnon waterfall could also be of a similar origin. It is important to note that, for the square phase, close to the minimum of the spin-wave intensity ( $\sim 14$  meV) there is a rattling phonon mode ( $\sim 13$  meV [21]). This indicates that there might be some phonon-magnon coupling in this vicinity. The existence of coupling between phonons and electrons has been suggested by various Raman and inelastic x-ray measurements [125, 126]. In fact it has been suggested that the electron-phonon coupling is beneficial for the thermopower of Na<sub>x</sub>CoO<sub>2</sub> [126]. In

principle, it would be of interest to calculate the magnon-phonon coupling. This may require details of the magnetic ground state beyond the A-type AFM, and the computational task is beyond the scope of this thesis.

Spin waves of a few different magnetic superstructure models were calculated in order to explain the waterfall effect observed in square phase  $\text{Na}_{0.8}\text{CoO}_2$ . Two different magnetic superstructure models were tested. The first model depends on low-spin  $\text{Co}^{4+}$  and  $\text{Co}^{3+}$  with  $S=1/2$  and  $S=0$  respectively. The placements of the spins are based on square phase DFT calculations [21,123], Coulomb potential calculations [17], and NMR measurements [19]. The second model is based on spin-orbital polaron model, where  $\text{Co}^{3+}$  can be in low spin or intermediate spin configurations which correspond to  $S=0$  and  $S=1$  respectively [117]. For this magnetic superstructure bipolarons were placed at the potential minimum of the Coulomb landscape as obtained from Ref. [17]. Neither of the magnetic superstructure models were capable of reproducing the magnetic waterfall. Using the magnetic superstructure models it is possible to recreate some of the measured spin-wave features such as the lack of intensity at  $\sim 14\text{meV}$  and the rapid drop in intensity as one approaches this energy. It is possible that using linear spin-wave theory, it is not possible to reproduce the magnon waterfall.

One possible way to improve the magnetic superstructure models is to introduce a mixture of localised and itinerant magnetism. Such a mixture of localised and itinerant magnetism was considered by Gao et al. [18]; however, in their model a random Na vacancy distribution was used. There are some experimental signatures that suggest a mixed localised-itinerant system. NMR measurements predict an itinerant  $\text{Co}^{3.5+}$  band and  $\text{Co}^{3+}$   $S=0$  moments localised under or above Na1 sites [19]. This information could be combined with the knowledge of the Na superstructures to create a mixed localised-itinerant system. There are many factors which make it difficult to solve the true magnetic superstructure experimentally. Aside from the

small moment size, a magnetic superstructure Bragg peak would have substantially lower intensity compared to a magnetic Bragg peak such as the (003) for example. In the likely scenario where structural and magnetic superstructure Bragg peaks overlap, there is very little chance of ever observing the magnetic signal.

The magnon waterfall could also be possibly caused by magnetic nano-domains as suggested by muon measurements of Ref. [111]. The muon data has been interpreted as clusters on the nanometer scale which are composed of spin-orbital polarons. Taking the waterfall wave vector  $|Q_{wf}|=0.37(2)\text{\AA}^{-1}$ , this would give a cluster size of  $d_{wf}=17(1)\text{\AA}$ . However, it is important to note that the NMR results can be interpreted as contrary to the polaron model. NMR data suggest only  $\text{Co}^{3+}$   $S=0$ , and an itinerant band of  $\text{Co}^{3.5+}$  [19]. For the polaron model some  $\text{Co}^{3+}$  must be in intermediate spin with  $S=1$ . If the polaron clusters did exist, they cannot be randomly distributed. Because, the observed spin-waves are relatively sharp [5]. Another observation which could be explained by a cluster model is the broadening in  $Q$  with energy for the in plane spin-waves. If the broadening is indeed caused by a decrease in correlation length as the rudimentary resolution calculations suggest, this could point towards a spacial inhomogeneity. However, more experiments are necessary before concluding that the correlation length is reducing with energy.

It is clear that any improvements on the magnetic model of  $\text{Na}_x\text{CoO}_2$  will also result in a better understanding of its high thermopower. The simple models considered so far suggest that  $\text{Co}^{3+}$  must have low spin  $S=0$  [16, 108]. However, there has been very little done in terms of explaining the high thermopower by using the various complex magnetic structures and mechanisms discussed in this thesis. It is necessary that any magnetic model suggested should explain the magnetic anomalies and the high thermopower.

### 3.6 Conclusion

The square, stripe and the 1/13th phase superstructures have very similar exchange interactions. The measurements of these superstructures agree with previous measurements of  $\text{Na}_{0.75}\text{CoO}_2$  with unknown superstructure [5]. The factor of two lower  $J_c$  observed in the  $\text{Na}_{0.82}\text{CoO}_2$  with unknown superstructure remains unexplained [4].

Both the stripe and square phase samples show anomalies along  $(hh3)$  dispersion, consistent with the anomalies reported previously in literature [4,5,113]. These anomalies were a rapid drop in intensity with increasing energy and a broadening in  $Q$  with increasing energy. In addition to these anomalies, the square phase sample produced the first ever observation of a magnetic waterfall, a spin-wave dispersion with infinite gradient. The magnetic nature of the waterfall was confirmed using three axis polarisation, which is capable of separating the pure magnetic cross section. Additional to the infinite gradient, the waterfall has another important feature. Before the waterfall feature starts, there is a dip in the intensity at  $\sim 14\text{meV}$ . This is surprising because in the same energy range there is a rattling phonon mode which is known to suppress thermal transport in  $\text{Na}_{0.8}\text{CoO}_2$  drastically. Previous observations of the waterfall effect in the literature have been originating from phonons only. In these systems, the waterfall has been qualitatively explained by a coupling between the optic and acoustic branches. In fact, for the thermoelectric material  $\text{PbTe}$ , it is believed that a rattler-like phonon mode is causing the coupling. [119,124]. This parallel between  $\text{PbTe}$  and  $\text{Na}_{0.8}\text{CoO}_2$  suggest that the waterfall in  $\text{Na}_{0.8}\text{CoO}_2$  might be explained by a phonon-magnon coupling scenario. Even though there is a very good understanding of the lattice dynamics in  $\text{Na}_x\text{CoO}_2$  [21], it is difficult to model magnon-phonon coupling due the confusion regarding the true magnetic structure of  $\text{Na}_x\text{CoO}_2$ .

The broadening of spin-wave measurements along  $(hh3)$  and  $(h03)$  was quantified

for the square phase sample. A steady increase in FWHM was observed for increasing energy. Simple calculations suggest that the resolution should stay constant or decrease with increasing energy. Therefore, the broadening in  $Q$  could mean a lowering of the correlation length for the spin-waves at higher energies. However, to confirm this, additional neutron measurements are necessary.

# Chapter 4

## Linarite ( $\text{PbCuSO}_4(\text{OH})_2$ )

### 4.1 Introduction

Linarite is a naturally occurring mineral with chemical formula  $\text{PbCuSO}_4(\text{OH})_2$  [22]. The Cu sites are closely spaced along the  $\mathbf{b}$  axis direction and each of them support a magnetic moment corresponding to spin 1/2. The magnetic interactions between spins along the  $\mathbf{b}$  axis are expected to be much stronger than for any other direction, therefore, linarite can be considered as a (quasi)one dimensional spin 1/2 chain [24–26]. For some one dimensional spin chains, theory predicts the existence of novel quantum phases. The existence of these novel phases depends on the strength of the magnetic interactions along the spin chain [38]. With the recent discovery of many Cu based quasi one-dimensional systems like linarite, this field started receiving more theoretical interest [38–42]. One of these materials,  $\text{LiCuVO}_4$ , has already shown compelling evidence for the existence of a novel quantum phase [44,127]. Although no direct evidence of such a phase has been observed for linarite, some experimental results indicate that it could be capable of supporting a novel quantum phase [24–26].

Inelastic neutron scattering experiments on linarite can establish the strength of

the magnetic interactions and in turn determine if linarite is capable of having a novel quantum phase. Also, neutron diffraction experiments can be used to search for more direct evidence of the novel quantum phases.

The introduction will start with the theory behind one dimensional spin chains and the novel quantum phases predicted from them. Later on, the physical properties of linarite will be discussed. In the experimental sections results from inelastic neutron scattering, neutron diffraction, and magnetisation measurements will be discussed. Finally, in the discussion, the possibility of a novel quantum phase in linarite will be considered in the light of all of the results obtained in this thesis.

#### 4.1.1 Classical $J_1$ - $J_2$ Chain

The  $J_1$ - $J_2$  chain is a one dimensional magnetic system which is visualised in figure 4.1 on page 125. Here, uniformly separated spins of magnitude  $S=1/2$  (or integer multiple of  $1/2$ ) create a spin “chain”. Exchange constants  $J_1$  and  $J_2$  are introduced between the nearest neighbour and next-nearest neighbour spins respectively. For the purposes of this thesis only the case where  $J_1$  is ferromagnetic ( $J_1 > 0$ ) and  $J_2$  is antiferromagnetic ( $J_2 < 0$ ) will be considered. Without  $J_2$ , the ground state is a simple ferromagnetic structure. However, with the introduction of an antiferromagnetic  $J_2$ , the two exchange interactions cannot be satisfied at the same time. Such systems are referred to as magnetically “frustrated”. For a brief introduction to frustrated magnetism refer to subsection 1.2.

The Hamiltonian of the  $J_1$ - $J_2$  chain can be presented in the following way:

$$\mathcal{H} = - \sum_{\langle ij \rangle_{n.n.}} \mathbf{S}_i \mathbf{J}_1 \mathbf{S}_j - \sum_{\langle ij \rangle_{n.n.n.}} \mathbf{S}_i \mathbf{J}_2 \mathbf{S}_j - g\mu_B H \sum_i S_i^z. \quad (4.1)$$

The first summation sums over the nearest neighbour (n.n.)  $\langle ij \rangle$  pairs whilst the second summation sums over next nearest neighbour (n.n.n.)  $\langle ij \rangle$  pairs.  $\mathbf{S}_i$  is



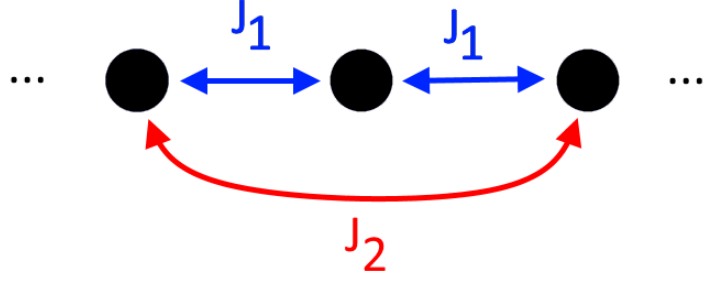


**Figure 4.1: One dimensional  $J_1$ - $J_2$  chain.** Between nearest neighbour and next-nearest neighbour spins exchange constants of  $J_1$  and  $J_2$  are introduced respectively.

a spin vector,  $S_i^z$  is the z component of the spin vector,  $g$  is the  $g$  factor,  $\mu_B$  is the Bohr magneton, and  $H$  is the applied magnetic field. In this scenario, the applied magnetic field is along the z direction. Here,  $\mathbf{J}_1 = J_1 \mathbf{I}_3$ , and  $\mathbf{J}_2 = J_2 \mathbf{I}_3$ , where  $\mathbf{I}_3$  is a  $3 \times 3$  identity matrix. This Hamiltonian in equation 4.1 is treated “classically”. This is done by treating spins not as quantum objects, but instead as vectors  $\mathbf{S}$  with fixed length of  $S$ . The classical  $J_1$ - $J_2$  chain is easier to work with and still provides valuable information regarding the magnetic structures and phase transitions of the system.

The properties of the  $J_1$ - $J_2$  chain are best described by the ratio  $\alpha = J_2/J_1$ . When there is no magnetic field applied, the system is ferromagnetic for  $\alpha > -0.25$ , but for  $\alpha \leq -0.25$  there is a helical magnetic structure. For a unit cell with one magnetic site, the propagation vector of the helix is given as  $q_{inc} = \cos^{-1}(-1/4\alpha)$  [128]. These helical structures can be confined to a particular spin-plane through an easy-plane anisotropy. For example, such an anisotropy can be introduced through  $\mathbf{J}_1$  in the following way:

$$\mathbf{J}_1 = J_1 \begin{pmatrix} 1 & 0 & 0 \\ 0 & 1 & 0 \\ 0 & 0 & 1 - \Delta \end{pmatrix} \quad (4.2)$$

Here,  $\Delta$  is the exchange anisotropy along the  $z$  axis direction. Note that a positive  $\Delta$  will cause an easy-plane in the  $xy$  plane. When there is no applied field, the spins will be confined to the easy plane. Helical magnetic structures are given different names depending of the orientation of the spin plane with respect to the magnetic propagation vector. If the propagation vector is contained in the spin plane it is referred to as a “cycloidal” magnetic structure. If the propagation vector is perpendicular to the spin plane it is referred to as a “proper screw” structure [37, 128]. The cycloidal and the proper screw structures are represented in figures 4.2(a) and (b) respectively.

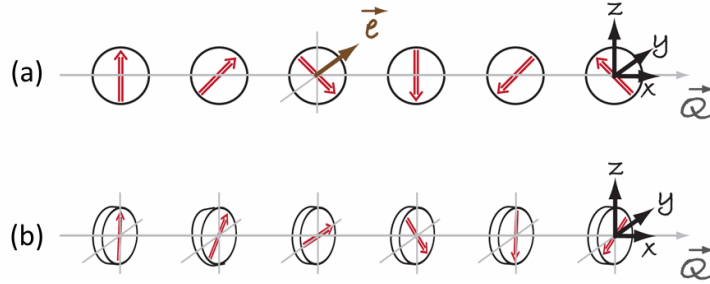


**Figure 4.2: Helical incommensurate structures.** (a) A helical magnetic structure is called a cycloidal structure if the spin plane is in the same direction as its propagation direction. (b) If the spin plane is perpendicular to the propagation direction it is called a “proper screw” structure [37, 128]. Images sourced from [37].

Helical magnetic structures have been subjected to interest from the field of multiferroics. It is suggested that a helical magnetic structure can spontaneously

create an electric polarisation  $\mathbf{P}$ . This is mostly based on experimental observations and the underlying mechanism is not completely understood [36]. However, it is suggested that having the normal of the spin plane,  $\mathbf{e}$ , perpendicular to the propagation vector,  $\mathbf{Q}$ , is more favourable for observation of ferroelectricity. In fact the polarisation  $\mathbf{P}$  is expected to be effected in the following way:  $\mathbf{P} \sim \mathbf{e} \times \mathbf{Q}$  [129]. Following this relation, for the cycloidal structure in figure 4.2(a),  $\mathbf{P}$  is expected to lie along the  $\mathbf{z}$  axis direction. Furthermore, one would not typically expect any ferroelectricity in the proper screw structure in figure 4.2(b) since  $\mathbf{Q} \parallel \mathbf{e}$ ; however, there is research to suggest that structures like these still might be able to produce ferroelectricity [37, 130].

The magnetic field phase diagram has been well studied for the classical  $J_1$ - $J_2$  chain [131, 132]. The orientation of the applied magnetic field with respect to easy plane is quite important. If the applied field is parallel to the easy plane, a number of different phases can be observed before the fully saturated ferromagnetic state. It was shown by Yoshimori et al. [128] that for small anisotropy energy and small applied field there exists a critical field  $H_c$  for which the spin plane will become perpendicular to the applied field. This kind transition is also referred to as a “spin-flop” transition. Nagamiya et al. [131] and Kitano et al. [132], were able to expand this model for different anisotropy and field strengths. The suggested phase diagram can be seen in figure 4.3 on page 128. Here  $K$  is proportional to the strength of the easy-plane anisotropy and the propagation vector  $\mathbf{Q}$  is assumed to be small. Above  $H_0$ , the system reaches a fully ferromagnetic state for all anisotropy strengths. For small anisotropies (i.e. small  $K$ ), two phase transitions are expected before the fully ferromagnetic phase. The first transition,  $H_c$ , is the spin-flop transition discussed previously. Above  $H_c$  a conical magnetic structure is expected. At higher fields there is a second transition,  $H'_c$ , into a sine oscillation phase (also called the “fan” phase), where the moments lie in the easy plane with angles smaller than  $90^\circ$  to the

field direction and the spin directions sinusoidally oscillate as function of sites along the chain. In the large anisotropy case, there is no spin-flop transition. Instead, with increasing field, the screw phase will become increasingly distorted until it arrives at  $H_t$  where it will turn into a fan phase. [131].

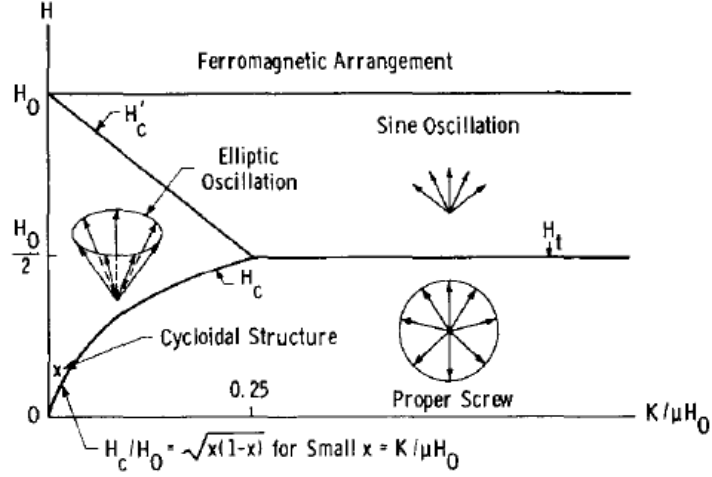


**Figure 4.3: Classical phase diagram** for a screw structure with an easy-plane anisotropy assuming a small propagation vector  $Q$ . The applied field is parallel to the easy plane. Here  $K$  is proportional to the easy-axis anisotropy. For low anisotropy (small  $K$ ) there are two phase transitions, first is from a proper screw into a cycloidal/conical structure and the second is from a conical structure into a fan phase. However, for high anisotropy (large  $K$ ), there is only one phase transition before saturation [131]. Image from Ref. [131].

#### 4.1.2 Heisenberg $J_1$ - $J_2$ Chain

A classical model is useful for understanding many features of the  $J_1$ - $J_2$  chain; however, for a comprehensive understanding, the quantum nature of the spins must be taken into account. Spin-interaction models which use quantum mechanics are

called Heisenberg models. This is done by changing the spin vectors  $\mathbf{S}$  with the quantum spin operators  $\hat{S}$ . The Heisenberg  $J_1$ - $J_2$  chain's Hamiltonian will have the form of:

$$\mathcal{H} = -J_1 \sum_{\langle ij \rangle_{n.n.}} \hat{S}_i \hat{S}_j - J_2 \sum_{\langle ij \rangle_{n.n.n.}} \hat{S}_i \hat{S}_j - g\mu_B H \sum_i \hat{S}_i^z \quad (4.3)$$

This system is purely one dimensional and in this thesis, only the  $S=1/2$  case with ferromagnetic  $J_1$  and antiferromagnetic  $J_2$  will be considered. The competing nearest and next-nearest interactions are expected to cause strong quantum fluctuations within the system. This combined with the low-spin and low-dimensionality of the system makes it a likely place to observe novel quantum phenomena [42]. For this system, an exotic quantum phase has been predicted for field strengths just below saturation. This phase has been described as a multi-magnon bound state with no long range order but quasi-long range spin-multipolar order [38–42].

In the  $J_1=0$  case, the system can be separated into two non-interacting AFM chains. For a one-dimensional AFM chain the exact analytical solution can be obtained using an approach called the Bethe ansatz [133]. The ground state of the one-dimensional AFM chain is referred to as a Tomaga-Luttinger liquid or simply the Luttinger liquid [29, 30]. In the Luttinger liquid, the excitations of the system are composed of spinons and holons which carry spin and charge respectively. For a detailed review of Luttinger liquid theory see ref. [134]. A non zero  $J_1$  can be introduced perturbatively into the system, which couples the two Luttinger liquids ferromagnetically [38]. This system is best parametrised by the ratio  $\alpha = J_2/J_1$ . Starting from zero field and increasing the field, the system will magnetise with steps  $\Delta S^z = 1$ . However, for certain regions of  $\alpha$ , there is a critical field strength after which the magnetisation increases in steps of  $\Delta S^z = 2, 3$ , or 4 instead. These phases have been interpreted as a bound state of  $p=\Delta S^z$  magnons (i.e. bound states of  $p$  spin flips). In figure 4.4 on page 131, the phase diagram of the multi-magnon bound

states can be seen for different  $m/m_{sat}$ , where  $m$  is the magnetisation and  $m_{sat}$  is the magnetisation at saturation (i.e. at fully FM phase). Here the  $p=2$  multi-magnon bound state extends to  $\alpha = -\infty$ . As the value of  $\alpha$  approaches  $\alpha=-0.25$  the number of magnons creating a bound state increases from  $p=2$  to  $p=3$  and  $p=4$ . Bound states with  $p>5$  do exist but are thought to be thermodynamically unstable [42]. These multi-magnon phases do not possess long-range order but instead possess quasi-long-range order. This can be seen from the longitudinal spin correlation function,  $\langle S_0^z S_r^z \rangle$ , which decays with distance  $r$  [39]. In contrast, the transverse spin correlations,  $\langle S_0^+ S_r^- \rangle$ , decay exponentially. This indicates the instability of single-spin-flip excitations within this phase. At higher fields, there is another correlation function which decays slowly, depending on the value of  $p$ . For  $p=2$  this is the quadrupolar correlation term,  $\langle S_0^+ S_1^+ S_{r+0}^- S_{r+1}^- \rangle$ . This shows that the principle excitations of the system consist of two spin-flips rather than one spin-flip. For arbitrary  $p$ , this slowly decaying correlation function has the form [42]:

$$\left\langle \prod_{n=0}^{p-1} S_{0+n}^+ \prod_{n=0}^{p-1} S_{r+n}^- \right\rangle. \quad (4.4)$$

The region where these correlations decay the slowest has been interpreted as one-dimensional analogue of a spin-multipolar phase. For  $p=2, 3, 4$  these correspond to nematic, triatic and quartic phases respectively [38, 39]. These spin-multipolar phases exist at high fields, close to magnetic saturation. As the magnetisation is lowered, the longitudinal spin-correlations,  $\langle S_0^z S_r^z \rangle$ , start to decay slower than the multipolar correlators. This crossover region is indicated by a white dashed line in figure 4.4. The region where longitudinal correlations are dominant can be thought of as a  $p$ -type spin density wave,  $SDW_{(p)}$  [42]. It is important to note that in one dimensional isotropic case, there is no phase transition between the  $SDW_{(p)}$  phase and the spin-multipolar phase. In both regions the magnetisation jumps in steps of  $\Delta S=p$ . The higher field region, which in this thesis is referred to as the spin-

multipolar phase, is often referred to as the “spin-nematic phase” in literature.

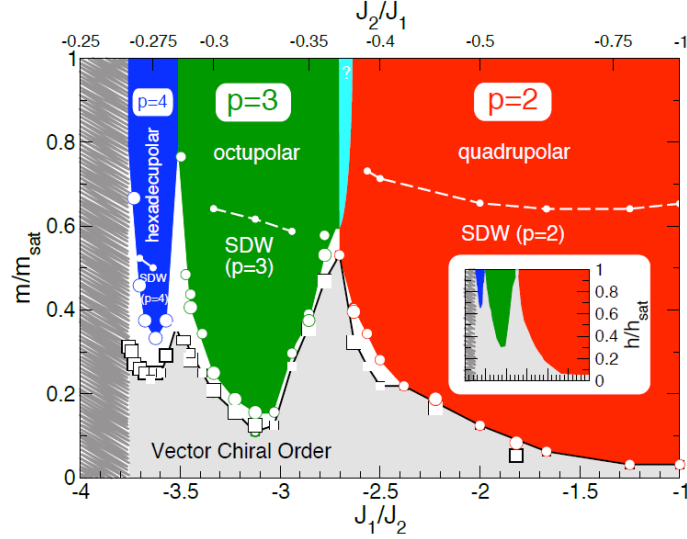


**Figure 4.4: Spin-multipolar Luttinger liquid phase diagram.**

The red, green, and blue regions indicate phases where  $p=2$ ,  $3$ , or  $4$  spin-flips become the primary excitations of the system. These phases represent quadrupolar, octupolar, and hexadecapolar order respectively. In these phases, at lower fields longitudinal rather than multipolar correlations become more dominant. Therefore, these regions have been identified by a  $p$ -type spin density wave,  $\text{SDW}_{(p)}$ . [42]. Image from Ref. [42].

There are two important experimental signatures of the spin-multipolar phases. The first is a field dependent magnetic characteristic vector. Using the longitudinal spin-correlators, it has been shown that the magnetic characteristic vector,  $q_{max}$ , will depend on the magnetisation in the following way:

$$q_{max} = \pi(1 - m/m_{sat})/p. \quad (4.5)$$

Here, a one spin per lattice size is used and the distance between two nearest neighbours is taken to be  $d_{NN} = 1$ . In figure 4.5 on page 132, this dependence has been

plotted for  $p=2, 3$ , and  $4$  in red, green, and blue dashed lines respectively. Neutron diffraction measurements in the  $\text{SDW}_{(p)}$  phase should be able to measure this as an incommensurate magnetic Bragg peak. At higher field strengths in the spin-multipolar phase, there should be no incommensurate magnetic Bragg peak [42]. The second experimental signature could be magnetisation. Upon increasing field, a first order metamagnetic transition is expected to occur as one enters spin-multipolar phases [42].

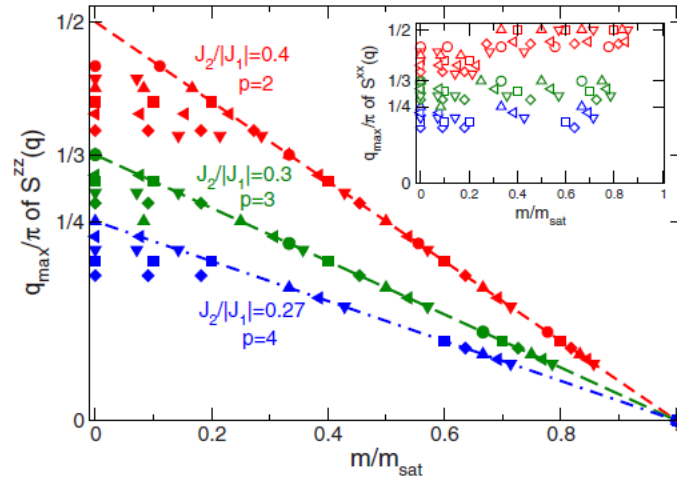


**Figure 4.5: Magnetic characteristic vector within the spin-multipolar phases.** Here the equation  $q_{max} = \pi(1 - m/m_{sat})/p$  is plotted for  $p=2, 3$ , and  $4$  in red, green, and blue dashed line respectively [42]. Image from Ref. [42].

A visualisation of a spin-multipolar phase for the case of a two-dimensional spin-1/2 frustrated-ferromagnet can be seen in figure 4.6. Here, the green sites are where spin-1/2 moments reside, and the blue surfaces show the spin fluctuations at bond centres. In this system there is no ordering of the spin-1/2 moments, but instead it is the spin fluctuations which form a quadrupolar order. The red cylinders represent the order parameter of the system [135].



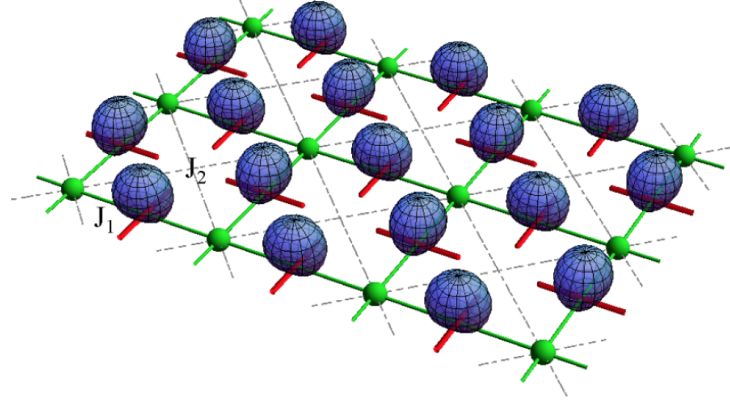


**Figure 4.6: Example of quadrupolar order for two-dimensional system.** The spin-fluctuation at bond centres are shown by the blue surfaces [135]. Image from Ref. [135].

The one dimensional  $J_1$ - $J_2$  chain has also been considered at zero field. Similar to the classical case, a helical magnetic structure is expected. However, due to quantum fluctuations, the propagation vector of the helix is different to its classical counterpart. Numerical models on finite size one dimensional models with  $\alpha < -1/4$  produced an approximation propagation vector of  $q_{inc} \sim (-\alpha - 1/4)^{0.29}$ . With increased field a small dependence on field was observed but it was not certain if this was a finite size effect [42].

So far the  $J_1$ - $J_2$  chain has been treated in a purely one dimensional manner. It is of interest to see how the introduction of inter chain coupling and anisotropy will have on the novel quantum phases predicted by the purely one-dimensional model. It is thought that an AFM inter-chain interaction might be detrimental to the stability of the spin-multipolar phases, whilst a FM interaction might strengthen it [136]. However, it was shown that the geometry of the inter-chain coupling can be as important as its strength. A coupling which is perpendicular with respect to the chain direction (i.e. a skew interaction) will affect the stability differently to a coupling which has a component along the chain direction (e.g. a diagonal

interaction) [137]. The stability of the spin-multipolar phases with respect to an AFM skew coupling,  $J_0^{IC}$ , can be seen in figure 4.7 on page 135. Here the  $p=2, 3$ , and 4 magnon multipolar phases are given in red, green and blue respectively. It can be seen that for large  $J_0^{IC}/J_2$ , these phases cannot be supported. It can be seen that the  $p=2$  phases are much more stable against the AFM inter-chain coupling as opposed to the  $p=3$  and  $p=4$  phases. Also in this figure, the effects of anisotropy on the stability of the spin-multipolar phase is shown. The Hamiltonian used to calculate the phase diagram in figure 4.7 has the following form:

$$\mathcal{H} = \mathcal{H}_0 - J_1 \sum_{\langle ij \rangle_{n.n.}} (\Delta - 1) \hat{S}_i^z \hat{S}_j^z - J_0^{IC} \sum_{\langle nm \rangle_{n.n.}} \hat{S}_n \hat{S}_m. \quad (4.6)$$

Here,  $\mathcal{H}_0$  is the Hamiltonian defined in equation 4.3,  $\Delta$  is the exchange anisotropy, and  $\langle nm \rangle_{n.n.}$  sums over nearest neighbours between two different spin chains. Note that  $\Delta = 1$  corresponds to the isotropic case whilst  $\Delta > 1$  and  $\Delta < 1$  correspond to the easy-axis and easy-plane scenarios respectively. For the easy-axis case, it will be energetically favourable for spins to be along  $z$  axis. However, for the easy-plane scenario, it will be energetically favourable for spins to be perpendicular to the  $z$  axis. In figure 4.7 it can be seen that for increasing easy-axis anisotropy, the stability region of the spin-multipolar regions can be greatly enhanced, whilst for an increasing an easy-plane anisotropy the stability is diminished [137, 138]. It is important to note that in this Hamiltonian, both the field and the anisotropy is introduced along the  $z$  axis. It is not clear how having the field perpendicular to the anisotropy axis would affect the stability of the spin-multipolar states. Introducing inter-chain coupling has another important effect on the system. For an isotropic system with weak inter-chain coupling, the  $SDW_{(p)}$  is much more likely to occur as opposed to a two dimensional spin-multipolar phase [139].

The inter-chain coupling strength was also found to be important for finding the saturation field. In the range  $0 < \alpha < 1$  the saturation field of the system is given

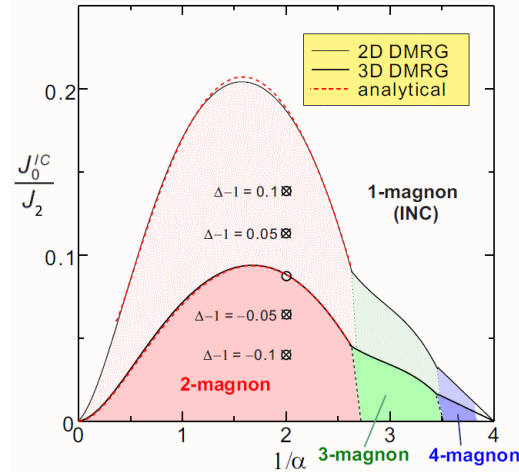


**Figure 4.7: The stability of spin-multipolar phases with inter-chain coupling and easy-axis anisotropy.** Here an AFM skew inter-chain interaction  $J_0^{IC}$  is used. The lightly shaded region is the enhanced stability due to an easy-axis anisotropy along field direction [137]. Image from Ref. [137].

only by the inter-chain coupling terms [140]. The suggested relationship is of the following form:

$$g\mu_B H_{sat} = N_{IC} \sum_i -J_i^{IC}. \quad (4.7)$$

Here,  $g$  is the  $g$  tensor,  $\mu_B$  is the Bohr constant,  $H_{sat}$  is the saturation field,  $N_{IC}$  is the number of nearest neighbours, and  $J_i^{IC}$  with  $i=0, 1, 2$ , etc. indicates the different types of inter-chain couplings in the system.

The fact that the spin-multipolar phases can still exist despite inter-chain couplings and anisotropies makes it more likely to observe the spin-multipolar phases in nature. Real spin systems within materials will always have some level of anisotropy and inter-chain coupling. The most promising materials to observe these novel quantum phases are the edge sharing copper oxides chains, which will be discussed in section 4.1.7. The effect of anisotropy in the zero field case has also been studied

in detail [141, 142] but will not be discussed here. The main objective of this thesis is to explore linarite's capabilities for establishing a spin-multipolar phase.

### 4.1.3 Crystal Structure

Linarite ( $\text{PbCuSO}_4(\text{OH})_2$ ) is a naturally occurring mineral [22] which crystallises in monoclinic space group  $\text{P}2_1/\text{m}$ . It has lattice parameters  $a=9.7\text{\AA}$ ,  $b=5.65\text{\AA}$ ,  $c=4.69\text{\AA}$ , and angle  $\beta=102.65^\circ$  [23, 143]. The crystal structure can be seen in figure 4.8 on page 137. Here we can see the Cu sites (blue) surrounded by six O atoms (red) creating a Cu-O octahedron (blue surface) which is elongated and distorted. These octahedra are separated by lead (grey) and sulphur (yellow) atoms along the **a** axis direction. Along the **c** axis direction the octahedra are much closer compared to the **a** axis direction. Along the **b** axis direction, the neighbouring octahedra have a common edge. If only the four closest O atoms to the Cu atoms are considered, a  $\text{CuO}_2$  ribbon structure becomes apparent, as seen in figure 4.8(c). It can be seen that this  $\text{CuO}_2$  ribbon is not straight, in fact there is a buckling of  $24.5^\circ$  between each neighbouring  $\text{CuO}_2$  plate.

It is useful to know the orientation of the  $\text{CuO}_2$  plates and the long axis of the octahedron with regards to the **a** axis. In an unit cell, there are two different octahedra and  $\text{CuO}_2$  plates. These plates have slightly different orientations. The average of the two normals to the  $\text{CuO}_2$  planes is at  $\mathbf{n}_\perp=(0.94, 0, -0.26)$  which is  $-15.35^\circ$  from the **a** axis. The long axis of the octahedron is not parallel to this but it is in fact  $-7.5^\circ$  from the **a** axis.

The structure which will be used for this thesis was obtained by Effenberger [23] and Araki [143] using single crystal x-rays diffraction. In literature there are seemingly two other structure solutions for Linarite. The first of these different structures was obtained by Bachmann and Zemann [144] using x-ray single crystal diffraction. The Bachmann structure has a different lattice parameter and monoclinic angle with

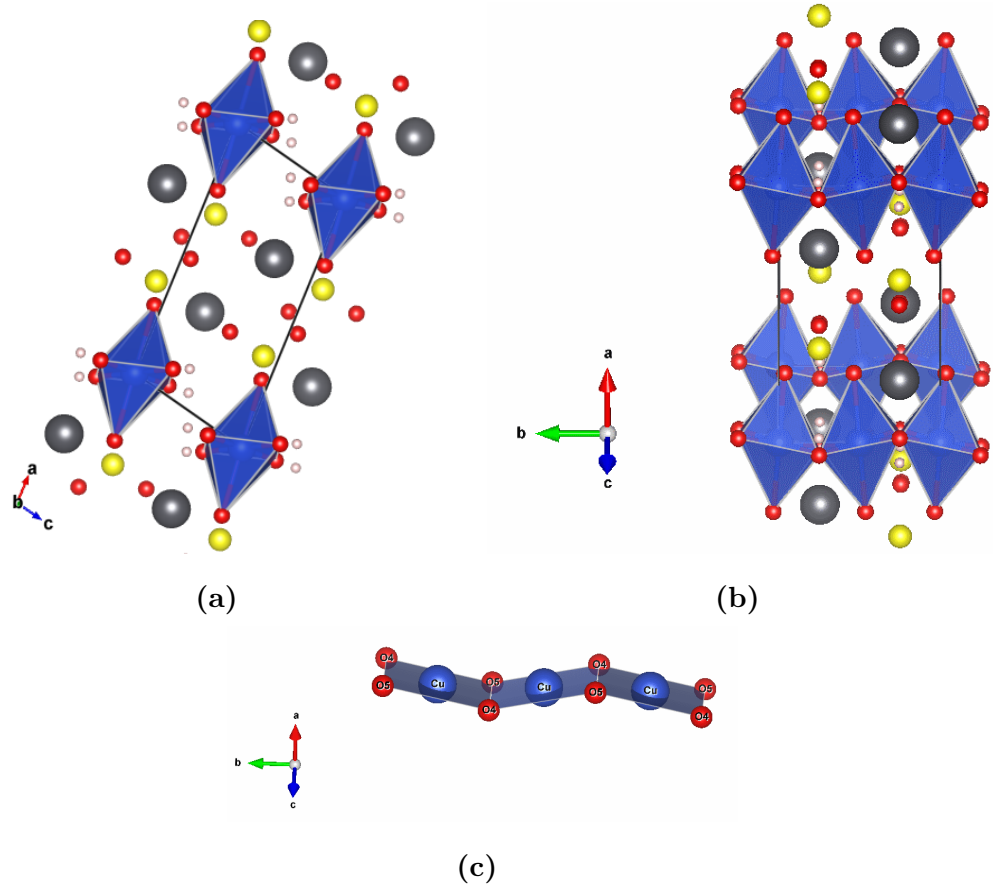


**Figure 4.8: Crystal structure of Linarite** with  $a=9.7\text{\AA}$ ,  $b=5.65\text{\AA}$ ,  $c=4.69\text{\AA}$ , and angle  $\beta=102.65^\circ$  [23, 143]. Here the Cu (blue) atoms are surrounded by O (red) atoms creating a distorted octahedron which is given by the blue surface. The Pb (grey) and S (yellow) atoms are situated between such Cu-O octahedra along the  $\mathbf{a}$  axis direction. The H (white) atoms are positioned at the edges of the Cu-O octahedra. **(a)** The Cu-O octahedra are closer along the  $\mathbf{c}$  axis then the  $\mathbf{a}$  axis direction. **(b)** Along the  $\mathbf{b}$  axis direction, the Cu-O octahedra share an edges, creating a Cu-O chain. **(c)** The  $\text{CuO}_2$  ribbon structure propagates along the  $\mathbf{b}$  axis direction and has a buckling of  $24.5^\circ$  between each neighbouring plane.

$a=9.81\text{\AA}$  and  $\beta=104.7^\circ$ , as well as different atom positions. However, the Bachmann structure is identical to the Effenberger-Araki structure. The only difference is the choice of lattice vectors. The lattice vectors of the two notations are transformed in the following way [145]:

$$\mathbf{a}_B = -\mathbf{a}_E - \mathbf{c}_E; \mathbf{b}_B = -\mathbf{b}_E; \mathbf{c}_B = \mathbf{c}_E; [000]_B = [000]_E \quad (4.8)$$

Here the subscripts of E and B describe the Effenberger-Araki and Bachmann notations respectively. The atom positions of the Effenberger-Araki notation and Bachmann notation can be related to one another in the following way [23]:

$$(xyz)_E = (xyz)_B \begin{pmatrix} -1 & 0 & -1 \\ 0 & -1 & 0 \\ 0 & 0 & 1 \end{pmatrix} \quad (4.9)$$

Another different structure solution for Linarite was suggested by Schofield et al. [146]. The lattice parameters were solved using x-ray powder diffraction and the atom positions were solved using single crystal neutron diffraction. The resulting Schofield structure has identical lattice parameters as the Effenberger-Araki structure; however, the Schofield atom positions agree with that of the Bachmann structure rather than that of the Effenberger-Araki structure. The most likely explanation is that for the neutron measurement, the Bachmann unit cell was used by mistake. The other structure solutions did not have this problem because the lattice parameters and the atom positions were solved at the same time from the same data. The one advantage of the Schofield solution is that by using neutrons, it was able to determine the position of the hydrogen atoms. It is then possible to transform these H positions into the Effenberger-Araki structure using equation 4.9.

The atomic positions of linarite can be seen in table 4.1 on page 140. Here, all the positions of the atoms except for the hydrogen and sulphur positions, are obtained from Effenberger [23]. In Effenberger's article the x position of sulphur is

incorrect; however in the inorganic crystal structure database (ICSD) [147], this x position is corrected. This corrected value is used in the table. The correct hydrogen positions are obtained by transforming the positions of Schofield et al [146] into the Effenberger-Araki structure. It is important to note that in the thesis work of Willenberg [148], single crystal neutron diffraction results are presented. In this work the lattice parameters and the atom positions were obtained from the same datasets. Their obtained structure is in agreement with the atomic positions stated in table 4.1.

This confusion in the structure will no doubt reflect on the rest of the literature. It will be important to make note of what structure notation each linarite publication uses. In summary it can be either the Effenberger-Araki notation, which will be used in this thesis, the Bachman notation, or the Schofield et al. notation. Unless stated otherwise, it can be assumed that the references in this thesis are using the Effenberger-Araki notation.

Atom	x(l.u.)	y(l.u.)	z(l.u.)
Cu	0	0	0
Pb	0.34201	0.25	0.32838
S	0.33190	0.75	0.88450
O1	0.47540	0.75	0.06560
O2	0.33470	0.75	0.56930
O3	0.25310	0.5355	0.94260
O4	0.03420	0.75	0.28264
O5	0.09520	0.25	0.26670
H1	0.05500	0.25	0.45050
H2	0.86820	0.25	0.61220

**Table 4.1: Atom positions for Linarite.** The hydrogen positions are obtained from transformation of the Schofield et al.’s results [146]. The sulphur position is obtained from the crystallography database ICSD [147], and the remainder is obtained from Effenberger [23]. The positions are given in lattice units (l.u.).

#### 4.1.4 Magnetic Structure

Using structural arguments alone it is possible to make some estimates about the magnetism of linarite. Linarite is an edge sharing copper oxide chain, which can be seen in detail in figure 4.8(c). According to the Goodenough-Kanamori-Anderson rules of superexchange [55–57, 149], the Cu-O-Cu bond angle will determine the nature of the interaction. At  $90^\circ$  bond angle, the interaction is expected to be FM and for larger bond angle it is expected to become AFM. For linarite, the nearest-neighbour interaction can be through Cu-O4-Cu or Cu-O5-Cu which correspond to bond angles of  $95^\circ$  or  $91.2^\circ$  respectively. However, the next nearest-neighbour



interaction must follow a Cu-O5-O4-Cu type of path which is much larger than  $90^\circ$ . Therefore, for the nearest-neighbours a ferromagnetic interaction is expected whilst for the next nearest-neighbours an antiferromagnetic interaction is expected [148]. DFT calculations performed for linarite agree with such a prediction [24, 26] (Note Ref. [26] uses the incorrect Schofield structure notation). This nearest neighbour FM, next-nearest neighbour AFM interaction model has also been suggested by magnetic susceptibility and specific heat measurements [24–26].

One of the signatures of a nearest neighbour FM, next-nearest neighbour AFM spin chain is having an incommensurate helical magnetic structure propagating along the chain direction. Specific heat measurements suggested the formation of a helical magnetic structure at a Néel temperature of  $T_N \sim 2.8\text{K}$  [24]. Using neutron diffraction, Yasui et al. [25] confirmed that below  $T_N$ , a magnetic incommensurate propagation vector of  $(0\ k\ 0.5)$  appears, where  $k \sim 0.189$ . The  $l=0.5$  component of the propagation vector points to an antiferromagnetic interaction along the  $\mathbf{c}$  axis direction. Magnetisation measurements of Yasui et al. showed spin-flop transition for a field applied in the Cu-O plane within the  $\mathbf{ac}$  plane. Therefore, they suggested a magnetic structure with spins in the Cu-O plane, which can be seen in figure 4.9(a) on page 142. However, neutron diffraction data from Willenberg et al. [150] found a different spin structure where the spins are  $-27(2)^\circ$  from the  $\mathbf{a}$  axis and structure is elliptical with slightly larger moment along  $\mathbf{b}$  axis  $0.833(10)\mu_B$  as opposed to  $\mathbf{ac}$  plane  $0.638(15)\mu_B$ . This structure can be seen in 4.9(b). It is important to note that Willenberg et al. cites the Schofield structural notation which means that their results are potentially incorrect. However, in the follow up article by Schäpers et al. [151], the same result is stated using the Effenberger-Araki structure notation for both the lattice parameters and the atomic positions. In the neutron diffraction experiment the structure and the magnetic structure is solved from the same data-set which greatly reduces the possibility of obtaining wrong orientation of the spin

plane. The same cannot be said for the results of Yasui et al. where it is possible to miss-orient the sample. This makes the magnetic structure in figure 4.9(b) obtained by Willenberg et al. the more definitive magnetic structure.

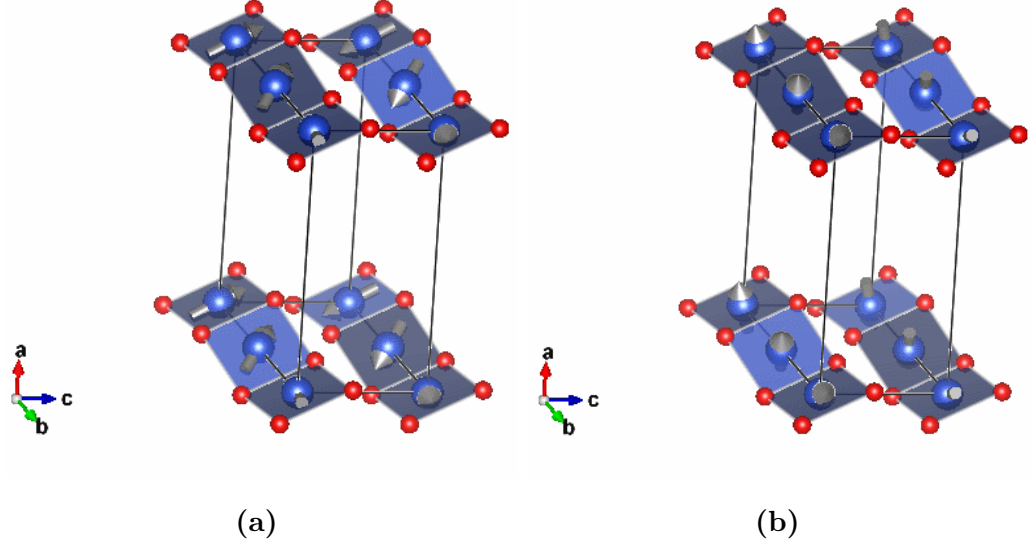


**Figure 4.9: Suggested helical magnetic structures for linarite.**

The two suggested magnetic structures are identical except for the orientation of the spin plane **(a)** Yasui et al's magnetisation data suggests a spin plane within the Cu-O plane [25] whilst **(b)** Willenberg et al's neutron diffraction data suggest a structure where the spins are almost perpendicular to the Cu-O plane ( $-27(2)^\circ$  from the  $\mathbf{a}$  axis) [150].

#### 4.1.5 Magnetic and Thermodynamic Properties

The measurements of the dielectric constant in linarite is a possible probe into its ferroelectric properties. As mentioned before in section 4.1.1, a helical magnetic structure can create a polarisation in the spin-plane. Crossing this ferroelectric transition it is possible to observe anomalies in the dielectric constant [36]. In the

previous section the two different magnetic structures were suggested by Yasui et al. [25] and Willenberg et al. [150]. The temperature dependence of the dielectric constant was measured by both groups. Yasui et al. found that when the electric field is applied along the  $\text{CuO}_2$  planes in the  $\mathbf{ac}$  plane, there is a noticeable peak at  $T_N$ . Such a peak was not observed for the electric field along the  $\mathbf{b}$  axis, or in the direction perpendicular to the  $\text{CuO}_2$  planes. It is important to note that, as discussed before, Yasui et al. may have miss oriented the sample, at least in their magnetisation measurements, since their proposed magnetic structure is very different from the more reliable neutron diffraction data. The capacitance measurements of Willenberg et al.'s samples are shown in thesis work of Willenberg [148]. Here, peaks were also observed in the dielectric constant but this time for a electric field applied  $\sim 35^\circ$  from their defined spin plane. The electric field could not be applied parallel to the spin plane due to experimental restrictions. Neither the work of Yasui et al. [25] or of Willenberg [148] is enough to make a direct link to a ferroelectric transition. The orientation of Yasui et al.'s crystal is not certain and Willenberg was unable to orient the electric field directly parallel to the spin plane. However, Willenberg was able to show that this peak in the capacitance follows the phase boundary of the helical structure (see phase I in figure 4.11 where the green dots indicate the phase boundary as obtained from capacitance measurements). This is a possible indication that this helical structure can be linked to ferroelectricity [148].

Magnetic susceptibility and specific heat data from linarite has been used to obtain fits to the  $J$  parameters for the  $J_1 - J_2$  spin 1/2 chain. Three attempts at this by different researchers has resulted in three very different sets of  $J$  parameters and different ratios for  $\alpha = J_2/J_1$  [24–26]. These different values can be seen in table 4.2. All of these measurements agree on a ferromagnetic  $J_1$  and an antiferromagnetic  $J_2$ . It is not clear why there is so much discrepancy between the results of the different groups. It is important to note that Wolter et al. [26] also expands on the

models by adding a small AFM inter-chain exchange interaction  $J^{IC}$  along the  $\mathbf{c}$  axis and by adding an easy-axis exchange anisotropy on  $J_1$ . The assumed strength of the effective interchain coupling  $J^{IC}$  was  $\sim -0.6\text{meV}$  and the easy axis was expected along the  $\mathbf{b}$  axis.

Ref.	$J_1(\text{meV})$	$J_2(\text{meV})$	$\alpha$
Baran et al. [24]	2.6	-1.3	-0.5
Yasui et al. [25]	1.1	-1.8	-1.6
Wolter et al. [26]	8.6	-3.1	-0.36

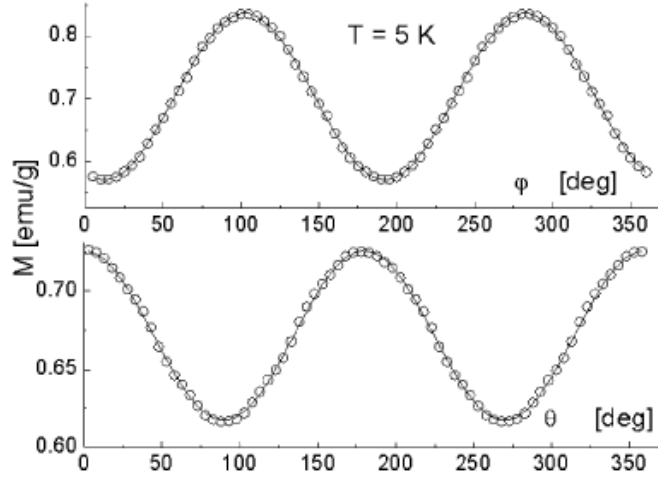
**Table 4.2: Suggested interaction schemes for linarite.** All suggested models agree on FM  $J_1$  and AFM  $J_2$ ; however, there is no agreement on the size of the  $J$  parameters [24–26].

From a fit to high temperature susceptibility measurements a Curie-Weiss temperature of  $\Theta_{CW}=27(2)$  is obtained. The positive  $\Theta_{CW}$  is an indication that FM interactions are dominant in linarite [26]. The maximum susceptibility occurs around  $\sim 5\text{K}$  for  $\mathbf{a}$ ,  $\mathbf{b}$ , and  $\mathbf{c}$  axis directions. However, the maximum susceptibility occurs at a slightly lower temperature for  $\mathbf{H} // \mathbf{b}$ , which could be interpreted as the  $\mathbf{b}$  axis being the easiest axis. The saturation field for the directions  $\mathbf{H} // \mathbf{b}$ ,  $\mathbf{H} // \mathbf{c}$ , and  $\mathbf{H} \perp \mathbf{bc}$  directions is given as  $\mu_B H_{sat} = 10.5\text{T}$ ,  $8.5\text{T}$ , and  $7.6\text{T}$  respectively according to Wolter et al. [26]. However, Wolter et al. references the Schofield structure solution, which could mean that these directions may not be exact. To be precise, the  $\mathbf{H} // \mathbf{b}$  measurement would be correct, as it is the  $\mathbf{b}$  axis is the same in all structure notations.

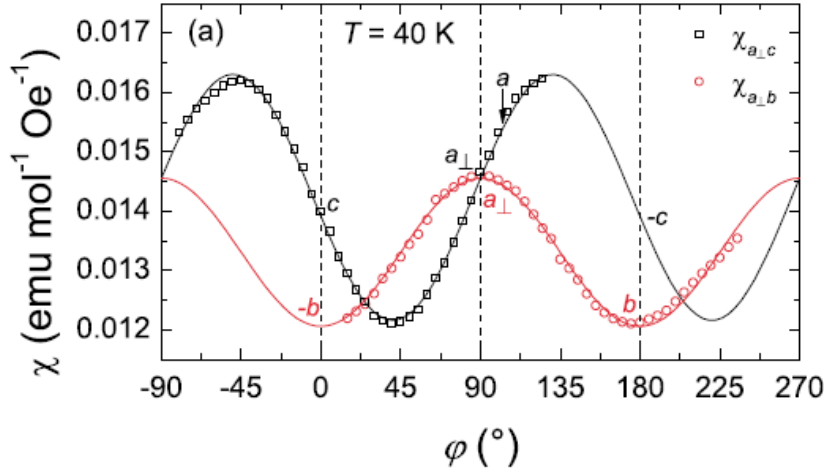
Magnetisation measurements have been performed on rotation stages [152, 153] which can be seen in figure 4.10 on page 146. These measurements indicate the level of anisotropy in the paramagnetic regime. The two groups which have performed these measurements obtain similar results; however, they disagree in the orientation

of their crystal with respect to these results. In figure 4.10(a) the measurements of Szymczak et al. performed at 5K can be seen [152]. In the top figure the change in magnetisation with a rotation is about the **b** axis and where the angle  $\phi$  is the angle between the **a** axis and the magnetic field direction. In the bottom figure the rotation is in the plane given by the **b** axis and the normal to the (-101) plane. The angle  $\theta = 90^\circ$  corresponds to the field parallel to the **b** axis. From these measurements it can be seen that the smallest moments are along the **b** axis and about  $10^\circ$  from the **a** axis [152]. These findings are contrary to the measurements of Schäpers et al. [153] which was performed at 40K and can be seen in figure 4.10(b). Here, the minimum in the **ac** plane is  $\sim 57^\circ$  from the **a** axis. This disagreement extends to the  $g$  factors as well. Schäpers et al. suggest that  $g_{a\perp} > g_c > g_b$  (here,  $a \perp$  is defined as the normal to the **bc** plane) whilst Szymczak et al. suggests  $g_c > g_b > g_a$ . The discrepancy between these two results is most likely related to the confusion in the structure of linarite in the literature. Both articles cite the Effenberger structure for linarite [23]. Schäpers et al. has the additional advantage that its structure was solved using neutron diffraction measurements [151] and it is definitively in the Effenberg-Araki structure notation. It is important to note that Szymczak et al. also performed a measurement at 25K which showed differences to the 5K data. The difference is most visible in the **ac** plane, where there is a shift as large as  $\sim 10^\circ$  [152].

Another important estimate of the anisotropies present in the magnetism of linarite comes from electron spin resonance (ESR) and nuclear magnetic resonance (NMR) measurements. Through ESR experiments, Wolter et al. was also able to obtain the  $g$  factors along **a**, **b**, and **c** axis directions respectively to be  $g_a = 2.34$ ,  $g_b = 2.1$ ,  $g_c = 2.2$ . These results agree with their later work (Schäpers et al. [153]) seen in figure 4.10(b) but it does not agree with the findings of Szymczak et al. [152]. It should be noted again that Wolter et al. [26] references the Schofield structure



(a)



(b)

**Figure 4.10: Magnetisation with rotation in paramagnetic regime.** (a) Szymczak et al. [152] measured the rotation in the ***ac*** plane(top) and in the ***b***-(-101) plane(bottom). Here,  $\phi=0$  corresponds to  $\mathbf{H} // \mathbf{a}$  and  $\theta=0$  corresponds to  $\mathbf{H} // (-101)$  [152].(b) These results do not agree with those of Schäpers et al., where the ***a*** axis is close to the maximum in susceptibility [153]. Images from [152] and [153] respectively.

solution therefore it is not sure how accurate the values of  $g_a$  and  $g_c$  are. Since there is some agreement with the Schäpers et al. [153] work, where the correct structure is stated, it is likely that the Wolter et al. is also using the correct structure. For temperatures above  $T_N$ , the anisotropy seen in the saturation field can be mostly explained via the anisotropy of the  $g$  factor. However, below  $T_N$ , this is no longer sufficient and it is necessary to consider different anisotropies such as exchange anisotropies and Dzyaloshinskii-Moriya interactions [26]. The ESR measurements do not show any change in linewidth down to  $T_N$  for the field along  $\mathbf{b}$  axis direction. However for  $\mathbf{H} // \mathbf{a}$  and  $\mathbf{H} // \mathbf{c}$  a change occurs as early as 50K. Similarly, NMR measurements of  $^{207}\text{Pb}$  and  $^1\text{H}$  signals also start show a broadening at  $\sim 75\text{K}$  and  $\sim 50\text{K}$  respectively. This is an indication that the system is strongly frustrated and that short range correlations start developing for temperatures much higher than  $T_N$  [26].

#### 4.1.6 Phase Diagram and Neutron Diffraction

The phase diagram for  $\mathbf{H} // \mathbf{b}$  field direction has been studied in great detail through many different physical properties measurements [148, 150, 154]. The phase diagram, which can be seen in figure 4.11 on page 148 [148], has five different phases. Here, phase II might not be a distinct thermodynamic phase but a crossover from phase I to phase IV. The magnetic structures of the remaining phases I, III, IV, and V has been solved using neutron diffraction methods and the different magnetic structures present in the phases can be seen in figure 4.12 on page 149 [148]. Here, phase I is the helical ground state with the spin plane  $-27^\circ$  from the  $\mathbf{a}$  axis as discussed earlier (figure 4.9(b)). In figure 4.12(a), the commensurate AFM structure of phase IV can be seen. The propagation vector for this phase is  $(0,0,0.5)$  and the spins are perpendicular to the  $\mathbf{b}$  axis and  $-27^\circ$  from the  $\mathbf{a}$  axis. The orientation of the spin plane in phase IV is identical to that of phase I. The structure of phase IV

was solved at 4T and 5T and a total magnetic moment of  $0.79(1)\mu_B$  and  $0.73(2)\mu_B$  was obtained respectively in the **ac** plane. This could be interpreted as a small canting towards the field direction for higher field. In phase III, a coexistence of the phase IV magnetic structure and an incommensurate magnetic helix similar to that of phase I was observed. The only difference between the two structures is that the phase III helix resides in the **bc** plane which can be seen in detail in figure 4.12(b). The Phase V magnetic structure is a sinusoidally modulating structure with the moments parallel to the **b** axis, which can be seen in figure 4.12(c).

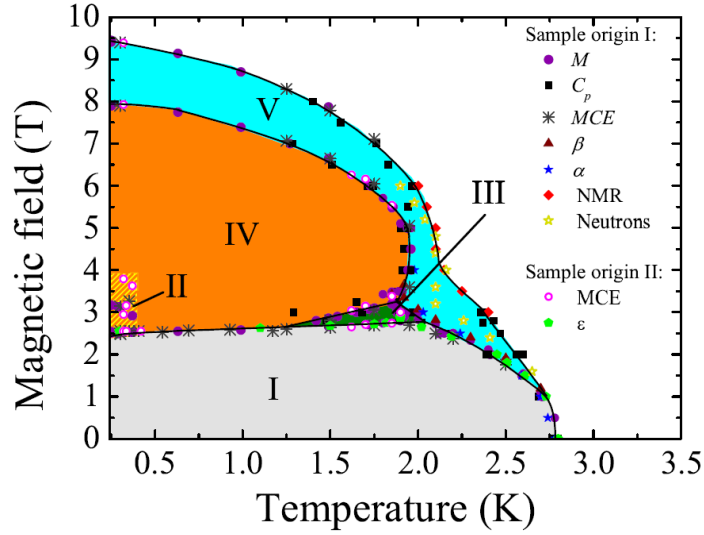


**Figure 4.11: Linarite phase diagram for  $H//b$ .** The phase diagram was obtained from many different physical properties measurements [148, 150, 155]. Image from Ref. [148].

The magnetic Bragg peak was measured in phase V for a few different temperatures above 1.8K and for a large range of field strengths. The points where the Bragg peaks were measured can be seen in figure 4.11 with gold stars. These Bragg peaks were of the form  $(0, k_y, 0.5)$  and it was found that  $k_y$  changes throughout phase V. This change in  $k_y$  can be seen in figure 4.13(a) on page 151. Here, the coloured



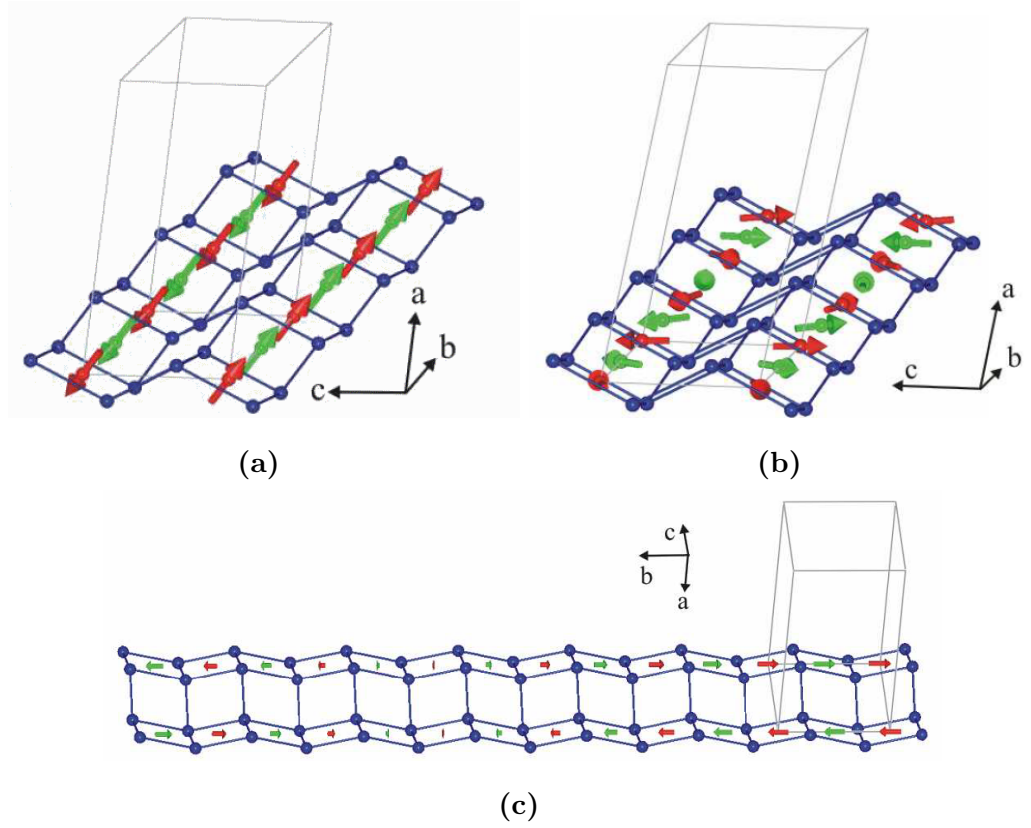


**Figure 4.12: Magnetic structures observed for  $H//b$  phase diagram.** (a) In phase IV, the magnetic structure is AFM with the spins tilted  $-27^\circ$  from the  $\mathbf{a}$  axis. (b) For phase III, there is a coexistence of two magnetic structures. One of these is the phase IV magnetic structure and the other is an incommensurate helix very similar to that of phase I. Unlike the phase I helix, the phase III helix resides in the  $\mathbf{bc}$  plane as seen in the figure. (c) The phase V magnetic structure is established as a sinusoidally spin modulated structure with spins along  $\mathbf{b}$  axis. Images from Ref. [148].

lines are the theoretical prediction of a  $\text{SDW}_{(p)}$  characteristic vector as given in equation 4.5. It can be seen that none of the theoretical predictions directly match

with the measured  $k_y$  positions [148, 155]. In order to explain the change in  $k_y$  with increasing field, Willenberg et al. [155] created a field dependent  $\alpha_{eff}(H)$  model. This was done by comparing the structure factor for two different models. The first was a single chain  $\tilde{J}_1 - \tilde{J}_2$  model, and the second model was a two chain  $J_1 - J_2$  model with an inter-chain coupling  $J^{IC}$ . The inter-chain coupling is assumed to be  $J^{IC} \sim -0.9\text{meV}$  and it is taken to be a diagonal interaction as seen in figure 4.13(b). For the two dimensional model, the  $J$  parameters obtained from Ref. [26] is used which has  $\alpha = -0.36$ . The magnetic structure factor is calculated for both the single chain and two chain models. The  $J$  parameters of the single chain  $\tilde{J}_1 - \tilde{J}_2$  model are altered so that its structure factor agrees with that of the two chain model. The effective frustration ratio of  $\alpha_{eff} = \tilde{J}_2/\tilde{J}_1$  is obtained for different field strengths. The calculated change in  $\alpha_{eff}$  with increasing magnetisation can be seen in figure 4.13(c). Using such an  $\alpha_{eff}$ , the expected  $\text{SDW}_{(p)}$  phase will change from  $p=5$  to  $p=8$  with increasing field, as shown in figure 4.13(d).

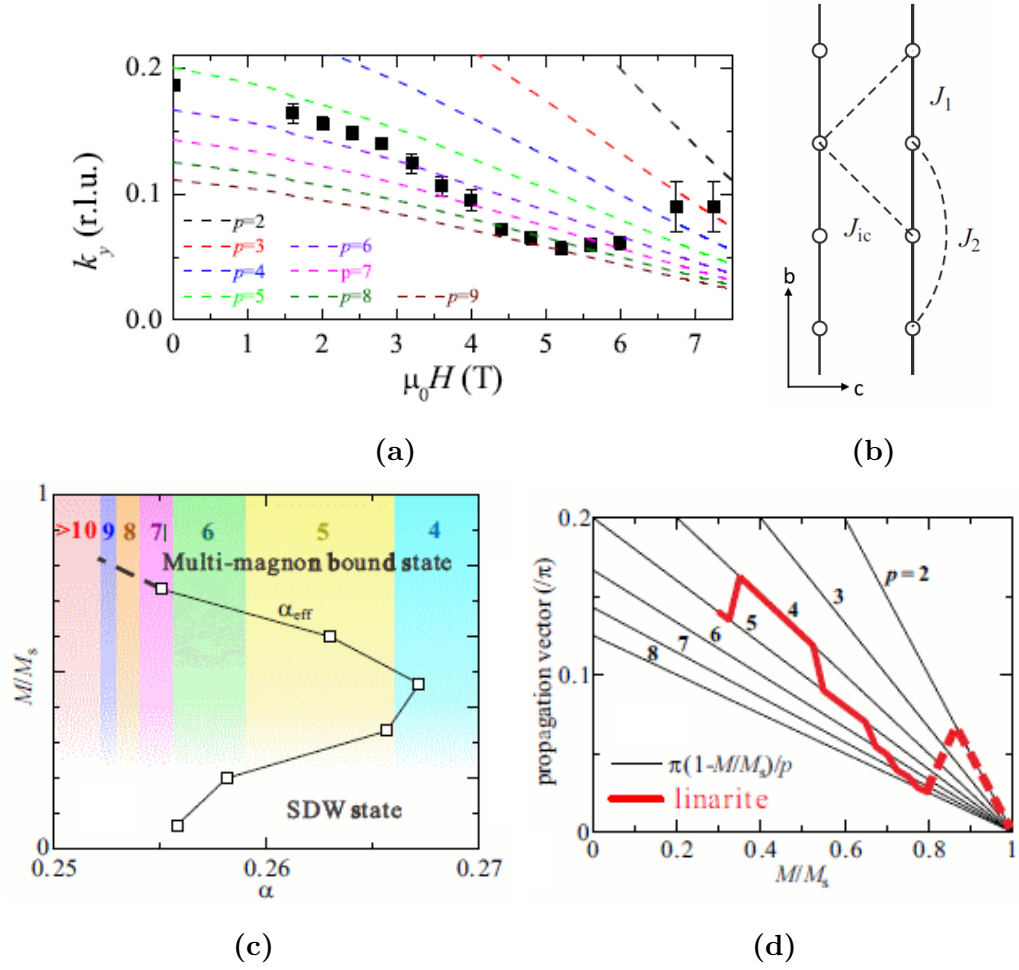


**Figure 4.13: The Willenberg et. al interoperation of linarite's  $k_y$  dependence.** (a) The position incommensurate propagation vector  $(0, k_y, 0.5)$  changes with different magnetic field strengths. The dashed lines are predictions of a  $SDW_{(p)}$  phase. These predictions do not directly agree with measured  $k_y$  values. (b) A diagonal AFM interaction of  $J^{IC}$  is assumed for the two chain model. (c) Structure factor comparisons between the one- and two-dimensional models give a field dependent  $\alpha_{eff}$ . (d) A field dependent  $\alpha_{eff}$  model like this would result in the observations of  $SDW_{(p)}$  phases where  $p$  changes from  $p=5$  to  $p=8$  with increasing field [155]. Images taken from Ref. [155].

### 4.1.7 Review of Cuprate $J_1 - J_2$ Chains

There are number of copper-oxide based quasi-one-dimensional systems which are analogues for the spin 1/2 Heisenberg  $J_1$ - $J_2$  chain where  $J_1$  is FM and  $J_2$  is AFM. The  $J$  values of some of these systems has been found using INS, magnetic susceptibility  $\chi$ , specific heat  $C_p$ , or optical conductivity  $\sigma$ . The details of some copper-oxide based quasi-one-dimensional systems can be seen in table 4.3 on page 153. These details include the obtained  $J$  values, the experimental method used to determine the  $J$  values, references, and magnetic structure information. For linarite ( $\text{PbCuSO}_4(\text{OH})_2$ ), there are three different articles with three different  $J$  parameters which are also represented in table 4.3. Similarly for  $\text{LiCu}_2\text{O}_2$  three different models are shown. Out of these three models only one of them (the  $J_1 = 7.0$  model) is a FM  $J_1$ - AFM  $J_2$  chain. The other two models have AFM  $J_1$  which is very different to linarite and to all of the other materials suggested in table 4.3.

For most cuprate  $J_1 - J_2$  chains, a helical order or FM order is observed along the spin chain direction. However, for some materials no long range order has been observed yet. An incommensurate helical magnetic structure is observed among linarite [150],  $\text{LiCuVO}_4$  [157],  $\text{NaCu}_2\text{O}_2$  [156, 164],  $\text{LiCu}_2\text{O}_2$  [163], and  $\text{Li}_2\text{ZrCuO}_4$  [158]. An FM order along the chain direction is observed for  $\text{Li}_2\text{CuO}_2$  [159, 165] and  $\text{Ca}_2\text{Y}_2\text{Cu}_5\text{O}_{10}$  [162]. An FM order along the chain for  $\text{Ca}_2\text{Y}_2\text{Cu}_5\text{O}_{10}$  is not surprising since because  $J_2/J_1 \gg -0.25$ . However, for  $\text{Li}_2\text{CuO}_2$  one might expect helical order instead considering  $J_2/J_1 < -0.25$  (see section 4.1.1). First-principle density functional theory calculations show that for  $\text{Li}_2\text{CuO}_2$  next nearest neighbour inter-chain interactions are responsible for the favouring of FM order over helical order [166]. Conversely,  $\text{A}_2\text{Cu}_2\text{Mo}_3\text{O}_{12}$  ( $\text{A}=\text{Rb}, \text{Cs}$ ) [161, 167] and  $\text{LiCuSbO}_4$  [160] do not show any magnetic order down to very low temperatures. The inelastic neutron powder spectrum of  $\text{LiCuSbO}_4$  does show a signal at an incommensurate position; however, there is no spin freezing down to 0.1K [160].

Material	Ref.	Method	$J_1$ (meV)	$J_2$ (meV)	$J_2/J_1$	Mag. Structure
NaCu <sub>2</sub> O <sub>2</sub>	[156]	$\chi$	4.1	-7.8	-2.41	Helical
Li <sub>2</sub> CuVO <sub>4</sub>	[157]	INS, $\chi$	1.6	-3.57	-2.23	Helical
Li <sub>2</sub> ZrCuO <sub>4</sub>	[158]	C <sub>p</sub> , $\chi$	38.8	-31.3	-0.30	Helical
Li <sub>2</sub> CuO <sub>2</sub>	[159]	INS, $\sigma$	19.8	-6.6	-0.33	Commensurate
LiCuSbO <sub>4</sub>	[160]	INS,C <sub>p</sub> , $\chi$	6.5	-2.9	-0.45	No L.R.O
Rb <sub>2</sub> CuMo <sub>3</sub> O <sub>12</sub>	[161]	C <sub>p</sub> , $\chi$	11.9	-4.4	-0.37	No L.R.O
Cs <sub>2</sub> CuMo <sub>3</sub> O <sub>12</sub>	[161]	C <sub>p</sub> , $\chi$	8.0	-2.8	-0.35	No L.R.O
Ca <sub>2</sub> Y <sub>2</sub> Cu <sub>5</sub> O <sub>10</sub>	[162]	INS	8.0	-0.4	-0.05	Commensurate
LiCu <sub>2</sub> O <sub>2</sub>	[163]	INS	-3.2	6.0	-1.86	Helical
LiCu <sub>2</sub> O <sub>2</sub>	[163]	INS	-52.8	-16.9	0.32	Helical
LiCu <sub>2</sub> O <sub>2</sub>	[163]	INS	7.0	-3.8	-0.54	Helical
PbCuSO <sub>4</sub> (OH) <sub>2</sub>	[24]	C <sub>p</sub> , $\chi$	2.6	-1.3	-0.5	Helical
PbCuSO <sub>4</sub> (OH) <sub>2</sub>	[25]	$\chi$	1.1	-1.8	-1.6	Helical
PbCuSO <sub>4</sub> (OH) <sub>2</sub>	[26]	C <sub>p</sub> , $\chi$	8.6	-3.1	-0.36	Helical

**Table 4.3: Summary of quasi-one-dimensional cuprate  $J_1$ - $J_2$  chains.** For each material, the reference, experimental method, obtained values of  $J_1$  and  $J_2$  and knowledge of magnetic structure is shown. For LiCu<sub>2</sub>O<sub>2</sub>, three spin-wave models have been suggested. Out of these three only one model (where  $J_1 = 7.0$ ) is a FM  $J_1$ - AFM  $J_2$  chain. The three proposed linarite (PbCuSO<sub>4</sub>(OH)<sub>2</sub>)  $J$  parameters are also presented for comparison. Note that the ratio  $J_2/J_1$  stated here is not always directly related to the frustration ratio  $\alpha$ . The materials for which no long range order has been observed are labelled as “no L.R.O.”.

As mentioned before in section 4.1.1 and 4.1.2, the most important parameter for the one dimensional  $J_1$ - $J_2$  chain is the ratio  $\alpha = J_2/J_1$ . In table 4.3, the values of

$J_2/J_1$  are given for each material. However, it is very important to note that these systems are not one dimensional systems. There is always some level of coupling between neighbouring spin chains. This means that the frustration ratio for these real materials cannot be defined as  $\alpha = J_2/J_1$ . The true frustration ratio must consider the inter-chain interactions as well. For example, in  $\text{LiCuVO}_4$  the spin-wave dispersion has been studied extensively using single crystal inelastic neutron scattering along many different directions and four different inter-chain coupling terms have been identified [157]. Two of these correspond to a coupling perpendicular to the chain direction. The other two correspond to a diagonal coupling, i.e. they have a component along the spin chain. Therefore, the frustration ratio for  $\text{LiCuVO}_4$  is calculated as  $\alpha = J_2/(J_1 + 2J_5 - 4J_6)$ . Here,  $J_5$  and  $J_6$  are the diagonal interactions and they are FM and AFM respectively. Also, compared to  $J_1$ ,  $J_5$  and  $J_6$  have twice and four times more equivalent neighbours respectively. When the inter chain interactions are also considered, the frustration ratio for  $\text{LiCuVO}_4$  is  $\alpha=-1.43$ , which is quite different to  $J_2/J_1=-2.23$  [157]. This is an important point to remember when trying to compare real systems like  $\text{LiCuVO}_4$  with one dimensional theoretical models discussed in sections 4.1.1 and 4.1.2.

Within the materials in table 4.3, only  $\text{LiCuVO}_4$  [157],  $\text{LiCu}_2\text{O}_2$  [163],  $\text{Li}_2\text{CuO}_2$  [159], and  $\text{Ca}_2\text{Y}_2\text{Cu}_5\text{O}_{10}$  [162] have been measured with single-crystal inelastic neutron scattering techniques. Therefore, only for these materials the inter-chain-exchange constants are known. For  $\text{LiCu}_2\text{O}_2$  [163] the spin wave was measured close to the magnetic Bragg peak along two high symmetry directions. The full dispersion was not measured, instead it was measured up to  $\sim 10\text{meV}$  energy transfer. Three different spin-wave models were suggested to explain the data which can be seen in table 4.3. According to the authors, the most likely model is composed of an AFM  $J_1$  and FM  $J_2$  and an equally strong fourth-nearest neighbour  $J_4$ , which is also AFM. If this is indeed the case this would make  $\text{LiCu}_2\text{O}_2$  considerably different from the

other materials discussed in table 4.3. For  $\text{Li}_2\text{CuO}_2$ , initial single-crystal INS measurements were interpreted as AFM  $J_1$  and AFM  $J_2$  [168]. However, later INS data found that there was an overlooked highly dispersive branch which was measured up to  $\sim 20\text{meV}$  along one high symmetry direction [159]. The fit to this data provided a FM  $J_1$  and AFM  $J_2$  as presented in table 4.3. For  $\text{Ca}_2\text{Y}_2\text{Cu}_5\text{O}_{10}$  the single-crystal inelastic neutron spectrum was measured along three high symmetry directions up to  $\sim 10\text{meV}$ . The AFM  $J_2$  interaction is very small for  $\text{Ca}_2\text{Y}_2\text{Cu}_5\text{O}_{10}$  and therefore its existence is not certain [162]. For the other materials on table 4.3, where single crystal INS data does not exist, the  $J$  parameters were mostly obtained using a one dimensional model without any inter-chain interaction or anisotropies. For  $\text{LiCuSbO}_4$  the INS experiments were performed on powder samples and therefore it was not possible to determine the strength of inter-chain interactions.

In the cuprate  $J_1 - J_2$  systems, obtaining the  $J$  parameters through inelastic neutron scattering is not always straight forward. The usual assumption is that LSWT can be used to extract the  $J$  parameters at zero field. However, the low dimensionality and low spin observed in the cuprate  $J_1 - J_2$  systems causes excitations which are not accurately described by LSWT. One way to overcome this problem is to apply a large enough magnetic field so that the system becomes fully FM. In this fully FM phase, the obtained  $J$  parameters will be the true parameters which describe the system. For the two dimensional frustrated quantum magnet  $\text{Cs}_2\text{CuCl}_4$ , the  $J$  parameters were obtained at zero field and within the fully FM phase using inelastic neutrons and LSWT. A clear difference was observed between the zero field and FM phase  $J$  parameters. This difference can be considered as “quantum normalisations” to the zero field  $J$  parameters [169]. This method cannot be performed on quasi-one-dimensional cuprates  $\text{LiCuVO}_4$  or  $\text{LiCuO}_2$  due to their large saturation fields of  $\sim 50\text{T}$  [44] and  $\sim 110\text{T}$ (estimate) [170]. However, the quantum normalisations on the  $\text{LiCuVO}_4$  parameters were obtained in a different way. It was expected

that the AFM interactions would be normalised by  $\pi/2$ , whilst the FM interactions should not be normalised. The high temperature susceptibility data was fitted with a model based on the INS results, except where only  $J_2$  was a free parameter. The obtained normalisation of  $J_2$  was found to be very close to  $\pi/2$  as expected [157].

The zero field inelastic spectrum of  $\text{LiCuVO}_4$  along chain direction  $k$  can be seen in figure 4.14(a) on page 157. It can be seen that instead of a clear spin-wave branch, there is a continuum. This is in fact a spinon continuum. Spinons are spin  $1/2$  bosons with no charge. They are one of the elementary excitations of the one dimensional AFM chain, the Luttinger liquid. Spinons are always created in pairs and can be thought of as propagating magnetic domain walls. In figure 4.14(b), the calculated two-spinon continuum can be seen. This calculation was performed using the “true”  $J$  parameters of  $\text{LiCuVO}_4$ , where the normalisations were taken into account. The similarity between the data and the calculations is another validation that the interaction scheme of  $\text{LiCuVO}_4$  is well understood [45].

In section 4.1.2 it was discussed that the one dimensional  $S=1/2$  Heisenberg  $J_1 - J_2$  chain has the possibility to display novel quantum phases described as multi-magnon bound states with spin-multipolar order. It was also shown that these exotic quantum phases can survive under inter-chain coupling and anisotropy. This makes it likely to observe these novel phases in real systems such as the quasi one-dimensional cuprate chains. In fact,  $\text{LiCuVO}_4$  has already shown major experimental evidence for the existence of a two-magnon spin-quadrupolar phase. This has originated from magnetisation measurements close to saturation [44] and from neutron diffraction measurements under an applied magnetic field [45]. These can be seen in figures 4.15(a) and (b) respectively on page 158. In the magnetisation data, between  $H_{c3}$  and  $H_{sat}$ , the magnetisation becomes linear; this has been interpreted as  $\text{LiCuVO}_4$  entering the spin-quadrupolar phase. Neutron diffraction experiments measured the dependence of the incommensurate magnetic Bragg peak



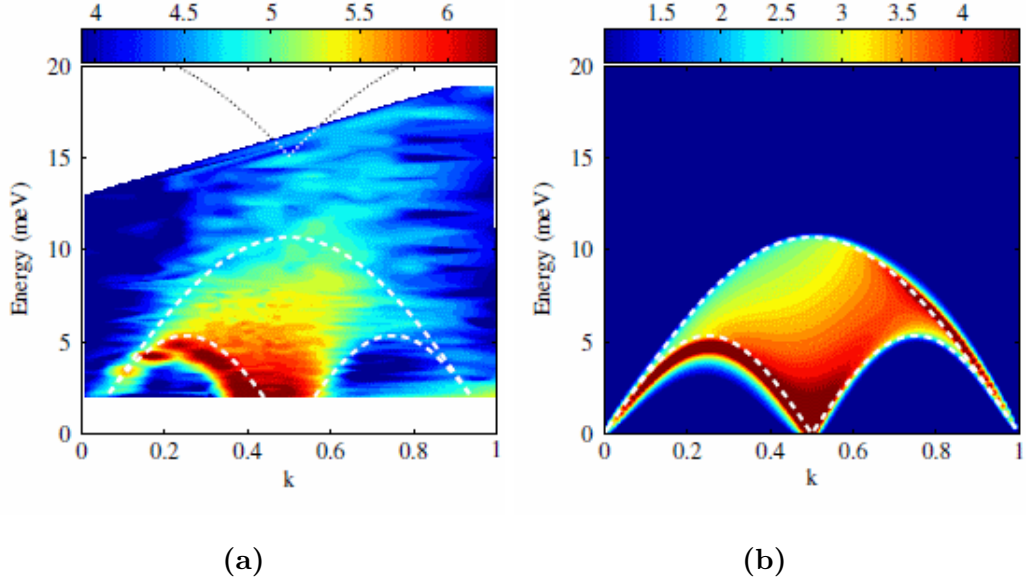


**Figure 4.14: LiCuVO<sub>4</sub> measured and calculated spinon spectrum.** (a) The inelastic neutron spectrum shows a continuum of excitations. There is little difference between this measurement and (b) the theoretical two-spinon continuum calculated using the “true”  $J$  parameters as obtained by Ref. [157]. Images taken from [127].

of LiCuVO<sub>4</sub> on an applied magnetic field. In figure 4.15(b) it can be seen that the magnetic Bragg peak does not change much until  $\sim 6$ T, after which it jumps in position and slowly decreases in  $\tilde{k}_{IC}$ . Here,  $\tilde{k}_{IC}$  is defined in a unit cell with one copper per unit cell, rather than the usual two and IC stands for incommensurate. The red line is the expected evolution of a SDW<sub>(2)</sub> phase as determined from equation 4.5. Here, it can be seen that beyond  $\sim 6$ T, the  $\tilde{k}_{IC}$  follows the exact dependence as expected from a SDW<sub>(2)</sub> phase. Additionally, the magnetic Bragg peaks were also measured along  $h$  and  $l$  directions. It was observed that beyond  $\sim 6$ T the Bragg peaks became broad in  $h$  and  $l$  directions. This effectively shows that below  $\sim 6$ T there is long range order (given in blue) whilst above  $\sim 6$ T there is only short range

order (given in red). The existence of quasi-long range order is another property expected from a spin-quadrupolar phase. These experimental signatures point towards the existence of a two-magnon spin-quadrupolar phase within  $\text{LiCuVO}_4$ .

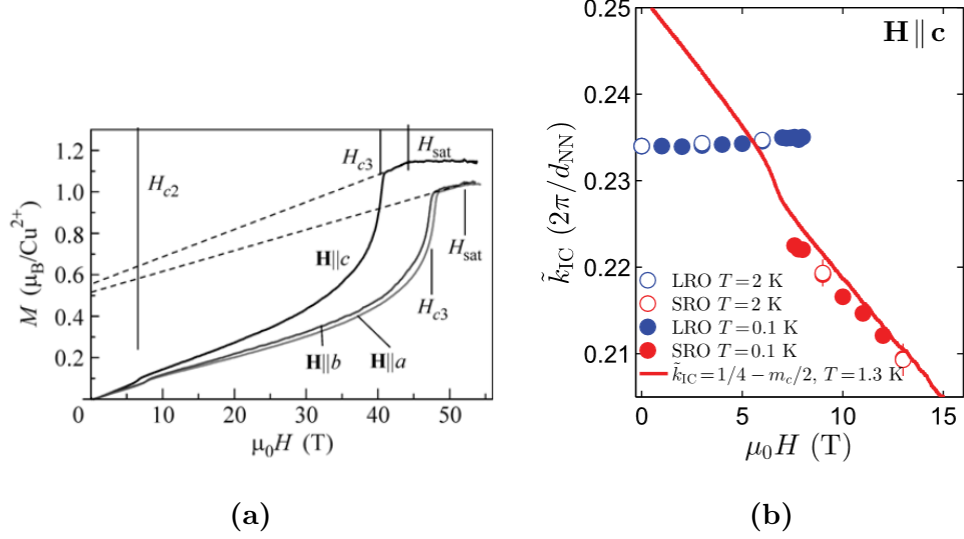


**Figure 4.15: Evidence of a two-magnon bound state for  $\text{LiCuVO}_4$ .** (a) Magnetisation measurements near saturation [44], and (b) field dependence of the magnetic Bragg peak [45] has been used to suggest two-magnon bound state might exist for  $\text{LiCuVO}_4$ . Images taken from Refs. [44] and [45] respectively.

As discussed in the previous section, linarite is considered a good candidate to observe a spin-multipolar phase. All of the suggested  $J$  parameters in literature, as stated in table 4.3, can support spin-multipolar phases in the purely one-dimensional isotropic  $J_1 - J_2$  model. The zero field magnetic Bragg peak is positioned at  $l = 0.5$  [25, 26], which indicates an AFM inter-chain coupling along  $c$  axis direction. This could be detrimental to the stability of a spin-multipolar phase. However, from ESR linewidths [26], a sizeable anisotropy is expected for linarite which could help with its stability. The prospect of a spin-multipolar phase in linarite is very interesting

due to linarite's relatively low saturation field of  $\sim 10T$  [26]. This would allow the study of the spin-multipolar phases all the way up to complete magnetic saturation using neutron scattering methods. Also, the spin-waves above saturation can be measured and the “true” interaction scheme of the material can be obtained. This is quite different to the other well studied quasi one-dimensional cuprates such as  $\text{LiCuVO}_4$  and  $\text{LiCu}_2\text{O}_2$  which have large saturation fields of  $\sim 50T$  [44] and  $\sim 110T$  [170] respectively.

The phase diagram of Linarite can be compared to that of the two well studied systems  $\text{LiCuVO}_4$  and  $\text{LiCu}_2\text{O}_2$ . These two systems are very similar. They both have a helical magnetic structure in the ***ab*** plane at low temperatures; they both show spin-flop transitions; and they both have high saturation fields of  $\sim 50T$ , and  $\sim 110T$  respectively [44, 170]. The simple phase diagram of  $\text{LiCuVO}_4$  can be seen in figure 4.16 on page 160. NMR measurements on  $\text{LiCuVO}_4$  show a spin-flop transition at  $H_{c1}=2.5T$  when a field is applied along either the ***a*** or ***b*** axis direction [171]. At  $H_{c2}=7T$  for all three field directions there is another transition into what has been described as a sinusoidally modulated spin structure with spins aligned along the field direction [172]. A third transition is observed close to the saturation from the magnetisation measurements. For ***H***//***c*** this third phase appears at  $H_{c3} \sim 40T$  but for ***H***//***a*** and ***H***//***b*** it appears at  $\sim 47T$ . This is followed by saturation at  $\sim 45T$  for ***H***//***a***, and at  $\sim 52T$  for ***H***//***b*** or ***H***//***c*** field directions. This third phase is considered as the two-magnon spin-quadrupolar phase [44].

The  $\text{LiCu}_2\text{O}_2$  phase diagram can be seen in figure 4.17 on page 161. A spin-flop transition was observed for ***H***//***a, b*** at  $\sim 4T$ . For all principle axis directions, a second transition is observed at  $\sim 15T$ . The phase above this second transition is thought to be a collinear spin modulated structure. The saturation field could not be accessed but is estimated to be as high as  $\sim 110T$  for the ***H***//***c*** direction. Different to  $\text{LiCuVO}_4$ ,  $\text{LiCu}_2\text{O}_2$  also has an additional transition at zero field. The

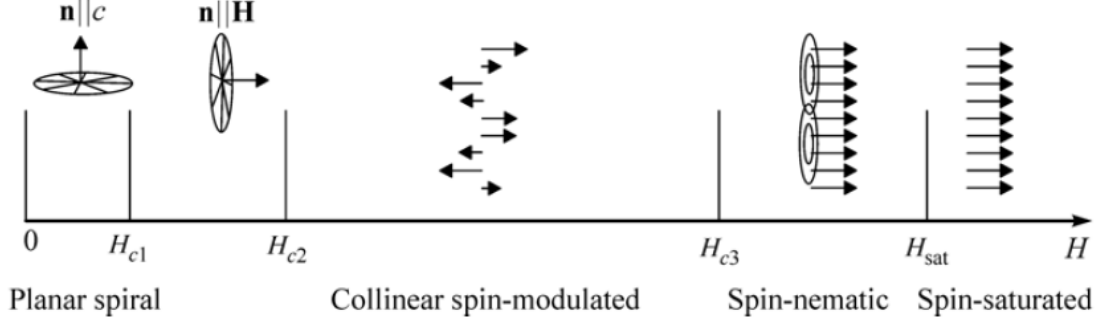


**Figure 4.16: Simple Phase diagram for  $\text{LiCuVO}_4$**  shows four different phases below saturation. The spin-flop transition  $H_{c1}$  only occurs for  $\mathbf{H} // \mathbf{a}$  or  $\mathbf{H} // \mathbf{b}$  as expected. Transition into a spin modulated structure,  $H_{c2}=7\text{T}$ , occurs at the same field for  $\mathbf{H} // (\mathbf{a}, \mathbf{b}, \text{ or } \mathbf{c})$ . The transition into the spin-nematic phase occurs at  $H_{c3} \sim 40\text{T}$  for  $\mathbf{H} // \mathbf{c}$  and  $H_{c3} \sim 47\text{T}$  for  $\mathbf{H} // (\mathbf{a} \text{ or } \mathbf{b})$ . Finally saturation occurs at  $H_{sat} \sim 45\text{T}$  for  $\mathbf{H} // \mathbf{c}$  and  $H_{sat} \sim 52\text{T}$  for  $\mathbf{H} // (\mathbf{a} \text{ or } \mathbf{b})$  [44]. Image from Ref. [44].

phase below  $T_{c2}$  is the helical phase and the phase above  $T_{c1}$  is the paramagnetic phase. However, the phase between  $T_{c1}$  and  $T_{c2}$  is a magnetic structure where only the component of the spiral along the  $\mathbf{a}$  axis appears, and the component along the  $\mathbf{b}$  axis fluctuates [170].

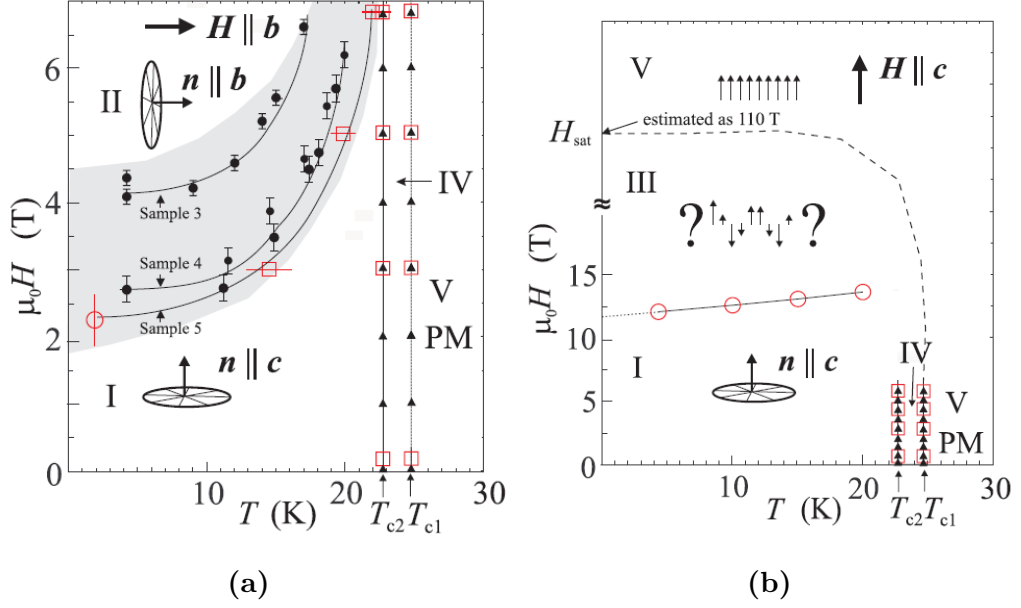


**Figure 4.17: The Phase diagram for  $\text{LiCu}_2\text{O}_2$ .** (a) For  $H \parallel b$  and  $H \parallel a$ , a spin flop is observed at  $\sim 4$  T as well as a second transition at  $\sim 15$  T. (b) For  $H \parallel c$ , only the  $\sim 15$  T is observed, above which a collinear spin modulated structure is expected. The saturation field is estimated to be as high as  $\sim 110$  T. Images obtained from Ref. [170].

Another two materials worth mentioning are  $\text{Li}_2\text{CuO}_2$  and  $\text{Ca}_2\text{Y}_2\text{Cu}_5\text{O}_{10}$ . For both of these materials the interaction scheme was obtained using inelastic neutron scattering methods. It was found that using their inter-chain interaction parameters alone, it is possible to predict their saturation field. This was done using the relatively simple equation 4.7 [140].

## 4.2 Crystals and Orientation

### Crystal Characterisation

All of the four Linarite crystals used in the experiments originated from Grand Reef Mine in Arizona, USA. The largest three crystals were co-aligned and used in inelastic neutron experiments. These crystals showed twinning, which is consistent of a shared  $\mathbf{a}^*$  and anti-parallel  $\mathbf{b}^*$  axis. This type of twinning is common for linarite [173]. The smaller two crystals did not show any twinning and were used in diffraction experiments. The list of the crystals and their approximate sizes can be seen in table 4.4. The crystals 1a and 1b used to belong to the same crystal and were characterised before the break happened.

	Size (mm <sup>2</sup> )	Twinning	Experiments
Crystal 1a	6x3x1	✓	Inelastic neutron
Crystal 1b	6x0.5x0.5	✓	Inelastic neutron
Crystal 2	6x2x1	✓	diffraction, Inelastic neutron
Crystal 3	4x1.5x0.5	X	diffraction, magnetisation
Crystal 4	4x1x1	X	diffraction

**Table 4.4: The table of linarite crystals used.** Crystal 1a, 1b, and 2 were often used co-aligned and they all showed twinning. Crystals 3 and 4 did not show twinning.

The sample characterisation was performed on TAS instrument IN3 at the ILL, Grenoble, France. In linarite the (001) and the (-101) Bragg peaks have very similar  $|Q|$  and can be confused easily. At IN3 the collimation was high enough to resolve the two peaks. However, the two peaks were still very close in  $2\theta$  (or A4 angle on TAS instrument) with  $29.9^\circ$  and  $30.4^\circ$  for (001) and (-101) respectively. The lattice parameters were in accordance with the Effenberger-Araki structure and not the

Bachmann structure. In order to be certain, 32 Bragg peak intensities were measured for the untwinned crystal 3 and these Bragg peak intensities were compared to the expected intensities for the Bachmann and Effenberger-Araki structures. For the structure factor calculations, the atom positions in table 4.1 were used for the Effenberger-Araki structure. For the Bachmann structure the atom positions were converted using equation 4.9. The measured and calculated Bragg peak intensities can be seen in tables 4.5 and 4.6 on pages 164 and 165 respectively. At each Bragg peak a rocking scan (A3 scan) was performed and from a Gaussian fit, the amplitude was obtained. In table 4.5, the obtained amplitude from this fit is given in “Amp.” and it is given in units of counts per second. The values under the “I(Q)” column are the same amplitudes but normalised to (020) amplitude and multiplied by 100 for clarity. The intensities for the Effenberger-Araki structure are calculated using  $I_{EA}(Q) = |F_{EA}(Q)|^2 / \sin(2\theta)$  where  $F_{EA}(Q)$  is the structure factor for Effenberger-Araki structure. The intensities for the Bachmann structure are calculated in a similar way. Both of the calculated intensities are normalised to their (020) amplitude and multiplied by 100 and presented under columns “I(Q)<sub>EA</sub>” and “I(Q)<sub>B</sub>” respectively in tables 4.5 and 4.6. From the last three columns in these tables, it can be seen that the Effenberger-Araki structure provides a much better description of the data. If two different  $\chi^2$  values are defined as  $\chi_{EA}^2 = \sum (I(Q) - I(Q)_{EA})^2$  and  $\chi_B^2 = \sum (I(Q) - I(Q)_B)^2$ , then this would result in  $\chi_{EA}^2 \sim 0.3\chi_B^2$ . This is not a comprehensive structure determination, therefore a perfect agreement is not expected between  $I(Q)$  and  $I(Q)_{EA}$ . However, it is sufficient to show that on IN3, the Effenberger-Araki structure of linarite can be identified successfully.

$h$	$k$	$l$	<b>Amp(cps)</b>	<b>I(Q)</b>	<b>I(Q)<sub>EA</sub></b>	<b>I(Q)<sub>B</sub></b>
0	2	0	120.7	100.0	100.0	100.0
-1	0	1	496.3	411.3	212.8	686.6
0	0	1	833.3	690.5	694.1	215.1
-3	0	1	379.9	314.8	61.9	38.1
-3	0	0	965.7	800.2	714.1	714.1
3	0	0	381.5	316.2	714.1	714.1
0	0	3	348.1	288.4	377.3	153.2
-3	0	2	182.9	151.5	67.1	1.0
1	0	1	266.5	220.8	88.2	57.1
-2	0	1	234.1	194.0	55.8	86.3
2	0	1	126.6	104.9	39.0	63.3
3	0	1	411.7	341.2	272.5	912.6
4	0	0	376.4	311.9	205.2	205.2
4	0	1	308.4	255.5	192.4	6.8
5	0	1	8.4	7.0	5.3	3.5
5	0	0	52.2	43.3	12.8	12.8

**Table 4.5: Effenberger-Araki vs Bachmann structure comparison (part 1).** The amplitude of the Bragg peaks, obtained by rocking scan at  $\mathbf{Q}=(hkl)$ , is presented under column “Amp” in units of counts per second. In “I(Q)” the value  $100 \times \text{Amp}(hkl) / \text{Amp}(020)$  is shown. In columns “I(Q)<sub>EA</sub>” and “I(Q)<sub>B</sub>” the calculated intensities of Effenberger-Araki and Bachmann structures after the same normalisation is presented. The Effenberger-Araki structure is a more accurate description of the measurements. Table continued in table 4.6.



$h$	$k$	$l$	<b>Amp(cps)</b>	<b>I(Q)</b>	<b>I(Q)<sub>EA</sub></b>	<b>I(Q)<sub>B</sub></b>
6	0	0	199.4	165.3	115.0	115.0
0	0	2	63.0	52.2	16.9	1.5
-4	0	1	831.6	689.1	894.4	267.1
-5	0	1	31.1	25.7	6.7	189.0
-5	0	2	67.4	55.8	17.6	62.1
-6	0	1	20.0	16.6	3.4	5.3
-6	0	2	334.9	277.5	3.0	464.9
-2	0	2	21.6	17.9	1.5	16.7
1	0	2	7.9	6.6	1.1	68.3
2	0	2	216.4	179.3	129.6	113.0
-4	0	2	205.0	169.9	110.5	126.7
3	0	2	126.8	105.1	63.5	18.1
-3	0	3	211.2	175.0	151.6	373.3
4	0	2	371.4	307.8	475.6	3.1
1	0	3	371.1	307.5	523.5	33.0
-4	0	3	80.4	66.6	32.5	515.0

**Table 4.6: Effenberger-Araki vs Bachmann structure comparison (part 2).** This table is a continuation of table 4.5.

The twinning of the large samples is most apparent in the ( $h0l$ ) scattering plane. On IN3 in this scattering plane a  $180^\circ$  rocking scan (A3 scan) at a  $2\theta$  corresponding to (001) results in two Bragg peaks for an untwinned sample and four Bragg peaks for a twinned sample. This can be seen in figure 4.18(a) on page 166. Here the untwinned and twinned sample measurements are given in blue and red respectively. The  $(00-1)_t$  and  $(10-1)_t$  belong to the twin crystal and they are both positioned  $-2.51^\circ$  from  $(-101)$  and  $(001)$  Bragg peaks respectively. This observation is consistent with the twinning composed of shared  $\mathbf{a}^*$  but anti parallel  $\mathbf{b}^*$ , which is visualised in figure

4.18(b). From the relative size of the (001) Bragg peaks in figure 4.18(a), it can be concluded that the two twins must have a similar volume, since their intensities are very similar. In fact a Gaussian fit to each of the (001) type peaks shows that the  $(001)_t$  is  $\sim 30\%$  smaller in intensity than (001) Bragg peak.

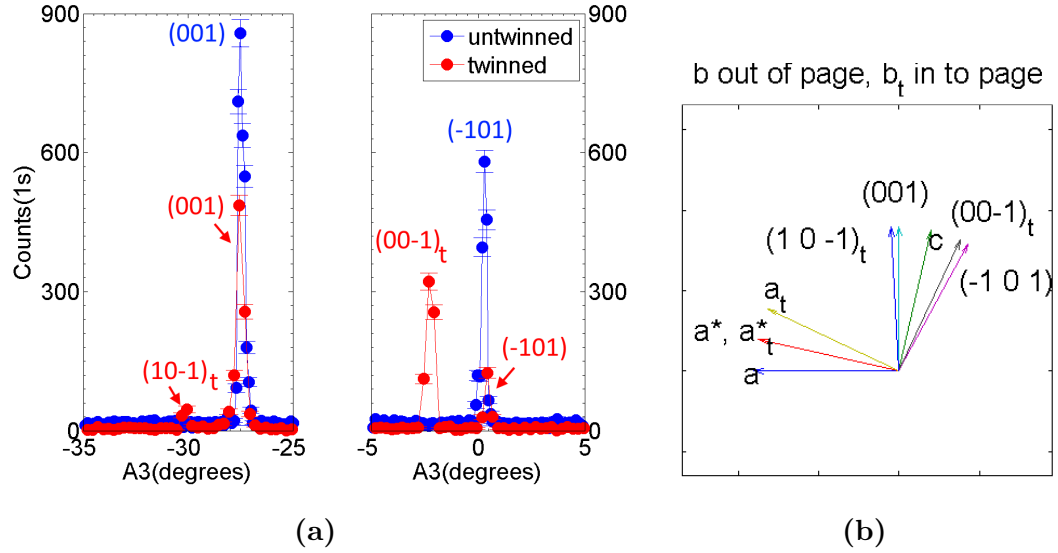


**Figure 4.18: Twinning in Linarite.** (a) The twinning can be seen in a IN3 A3 scan in the  $ac$  plane. Due to similar  $|Q|$  both (001) and (-101) type peaks can be seen in such a scan. For an untwinned crystal only two peaks in  $180^\circ$  is observed. For twinned crystals four peaks are observed in  $180^\circ$ . (b) This indicates a twinning where  $\mathbf{b}$  and  $\mathbf{b}_t$  at anti-parallel and  $\mathbf{a}^*$  and  $\mathbf{a}_t^*$  is parallel.

### Orientations of Co-aligned Crystals in INS Experiments

The twinned crystals were co-aligned in order to gain more intensity in INS experiments. The crystals were glued onto a thin plate of aluminium using GE varnish. The co-alignment was always accurate along  $\mathbf{b}$  axis direction; however, the alignment along  $\mathbf{c}^*$  axis direction was not accurate. In all of the experiments, at

least one of the samples was in the  $(0kl)$  scattering plane; however, the other crystals were rotated about the  $\mathbf{b}$  axis direction to some extent. This has consequences to the LSWT models used, therefore a detailed description of the orientation of each crystal for each INS experiment is necessary.

The IN14 March 2013 experiment was carried out with at 12T cryomagnet. For experiments with cryomagnets there is no usually capability to tilt the sample in order to access a different scattering plane. Therefore, it is very difficult to know the exact orientation during an experiment with the cryomagnet. There is a reliance on previous experiments to determine the orientation. An experiment was carried out at IN20 March 2013 where the orientations of the crystals were explored in detail. At the IN20 experiment there were three samples co-aligned: crystals 1a, 1b and 2. Crystal 1a and 1b used to be one piece; however, whilst the glue was drying, Crystal 1b (roughly 1/10th of the original crystal) broke off and rotated slightly about the  $\mathbf{b}$  axis. The rocking scans (A3 scans) around (020) and (001) Bragg peaks positions resulted in three peaks as seen in figure 4.19(a,b) on page 168. From left to right these Bragg peaks most likely correspond to crystals 1b, 2, and 1a respectively. An upper goniometer scan (GU scan) of the large (020) peaks at  $A3=72^\circ$  showed that they were only  $0.5^\circ$  out of plane. A lower goniometer scan (GL scan) was performed on each one of the three peaks in the (001) A3 scan. The results are summarised in figure 4.19(c). Note that in each GL scan there are in fact two peaks separated by  $2.51^\circ$ . One of these will correspond to a (001) type peak and the other will correspond to a (-101) type peak. The (-101) type peak is identifiable by its lower intensity compared to the (001). Because of the twinning, the data have been fitted to two Gaussian functions. Constraints are used so that the two Gaussians are  $2.51^\circ$  apart and they have the same full width and half maximum. If the (-101) type peak is the left of an (001) type peak, these peaks must be  $(-101)_t$  and (001) respectively. If the (-101) type peak is the right of an (001) type peak, these peaks must be  $(10-1)$

and  $(00-1)_t$  respectively. Using this information the Bragg peaks in figure 4.19 has been indexed. This means that the two large crystals, Crystal 2 and Crystal 1a, are  $1.4^\circ$  and  $3.4^\circ$  out of plane respectively but Crystal 1b is  $-29.1^\circ$  out of plane.

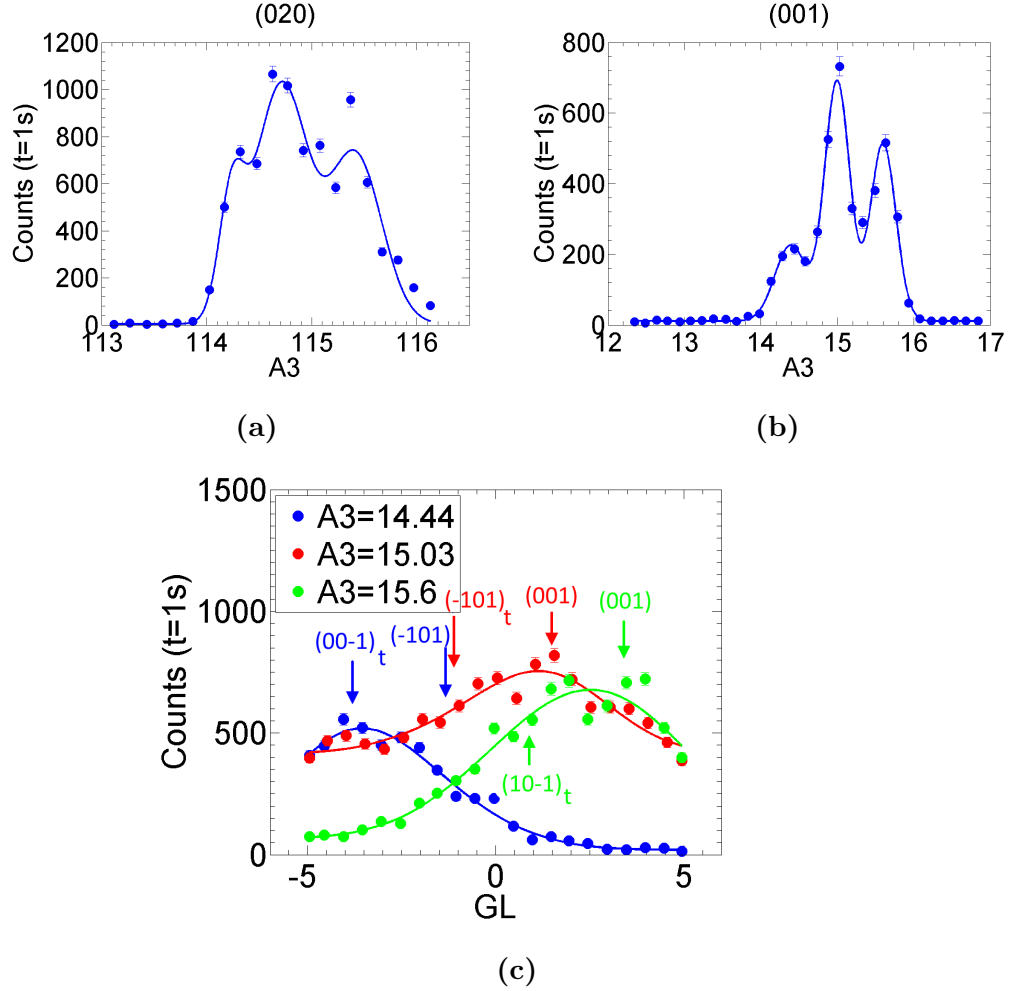


**Figure 4.19: Orientation from IN20 March 2013 data.** (a) An A3 scan at the position of (020) reveals three peaks. (b) Similarly an A3 scan at the position of (001) reveals three peaks. (c) A GL scan is performed for each of these (001) peaks in (b). From Gaussian fits and knowledge of the twinning in the sample, the orientation is obtained.

The IN14 March 2013 experiment, where the 12T cryomagnet was used, was performed very shortly after the IN20 March 2013 experiment. Therefore, there should not be a large change in the orientation. In fact very little difference is observed for (020) between the two experiments as seen in figure 4.20(a). However, a slight difference is observed for the (001) Bragg peaks which can be seen in figure 4.20(b). Here only two peaks are apparent, but by comparing intensities with IN20 March 2013 data, it is clear that two different crystals contribute to the  $\sim 27^\circ$  Bragg peak. The Bragg peak on the right, which most likely originates from Crystal 1a, appears to have a slightly weaker signal than expected. This might indicate the Crystal 1a has moved by  $\sim +2^\circ$  out of the scattering plane.

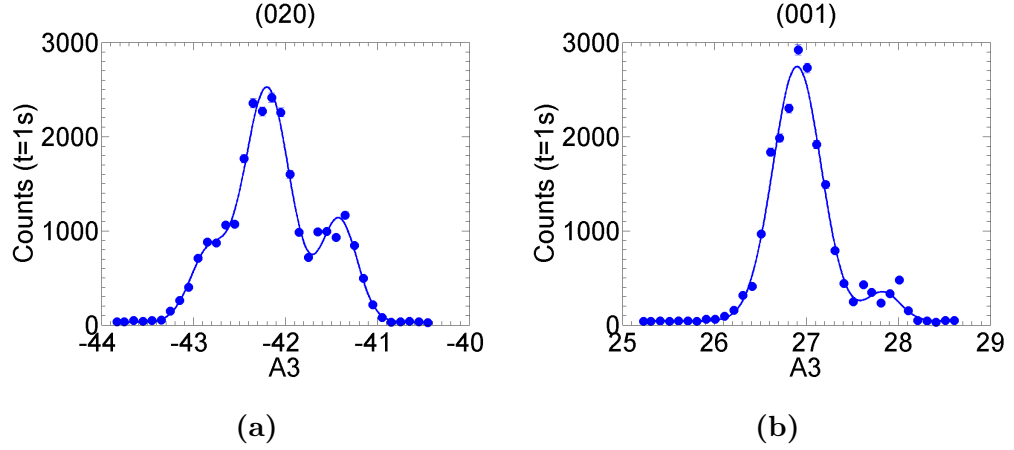


**Figure 4.20: Orientation information from IN14 March 2013 data.** (a) An A3 scan at the position of (020) reveals three peaks. (b) An A3 scan at (001) reveals only two peaks; however, the peak at  $\sim 27^\circ$  is likely to contain two Bragg peaks from two different crystals.

The next experiment where the co-aligned crystals were used was the IN14 April 2013 experiment where a 15T cryomagnet was used. In this experiment the orientation of the crystals very clearly changed once the field was applied. This change was apparent at 14.5T for (020) Bragg peaks as seen in figure 4.21(a) on page 170.

For the (001) Bragg peaks a change was observed both at 11T and 14.5T. It is important to note that at the end of the experiment it was observed that Crystal 1a was no longer attached to the sample mount; however, crystals 1b and 2 were still in place. The most likely explanation is that at 14.5T Crystal 1a falls off the sample mount. For the (001) Bragg peaks there is a change at 11T and at 14.5T. The disappearance of the  $\sim 29^\circ$  peak is in agreement with Crystal 1a detaching. The halving of intensity between 0T and 11T of the  $\sim 27^\circ$  (001) Bragg peak is harder to explain. Either one or both crystals were rotating about the **b** axis. From figure 4.19(c) it can be seen that these Bragg peaks have a full width half maximum of  $\sim 2.5^\circ$ . Therefore, the rotation about the **b** axis of crystals Crystal 1b and Crystal 2 cannot be much larger than  $\sim 2.5^\circ$ .

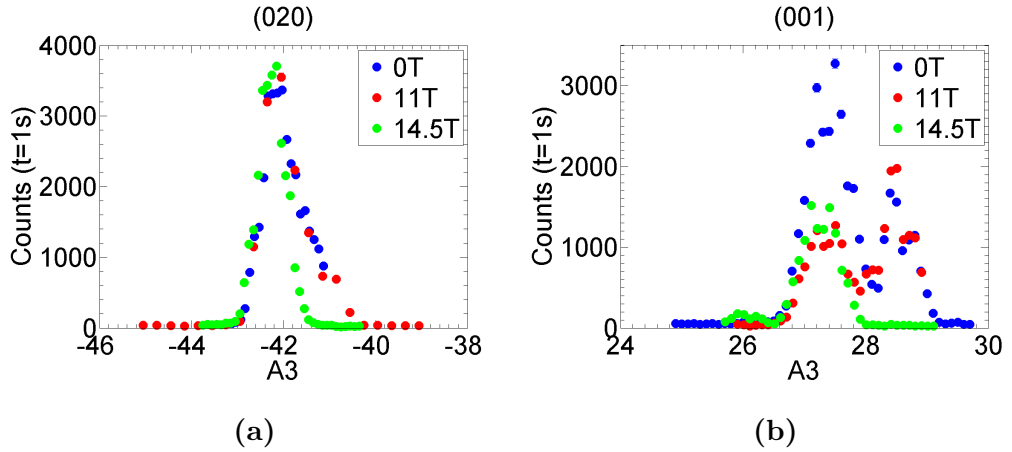


**Figure 4.21: Orientation information from IN14 April 2013 data.** (a) The (020) A3 scan shows one large peak with possibly a second smaller peak on the right hand side. This smaller peak disappears at 14.5T. (b) The (001) A3 scan shows that one crystal is lost at 11T and some more intensity is lost at 14.5T.

The last inelastic neutron experiment with a cryomagnet was the IN20 June 2013 experiment where an 11T cryomagnet was used. IN3 was used to co-align the

crystals Crystal 1a and Crystal 2 on the same mount from the previous experiments. The small Crystal 1b which was in previous experiments was not used. The results from the IN3 May 2013 experiment, where the sample was co-aligned, can be seen in figure 4.22. The (020) A3 scan shows that the two crystals are perfectly co-aligned along this direction. However, a GL scan at (001) reveals three different peaks. The Bragg peaks at  $\sim 15^\circ$  and  $\sim 12^\circ$  must belong to the same crystal as this is the  $25.3^\circ$  separation of the (001) and  $(00-1)_t$  Bragg peaks of the same crystal (see figure 4.18). For the large peak at  $\sim 5^\circ$ , it is not clear if the (001) type peak is on the left or the right. A two Gaussian fit is performed to this peak with the constraint that they must be separated by  $2.51^\circ$ . Such a fit suggest that the peak at  $3.3^\circ$  is of larger intensity and therefore this must be the  $(00-1)_t$  Bragg peak. Therefore, the two crystals are  $-22^\circ$  and  $-14.5^\circ$  out of plane. It is important to note that the  $(00-1)_t$  Bragg peaks are only  $3.3^\circ$  and  $10.8^\circ$  out of plane.

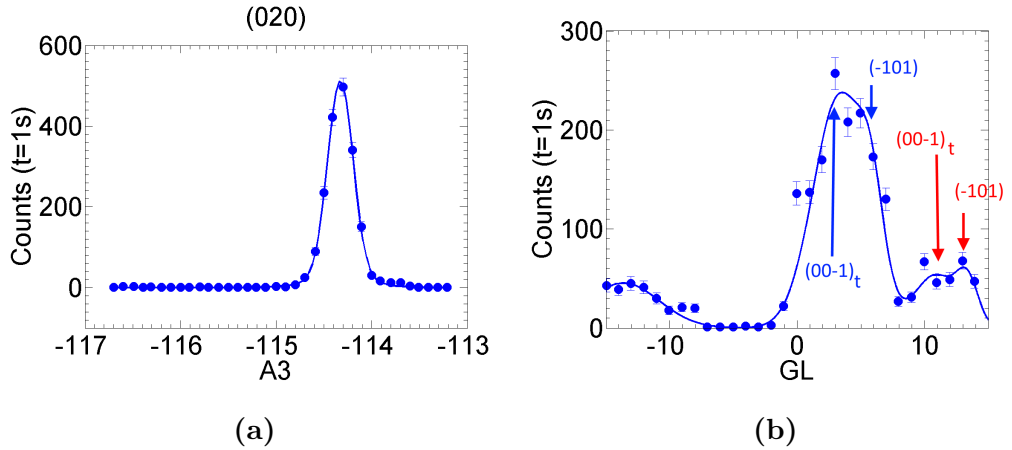


**Figure 4.22: Orientation information from IN3 May 2013 data.**

(a) The (020) A3 scan shows one peak. (b) A GL scan at (001) reveals three peaks each composed of two peaks.

At the IN20 June experiment, where the 11T cryomagnet was used, the (020) and (001) A3 scans revealed two Bragg peaks very close together. This can be seen

in figure 4.23(a,b). The two peaks in (001) could be an indication that the crystal, which was  $10.8^\circ$  away in IN3 May 2013 experiment, could potentially be much closer to zero.

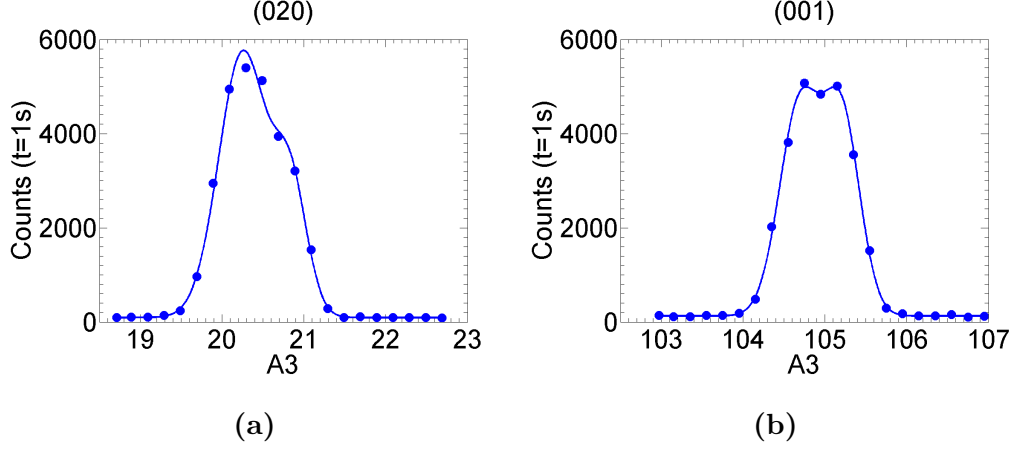


**Figure 4.23: Orientation information from IN20 June 2013 data.** A3 scans at (a) (020) and (b) (001) reveals two peaks unlike the IN3 May 2013 experiments where one peak was observed.

From the presented information so far, it is not possible to fully know the orientation of each crystal in each INS experiment where a cryomagnet was used. However, in the experiments where no cryomagnet were used, the exact orientations are known and using this information it is possible to extrapolate the orientations for all of the experiments. The orientation of each crystal in each experiment can be seen in table 4.7 on page 173. Here the angle between the  $(0kl)$  plane and the scattering plane is shown. It is assumed that the relative orientation of each crystal does not change between the first three experiments. This allows the intensities in figure 4.19(c) to be compared to (001) A3 scan intensities for each IN14 experiment. It is important to note that for IN14 April 2013 experiment, Crystal 1a detached from the sample mount during the experiment and did not contribute to inelastic measurements. Also for IN3 May 2013 and IN20 June 2013 experiments Crystal



1b was not used. From table 4.7 it may appear that most of the crystals are quite drastically misaligned; however, an angle of  $-25.3^\circ$  would correspond to  $(00-1)_t$  being in the scattering plane, which is equivalent to having (001) in the scattering plane. Therefore, in the first three experiments in table 4.7, the maximum deviation from (001) or  $(00-1)_t$  is  $5.4^\circ$ . For the last two experiments the maximum deviation from  $(00-1)_t$  is  $10.8^\circ$ . For the experiments using a cryostat, the stated value is likely  $\sim 3^\circ$  within the actual orientation. This is based on a typical full-width at half-maximum from a GL scan of (001) Bragg peaks, for example in figure 4.19(c).

Experiment	Crystal 1a	Crystal 1b	Crystal 2
IN20 March 2013 (no cryomagnet)	$1.4^\circ$	$-29.1^\circ$	$3.4^\circ$
IN14 March 2013 (12T cryomagnet)	$3.4^\circ$	$-27.1^\circ$	$5.4^\circ$
IN14 April 2013 (15T cryomagnet)	-	$-28.1^\circ$	$4.4^\circ$
IN3 May 2013 (no cryomagnet)	$-14.5^\circ$	-	$-22^\circ$
IN20 June 2013 (11T cryomagnet)	$-14.5^\circ$	-	$-22^\circ$

**Table 4.7: The orientations of each crystal in INS experiments with a cryomagnet.** The angle between  $(0kl)$  plane and the scattering plane is presented for each crystal. For each experiment with a cryomagnet estimates are most likely within  $\sim 3^\circ$ .

Aside from the experiments listed in table 4.7, three different INS experiments were carried out which did not use a cryomagnet. These zero field experiments benefited from the use of goniometers which allowed the sample to be tilted out of the original scattering plane. This way the exact orientation for at least one of the crystals could be obtained.

No modifications were made to the co-alignment between IN20 June 2013 and IN12 November 2014. Therefore, they most likely have the same orientations. In the IN12 November 2014 experiment, two peaks  $0.8^\circ$  apart were observed in an

(020) and (001) A3 scans which can be seen in figure 4.24(a,b) on page 175. A GU scan at (001) revealed large peak centred at  $2.5^\circ$  can be seen in figure 4.24(c). A two Gaussian fit to this places the (001) type peak at  $0.6^\circ$ . This observation is in agreement with the previous IN20 experiment. Even though the second crystal's (001) or (-101) type Bragg peak was not directly measured in this experiment, its relative position is likely unchanged from the last experiment. Therefore, the best estimate of angle between (001) and the scattering plane for the two crystals is  $-24.7^\circ$  and  $-17.1^\circ$  respectively.

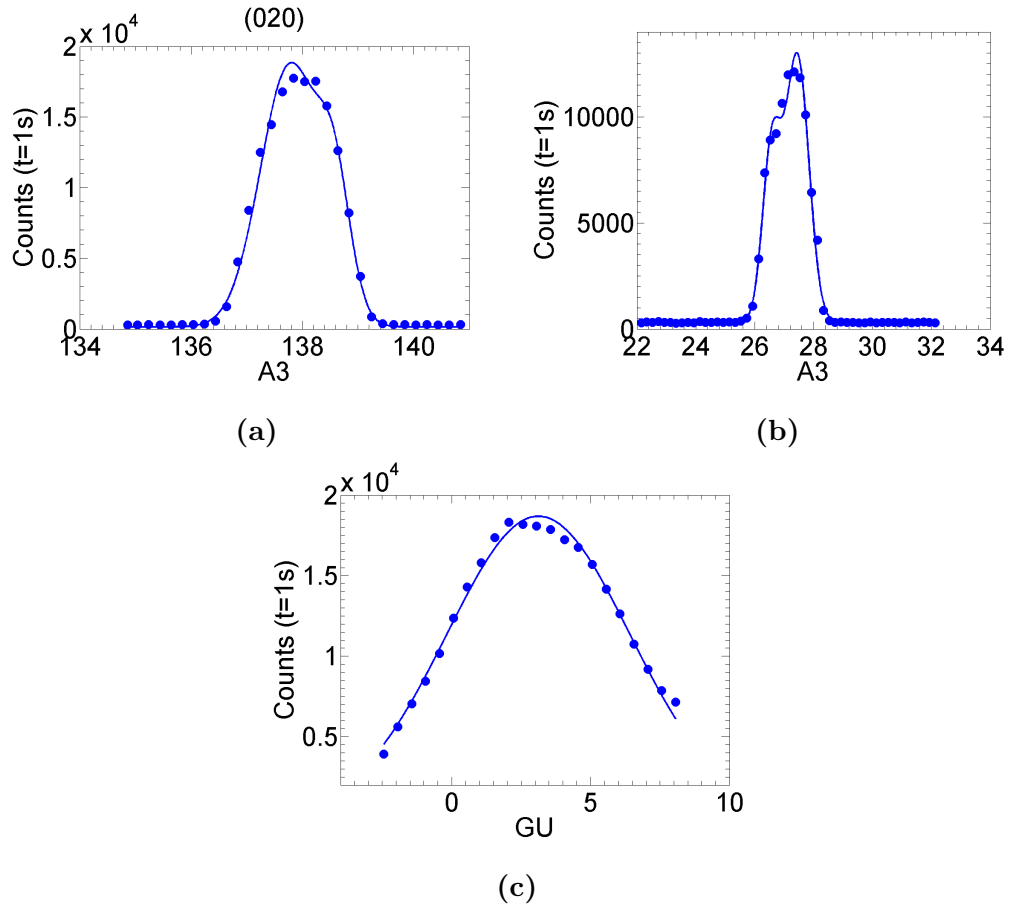


**Figure 4.24: Orientation information from IN12 December 2014 data.** (a,b) The (020) and (001) A3 scan shows two peaks  $0.8^\circ$  apart. (c) A GU scan at (001) reveals only one large peak.

The ThALES December 2014 experiment was carried very shortly after the IN12 experiment. However, surprisingly, the (020) and (001) Bragg peaks show three peaks in A3 scans which can be seen in figure 4.25(a,b) on page 176. This is contrary to the IN12 experiment where only two peaks were observed. A GU scan about (001) identifies the  $(00-1)_t$  peak at  $-0.2$ , which can be seen in figure 4.25(c). Even though the orientation of the second crystal was not determined directly, it can be assumed that it has the relative rotation between the crystals have not changed since the

IN20 June 2013 experiment. Therefore, the orientations of the two crystals must be  $-25.1^\circ$  and  $-17.6^\circ$  respectively.

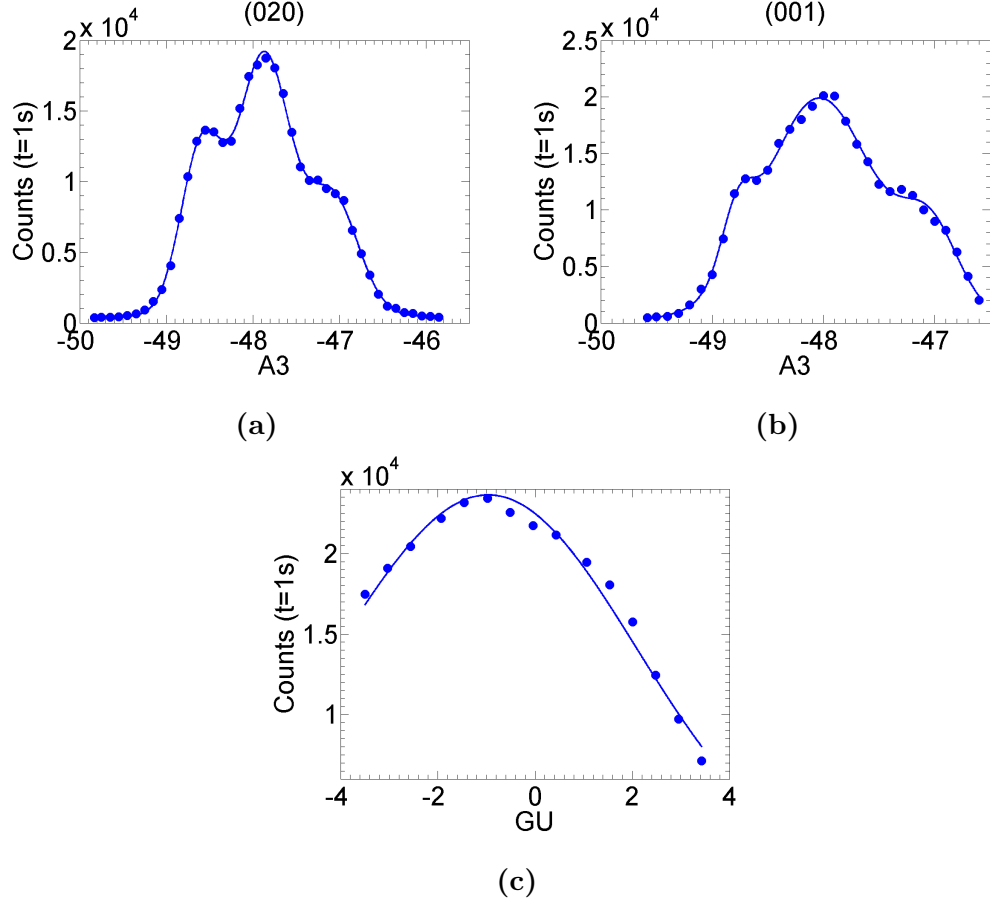


**Figure 4.25: Orientation information from ThALES December 2014 data.** (a,b) The (020) and (001) A3 scan shows three peaks. (c) A GU scan at (001) reveals only one large peak.

For the ThALES April 2015 experiment a better co-alignment was achieved. This was done by gluing the  $\mathbf{a}^*$  faces of the two crystals together. In the (020) and (001) A3 scans there were two Bragg peaks  $\sim 0.4^\circ$  apart, which can be seen in figure 4.26(a,b) on page 177. The (001) GU scan showed one large peak which is given in 4.26(c). From fitting two Gaussians to this data it is expected that the (001) type

peak is at  $-1.2^\circ$ .

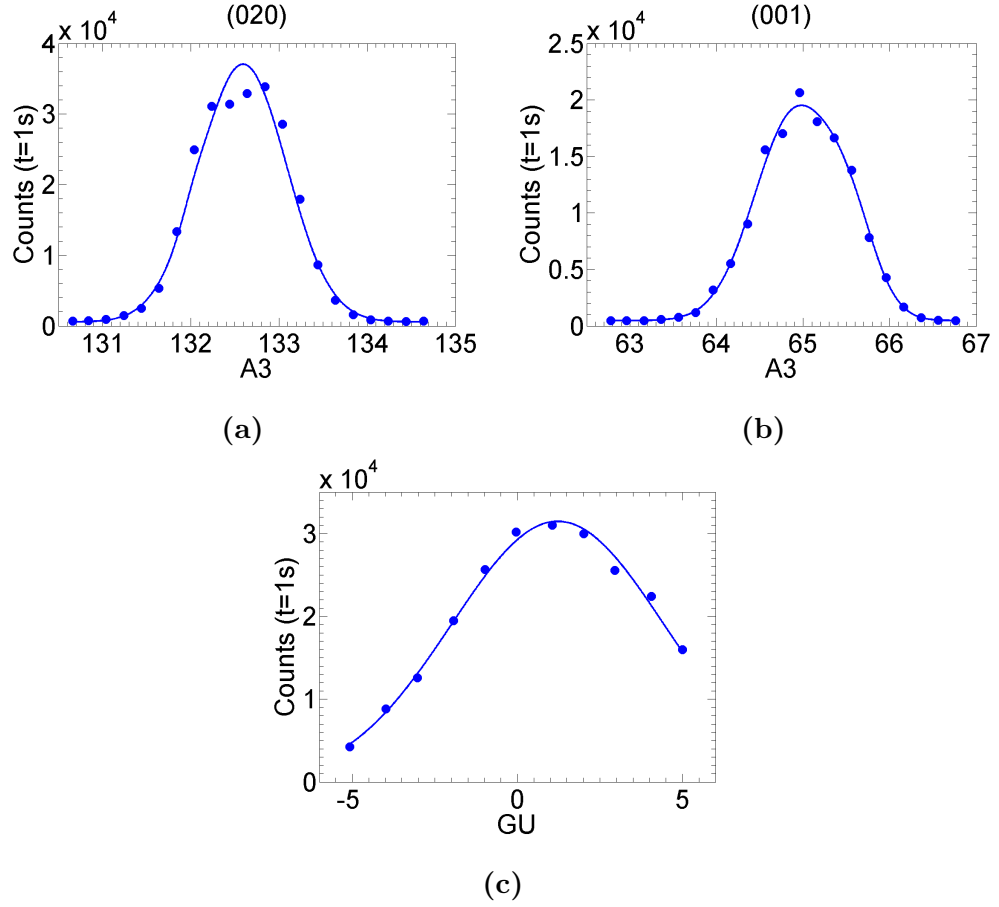


**Figure 4.26: Orientation information from ThALES April 2015 data.** (a,b) The (020) and (001) A3 scan shows two peaks. (c) A GU scan at (001) reveals only one large peak.

The orientations of the crystals for the INS experiments performed at zero Tesla are summarised in table 4.8 on page 178. Here the angle between the  $(0kl)$  plane and scattering plane is presented in degrees for each crystal. In the IN12 November 2014 and ThALES December 2014 experiments Crystal 1a was not directly observed, therefore its position was extrapolated by using the relative crystal orientations from the IN20 June 2013 experiment. For ThALES April 2015 experiment only

one peak was observed in GU, therefore it was assumed that their orientations were identical. It is important to remember that  $-25.3^\circ$  corresponds to  $(00-1)_t$  being in the scattering plane. The choice of labelling  $(00-1)_t$  over  $(001)$  is arbitrary. In these experiments, the samples were tilted so that the Crystal 2  $(00-1)_t$  Bragg peak was in the scattering plane. This meant that for the IN12 and ThALES December 2014 experiment Crystal 1a could be as much as  $\sim 8^\circ$  out of plane. In the ThALES April 2015 experiment both crystals should be perfectly in the  $(0kl)$  plane.

Experiment	Crystal 1a	Crystal 2
IN12 November 2014	$-17.1^\circ$	$-24.7^\circ$
ThALES December 2014	$-17.6^\circ$	$-25.1^\circ$
ThALES April 2015	$-26.5$	$-26.5$

**Table 4.8: The orientations of each crystal in INS experiments without a cryomagnet.** The angle between  $(0kl)$  plane and the scattering plane is presented for each crystal. The orientations of Crystal 1a for the first two experiments are extrapolated using information from the IN20 June 2013 experiment.

### 4.3 Spin-wave Measurements Above Saturation Field

As discussed in the introduction, there is some confusion in the literature regarding the value of the exchange parameters for Linarite. Inelastic neutron scattering measurements provide a more direct way of measuring the  $J$  parameters and therefore could resolve the discrepancy in literature. Additionally, this method can obtain the full interaction scheme of linarite, including inter-chain interaction terms and exchange anisotropies. In order to obtain the true  $J$  parameters of linarite, the

experiments must be carried out above saturation (i.e. in the fully FM phase). This is done with the use of a cryomagnet, which can supply large enough magnetic field strengths to saturate linarite. This method of saturating the system and measuring the interaction parameters was developed for a two dimensional frustrated system  $\text{Cs}_2\text{CuCl}_4$  [169].

### 4.3.1 Experimental Set-Up

The inelastic neutron experiments were performed on TAS instruments IN14 and IN20 at the ILL, Grenoble, France. Over three experiments and three different vertical cryomagnets, INS measurements were performed at field strengths 10T, 11T, and 14.5T. The 10T, 11T, and 14.5T datasets were obtained in IN20 June 2013, IN14 March 2013, and IN14 April 2013 experiments respectively. For all of the experiments two or three twinned linarite crystals were used. The orientations of each crystal in each experiment is discussed in detail in section 4.2 and summarised in table 4.7. For each experiment the desired scattering plane was the  $(0kl)$  plane which corresponds to  $\mathbf{H} // \mathbf{a}$ . The maximum deviation from this orientation should be  $\sim 5^\circ$  for the 11T and 14.5T dataset experiments whilst for the 10T dataset experiment a deviation of  $\sim 11^\circ$  is possible. The typical experimental set up for IN14 can be seen in figure 2.10. The experimental set up is similar to that of IN12 in figure 2.9; however IN14 does not have a velocity selector. Similarly the experimental set up of IN12 can be seen in figure 2.8.

The 11T dataset was measured on IN14 using the 12T vertical cryomagnet. The maximum field strength used was 11T and a base temperature of  $\sim 1.7\text{K}$  was maintained throughout the experiment. Pyrolytic graphite (PG) crystals (002) reflection was used for both the monochromator and the analyser. Vertical focusing was used on the monochromator and horizontal focusing was used for the analyser. The experiment was performed in fixed  $k_f$  mode with  $k_f = 1.5\text{\AA}^{-1}$ . The monitor M1 was

placed after the monochromator. Diaphragms with vertical and horizontal slits were placed on either side of the cryomagnet in order to minimise the background. The diaphragms were placed as close as possible to the cryomagnet. The diaphragms were closed down as much as possible without reducing the signal from the sample. This was done by checking two strong nuclear Bragg peaks  $90^\circ$  apart. Using the size of the first set of diaphragms and the size of the sample, it is possible to calculate the optimum size of the second diaphragm. This optimum size corresponds to the position where any neutron passing through the sample can reach any part of the analyser without being blocked by the second diaphragm. After the second diaphragm, a beryllium filter (cooled down to liquid nitrogen temperatures) was placed to remove second order neutrons (i.e. neutrons with twice the wavenumber).

The 14.5T dataset was measured on IN14 using the 15T vertical cryomagnet. The maximum field strength used was 14.5T and a base temperature of  $\sim 1.6\text{K}$  was maintained throughout the experiment. The experimental set up was very similar to that of the 11T experiment. The same monochromator, analyser with the same focusing and fixed  $k_f$  was used. The monitor M1 was placed after the monochromator. Diaphragms placed before the cryomagnet allowed a beam size of 8mm horizontally and 20mm vertically to pass through. Similarly for the diaphragms after the cryomagnet, beam size was reduced to 32mm horizontally and 37mm vertically. A beryllium filter was also used in this experiment; however, it was placed before the sample, between the monitor M1 and the first diaphragm.

The 10T dataset was measured on IN20 using the 11T vertical cryomagnet. The maximum field strength used was 10T and a base temperature of  $\sim 1.6\text{K}$  was maintained throughout the experiment. Si (111) monochromator was used in conjunction with a PG(002) analyser. Vertical and horizontal focusing were used for the monochromator and analyser. The experiment was performed in fixed  $k_f$  mode with  $k_f = 2.662\text{\AA}^{-1}$ . Diaphragms were placed on either side of the cryomagnet. The



openings of each diaphragm were optimised in the same manner as discussed before for the 11T experiment. A PG filter was placed between the second diaphragm and the analyser in order to remove second order neutrons.

### 4.3.2 Data Reduction

In the 14.5T and 10T experiments the focus was to measure as many points as possible of the spin-wave branch in order to get a good fit to the interaction scheme of linarite. A detailed background subtraction is unnecessary for these datasets because the spin-wave signal is strong enough and it can be clearly distinguished from any other possible backgrounds. For example, in the energy scans, the excitation is always far away enough from the tail end of the incoherent signal so that they can both be clearly distinguished. In the 11T dataset however, the motivations were different. It was the first inelastic neutron scattering experiment on linarite, therefore a large amount of time was spent exploring a large region of reciprocal space. Some of the observed signals were rather weak, making it more important to understand the background better. This meant that the 11T dataset required plenty of treatment before analysis whilst the 10T and 14.5T datasets required no such treatment.

The first step in the treatment of 11T data was the removal of inconsistent data. A problem with the electronics resulted in some counts becoming artificially large. It was possible to identify seven inconsistent points using the methods outlined by Ref. [174]. Assuming Poisson statistics, multiple measurements performed at the same Q and energy can be combined. The total count  $I$ , is obtained by the sum of all the counts  $I = \sum_n I_n$ , and similarly the total monitor  $M$  is given by  $M = \sum_n M_n$ . If this were obtained in a single measurement the error would be  $\sigma_{sum}^2 = I/M^2$ . However, the error for  $N$  separate measurements (assuming same monitor for each

run) is given by:

$$\sigma_{set}^2 = \sum_{n=1}^N \frac{M_n}{M} \left( \frac{I_n}{M_n} - \frac{I}{M} \right)^2 \quad (4.10)$$

For  $R = \sigma_{set}/\sigma_{sum} \sim 1$  the dataset is considered consistent. By plotting  $R$  for each point in  $Q$ , it is possible to identify the artificially large data point. An example of the inconsistent data can be seen in figure 4.27 for the (0 0.4 0.5) energy scan. Here the coloured markers with error bars are the counts from the seven different runs. The red markers connected by lines are the calculated  $R$  values for that energy. The point indicated by the arrow is one of the inconsistent points which were removed. It can be seen that for this energy  $R \sim 4$ . For the 11T dataset, any point which caused  $R > 3$  was removed. This meant the removal of seven points in total.

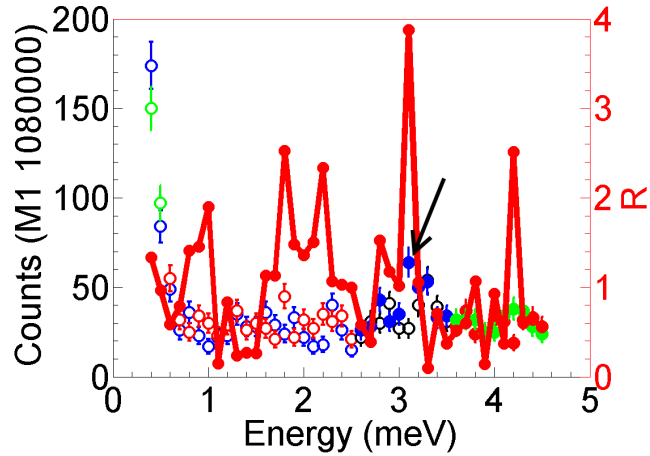


**Figure 4.27: Inconsistent point example for (0 0.4 0.5) energy scan.** Here the coloured markers with error bars represent the seven different runs performed. The red markers connected with lines indicate the calculated  $R$  value for that  $Q$  and energy. The inconsistent point which causes  $R \sim 4$  is indicated by the arrow.

The second step for the 11T dataset was to apply a correction to the measured

counts, due to the relative position of monitor M1 and the beryllium filter. If the beryllium filter is placed after the monitor M1 and fixed  $k_f$  setting is used on IN14, the measured detector counts must be multiplied by  $1+0.77999 k_i^{-2.3608}$ . This is because the monitor M1 is subjected to the second order neutrons whereas the detector is not. If M1 was not subjected to second order neutrons on the detector the counts divided by the monitor counts would provide a quantity proportional to scattering function  $S(Q,\omega)$ . However, if the M1 is subjected to second order neutrons, this is no longer the case. To get around this problem, the amount of second order neutrons is measured specifically for IN14, from this information the correction  $1+0.77999 k_i^{-2.3608}$  was established. This way the corrected detector counts divided by the monitor M1 counts will provide a quantity proportional to scattering function  $S(Q,\omega)$ .

The third correction was to account for the low A4 signal. As A4 angle decreases, the sample gets closer to the direct beam, thus the background increases. To find the A4 dependence in the data, first all the energy scans are plotted as a function of A4 as seen in figure 4.28(a) on page 184. Here the large jumps in intensity are due to the energy scan entering the incoherent signal at lower energies. In order to fit the A4 dependence clearly, all of the incoherent signal must be removed. Additionally, any spin-wave signal must be removed as well, so that the only remaining signal is from the background. With this in mind many of the data points are manually rejected leaving the A4 dependence which can be seen in figure 4.28(b). Here a Gaussian function centre  $A4=0^\circ$  is fitted and a height of 48 counts, with  $\text{fwhm}=28^\circ$  is obtained. From this fit it can be seen that the signal increase is most prominent at high energies for the scans with low Q, (0,0,0.5) and (0,-0.1,0.5). A similar A4 background probably also exists for the 14.5T dataset since they were both measured on IN14. However, in the 14.5T dataset, there are only a few measurements where A4 angle is low. In the few energy scans performed close to (0,0,0.5) there

is no obvious indications of a low-A4 signal. For the 10T datasets there are a few measurements where low-A4 could be a problem. However, in this case the background is subtracted by using a zero field measurement. Therefore, low-A4 signal contribution is not considered for the 14.5T and 10T dataset.

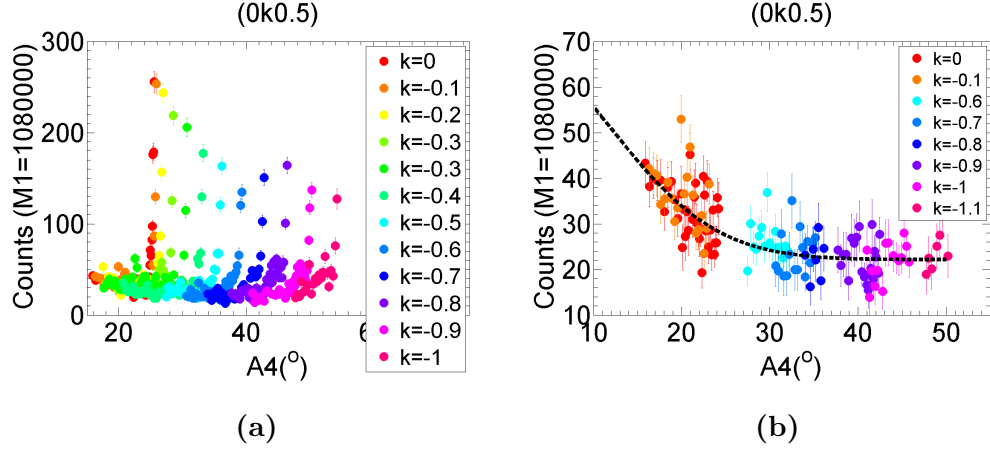


**Figure 4.28: Fitting  $A_4$  dependence of the 11T dataset. (a)**

All of the energy scans are plotted as a function of  $A_4$ . (b) All of the incoherent and spin-wave signal is removed to give the background's dependence on  $A_4$ . A Gaussian centred around  $A_4=0^\circ$  is fitted and a fit with height of 48 counts, with  $\text{fwhm}=28^\circ$  is obtained.

### 4.3.3 Experimental Results

The 11T and 14.5T datasets were obtained on IN14, where the low energy part of the dispersion was accessed. The 10T datasets was performed at IN20, where much higher energies could be accessed.

The 14.5T dataset performed on IN14 is the most useful dataset as at this field strength, the spin-wave is sufficiently lifted above the incoherent line. Energy scans performed at different points along  $(0, k, 0.5)$  show a clear excitation around 1meV which can be seen in figure 4.29(a) on page 186. The numerous Q scans were

performed to follow this excitation towards higher energies which can be seen in figure 4.29(b). Here the colour represents the number of counts in a monitor of M1=1080000 and the colour to counts conversion is indicated in the colour bar. The dispersion was also measured along  $(00l)$ , which can be seen in figure 4.29(c). Here, having a minimum at  $(0,0,0.5)$  instead of  $(001)$  indicates that coupling along this direction is of AFM nature. The measurement at  $(001)$  was performed at two field strengths which can be seen in figure 4.29(d).

The dispersion was also measured along  $(0,k,1)$  with an energy scan and Q scan. These can be seen in figures 4.30(a) and (b) respectively on page 187.

The 11T data required some treatment before being viewed. This treatment is clearly identified in section 4.3.2. In the 11T data there appears to be two different excitations. One of these excitations is similar to the spin-wave dispersion observed in the 14.5T dataset. The second is a lower energy excitation, which is visible in the vicinity of  $(0,-0.9,0.5)$  at 1meV. In figure 4.31(a) on page 188, the energy scans after these various corrections can be seen. Here, the low energy excitation around  $k=-0.9$  at 1meV can be seen clearly; however, the spin-wave like dispersion is not easily identified. There are only two energy scans where the dispersion can be seen; these are the  $k=-0.3$  and  $k=-0.4$  scans at 1.5meV and 3meV respectively. The spin-wave like dispersion can be identified easily with the performed Q scans which can be seen in figure 4.31(b). The energy scans for different  $(00l)$  can be seen in figure 4.31(c). In all of these energy scans there seems to be two peaks, unlike the 14.5T dataset. The first peak most likely corresponds to the excitation which was also observed in the 14.5T data. Perhaps the second peak in these scans belong to the same excitation which is observed at  $(0 -0.9 0.5)$  1meV. In figure 4.31(d) an important feature of the spin-wave like dispersion can be seen: two clear modes instead of one. Even though a clear separation can only be made at this Q scan, other Q scans do have features which appear like a second spin-wave branch. This second branch most

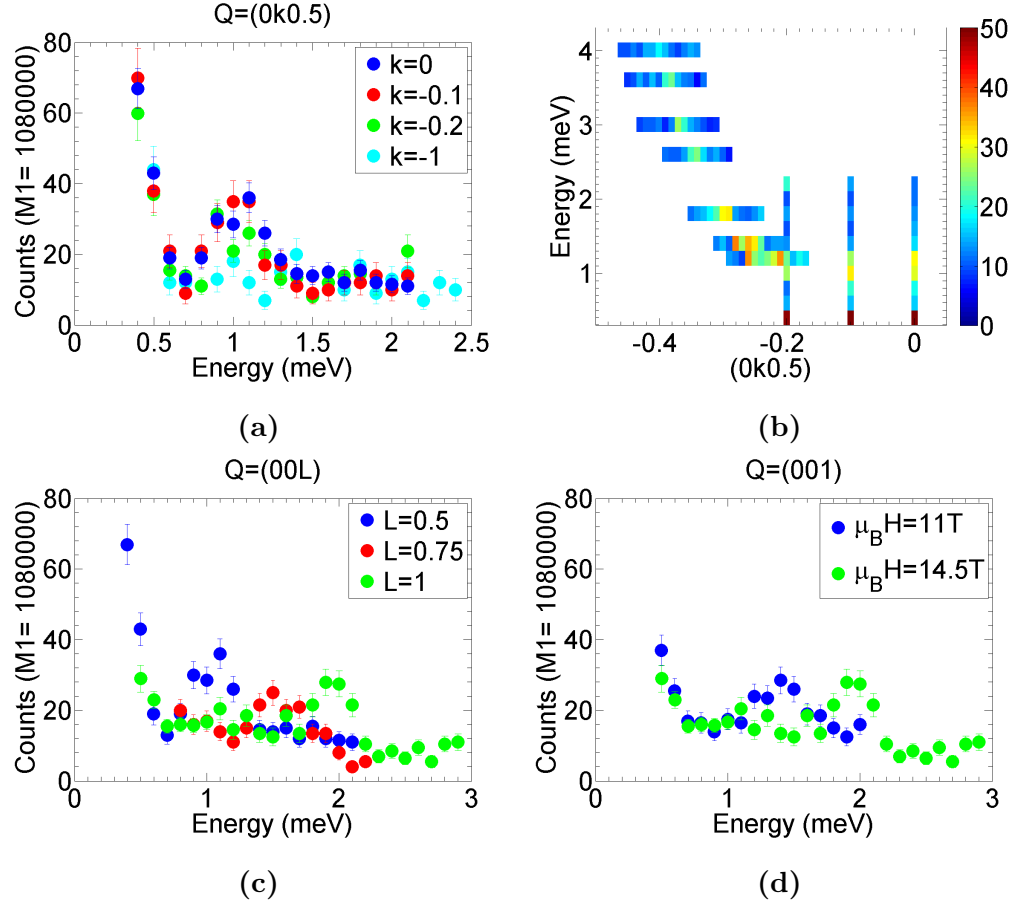


**Figure 4.29: 14.5T INS dataset.** (a) There is a clear excitation at  $\sim 1$  meV at  $k=0$  to  $k=-0.2$ . (b) Numerous  $Q$  scans show that this excitation branch continues to 4 meV at  $k=-0.4$ . (c) Measurements along  $(00l)$  highlight an AFM inter-chain interaction. (d) Energy scans performed at  $(001)$  but at different field strengths.

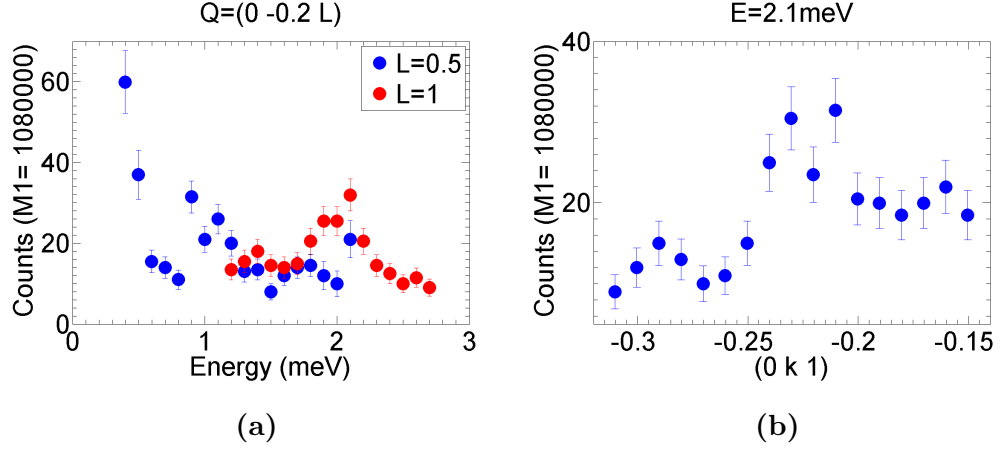


**Figure 4.30: 14.5T INS dataset, other directions.** The dispersion was also measured along  $(0,k,1)$  with (a) energy and (b) Q scans.

likely originates from the crystal twin. The dispersion for the twin would be close to  $\sim(0.453 -k -0.5)$ . The nearest Cu-Cu distance along the  $\mathbf{a}$  axis direction is much larger than along the  $\mathbf{b}$  or  $\mathbf{c}$  axis direction. Furthermore, along the  $\mathbf{a}$  axis direction the Cu atoms are separated by Sulphur and Lead atoms. Therefore, a very small exchange coupling constant along the  $\mathbf{a}$  axis direction is expected. This would result in very similar spin-wave energies for  $(0.453, -k, -0.5)$  and  $(0, k, 0.5)$  dispersions. Since the volume fractions of twins should be identical, the two branches should also have similar intensities. These two points combined make a very good argument that the secondary dispersion originates from the twin crystal.

In figure 4.32(a) on page 190 the excitations around  $(0, -0.9, 0.5)$ , 1meV can be seen in more detail. These excitations seem to have a maximum at  $\sim 1\text{meV}$  and highest in energy at  $k=-0.9$ . These excitations appear to be slightly broader compared to the 14.5T  $(0,0,0.5)$  excitations (figure 4.29(a)). Additionally, these 11T excitations in figure 4.32(a) appear asymmetric, with more intensity in the positive energy direction. This measurement of the broad excitation near  $k=-0.9$  could not be reproduced in a later experiment. The first measurement was performed on the

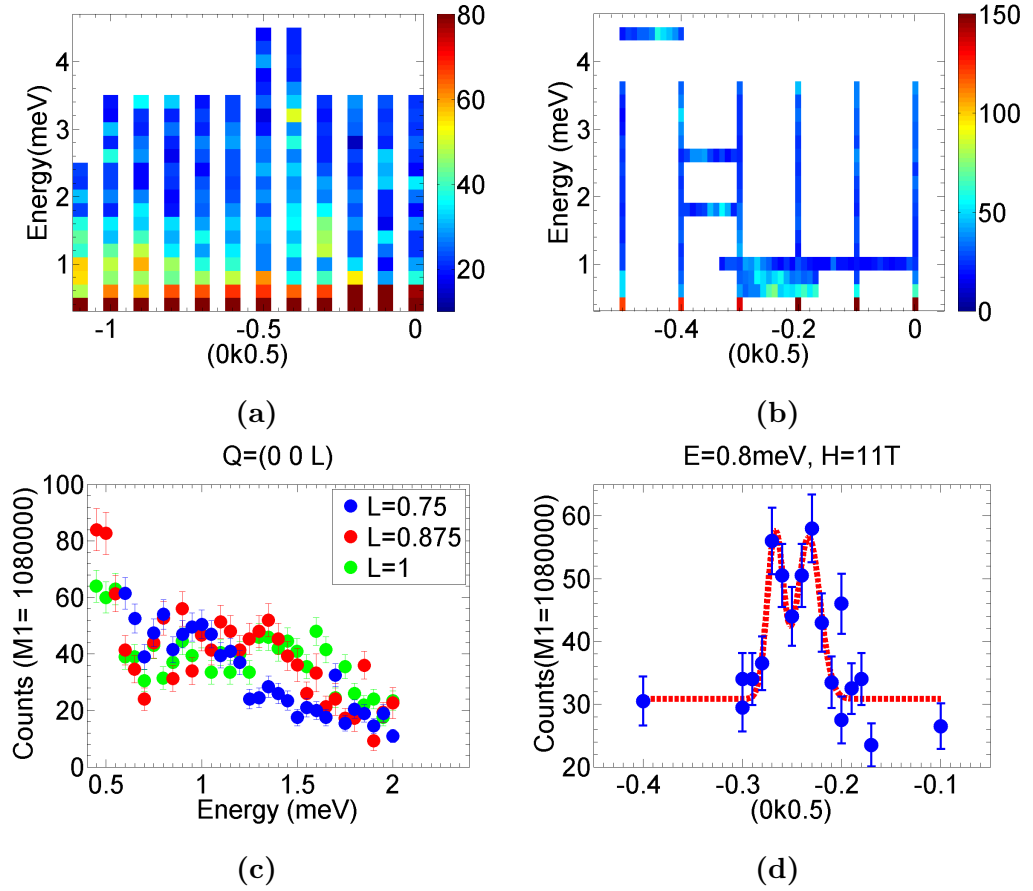


**Figure 4.31: 11T INS dataset after necessary corrections.** (a) Energy scans show two different excitations. The first is similar to the excitations observed for 14.5T dataset and are visible at  $k=-0.4$ , 3meV and  $k=-0.2$ , 1.5meV. The second excitation is a broad excitation visible around  $k=-0.9$ , 1meV. (b) The spin-wave like excitation can be seen very clearly from the  $Q$  scans. (c) Scans along  $(00l)$  show two peaks, which could originate from the two different excitations seen previously. (d) In this scan two clear excitations instead of one can be seen.

12T vertical cryomagnet on March 2013. The second measurement was performed on April 2013 on the 15T vertical cryomagnet (this is the experiment where the



majority of the 14.5T dataset was obtained). Both measurements were performed at the same temperature of 1.7K and field strength of 11T at IN14 with very similar experimental conditions. These two measurements can be seen in figure 4.32(b). No scaling is performed between the datasets; however, the experimental conditions were very similar and therefore very similar signal to background ratio is expected. Here it can be seen that in the IN14 April 2013 data there is no excitation at  $(0, -0.9, 0.5)$  around 1meV. There are two major differences between the two experiments. In the March 2013 experiment there are three crystals, crystals 1a, 1b, and 2, but in the April 2013 there are only two crystals, crystals 1b and 2. The  $(0, -0.9, 0.5)$ , 1meV signal could be unique to the Crystal 1a which was only measured in March 2013. The second major difference is orientation. As mentioned in section 4.2, crystals were aligned well along  $\mathbf{b}^*$  axis direction but not so well along  $\mathbf{c}^*$  axis direction. In the IN14 April 2013 data, the (001) Bragg peak roughly halves in intensity at high fields, which could correspond to both crystals moving by  $\sim 2^\circ$  or by only one crystal moving more than  $5^\circ$ . If both crystals have rotated by  $\sim 2^\circ$ , this should not cause a large change in the INS spectrum. If only one crystal moved more than  $5^\circ$ , this would require the other crystal to not move. Therefore, there should still be some remnant of the  $(0, -0.9, 0.5)$ , 1meV signal. Regardless, the  $(0, -0.9, 0.5)$ , 1meV signal could not be reproduced experimentally with what should be very similar conditions. Since its origin is unknown, it will not be considered any further in this thesis.

A similar observation can be made for the (001) energy scan. The (001) energy scan at 11T was also repeated in the later experiment (the experiment of the 14.5T dataset). The initial (001) measurement (figure 4.31(c), green) shows an unclear signal which is most likely composed of two excitations centred at 1meV and 1.4meV. The second measurement at a later date (figure 4.29(d), blue) shows a clear single excitation centred at 1.4meV. Therefore, the signal centred around 1meV in the

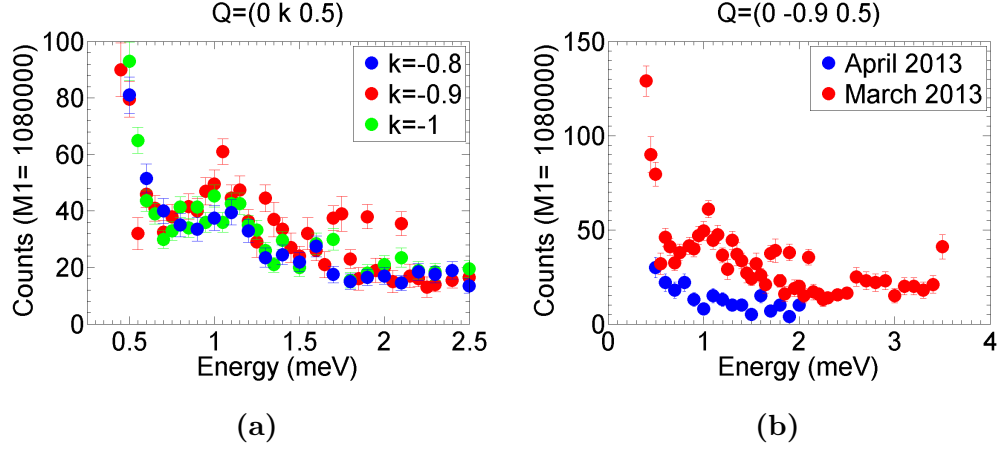


**Figure 4.32: 11T, (0,-0.9,0.5), 1meV signal.** (a) In the vicinity of (0,-0.9,0.5), an asymmetric broad excitation can be seen. (b) This excitation disappears in the April 2013 experiment.

first (001) 11T measurement (figure 4.31(c), green) is most likely related to the (0,-0.9,0.5) 11T 1meV signal.

In order to measure the higher energy part of the dispersion, measurements were made on IN20 using a 10T magnet. The resulting Q scans can be seen in figure 4.33 on page 191. Measurements were performed along  $(0,k,0.5)$  and  $(0,k,1.5)$  and are shown in figures 4.33(a) and (b) respectively. Here the 10meV scan in figure 4.33(a) was performed in the vicinity of  $k=-1.4$  but for simplicity the  $k+2$  value is stated instead. The higher energy scans show a larger, sloped background which makes it difficult to identify the position of the excitation. Therefore, for energies above 10meV, measurements were performed at 0T and 10T. This can be seen 4.33(c) where 0T and 10T data are shown using squares and circles respectively. The 0T measurements can be used as a background for the 10T data. Here the assumption has been made that there is no magnetic signal at 0T in 13meV and higher. This assumption can be justified by later experiments which will be shown in section 4.4. In this section it will be shown that at 0T, the magnetic excitations lose their

intensity very rapidly and cannot be easily identified above background for energies above 1.5meV.

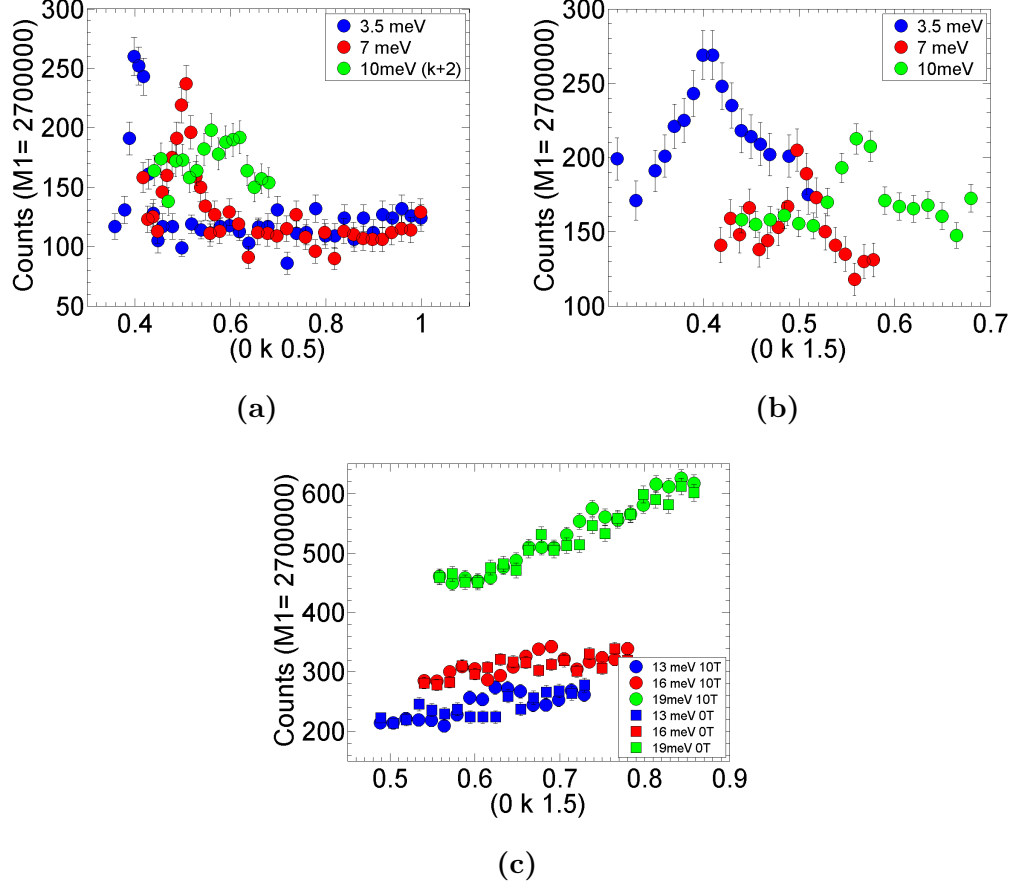


**Figure 4.33: 10T INS measurements.** Excitations were measured along (a)  $(0, k, 0.5)$  and (b)  $(0, k, 1.5)$  directions. (c) At higher energies measurements were performed at 0T and 10T shown in squares and circles respectively.

#### 4.3.4 Analysis

In this section the measured spin-wave excitations will be compared to linear spin-wave theory models. Fits to  $J$  parameters will be obtained for such models.

The initial challenge is to identify the positions of spin-wave excitation using the Q and energy scans. For each scan, a fit to a Gaussian function was performed. The peak position obtained from this fit is later on used in the linear spin-wave fit. An example of a Q scan and an energy scan fit can be seen in figure 4.34(a) and (b) respectively on page 193. Here it can be seen that for the Q scan a constant background has been assumed. For all Q scan fits, this background is kept as a free parameter. For the energy scans the background is more complicated. For all energy scans there is a large signal centred at  $E=0$  which corresponds to the incoherent signal. To model this, each energy scan is fitted using two Gaussian functions and a constant background. The centre of one of the Gaussians is fixed with  $E=0$ . One of the Q scans shows two clear peaks instead of one. For this scan two Gaussian functions are used to describe each peak, and the fit can be observed in figure 4.31(d). A more complicated method was required for obtaining the background for the 10T dataset's, 13meV, 16meV and 19meV Q scans. For these energies measurements were taken at 0T and 10T. The 0T measurements were fitted using a constant and linear background. The parameters obtained from 0T were used to describe the 10T Q scan's background. Similarly as the other Q scans, a Gaussian function was used to find the peak centres. The fit performed on the 13meV Q scan can be seen in detail in figure 4.34(c). Here the 0T and 10T measurements are given in red and blue respectively.

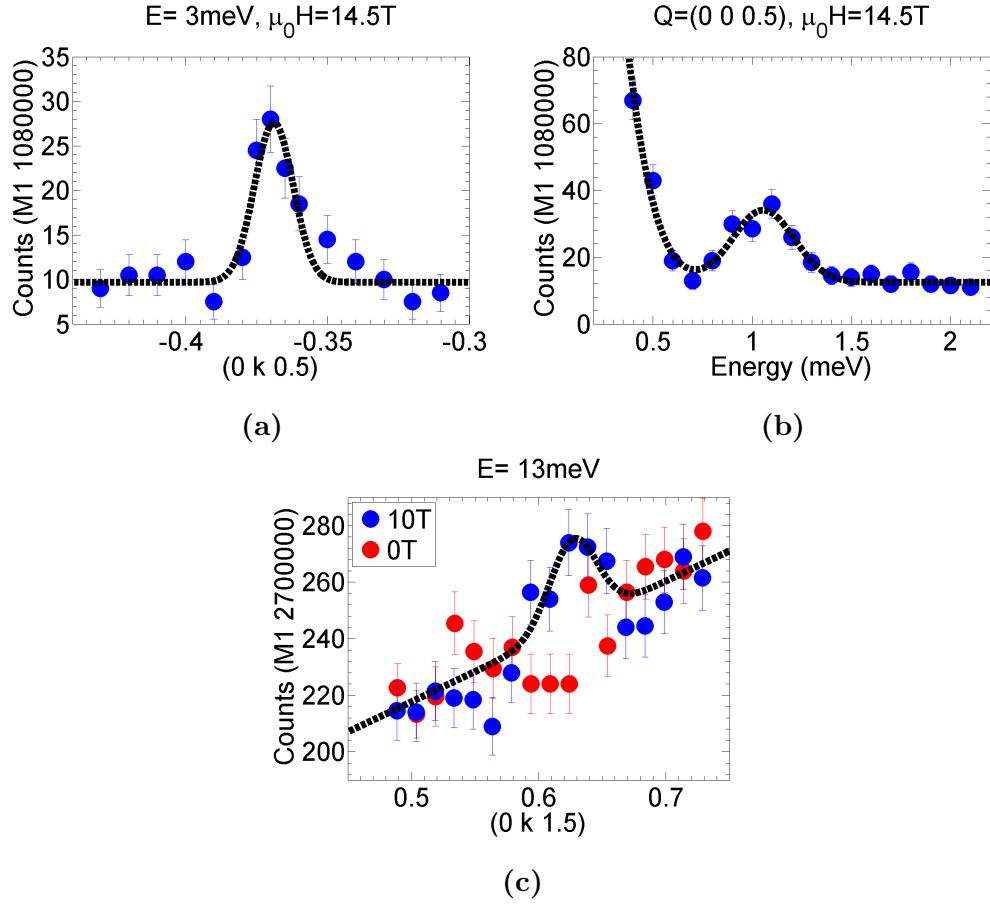


**Figure 4.34: Finding the position of spin-wave excitations.** (a) Q scans were fitted with a constant background and a Gaussian function. (b) The energy scans required an additional Gaussian function centred about  $E=0$  to consider the incoherent signal. (c) The high energy Q scans of the 10T dataset required a sloped background. This background was fitted using the 0T data (red).

There are 32 different excitation positions identified via fits to such Q or energy scans, as shown in figure 4.34. The full table of these fits can be seen in tables 4.9 and 4.10 on pages 194 and 195 respectively. Here the 11T (001) scan is given with an asterisk, as this measurement was made with the experiment of the 14.5T

dataset. Also the 9.5T measurement belongs to the 10T dataset experiments.

$\mu_B H$ (Tesla)	E (meV)	(0 k 0.5)	$\Delta k$
11	0.65	-0.2453	0.0016
11	0.8	-0.2662	0.0022
11	0.8	-0.2322	0.0021
11	1	-0.2797	0.0024
11	1.8	-0.3346	0.0019
11	2.5	-0.3695	0.0019
11	4.5	-0.4335	0.0016
14.5	1.4	-0.2606	0.0017
14.5	1.8	-0.2985	0.0016
14.5	2.5	-0.3480	0.0016
14.5	3	-0.3687	0.0016
14.5	3.5	-0.3869	0.0021
14.5	4	-0.4040	0.0021
9.5*	3.5	0.4096	0.0011
10	3.5	0.4067	0.0011
10	7	0.5007	0.0020

**Table 4.9: Fits to Q and energy scans of 10T, 11T and 14.5T datasets (part 1).** Here the 9.5T measurement with the asterisk belongs to the 10T dataset.

$\mu_B H$ (Tesla)	<b>Q</b>	<b>E (meV)</b>	<b><math>\Delta E</math> (meV)</b>
11	(0 -0.3 0.5)	1.262	0.020
11	(0 -0.4 0.5)	3.275	0.014
14.5	(0 0 0.5)	1.055	0.016
14.5	(0 -0.1 0.5)	1.013	0.020
14.5	(0 -0.2 0.5)	1.039	0.034
14.5	(0 0 0.75)	1.556	0.036
14.5	(0 0 1)	1.952	0.019
11*	(0 0 1)	1.386	0.035
14.5	(0 -0.2 1)	2.007	0.024
$\mu_B H$ (Tesla)	<b>E(meV)</b>	<b>(0 k 1)</b>	<b><math>\Delta k</math></b>
14.5	2.1	0.2228	0.0034
$\mu_B H$ (Tesla)	<b>E (meV)</b>	<b>(0 k 1.5)</b>	<b><math>\Delta k</math></b>
10	3.5	0.4076	0.0035
10	7	0.5023	0.0026
10	10	0.5626	0.0029
10	13	0.6272	0.0067
10	16	0.6790	0.0050
10	19	0.7351	0.0057

**Table 4.10: Fits to Q and energy scans of 10T, 11T and 14.5T datasets (part 2).** Here the 11T measurement with the asterisk belongs to the 14.5T dataset.

Now that the position of the spin wave is known at 32 different points, it is possible to compare these positions to theoretical spin-wave models and obtain a fit. In order to obtain the best fitting parameters for a given theoretical model, chi-squared minimisation algorithms are used. The  $\chi^2$  was defined in the following

form:

$$\chi^2 = \chi_Q^2 + \chi_E^2 \quad (4.11)$$

$$\chi_Q^2 = \sum_n \frac{(Q_n - Q_{theory}(E_n))^2}{(\Delta Q_n)^2}, \quad \chi_E^2 = \sum_m \frac{(E_m - E_{theory}(Q_m))^2}{(\Delta E_m)^2} \quad (4.12)$$

Here  $\chi_Q^2$  and  $\chi_E^2$  are contributions from Q scans and energy scans respectively. The measured spin-wave position is given by  $Q_n$  with an error of  $\Delta Q_n$  for the  $n$ 'th Q scan performed at energy  $E_n$ . Similarly, the measured spin-wave position is given by  $E_m$  with an error of  $\Delta E_m$  for the  $m$ 'th energy scan performed at position  $Q_m$ . The position of the theoretical model is given by  $Q_{theory}$  and  $E_{theory}$ . Assuming a single magnon branch,  $E_{theory}(Q_m)$  has a unique value for any value of  $Q_m$ . However,  $Q_{theory}(E_n)$  does not have a valid value for energies above or below the magnon excitation. In these regions, the  $\chi^2$  is set to a large constant. This way, the minimisation algorithm will avoid entering these invalid regions.

Using linear spin-wave theory, it is possible to create models to apply to the data. For simplicity, it will be assumed that the two Cu sites in linarite are equivalent. Therefore, in the fully saturated phase, there is only one site per magnetic unit cell. For the moment, it will also be assumed that all interactions are isotropic. Anisotropic models will be considered later on in this section. The interaction scheme used can be seen in figure 4.35 on page 197. Here  $J_1$  and  $J_2$  are nearest and next nearest interactions along the **b** axis direction respectively. In the **bc** plane, the spin chains are coupled by a skew interaction  $J_{c0}$  and a diagonal interaction  $J_{c1}$ . Along the **a** axis, another skew inter-chain interaction  $J_a$  is considered. From the experimental data it should be possible to obtain a unique solution to these parameters. Any additional interaction beyond this model would correspond to large distances, and therefore the effects of such an interaction should be very small.



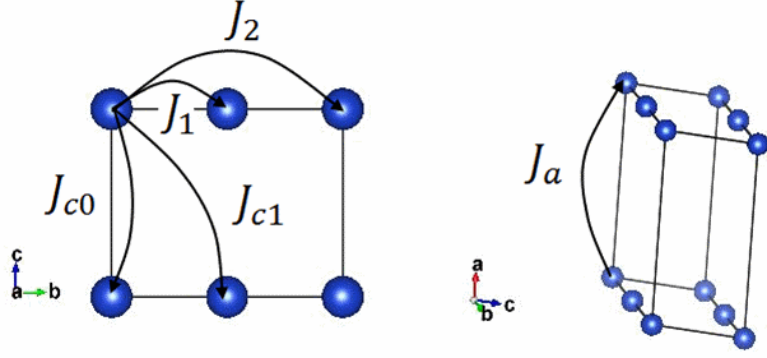


**Figure 4.35: Interaction scheme of Linarite.**

The magnon dispersion for a ferromagnetic structure with  $\mathbf{H} // \mathbf{a}$  is given by equation 4.13 below [58]:

$$\hbar\omega(\mathbf{q}) = 2S[\mathcal{J}(0) - \mathcal{J}(\mathbf{q})] + g_a\mu_B H \quad (4.13)$$

Here  $\mathcal{J}(\mathbf{q})$  is the Fourier transform of the exchange integral and it has the form [58]:

$$\sum_{\mathbf{q}} \mathcal{J}(\mathbf{q}) = \sum_{\boldsymbol{\rho}} J(\boldsymbol{\rho}) e^{i\mathbf{q}\boldsymbol{\rho}} \quad (4.14)$$

Using the interaction scheme in figure 4.35, this becomes:

$$\mathcal{J}(\mathbf{q}) = J_1 \cos(\pi k) + J_2 \cos(2\pi k) + J_{c0} \cos(2\pi l) + 2J_{c1} \cos(2\pi l) \cos(\pi k) + J_a \cos(2\pi h) \quad (4.15)$$

Therefore, the spin-wave dispersion becomes:

$$\begin{aligned} \hbar\omega(\mathbf{q}) = & -J_1 \cos(\pi k) - J_2 \cos(2\pi k) - J_{c0} \cos(2\pi l) - 2J_{c1} \cos(2\pi l) \cos(\pi k) - J_a \cos(2\pi h) \\ & + J_1 + J_2 + J_{c0} + 2J_{c1} + J_a + g_a\mu_B H \end{aligned} \quad (4.16)$$

It is important to note that the crystals used for these experiments were twinned. Therefore, one would expect two different spin-wave dispersions to appear,  $\hbar\omega$  and  $\hbar\omega_t$ . Here the dispersion of the twin is given by:

$$\hbar\omega_t(\mathbf{q}) = 2S[\mathcal{J}(0) - \mathcal{J}(\mathbf{q}_t)] + g_{a'}\mu_B H \quad (4.17)$$

Here  $g_{a'}$  and  $\mathbf{q}_t$  account for the slightly different orientation of the twinned crystal with respect to the magnetic field and scattering plane. Since the geometry of the twinning is known,  $\mathbf{q}_t$  can be obtained from  $\mathbf{q}$ . The twinning corresponds to a  $180^\circ$  rotation about the  $\mathbf{a}^*$  axis. The following relation can be derived if starting with a right handed coordinate system where  $\mathbf{a}^*//\hat{\mathbf{x}}$  and  $\mathbf{b}^*//\hat{\mathbf{y}}$ :

$$\mathbf{q}_t = \mathbf{q} \begin{pmatrix} 1 & 0 & 0 \\ 0 & -1 & 0 \\ -\frac{2a}{c}\cos(\beta) & 0 & -1 \end{pmatrix} \quad (4.18)$$

Using the lattice parameters from the Effenberger-Araki structure  $-\frac{2a}{c}\cos(\beta) = 0.906$  is obtained. Considering the twin in a spin-wave fit requires some care. There is only one Q scan (0.8meV 11T Q scan) where both dispersions can be individually identified (figure 4.31(d)). Upon careful inspection, it is possible to see that in the 11T, 0.65meV Q scan only the lower branch can be identified. The second higher branch must be almost parallel to  $\mathbf{q}$  at this energy, therefore its intensity spread out in this scan. Assuming  $J_a$  is ferromagnetic,  $\hbar\omega_t$  would reside above  $\hbar\omega$  along  $q = (0, k, 0.5)$ . This assumption must be valid since at zero field, the ground state magnetic structure has a propagation vector  $q = (0, k, 0.5)$ . It is important to note that this same propagation vector of  $q = (0, k, 0.5)$  was measured in untwinned crystals as well (see section 4.5). Therefore, this magnetic Bragg peak at  $q = (0, k, 0.5)$  corresponds to the true crystal and not to the twin crystal, i.e. the magnetic propagation vector cannot be  $q \sim (-0.453, k, 0.5)$ . This gives us one direct data point for  $\hbar\omega_t$  and two for  $\hbar\omega$ . The remaining 29 other points cannot be simply fitted to  $\hbar\omega$  or  $\hbar\omega_t$ . Therefore, the remaining points were fitted to the average of the two excitations  $(\hbar\omega + \hbar\omega_t)/2$ . There are a number of justifications for this. During

the sample characterisation process, Bragg peaks of both the twins were measured using neutron diffraction. The observations from these measurements are consistent with similar sized twin volumes (see section 4.2). If the twin volumes are roughly the same, spin-wave branches should be of similar intensity for both  $\hbar\omega$  and  $\hbar\omega_t$ . In fact, in the Q scan where the two excitations can be identified (figure 4.31(d)), the intensity of the branches are very similar, in agreement with the equal twin-volume concept. Therefore, using the average magnon dispersion to obtain a fit should be sufficiently accurate.

In section 4.2, the orientations of each crystal in the three main inelastic neutron experiments were detailed. For the 11T and 14.5T datasets the crystals were most likely within  $\sim 5^\circ$ ; however for the 10T dataset, one of the crystals was as much as  $\sim 10^\circ$  out of plane. Additionally, the knowledge of the orientations is not from the same experiment but relies on previous experiments. The only true information is that for each experiment at least one crystal was sufficiently in plane to provide a Bragg peak at (001). An ideal spin-wave model should incorporate the orientation of each crystal. For example the crystal which was  $\sim 10^\circ$  out of plane might have a sufficiently different  $g$  factor than the others. Such a model would have too many parameters to fit and they would be based on incomplete orientational information. For this reason, it will be assumed that all of the crystals are perfectly within the ( $0kl$ ) plane.

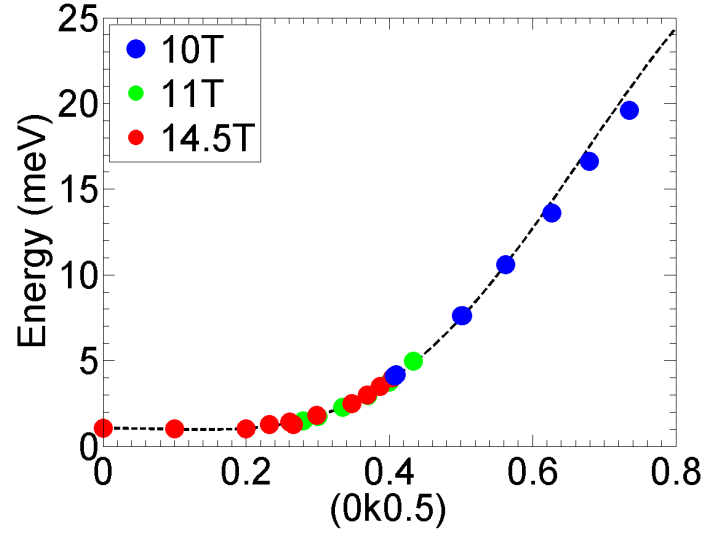
This twinned spin-wave model has seven free parameters (5  $J$  parameters,  $g_a$  and  $g_{a'}$ ) which can be fitted to the 31 data points obtained from Q and energy scans. The fitting parameters displayed a strong level of correlation. Some minimisation routines do not consider correlation between parameters which can lead to incorrect confidence intervals of the parameters. For the minimisation of  $\chi^2$  the MINUIT [120] software package was used through its MATLAB interface fminuit [121]. The best fit to the isotropic-exchange and twinned linarite model has a  $\chi^2$  of 101, the values

of the parameters and their confidence intervals can be seen in table 4.11. The consideration of the correlation also results in a very small confidence interval for  $\alpha = J_2/J_1$ . In a  $\chi^2$  where the  $\alpha$  parameter is refined instead of  $J_2$ ,  $\alpha=-0.275(1)$  can be obtained. Note that amongst the inter-chain interactions,  $J_{c0}$  is dominant. The other inter-chain interactions  $J_{c1}$  and  $J_a$  are very close to zero. One can also notice that both  $g_a$  and  $g_{a'}$  have relatively large error bars as well. However, if the average  $g_{avg} = (g_a + g_{a'})/2$  is refined instead of  $g_a$  one can see that it has a much smaller confidence interval of  $g_{avg} = 2.36(3)$ .

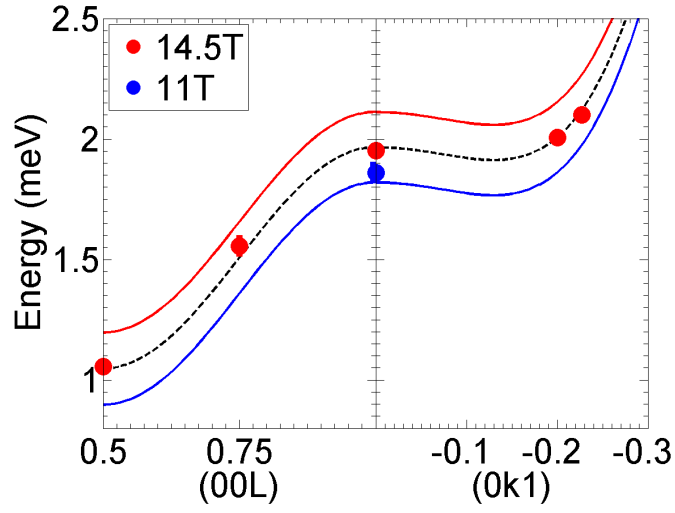
Parameter	$J_1$	$J_2$	$J_{c0}$	$J_{c1}$	$J_a$	$g_a$	$g_{a'}$
Value	14.5(1)	-3.99(4)	-0.6(1)	0.06(3)	0.04(17)	2.25(24)	2.47(29)

**Table 4.11:** The isotropic-exchange spin-wave fit result for linarite above saturation.

The comparison between the fit and the data can be seen in figure 4.36 on page 201 for different Q directions. The majority of the data was taken along  $(0,k,0.5)$  direction, which can be seen in figure 4.36(a). Here the red, green and blue data sets represent spin-wave measurements made at 10T, 11T and 14.5T respectively. The 10T and 11T datasets have been lifted up in energy by  $g_{avg}\mu_B(14.5\text{-H})$  for the purpose of clarity. The black dashed line is the average of  $\hbar\omega$  and  $\hbar\omega_t$ , calculated using the values from table 4.11. Almost all of the data is fitted to this average spin-wave because the individual dispersions cannot be resolved. In figure 4.36(b) the dispersion measured along  $(00l)$  and  $(0k1)$  can be seen. Here the blue and the red lines correspond to dispersions of  $\hbar\omega$  and  $\hbar\omega_t$  respectively. The suggested fit to the model must be unique since it is composed of three different directions and the twinning essentially provides another additional direction of  $\sim(0.453,k,0.5)$ .



(a)



(b)

**Figure 4.36: The spin-wave fit to saturated data.** (a) the fit along the  $(0,k,0.5)$  direction is given by the black dotted line which is the average of  $\hbar\omega$  and its twin  $\hbar\omega_t$ . The 10T and 11T data are lifted in energy by  $g_a\mu_B(14.5-H)$ . (c) The fit to the dispersion along  $(00l)$  and  $(0k1)$  was made using 14.5T data. Here  $\hbar\omega$  and its twin  $\hbar\omega_t$  are given in blue and red respectively.

It is necessary to take a closer look at the lower energy part of the dispersion along  $(0,k,0.5)$  to see the good agreement the twinned model brings. In figure 4.37 on page 203 and figure 4.38 on page 204, the 11T and 14.5T Q scan intensity colour maps can be seen with the fitted dispersion and the data points used for the fit. Here  $\hbar\omega$  and its twin  $\hbar\omega_t$  are given in blue and red respectively and their average is given in the black dashed line. In figure 4.37 at 0.65meV and 0.8meV are the only three points which were fitted to either  $\hbar\omega$  or  $\hbar\omega_t$  and not their average. Aside from being a relatively good fit, this model manages to explain some of the intensity features in the Q scans. In figure 4.37 at 0.65meV at  $k \sim 0.185$  the intensity feature in the colour map agrees perfectly with the position of the  $\hbar\omega_t$  dispersion given in red. In the 14.5T dataset the 1.2meV Q scan has a two peak like feature; however, it could not be fitted with one or two Gaussians therefore it was omitted from the spin-wave fit. However, its intensity features are in perfect agreement with the expected this dispersions. This can be seen in figure 4.38, where at 1.2meV, the increased intensity at  $k \sim 0.21$  and  $k \sim 0.26$  agree perfectly with the positions of  $\hbar\omega_t$  and  $\hbar\omega$  respectively. The 1.4meV scan also shows some double peak features which are consistent with the twinning model.

The isotropic exchange parameter spin-wave model is successful in explaining many components of the data. It is a relatively simple model with few parameters. It has the added advantage that the calculations are much simpler because no anisotropy is considered. However, the model has three main shortfalls. The first shortfall is the lack of a good fit to the high energy points of 10T. In figure 4.36(a), it can be seen that the three highest energy points are lower than the results the spin-wave model expects. The addition of anisotropy to the spin-wave model could provide a better fit the 10T data. The second shortfall is to do with the value of the  $g$  factors. This isotropic model underestimates the value of the average  $g$  factor,  $g_{avg}$ . This is most apparent from the energy scans performed at  $(001)$ . At  $(001)$  there

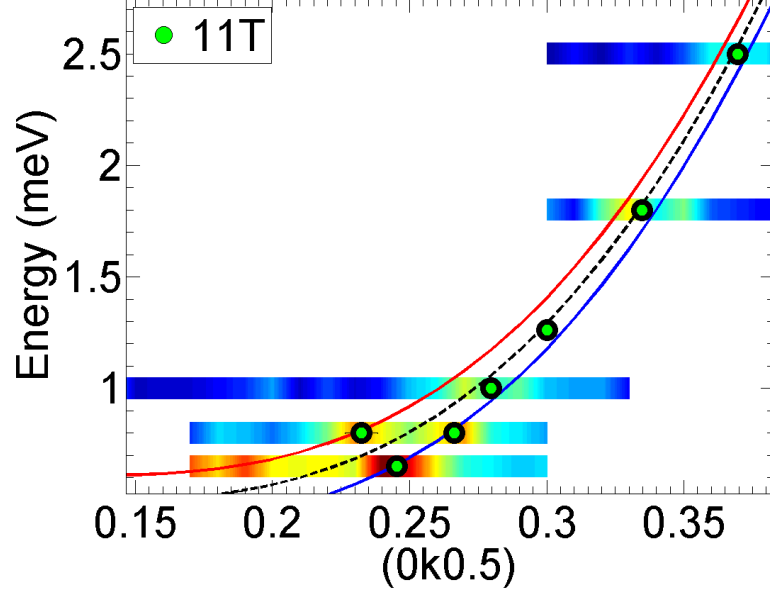


**Figure 4.37: The spin-wave fit to 11T data, visible twinning at low energies.** The 11T Q scans are presented as an intensity colour map. The green points are the fits to these Q scans and the blue, red and black lines are the obtained best fits to  $\hbar\omega$ ,  $\hbar\omega_t$  and their average respectively. The 0.65meV and 0.8meV data points are the only ones to be fitted to either  $\hbar\omega$ ,  $\hbar\omega_t$ . The twinned spin-wave model manages to explain some of the intensity features, such as the  $k \sim 0.185$  intensity feature at 0.65meV.

are two energy scans performed at different field strengths, one at 11T and another at 14.5T. It is important to note that both of these measurements were performed during the same experiment. The energy shift of the average dispersion from 11T to 14.5T is given by  $g_{avg}\mu_B(14.5 - 11)$ . If the  $g_{avg}$  was calculated solely based on these two measurements one would expect  $g_{avg}=2.79(2)$ . This is very different from the spin-wave fit of  $g_{avg}=2.36(3)$ . It is important to note that at room temperature  $g_a = 2.34$  was found by ESR measurements [26]. This ESR value supports the spin-

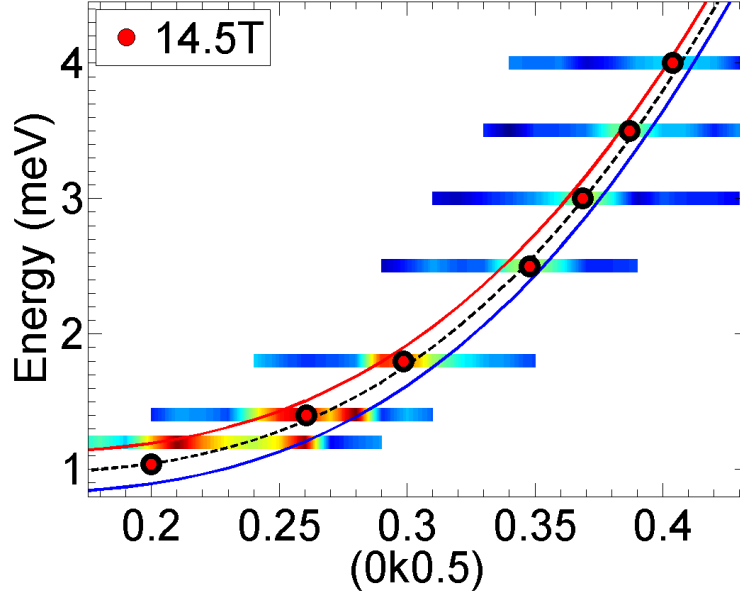


**Figure 4.38: The spin-wave fit to 14.5T data, visible twinning at low energies.** The 14.5T Q scans are presented as an intensity colour map. The red points are the fits to these Q scans and the blue, red and black lines are the obtained best fits to  $\hbar\omega$ ,  $\hbar\omega_t$  and their average respectively. The intensity features at 1.2meV,  $k \sim 0.21$  and  $k \sim 0.26$  can be explained by this spin-wave model.

wave fitted result rather than the  $g_{avg}=2.79(2)$  result. The third shortfall of the isotropic model comes from the estimation of the saturation field. A lower estimate for the saturation field can be obtained by considering the field strength for which the minimum of the magnon branch will touch zero energy. The minimum of the dispersion occurs at  $(0,k,0.5)$ , where  $\cos(\pi k) = (2J_{c1} - J_1)/(4J_2)$ . Depending on the choice of the  $g$  factor, three different saturation fields can be obtained at this position. With  $g_a=2.25(14)$ , a rather high saturation field of  $\mu_0 H^{sat} = 7.95\text{T}$  is found. By using the average  $g$  factor from the spin-wave fit,  $g_{avg}=2.36(3)$ , a lower saturation field of  $\mu_0 H^{sat} = 7.36\text{T}$  is obtained. If one uses the average  $g$  factor as obtained from



(001) energy scans,  $g_{avg}=2.79(2)$ , a much lower saturation field of  $\mu_0 H^{sat}=6.18\text{T}$  is obtained. Magnetisation measurements at  $T=1.8\text{K}$  have found a saturation field of  $\mu_0 H_{a^*}^{sat} \sim 7.6\text{T}$  [26]. Note that this estimate is for  $\mathbf{H}/\mathbf{a}^*$  rather than  $\mathbf{H}/\mathbf{a}$  used in this thesis work. However considering the difference in orientation is only  $12.65^\circ$ , the two directions should have similar saturation fields.

So far the spin-wave model considered has been isotropic. Earlier in the introduction it was discussed that linarite shows strong indications of anisotropy, and that this anisotropy cannot simply be attributed to the anisotropy of the  $g$  factor [26]. One way to consider the anisotropy is by introducing it in the exchange couplings matrices. The biggest contribution for the exchange anisotropy will come from the  $\mathbf{J}_1$  or  $\mathbf{J}_2$  matrices since they are the two largest interactions in the system. The anisotropy should also be of such form that it produces a helical magnetic structure at zero field. One of the simplest anisotropies which can be applied is an easy-axis anisotropy. Such an anisotropy can be introduced to  $\mathbf{J}_1$  and  $\mathbf{J}_2$  in the following way:

$$\mathbf{J}_1 = J_1 \begin{pmatrix} 1 & 0 & 0 \\ 0 & 1 & 0 \\ 0 & 0 & 1 - \Delta_1 \end{pmatrix}, \quad \mathbf{J}_2 = J_2 \begin{pmatrix} 1 & 0 & 0 \\ 0 & 1 & 0 \\ 0 & 0 & 1 - \Delta_2 \end{pmatrix} \quad (4.19)$$

Here the isotropic system corresponds  $\Delta_1 = \Delta_2 = 0$ . For  $\Delta_2=0$ , a positive  $\Delta_1$  will produce an easy-plane anisotropy, whilst negative  $\Delta_1$  will produce an easy-axis anisotropy. The calculations of the spin-wave which included these anisotropies were made using the SpinW programme [122]. To simplify the calculations, the unit cell was reduced to one Cu site along  $\mathbf{b}$  axis and  $\beta$  was changed to  $\beta = 90^\circ$  to create an orthorhombic system. Both  $\Delta_1$  and  $\Delta_2$  are along the  $\mathbf{z}$  axis. In linarite, this direction will correspond to the normal to the spin plane. From neutron diffraction results it is known that the spin plane is  $-27^\circ$  from the  $\mathbf{a}$  axis. It will be shown in section 4.6 that this result is in agreement with magnetisation measurements

performed for this thesis. In the INS experiments the field is applied along the  $\mathbf{a}$  axis, therefore the angle between the normal of the spin plane and the field direction is  $63^\circ$ . This angle is different for the twin crystal since the field is along the  $\mathbf{a}$  axis and not along  $\mathbf{a}_t$ . Therefore, for the twin, the angle between the normal of the spin plane and the field direction is  $-37.7^\circ$ . To consider this in the anisotropic spin-wave model, the field is applied  $63^\circ$  from the  $\mathbf{z}$  axis and for the twin the field is applied  $-37.7^\circ$  from the  $\mathbf{z}$  axis. For both cases the magnetic structure is chosen such that the spins are parallel to the respective field direction.

Before the anisotropic models are used, the SpinW model is tested for the isotropic case of  $\Delta_1 = \Delta_2 = 0$ . The calculated SpinW dispersion is found to be identical to the analytical method described in this section. Two different anisotropic models were used for linarite. In the anisotropic  $\mathbf{J}_1$  model only  $\Delta_1$  was used and  $\Delta_2$  was set to zero. In the anisotropic  $\mathbf{J}_1 - \mathbf{J}_2$  model both  $\Delta_1$  and  $\Delta_2$  were refined. The minimisation of  $\chi^2$  was also performed using fminuit for these two models. For the anisotropic models, an additional constraint was used for fitting. It was assumed that at (001) the difference between  $\hbar\omega$  and  $\hbar\omega_t$  cannot be larger than 0.5meV. This is because the fits to the energy scans have a full width at half maximum of  $\sim 0.4$ meV. Therefore, to have any larger separation would not be in agreement with the data. The resulting fits to these models, as well as that of the isotropic model (which was solved analytically), can be seen in table 4.12 on page 212. One problematic feature of the anisotropic models is their large  $g_a$  values which are not realistic. Using SpinW, an attempt was made to calculate the saturation field for the anisotropic models. The smallest possible field where the spin-wave branches were still positive was found. For the anisotropic  $\mathbf{J}_1$  model and the anisotropic  $\mathbf{J}_1 - \mathbf{J}_2$  model, the saturation fields were found to be  $\mu_0 H^{sat} \sim 9.3$ T and 8.8T.

The comparison between data and the anisotropic model dispersions can be seen in figures 4.39 and 4.40 on pages 208 and 209 respectively. It can be seen that

neither anisotropic model is capable of explaining the two main problems discussed earlier in this section. The fit for the 10T, high energy points along  $(0,k,0.5)$  has not improved. The (001) 14.5T and 11T points are still a distance apart. Aside from this, the anisotropic models bring additional problems. At 14.5T, both anisotropic models predict very little splitting between the two branches along  $(0,k,0.5)$ . On the contrary, the data is consistent with considerable splitting between the two branches at 14.5T.

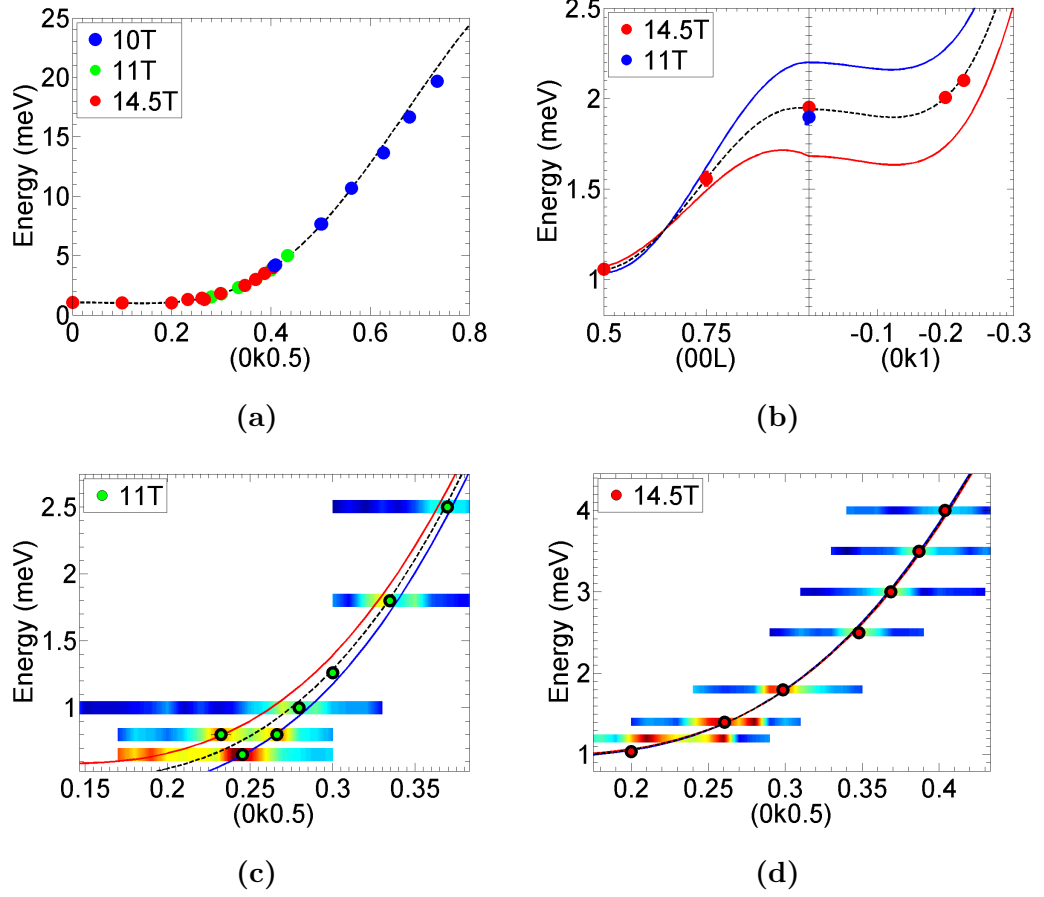


**Figure 4.39: The anisotropic  $J_1$  model fits.** (a) The average spin-wave dispersion along  $(0,k,0.5)$  can be seen in black dashed line calculated for 14.5T, with all data points energies lifted up to 14.5T by  $g_{avg}\mu_B(14.5 - H)$ . (b) For the  $(00l)$  and  $(0k1)$  directions the  $\hbar\omega$  and  $\hbar\omega_t$  dispersions are shown in blue and red respectively. The blue data point represents the 11T  $(001)$  measurement which has been lifted by  $g_{avg}\mu_B(14.5 - 11)$ . (c) The 11T dataset can be compared to the dispersion evaluated at 11T. (d) Similarly, the 14.5T dataset can be compared to the dispersion evaluated at 14.5T.

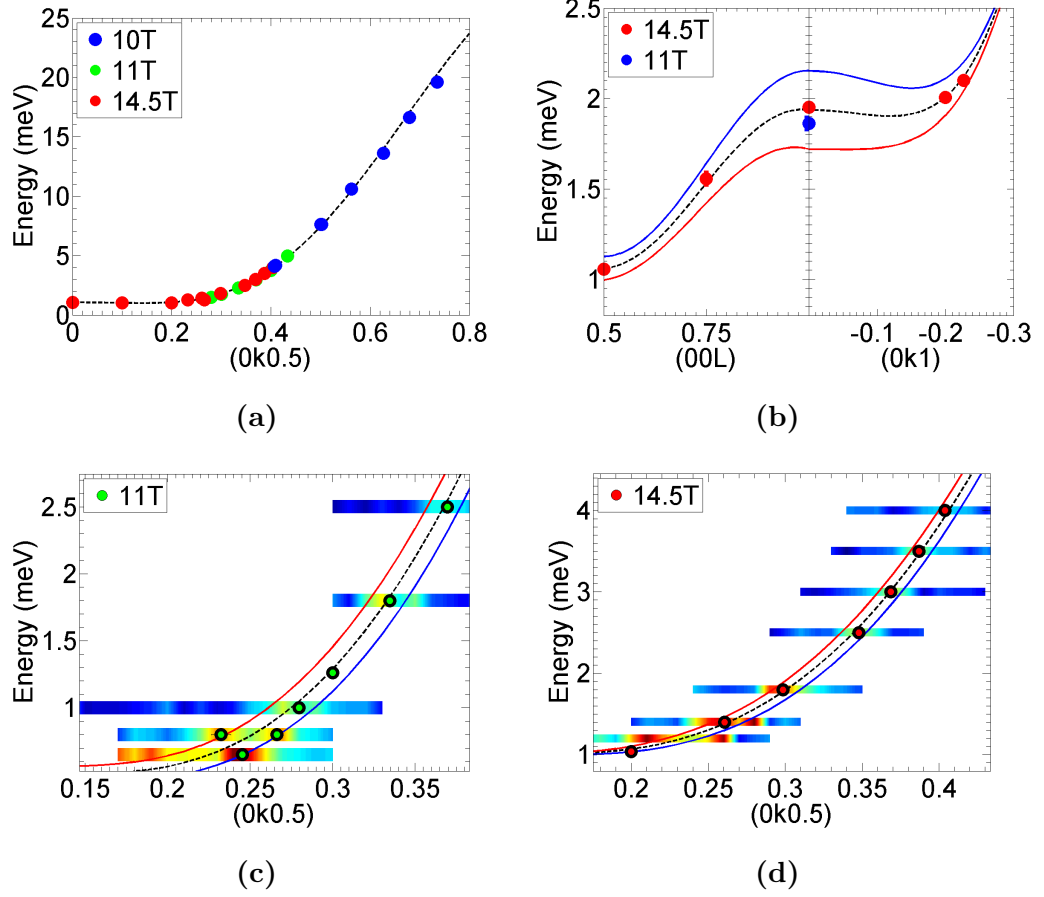


**Figure 4.40: The anisotropic  $J_1 - J_2$  model fits.** (a) The average spin-wave dispersion along  $(0,k,0.5)$  can be seen in the black dashed line calculated for 14.5T, with all data point's energies lifted up to 14.5T by  $g_{avg}\mu_B(14.5 - H)$ . (b) For the  $(00l)$  and  $(0k1)$  directions the  $\hbar\omega$  and  $\hbar\omega_t$  dispersions are shown in blue and red respectively. The blue data point represents 11T (001) measurement which has been lifted by  $g_{avg}\mu_B(14.5 - 11)$ . (c) The 11T dataset can be compared to the dispersion evaluated at 11T. (d) Similarly, the 14.5T dataset can be compared to the dispersion evaluated at 14.5T.

A second isotropic exchange model was created to try and address the main two

discrepancies observed so far. The first is the unexpected large energy shift from 11T to 14.5T observed at (001). In LWST, an isotropic exchange model will linearly increase in energy with increasing field strength. For this second isotropic model, this will not be the case. The  $g_a\mu_B H$  term will be removed from the spin-wave equation and will be replaced with  $\Delta E(H)$ . There are measurements at four different field strengths in total: 9.5T, 10T, 11T, and 14.5T. For each one of these datasets  $\Delta E(H)$  will be set as a free parameter. The second discrepancy observed so far is the inadequate description of high energy 10T data along (0, $k$ ,0.5). To address this issue this second isotropic exchange model will also have a third-nearest neighbour interaction along the **b** axis direction,  $J_3$ . The result of such a fit is tabulated in table 4.13 on page 212. A  $\chi^2$  fit of 36 is obtained from these ten parameters. When the strong correlation between  $J_1$  and  $J_2$  is considered the resulting ratio  $\alpha = J_2/J_1$  has a smaller confidence interval with  $\alpha=-0.259(4)$ . By looking at the four different  $\Delta E(H)$  values an interesting observation can be made. It would be expected that the spin-wave energy would always increase with increasing field strength; however, at 10T, the energy gain is larger than it is for the 11T dataset. Another interesting observation can be made by converting these four energies into an average  $g$  factor,  $g_{avg}$ , for each field strength. For 9.5T, 10T, 11T, and 14.5T field strengths,  $g_{avg}= 2.45(7), 2.49(6), 2.22(3), 2.31(2)$  values are obtained respectively. Each of the individual  $g$  factors are sensible on their own; however, it is not clear how they could change for different field strengths. The saturation fields based on these  $g$  factors are  $\mu_0 H^{sat}=7.5\text{T}, 7.3\text{T}, 8.2\text{T},$  and  $7.9\text{T}$  respectively.

The result of the second isotropic fit can be seen in further detail in figure 4.41 on page 211. Here it can be seen that this model tackles the previous two problems observed in other spin-wave fits. The high energy 10T data has a much better fit and the (001) data points at 11T and 14.5T are very close.

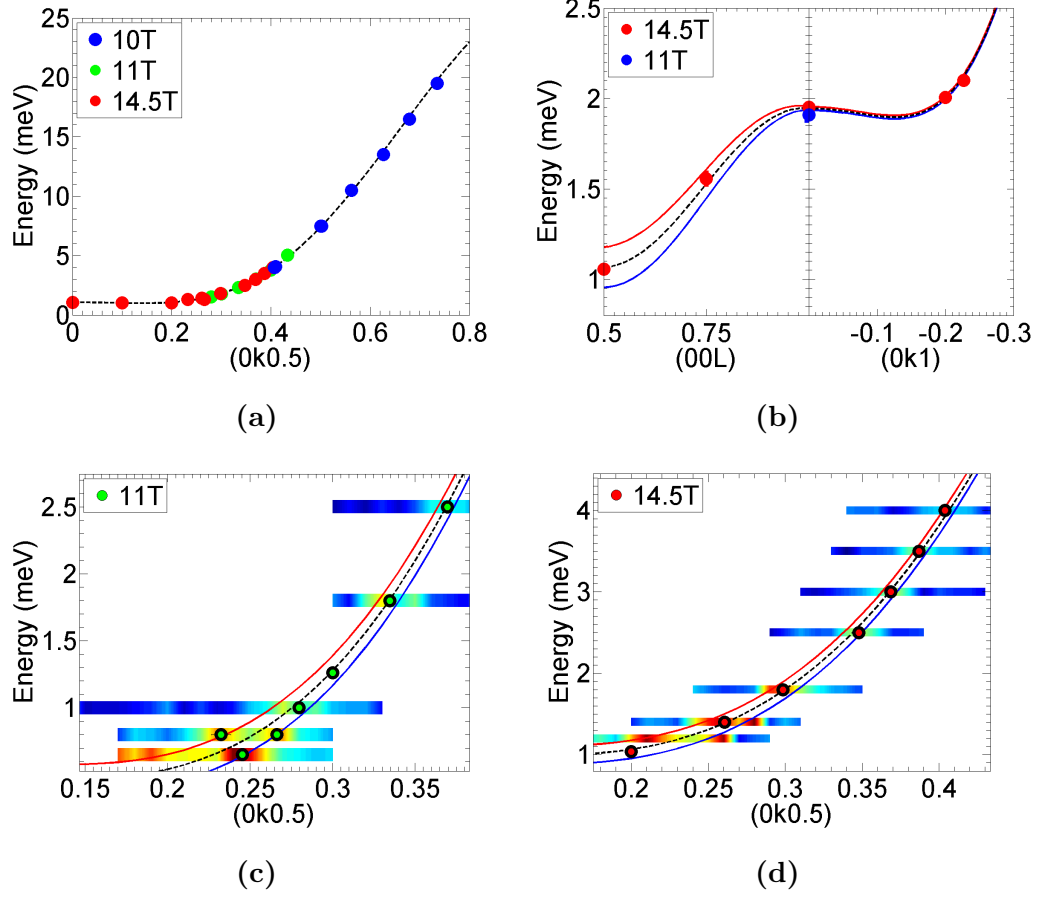


**Figure 4.41: The second isotropic exchange model.** In this model, a non-linear field dependence, and a third nearest-neighbour interaction along the  $\mathbf{b}$  axis direction,  $J_3$ , is introduced. **(a)** The average spin-wave dispersion along  $(0,k,0.5)$  can be seen in the black dashed line calculated for 14.5T, with all data points energies lifted up to 14.5T. **(b)** For the  $(00l)$  and  $(0k1)$  directions the  $\hbar\omega$  and  $\hbar\omega_t$  dispersions are shown in blue and red respectively. The blue data point represents the 11T  $(001)$  measurement which has been lifted 14.5T. **(c)** The 11T dataset can be compared to the dispersion evaluated at 11T. **(d)** Similarly, the 14.5T dataset can be compared to the dispersion evaluated at 14.5T.

Model	$\chi^2$	$J_1$	$J_2$	$J_{c0}$	$J_{c1}$	$J_a$	$g_a$	$g_{a'}$	$\Delta_1$	$\Delta_2$
<b>1</b>	111	14.6(1)	-3.99(4)	-0.6(1)	0.06(3)	0.04(17)	2.2(2)	2.5(3)	-	-
<b>2</b>	88.6	14.6(1)	-3.97(4)	-0.7(1)	0.07(0)	0.3(2)	3.1(3)	1.9(3)	0.04(1)	-
<b>3</b>	83.3	14.6(1)	-4.3(2)	-0.6(1)	0.05(3)	0.2(2)	2.7(4)	2.0(3)	0.18(4)	0.6(2)

**Table 4.12: The isotropic-exchange and anisotropic-exchange spin-wave fit results for linearite above saturation.** Models 1, 2 and 3 correspond to the isotropic model, the anisotropic  $\mathbf{J}_1$  model and the anisotropic  $\mathbf{J}_1 - \mathbf{J}_2$  model. The  $J$  parameters are presented in units of meV.

$\chi^2$	$J_1$	$J_2$	$J_3$	$J_{c0}$	$J_{c1}$	$J_a$	$\Delta E(9.5\text{T})$	$\Delta E(10\text{T})$	$\Delta E(11\text{T})$	$\Delta E(14.5\text{T})$
36	13.6(2)	-3.5(1)	-0.65(5)	0.08(3)	0.114(8)	-0.11(3)	1.35(4)	1.44(4)	1.41(2)	1.94(2)

**Table 4.13: An isotropic-exchange model with  $J_3$  and a non-trivial magnetic field dependence introduced.** The  $J$  parameters and the energy shifts  $\Delta E(\text{H})$  are given in units of meV.



## 4.4 Spin-wave Measurements at Zero Field

At zero field it is known that linarite has a helical magnetic structure [150]; however, the nature of its excitations is not known. In  $\text{LiCuVO}_4$ , which also has a helical magnetic structure, inelastic neutron scattering experiments reveal a spinon continuum [127]. A similar excitation spectrum could be expected for linarite. Regardless, the measurement of the excitation spectrum at zero field is likely to shed information to the nature of zero field ground state.

### 4.4.1 Experimental Set-up

Inelastic neutron scattering experiments at zero field were carried out on linarite. The experiments were carried out at the cold triple axis instruments IN12 and ThALES, ILL, Grenoble. For all experiments very similar set up was used, which can be seen in detail in figure 2.9. An orange cryostat was used to achieve a base temperature of  $\sim 1.6\text{K}$ . A PG(002) monochromator and analyser was used with fixed  $k_f$  mode with  $k_f = 1.5\text{\AA}^{-1}$ . A velocity selector and a beryllium filter was used to filter some of the neutrons with wavenumber  $2k_f$  and  $3k_f$ . Vertical and horizontal slits were used before and after the sample to reduce the beam size. The slits before the sample were closed as much as possible without cutting into the intensities of the (020) or (001) Bragg peaks. The slits after the sample were set using the information about the sample size, analyser height, analyser effective width, and distances between the sample, slits, and the analyser.

For the IN12 November 2014 experiment the PG(002) analyser with vertical focusing and monochromator with vertical and horizontal focusing was used. A velocity selector was used to filter out the higher order neutrons. The size of the beam after the sample was reduced to 15.5mm and 31mm vertically and horizontally with the help of slits.

For the ThALES December 2014 experiment, the PG(002) monochromator with horizontal focusing and analyser with vertical and horizontal focusing was used. The top slit before the sample could not be moved during the experiment, therefore it is possible that it was cutting into the intensity of the (020) or (001) Bragg peak. Horizontal and vertical slits reduced the beam size after the sample to 29mm high and 26mm wide. For the ThALES April 2015 experiment, the set up was the same except for a slightly different sized opening for the beam after the sample.

#### **4.4.2 Data Reduction**

For the zero field INS data, no major alteration to the data was necessary. The raw data without any correction is presented within the experimental results in section 4.4.3. The data is normalised to monitor M1 for the IN12 November 2014 and ThALES April 2015 experiment; however, for the ThALES December 2014 experiment, no monitor was used. This meant that the counts had to be normalised to time instead. This is not ideal, as any large fluctuation in the reactor power will have an effect in the INS measurements.

In the analysis section, the incoherent elastic background is modelled by using the (0,-1,0.5) energy scan. These can be seen in figure 4.42 on page 215 for IN12 and ThALES April 2015 experiments. Here a Gaussian centred at zero energy and a constant is used to model the background. For the Q scans only a constant background is used. For the spin-wave fits this background is left as a free variable for the Q scans.

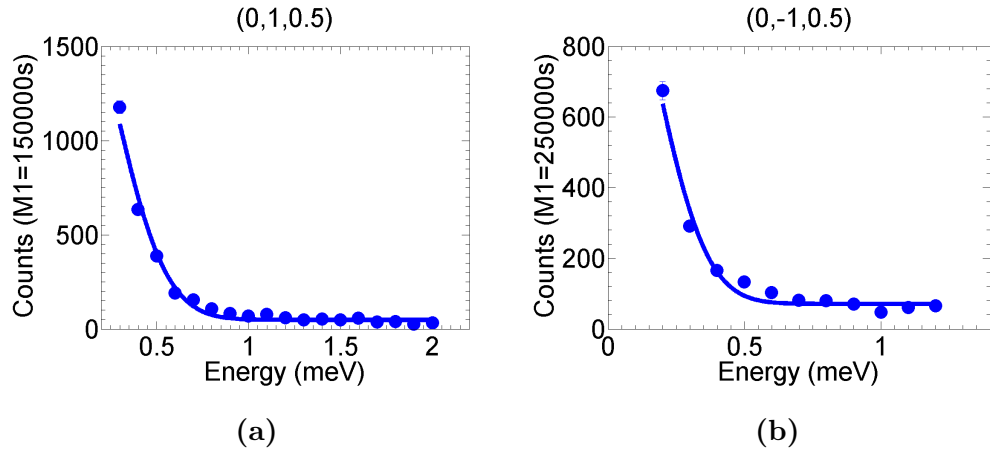


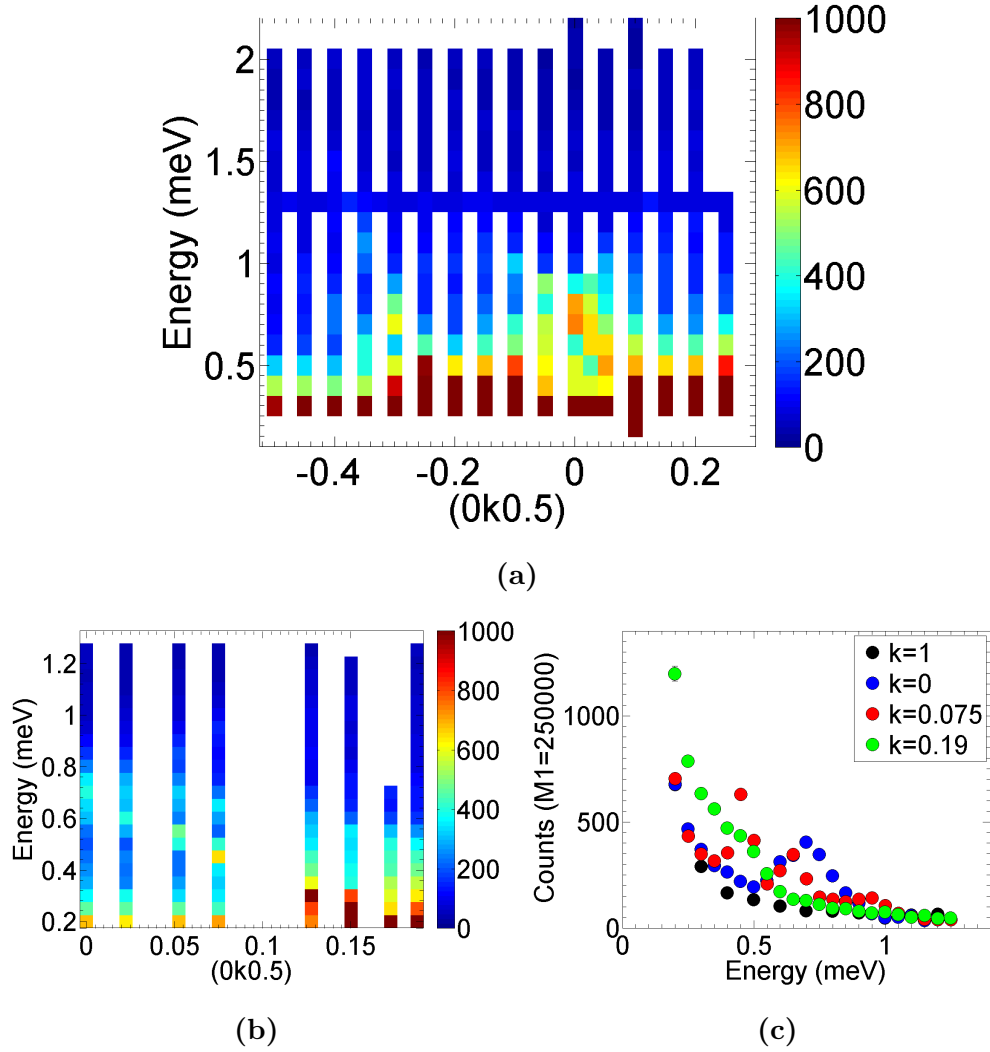
**Figure 4.42: Incoherent elastic background.** (a) The background is obtained from fitting the (0,1,0.5) energy scan for IN12. (b) For ThALES April 2014, the fit is performed on the (0,-1,0.5) energy scan.

### 4.4.3 Experimental Results

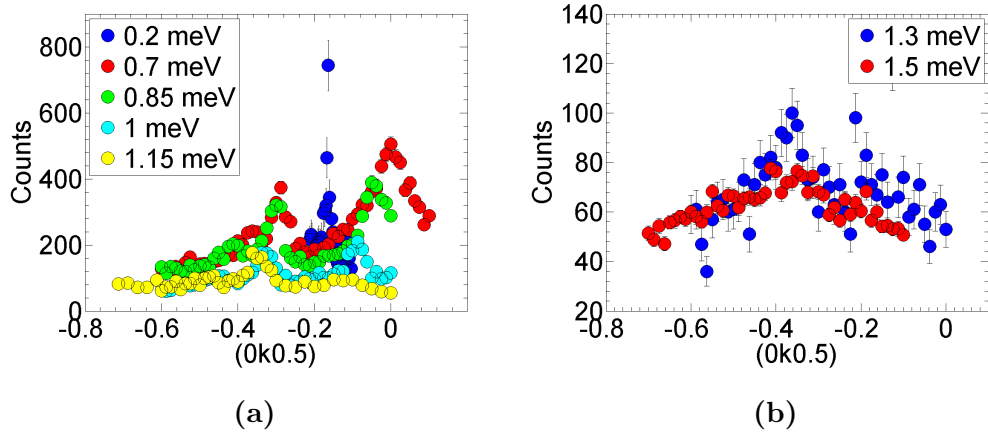
Inelastic neutron scattering measurements were performed at zero field for linarite. The resulting spectrum has sharp excitations with at least three distinct branches coming out of the incommensurate Bragg peak with possibly one of the branches gapped. The data was collected from ThALES and IN12 at ILL, Grenoble, France. In figure 4.43 on page 217(a) the IN12 data along  $(0,k,0.5)$  is presented in an intensity colour map. Here a branch can be seen originating from the Bragg peaks at  $k \simeq \pm 0.19$  and reaching  $\sim 0.8 \text{ meV}$  at  $k=0$ . Two other branches can be seen emerging from  $k=-0.19$  and increasing in energy towards negative  $k$ . In figure 4.43(b) a similar colour map shows the data obtained from ThALES April 2015 experiment, where the focus was on the low lying excitations between  $k=0$  and  $k=0.19$ . Here two branches can be identified in the scans  $k=0.025$  to  $k=0.075$ . The lower branch might not have any energy gap at the Bragg peak position; however, the higher energy branch seems to have a gap of  $\sim 0.4 \text{ meV}$ . This can be seen more clearly in

figure 4.43(c) where individual energy scans are compared. Here at  $k=0$  there is a broad hump which most likely contains two excitations; at  $k=0.075$  three branches can be identified: 0.4, 0.6, and 0.9meV (the latter is not focused due to tilting of the resolution ellipsoid); finally, at  $k=0.19$  there is still at least one, possibly two branches between 0.2meV and 0.6meV. The  $k=1$  scan can be used as a guide for the incoherent elastic signal. It is important to note that some of these low energy signals close to  $k=0.19$  might be a spurious signal which originates from the tail of the resolution ellipsoid being close to a Bragg peak. This kind of spurious signal has a linear dispersion originating from the Bragg peak and a rapid intensity gain as one gets closer to the Bragg peak.

In order to identify the branches above 1meV, Q scans were performed on the ThALES April 2015 experiment and the ThALES December 2014 experiment, which can be seen in figure 4.44 on page 218. All these Q scans show the same thing: three distinct excitations, one between  $k=-0.19$  and  $k=0$  and two others between  $k=-0.19$  and  $k=-0.5$ . The intensities of the excitations drop quite quickly and becomes difficult to detect above 1.15meV. The 0.2, 0.7, 1, and 1.3meV Q scans were obtained from ThALES December 2014 experiment where no monitor was used; therefore their counts here are normalised to 300 seconds. The remaining Q scans were measured during the ThALES April 2015 experiment and are normalised to a monitor of M1=260000.



**Figure 4.43: Zero field INS energy scans.** (a) Energy scans performed at IN12 show three clear branches leaving the magnetic Bragg peak. (b) Measurements performed on ThALES April 2015 experiment show that there are in fact two branches between  $k=0$  and  $k=0.19$ . (c) From individual scans of the ThALES April 2015 data it is clear that at least one of these branches remains at  $\sim 0.4$  meV at the Bragg peak position.



**Figure 4.44: Zero field INS Q scans.** (a) From the Q scans three clear branches can be seen: one between  $k = -0.19$  and  $k = 0$  and two others between  $k = -0.19$  and  $k = -0.5$ . (b) At higher energies the intensity drops rapidly and the branches become hard to resolve. The 0.2, 0.7, 1, and 1.3 meV Q scans are normalised to 300 seconds and the other Q scans are normalised to monitor of  $M1 = 260000$ .

#### 4.4.4 Analysis

Estimating the branches of the zero field spin waves was not as straight forward as for the saturated phase. At zero field, there is the possibility of other types of magnetic excitations occurring, such as a spinon continuum. For this reason the first step was to find all possible excitations in all energy and Q scans. Some of the fitted peaks have a very small intensity and therefore might not be a real signal. The results for such a fit for ThALES and IN12 data can be seen in figure 4.45 on page 219 in red and black points respectively. Here the colour map is given by IN2 energy cuts after removal of the incoherent elastic background and some interpolation. The incoherent elastic background was modelled on the  $(0,1,0.5)$  energy scan which can be seen in figure 4.42. For the interpolation a two dimensional interpolation function

from MATLAB was used. In the background removed colour map, to the left of both incommensurate Bragg peaks, a large spurious signal can be seen. This spurious signal is created by the tail of the resolution ellipsoid coming close to the Bragg peak. The black and red points in figure 4.45 correspond to the fits to the IN12 energy scans and ThALES Q scans respectively.

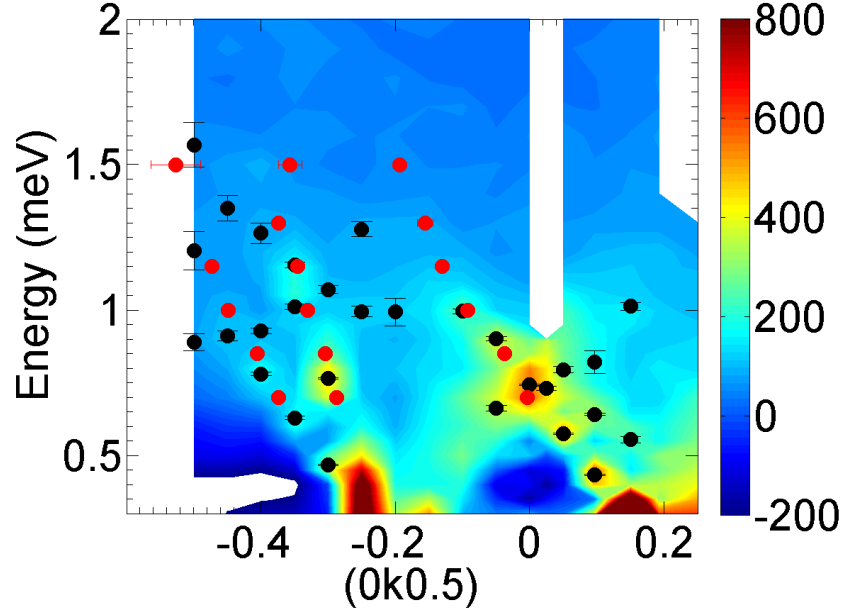


**Figure 4.45: Zero field IN12 colour map with the spin-wave fits.**

Here the black points are fits to IN12 energy scans and red points are fits to ThALES Q scans.

Note that in figure 4.45, from the ThALES Q scan fits (red points), three clear branches can be seen. However, there are many IN12 energy scan fits (black points) that do not lie on these three branches, such as the 1meV,  $k=-0.25$  signal. This  $k=-0.25$ , 1meV signal could not be reproduced on a ThALES April 2015 experiment, where a better crystal co-alignment was implemented. It is not clear if in the ThALES April 2015 experiment the signal to background ratio was unfavourable or if the  $k=-0.25$ , 1meV signal is due to the imperfect alignment in IN12 experiment.

The comparison between ThALES April 2015 and IN12 scans can be seen in figure 4.46 on page 221. Here the black squares are the  $k = \pm 1$  energy scans and are a guide to the incoherent background. For the ThALES April 2015 data in figure 4.46(b), the data has been normalised to a much larger monitor so that the (0,0,0.5) inelastic intensity at  $\sim 0.6\text{meV}$  are similar for both experiments. Here it can be seen that for the IN12 experiment in figure 4.46(a) at  $1\text{meV}$ , there is higher intensity at  $k=-0.25$  compared to  $k=-1$ . However, for ThALES April 2015 data in figure 4.46(b), the intensities are the same at  $k=-0.25$  and  $k=1$ . Note that, the  $k=1$  scan is not a great estimate for the  $k=0$  incoherent background therefore it might not be an accurate estimate for the  $k=-0.25$  incoherent background either. Two different scenarios can be considered: either the  $k=-0.25$  signal is real but it could not be measured on ThALES April 2015 experiment due to its small intensity or the  $k=-0.25$  signal originates from the imperfect orientation used on IN12. Even though there is insufficient evidence to show that the  $k=-0.25$ ,  $1\text{meV}$  signal is spurious, it will still be removed. Similarly, other features which do not fit in with the three clear branches, as identified by the Q scans, will be removed and not considered. For spin-wave fits, only the Q scan fits will be used.

In order to understand the low energy part of the dispersion, a set of energy scans were performed in the ThALES April 2015 experiment, which can be seen in figure 4.47 on page 222 in the form of a colour map. The incoherent elastic signal has been modelled through the (0,-1,0.5) energy scan, which can be seen in figure 4.42. This background was removed from the ThALES April 2015 energy scans and a two dimensional interpolation was performed. Note that there is a discontinuity in the colour map at  $k=0.1$ . This is not a real effect. It originates from interpolation of data from  $k=0.075$  to  $0.125$ . Since no measurement was performed at  $k=0.1$  on ThALES, the transition appears discontinuous at this point. Aside from this, there is an indication that a lower branch is heading toward the magnetic Bragg peak,



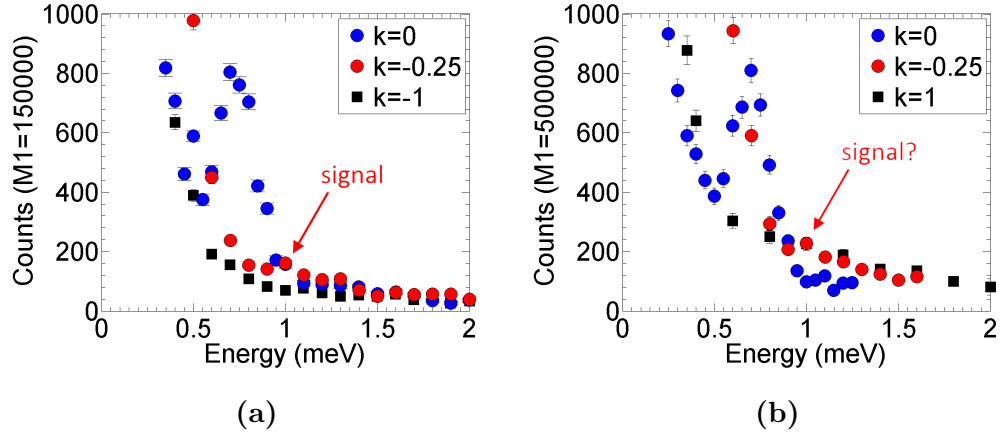


**Figure 4.46: Comparing  $(0,-0.25,0.5)$  energy scans for IN12 and ThALES April 2015 experiments.** (a) In the IN12  $(0,-0.25,0.5)$  energy scan there is a signal at  $\sim 1\text{meV}$ . (b) In the ThALES April 2015  $(0,-0.25,0.5)$  energy scan it is not clear if there is a signal at  $\sim 1\text{meV}$ . Here the monitors have been scaled so that for both experiments the  $(0,0,0.5)$   $\sim 0.7\text{meV}$  signal is of a similar size.

while and upper branch is staying at  $0.45\text{meV}$  at  $k=0.19$ . In figure 4.47 the fits to the spin waves are given in circles and squares for the IN12 data and the ThALES April 2015 data respectively. The fits above  $0.8\text{meV}$  are defocused due to the tilt of the resolution ellipsoid and therefore can be ignored.

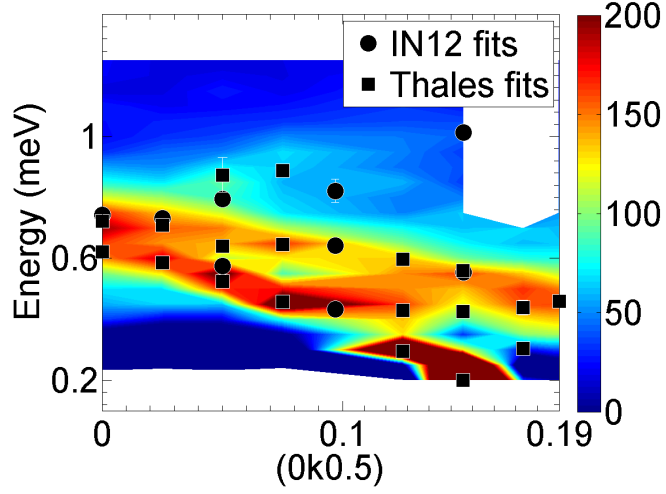


**Figure 4.47: Zero field ThALES April 2015 colour map with fits to spin waves.** Here the focus is on the lower energy part of the spectrum. There seems to be at least two branches with one approaching zero energy at the incommensurate Bragg peak position and the other one remaining at 0.45meV. The circles and the squares are fits obtained from IN12 and ThALES April 2015 experiments respectively.

The fits to excitations in energy and Q scans can be seen in more detail in figure 4.48 on page 223. Here in figure 4.48(a,b) IN12 energy scans at  $(0,-0.4,0.5)$  and  $(0,-0.097,0.5)$  are presented. The black dashed line is the fixed background obtained from the  $(0,1,0.5)$  energy scan. In figure 4.48(c,d) the ThALES December 2014 and April 2015 Q scans can be seen respectively. Here the background was described by a constant and was used as a free parameter. It can be seen that at 1meV the three branches can be clearly identified. However, at 1.5meV, the intensity drops and the excitations appear broader. The complete table of fits can be seen in tables 4.14 to 4.16. on pages 224 to 226.

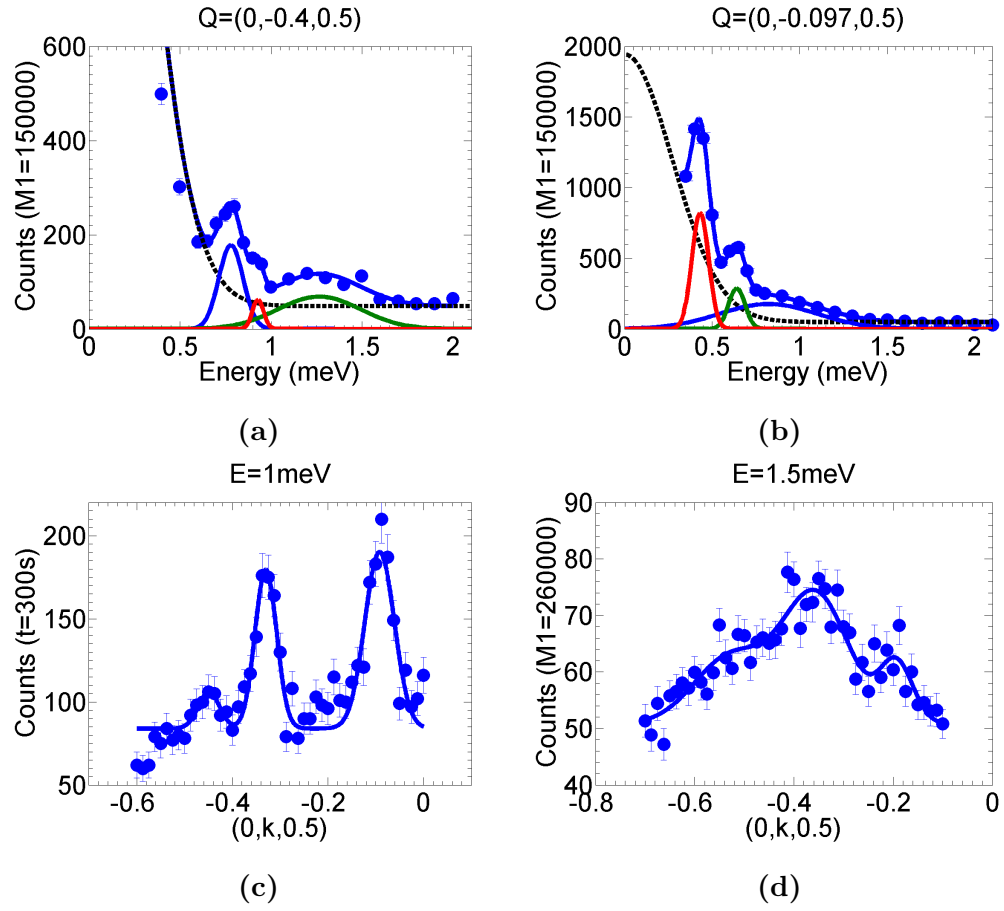


**Figure 4.48: Examples to spin-wave fits for zero field INS data.**  
 (a,b) Three branches can be seen for both IN12 energy scans presented.  
 (c) Thales December 2014 Q scan shows three clear branches at 1meV.  
 (d) At 1.5meV, the ThALES April 2015 data also shows three branches; however, they are much lower in intensity.

Experiment	(0 k 0.5)	En (meV)	$\Delta$ En (meV)
IN12	-0.5	0.8896	0.0299
IN12	-0.5	1.2039	0.0650
IN12	-0.5	1.5680	0.0769
IN12	-0.45	0.9114	0.0172
IN12	-0.45	1.3505	0.0439
IN12	-0.4	0.7796	0.0059
IN12	-0.4	1.2641	0.0352
IN12	-0.4	0.9277	0.0094
IN12	-0.35	0.6290	0.0061
IN12	-0.35	1.1550	0.0089
IN12	-0.35	1.0112	0.0089
IN12	-0.3	0.7643	0.0028
IN12	-0.3	1.0706	0.0142
IN12	-0.3	0.4680	0.0026
IN12	-0.25	0.9945	0.0183
IN12	-0.25	1.2774	0.0262
IN12	-0.2	0.9927	0.0474
IN12	-0.1	0.9960	0.0087
IN12	-0.05	0.6619	0.0094
IN12	-0.05	0.9011	0.0064

**Table 4.14: Fits to all of the energy scans as obtained from the IN12 experiment and the ThALES April 2014 experiment (part 1).** Continued in table 4.15.

Experiment	(0 k 0.5)	En (meV)	$\Delta$ En (meV)
IN12	0.0	0.7447	0.0025
IN12	0.025	0.7306	0.0065
IN12	0.05	0.5741	0.0025
IN12	0.05	0.7947	0.0108
IN12	0.1	0.8210	0.0382
IN12	0.1	0.6409	0.0032
IN12	0.1	0.4326	0.0017
IN12	0.15	0.5545	0.0110
IN12	0.15	1.0123	0.0144
ThALES 04/15	0	0.6214	0.0137
ThALES 04/15	0	0.7221	0.0102
ThALES 04/15	0.025	0.5859	0.0091
ThALES 04/15	0.025	0.7086	0.0125
ThALES 04/15	0.05	0.525	0.0007
ThALES 04/15	0.05	0.6407	0.0092
ThALES 04/15	0.05	0.8736	0.0571
ThALES 04/15	0.075	0.4568	0.0022
ThALES 04/15	0.075	0.6446	0.0041
ThALES 04/15	0.075	0.8877	0.0125
ThALES 04/15	0.125	0.2964	0.0022
ThALES 04/15	0.125	0.4299	0.0126
ThALES 04/15	0.15	0.4773	0.0105
ThALES 04/15	0.19	0.4599	0.0086

**Table 4.15: Fits to all of the energy scans as obtained from the IN12 experiment and the ThALES April 2014 experiment (part 2).** Continued from table 4.14.

Experiment	(0 k 0.5)	En (meV)	$\Delta k$
ThALES 12/14	0.1643	0.2	0.0005
ThALES 12/14	0.2074	0.2	0.0013
ThALES 12/14	-0.0033	0.7	0.0024
ThALES 12/14	-0.2875	0.7	0.0023
ThALES 12/14	-0.3735	0.7	0.0054
ThALES 12/14	-0.0920	1.0	0.0022
ThALES 12/14	-0.3301	1.0	0.0021
ThALES 12/14	-0.4492	1.0	0.0079
ThALES 12/14	-0.3743	1.3	0.0076
ThALES 12/14	-0.1552	1.3	0.0116
ThALES 04/15	-0.3457	1.15	0.0022
ThALES 04/15	-0.4735	1.15	0.0084
ThALES 04/15	-0.1294	1.15	0.0072
ThALES 04/15	-0.0378	0.85	0.0028
ThALES 04/15	-0.3046	0.85	0.0017
ThALES 04/15	-0.4049	0.85	0.0060
ThALES 04/15	-0.3567	1.5	0.0177
ThALES 04/15	-0.5273	1.5	0.0372
ThALES 04/15	-0.1932	1.5	0.0081

**Table 4.16: Fits to all Q scans as obtained from the ThALES December 2014 and ThALES April 2015 experiments.**

A fit was obtained from the zero field data using the SpinW [122] programme. In order to obtain a fit, a number of simplifications were introduced. Firstly, it was assumed that the system is fully isotropic. SpinW uses a rotating coordinate system to work with incommensurate magnetic structures and the introduction of an aniso-

tropy breaks this rotational symmetry. Therefore, an isotropic system is mandatory. This also means that the considered magnetic structure is a perfectly circular helix and not an elliptical one as neutron diffraction studies suggest [150]. Secondly, it was assumed that the ground-state magnetic structure and its excitations behave classically. It is known that for quasi-1D systems, quantum fluctuations can change  $k_{ic}$  drastically from its classical value. Despite this, the magnetic structure was calculated using classical Monte Carlo methods within SpinW. The output  $k_{ic}$  from this algorithm was compared to previously measured  $k_{ic}$  and included in the  $\chi^2$  calculation. Here the  $\chi^2$  definition is the same as the one used previously for spin-waves above saturation field. Twinning is apparent in the (0,0,0.5) ThALES energy scans where two peaks are visible. The energy difference of 0.1meV between the two branches is used to fix  $J_a=0.5(1)$ . Because of this twinning the average spin-wave position is calculated for comparison with the data. The average used is simply  $(\hbar\omega + \hbar\omega_t)/2$ , and does not consider the relative intensities of the two branches. The calculated average spin-wave was fitted to the ThALES Q scans only, where each branch can be clearly identified. Using the 18 data points a fit with  $\chi^2 = 175$  was obtained by varying the four free parameters. The fitted parameters can be seen in table 4.17. Similar to the saturated case, the correlation between the parameters were considered for the estimation of the confidence intervals. Also due to the correlation, the error of  $\alpha$  is very small with  $\alpha = -0.3035(6)$ .

Parameter	$J_1$	$J_2$	$J_{c0}$	$J_{c1}$	$J_a$
Value	6.38(4)	-1.94(1)	-0.398(8)	0.0000(1)	0.05(1)

**Table 4.17: The spin-wave fit result for Linarite at zero field.**

The  $J$  parameters are stated in units of meV.

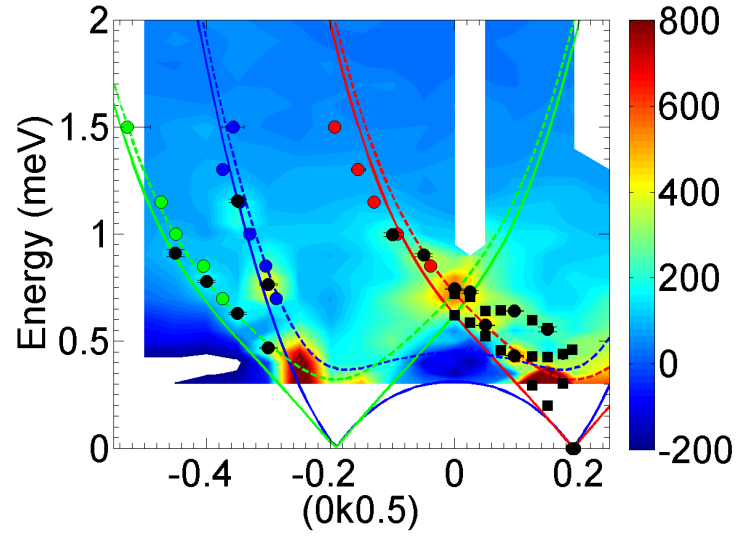
The calculated spin-wave spectrums can be compared to the IN12 and ThALES colour maps as it can be seen figure 4.49 on page 229 and figure 4.50 on page

230 respectively. Here the data points used in the fit are given in red, blue, and green and they correspond to the spin-wave branch of the same color. The solid lines correspond to the crystal in  $(0kl)$  orientation, whilst the dashed lines are the contributions of the twin. The calculated spin-wave model can explain the majority of the features observed in the data. For example, the  $k=0.19$ ,  $0.45\text{meV}$  signal could have been interpreted as a gapped excitation, instead this spin-wave model showed that it originates from the twinned crystal.

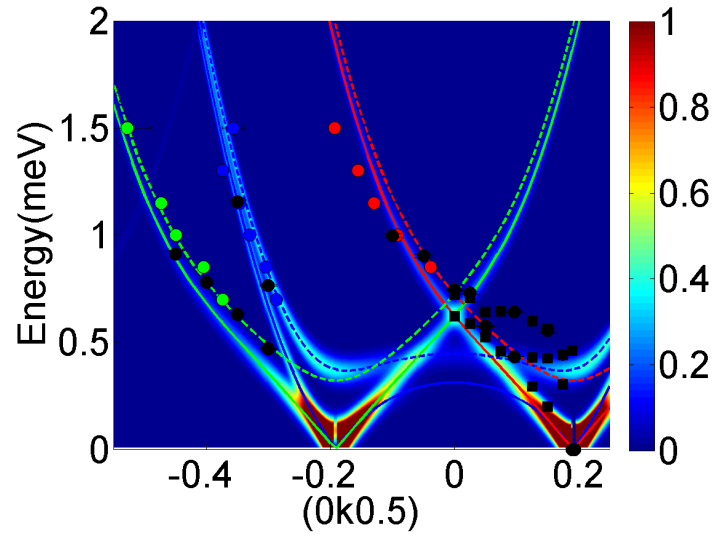
There are two major issues which the used spin-wave model fails to explain. The first issue is the models failure to reproduce the magnon branch in the region  $k=0.05\text{--}0.14$ ,  $\sim 0.6\text{meV}$  (see figure 4.50(a)). The second issue is the sudden drop in intensity above  $\sim 0.8\text{meV}$ . This drop in the area of the branches obtained from the Q scans can be seen in figure 4.51(a) on page 231. In figure 4.51(b) it can be seen that the FWHM does not change drastically over this region. Here the three branches are given in blue, red, and green and correspond to the branches of same colour seen in figure 4.49. It is important to note that the squares and circles represent the ThALES December 2014 and ThALES April 2015 experiments respectively. In the Thales December 2014 experiment no monitor was installed and for this reason counts were only normalised to time. However, even with the square data points removed, the overall trend remains the same. It is also important to note that for each Q scan a constant background was fitted which was left as a free parameter.

Overall the suggested simple method was successful in reproducing many of the observed features. It is possible that with the addition of anisotropy the missing features can be reproduced. In future experiments measurements along the  $(00l)$  direction would help determine the inter-chain interactions in a more rigorous way.





(a)



(b)

**Figure 4.49: Zero field spin-wave fit IN12 comparison.** Here the (a) IN12 intensity colour map and (b) calculated neutron intensity are shown. The red blue and green lines were fitted to the Q scans of the same colour. The solid lines correspond to the crystal in  $(0kl)$  orientation whilst the dashed lines are the contributions of the twin.

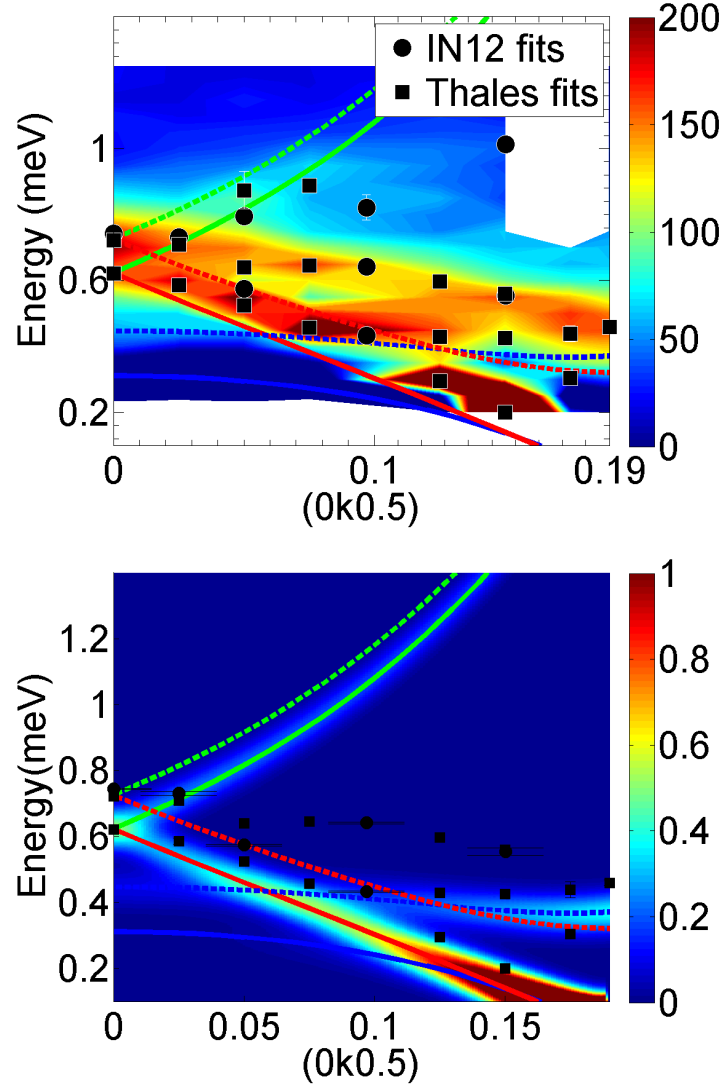


**Figure 4.50: Zero field spin-wave fit ThALES comparison.** Here the (a) ThALES intensity colour map and (b) calculated neutron intensity are shown. The solid lines correspond to the crystal in  $(0kl)$  orientation whilst the dashed lines are the contributions of the twin.

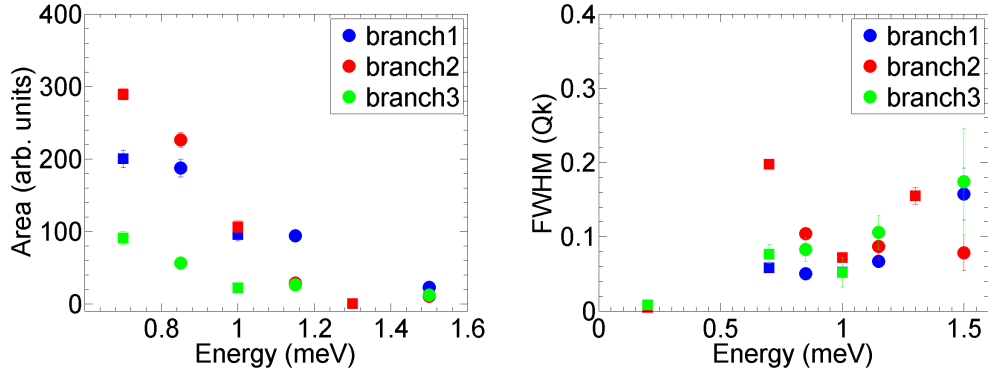


**Figure 4.51: Intensity and FWHM of the three branches.** (a) The fitted area of all three branches drop sharply; however (b) the FWHM does not change much. Here the three branches are given in blue, red, and green and correspond to the branches of same colour seen in figure 4.49. The square and circles represent two different experiments.

## 4.5 Diffraction Measurements with an Applied Field

It was discussed earlier, in section 4.1.2, that one of the predictions of a  $\text{SDW}_{(p)}$  phase is a characteristic vector dependent on magnetisation given by equation 4.5. For  $\text{LiCuVO}_4$ , the behaviour of the incommensurate Bragg peak above  $\sim 6\text{T}$  has already been interpreted as an entry from a helical phase into a  $\text{SDW}_{(2)}$  phase [45]. For linarite, a change in the magnetic propagation vector  $(0, k_{ic}, 0.5)$  was observed with increasing magnetic field for  $\mathbf{H} // \mathbf{b}$ . This dependence was observed in the phase V of the  $\mathbf{H} // \mathbf{b}$  phase diagram as shown in figure 4.11. Neutron diffraction measurements indicate that magnetic structure of phase V is a SDW. The observed movement change in  $k_{ic}$  with increasing field within phase V was interpreted as the existence of a  $\text{SDW}_{(p)}$  phase, where  $p$  varied from  $p=4$  to  $p=8$  with changing field [154]. However, these measurements were not performed at the same temperature. It would be more compelling evidence if  $k_{ic}$  showed a similar field dependence at fixed temperature. For this reason the  $\mathbf{H} // \mathbf{b}$  measurement is performed at  $\sim 50\text{mK}$

temperatures. Additionally, the  $\mathbf{H} // \mathbf{a}$  direction is also measured for the first time.

#### 4.5.1 Experimental Set-up

The measurements of the magnetic Bragg peaks at different field strengths were carried out using the TAS instrument IN14 and the diffractometer D23 at ILL, Grenoble, France.

The majority of the data presented in this section originates from D23. The typical configuration of D23 can be seen in figure 2.11. For the measurements, a PG (002) monochromator was used without focusing in order to obtain a wavelength of  $\lambda = 2.38\text{\AA}$ . A  $^3\text{He}$  stage was used in conjunction with a 12T vertical cryomagnet which supplied a base temperature of  $\sim 50\text{mK}$  throughout the experiment. A PG (002) filter was placed between the monochromator and the cryomagnet in order to reduce the amount of second order reflections. For the  $\mathbf{H} // \mathbf{b}$  experiment pieces of boron carbide ( $\text{B}_4\text{C}$ ) based shielding were taped to the sides of the cryomagnet in order to vertically reduce the opening to 8mm both before and after the sample. The intensity of the (300) and (003) Bragg peaks were monitored to make sure no sample intensity was lost. For  $\mathbf{H} // \mathbf{a}$  instead of such shielding circular slits of 10mm were used before and after the sample. The most common type of measurement was along  $(0, k, 0.5)$ . For  $\mathbf{H} // \mathbf{a}$ , the scattering plane is  $(0kl)$  therefore any value of  $k$  can be accessed easily. However, for  $\mathbf{H} // \mathbf{b}$ , in order to access a non zero value  $k$ , the detector has to move up or down vertically. This limits the range of  $k$  which can be studied. The difference in configuration means that  $\mathbf{H} // \mathbf{b}$  and  $\mathbf{H} // \mathbf{a}$   $(0, k, 0.5)$  measurements will not have the same resolution in  $k$ .

The crystals used in D23 experiments were untwinned crystals. This was confirmed previously on IN3 at the ILL, Grenoble, France. Crystal 3 from table 4.4 was mounted with the  $\mathbf{b}$  axis vertically, whilst crystal 4 was mounted with  $\mathbf{a}$  axis vertically. On D23, a number of Bragg peaks were measured to ensure that the

Effenberger-Araki structure was used. The crystal in the  $\mathbf{H} // \mathbf{b}$  set up broke during the D23 experiment, which drastically limited the quality of the dataset.

Measurements were also performed on IN14 on coaligned crystals with  $\mathbf{H} // \mathbf{a}$ . The relative orientations of the crystals is discussed in detail in section 4.2. The best estimate of the orientation is that Crystal 1b and Crystal 2 were perfectly aligned along  $\mathbf{b}^*$  but the  $\mathbf{c}^*$  axes were  $\sim 4^\circ$  and  $\sim 3^\circ$  out of plane respectively. The incommensurate Bragg peak at  $(0, k_{ic}, 0.5)$  was measured at a base temperature of  $\sim 1.6\text{K}$  and at field strengths ranging from 0T to 5.5T. The main purpose of this experiment was to measure spin waves at 14.5T. The detailed experimental set up of this experiment has already been stated in subsection 4.3.1.

#### 4.5.2 Experimental Results

For the  $\mathbf{H} // \mathbf{b}$  direction, measurements were made at 7T and above which can be seen in figure 4.52 on page 234. Both 7T and 8T measurements show a large peak at  $(0, 0, 0.5)$ ; however, the 8T measurement also shows a smaller peak at  $k_{ic} \cong 0.1$ . For measurements at 8.5T and above the  $k=0$  peak does not exist. The  $k_{ic} \cong 0.1$  peak is most intense at 8.5T and with increasing field strength, it shrinks in intensity and moves towards slightly larger  $k_{ic}$  until it is no longer visible at 9.5T.

The magnetic Bragg peaks were also measured with scans along  $h$  and  $l$  directions. These can be seen in figure 4.53 on page 234. These scans show no obvious signs of broadening with increasing field. Here 7T data is divided by 5 and scaled up by 300 for clarity.

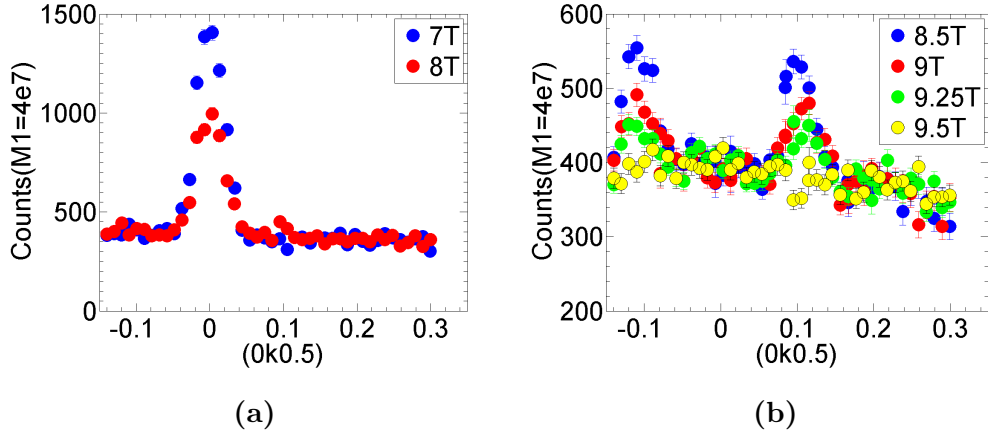


**Figure 4.52:  $H//b$   $k_{ic}$  dependence.** (a) 7T and 8T show a large peak at  $k=0$ , but 8T also show a small peak at  $k_{ic} \cong 0.1$ . (b) above 8T, this small peak shrinks in intensity and moves towards larger  $|k_{ic}|$  until it is no longer visible at 9.5T.

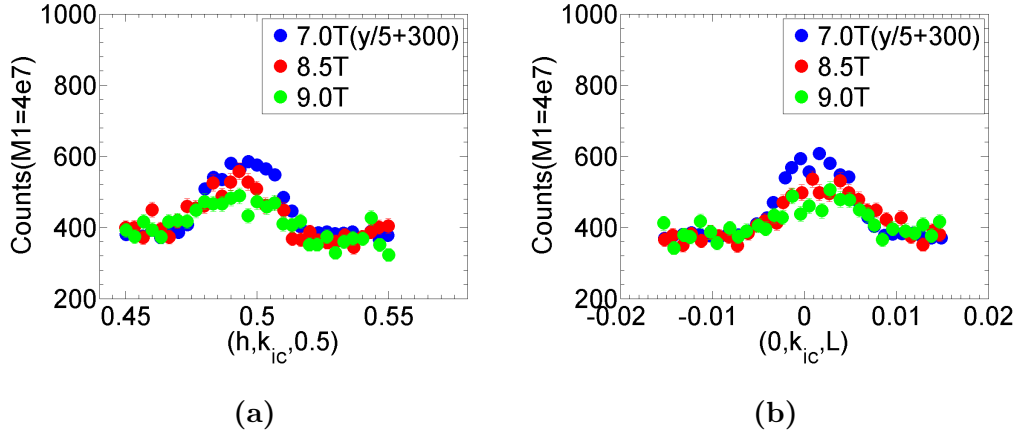


**Figure 4.53:  $H//b$  incommensurate Bragg peak  $h$  and  $l$  scans.** No broadening is observed for (a)  $(h, k_{ic}, 0.5)$  nor (b)  $(0, k_{ic}, l)$  scans. Here  $k_{ic}$  is obtained initially from a  $(0, k, 0.5)$  scan. Note that the counts in 7T data are divided by 5 and scaled up by 300 counts for clarity.

The  $H//a$  D23 dataset can be seen in figure 4.54(a) on page 236. Here  $|k_{ic}|$

dependence can be summarised in the following way: from 0T to 1.5T  $|k_{ic}| \cong 0.19$  is constant, from 1.5T to 3T  $|k_{ic}|$  slowly decreases, from 3T to 3.25T it rapidly increases to  $|k_{ic}| \cong 0.2$ , from 3.25T to 4.75T it slowly decreases, from 4.75T to 5.75T it rapidly decreases to  $|k_{ic}| \cong 0.13$ , from 5.75T to 6.25T it slowly increases. In a general sense, there are three regions where  $k_{ic}$  is roughly constant ( $|k_{ic}| \cong 0.19, 0.2, 0.13$ ) and two regions where  $|k_{ic}|$  changes with field. These regions can be seen in more detail in figure 4.54(b). The region where  $|k_{ic}| \cong 0.13$  can be seen in more detail in figure 4.54(c). Here with increasing field, the Bragg peak weakens and moves towards larger  $|k_{ic}|$ . Here the 0T measurement is given in black as a guide for the background. This helps to identify the small amount of intensity left at 6.25T. This signal at 6.25T is small, with only four data points above the 0T data points. It is possible to construct a better estimate of the background rather than just using the 0T measurement. If one assumes that at 7T the system is fully saturated, all the scans from 7T onwards can be combined with the 0T to create a “better” estimate of the background. No statistically significant difference is observed between the measurements performed at 0T, 7T, or above 7T in the near vicinity of  $k=-0.13$ . Therefore, it is possible that all of these measurements describe the same background. In figure 4.55 on page 237 the 6.25T measurement can be compared to the 0T and to the “better” estimate of the background (given in black). Here it can be seen that if this background is correct, it can be argued that at 6.25T there is still some Bragg peak intensity. Note that for  $\mathbf{H} // \mathbf{b}$  a magnetic Bragg peak at  $k=0$  was also observed. For  $\mathbf{H} // \mathbf{a}$  scans were also made in the vicinity of  $k=0$  for few field strengths as seen in figure 4.54(a). None of these measurements observed a magnetic signal at  $k=0$ .

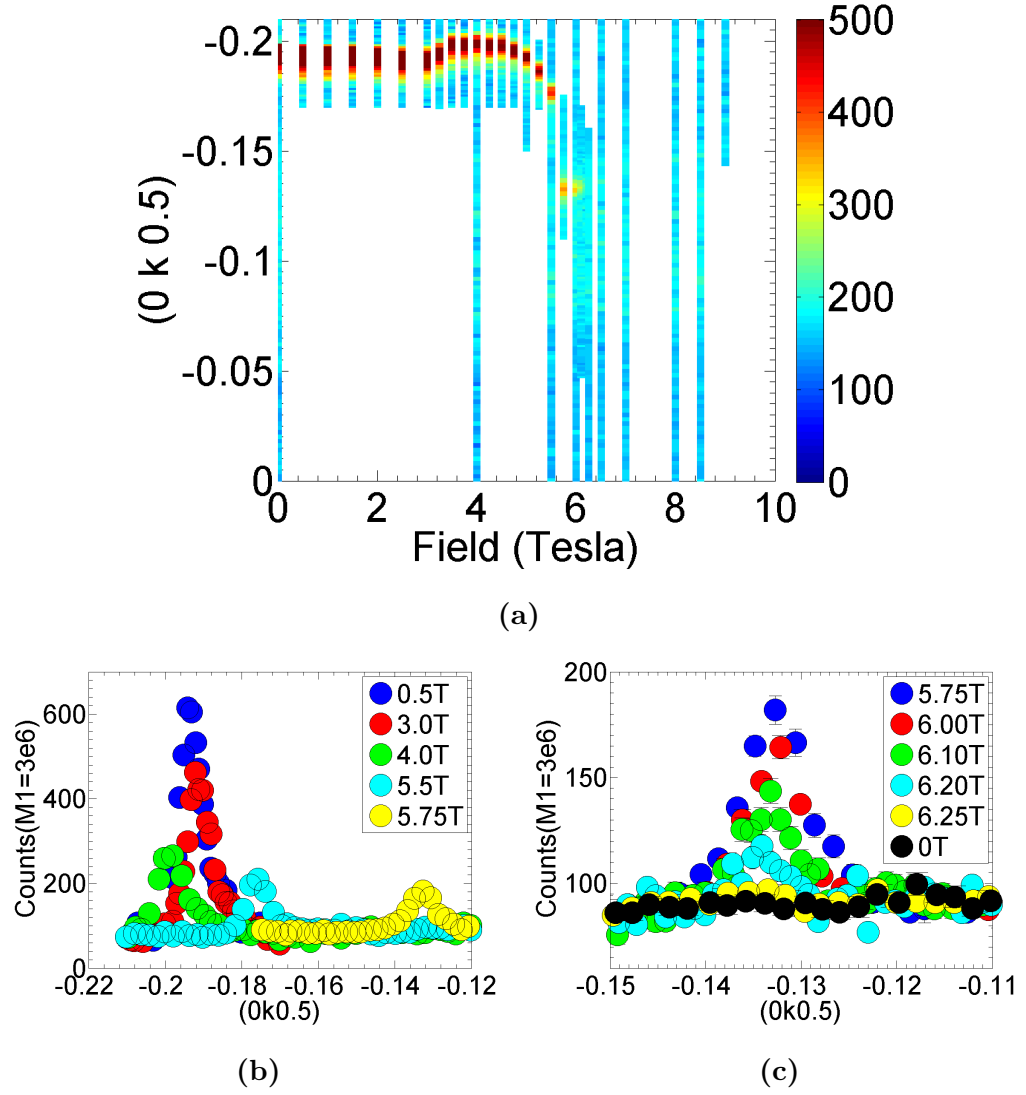


**Figure 4.54:  $H//a$   $k_{ic}$  field dependence for 50mK.** (a) Here the Q scans are represented in a  $k_{ic}$ -field colour map. The colour corresponds to the neutron intensity normalised for a monitor of  $M1=6000000$ . There are three regions where  $k_{ic}$  is roughly constant. (b) Some of the individual scans can be seen in detail. The 0.5T, 4T, and 5.75T are the three regions where  $k_{ic}$  is roughly constant. (c) In the  $k_{ic} \sim 0.13$  region,  $|k_{ic}|$  is increasing with increasing field. There is a small amount of intensity left at 6.25T.



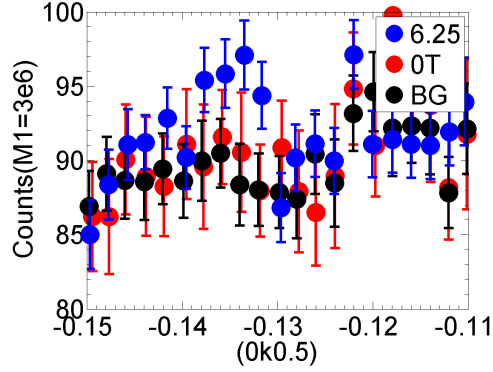


**Figure 4.55: Statistical significance of 6.25T peak.** The 6.25T signal (blue) is compared to the 0T measurement (red) and to a “better” background attempt (black). The “better” background is created by combining 0T with measurements at and above 7T.

The incommensurate Bragg peak was also measured along the  $(0, k_{ic}, l)$  direction as well and can be seen in figure 4.56. Here  $k_{ic}$  used was obtained from the  $(0, k_{ic}, 0.5)$  scans. Similar to the  $\mathbf{H} // \mathbf{b}$  measurements in figure 4.53, no obvious signs of broadening can be seen. The lack of broadening is an indication that long range order is preserved both for  $\mathbf{H} // \mathbf{a}$  and  $\mathbf{H} // \mathbf{b}$ .

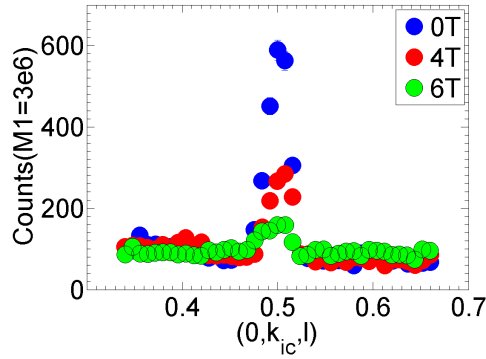


**Figure 4.56:  $\mathbf{H} // \mathbf{a}$   $(0, k_{ic}, l)$  scans** were performed at 0T, 4T, and 6T. These showed no obvious signs of broadening for increasing field strength.

The 1.6K  $\mathbf{H} // \mathbf{a}$  measurements were performed on IN14 on two twinned co-aligned crystals, the results can be seen in figure 4.57. Here measurements were made every 0.5T up to 5.5T. The overall behaviour of  $k_{ic}$  seems similar to the 50mK version with a few major differences. Firstly,  $k_{ic}$  is unchanged only up to  $\sim 0.5$ T ( $\sim 1.5$ T for 50mK). The movement of  $|k_{ic}|$  between 1T and 3.5T is much more exaggerated compared to the 50mK data. The  $k_{ic} \cong -0.2$  region appears to be only  $\sim 0.5$ T wide (rather than  $\sim 1$ T wide for 50mK data). Most importantly, it is not clear if there is a  $k_{ic} \cong -0.13$  phase for 1.6K because the measurements did not extend to this range.

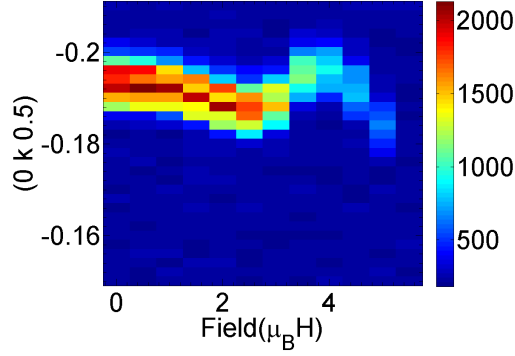


**Figure 4.57:  $\mathbf{H} // \mathbf{a}$   $k_{ic}$  dependence for 1.6K.** The results are very similar to the 50mK results. It is not clear if a  $k_{ic} \cong -0.13$  phase exists, as measurements did not extend to this range.

It is important to note that this IN14 measurement presented in figure 4.57 was significantly different to the D23 experiments where a single untwinned crystal was used. In this IN14 experiment there are two main problems. The first one is that it is not possible to know if the measured magnetic Bragg peak belongs to the twin or not. If it did belong to the twin, the true magnetic Bragg peak would be  $(-0.453, k, 0.5)$  instead of at  $(0, k, 0.5)$ . Note that untwinned samples only produced a magnetic Bragg peak of the type  $(0, k, 0.5)$  and not of  $(-0.453, k, 0.5)$  at 0T. Therefore, it is safe

to assume that in the IN14 experiments the Bragg peaks are also of  $(0,k,0.5)$  type. The second problem is the imperfect co-alignment of the sample. The two crystals used were roughly in the  $(0,k,l)$  scattering plane. Despite this their orientations are not the same because of the twinning. For one crystal the (001) Bragg peak of its twin is  $25^\circ$  out of the scattering plane whilst for the other crystal it is  $-25^\circ$  out of the scattering plane. Therefore, the two crystals might not have the same response in  $k_{ic}$  with increasing field.

The intensity of the incommensurate magnetic Bragg peak is lost between 6.25T-6.5T and 9.25T-9.5T for  $\mathbf{H}//\mathbf{a}$  and  $\mathbf{H}//\mathbf{b}$  field directions respectively. One might imagine that this disappearance of intensity corresponds to an entry into a fully saturated phase, i.e. FM phase. This idea can be checked by measuring the intensity of an FM Bragg peak. As demonstrated in section 2.1.2, the magnetisation of the system is proportional to the square of the intensity of the FM Bragg peak. Therefore, by measuring the intensity of a FM Bragg peak with increasing field, it will be possible to determine the saturation field both  $\mathbf{H}//\mathbf{a}$  and  $\mathbf{H}//\mathbf{b}$ . The (200) and (002) Bragg peaks were measured with a rocking scan for  $\mathbf{H}//\mathbf{b}$  and  $\mathbf{H}//\mathbf{a}$  field directions respectively. These Bragg peaks were chosen for their large Cu contribution in their structure factor but overall weak nuclear intensity. This can be seen in table 4.18 on page 240 where the structure factor,  $F$ , and the Cu contribution to the structure factor,  $F_{Cu}$ , can be seen. The Bragg peaks neutron intensity is proportional to  $FF^*$ . If only Cu atoms were present, the intensity would be given by  $F_{Cu}F_{Cu}^*$ . From table 4.18 it can be seen that the (200) Bragg has a very weak overall intensity but it has a large Cu contribution. The (002) Bragg peak has a stronger overall intensity but it still has a strong Cu contribution. The structure factor calculations were carried out using the atom positions given in table 4.1.

The (002) and (200) Bragg peaks both gained intensity with increasing field strength. A Gaussian was fitted to each rocking scan to obtain the area under the

Bragg Peak	$F$	$F_{Cu}$	$FF^*$	$F_{Cu}F_{Cu}^*$
(002)	9.2	15.4	85.2	238.3
(200)	-3.1	15.4	9.9	238.3

**Table 4.18: The structure factors of (200) and (002).** Here  $F_{Cu}$  is the structure factor with only Cu intensity. Both Bragg peaks have a large Cu contribution.

curve. The end results can be seen in figure 4.58 on page 241. Here the plotted quantity is  $m = \sqrt{A(H) - A(0)}$  where  $A(H)$  is the area obtained from the rocking scan at field strength  $\mu_0 H$ . This quantity,  $m$ , is now proportional to the magnetisation of the system. In order to determine the saturation field, a fit is performed on  $m$ . The fitted function has the functional form given below:

$$m(H) = \begin{cases} a_1 + b_1 H & H \leq H_{sat} \\ a_2 + b_2 H & H > H_{sat} \end{cases} \quad (4.20)$$

Using these equations  $\mu_0 H_{sat} = 9.25 \pm 0.25 \text{ T}$  and  $6.05 \pm 0.05 \text{ T}$  were obtained for  $\mathbf{H} // \mathbf{b}$  and  $\mathbf{H} // \mathbf{a}$  respectively. The fits for these equations are plotted in red in figure 4.58. It is important to note that a linear fit to magnetisation is not ideal. The main aim of these fitted curves was to try and identify the discontinuity in the magnetisation. This discontinuity is very obvious in figure 4.58(a) but not as clear for figure 4.58(b). There is not sufficient data in (200) to determine the transition point accurately. Additionally in figure 4.58(b),  $m$  seems to increase above  $\mu_0 H_{sat}$ . For both  $\mathbf{H} // \mathbf{b}$  and  $\mathbf{H} // \mathbf{a}$ , it would be beneficial to confirm these results with a physical property measurements.

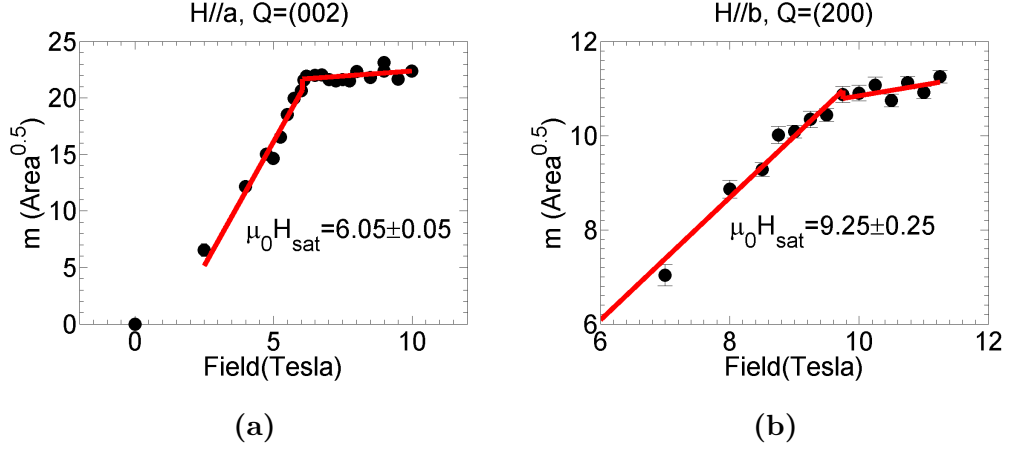


**Figure 4.58: Magnetisation** as obtained from rocking scans on Bragg peaks with large Cu contribution. For (a)  $H//a$  direction the (002) Bragg peak and for (b)  $H//b$  the (200) Bragg peak was measured. The red lines are the fit obtained by using equation 4.20.

### 4.5.3 Analysis

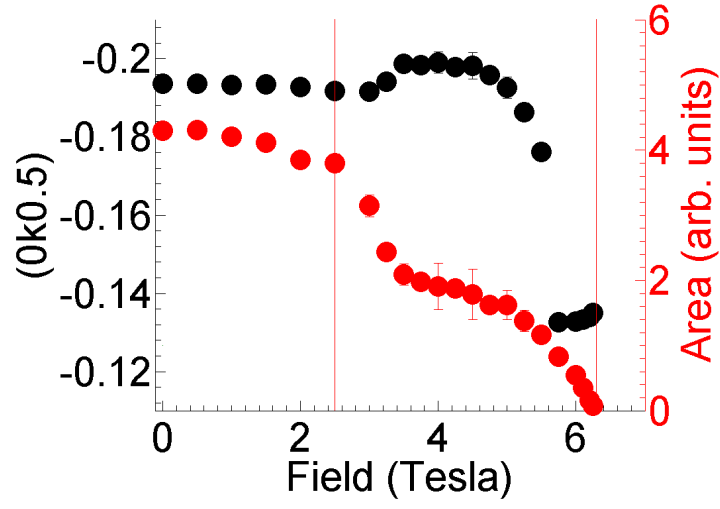
The change in the incommensurate Bragg peak position  $(0, k_{ic}, 0.5)$  with field could be an indication of a  $\text{SDW}_{(p)}$  phase. In order to check this, a Gaussian fit is performed to all  $Q$  scans. The obtained  $k_{ic}$  field dependence is compared to the theoretical predictions of a  $\text{SDW}_{(p)}$  phase. From the Gaussian fits, it is also possible to quantify the change in the area of the incommensurate Bragg peaks. The area of the Bragg peaks is related to  $\mathbf{M}_{\perp}$ , the magnetic moment perpendicular to  $Q$ . Therefore, any discontinuity in the derivative of the Bragg peak area is indicative of a phase transition.

The Bragg peak position and area are plotted together in figure 4.59(a) on page 243, in black and red respectively for the  $H//a$ , 50mK dataset. Here, red vertical lines are presented at 2.5T and 6.29T where there appears to be a phase transition. The 2.5T phase transition is apparent from the large change in the derivative of

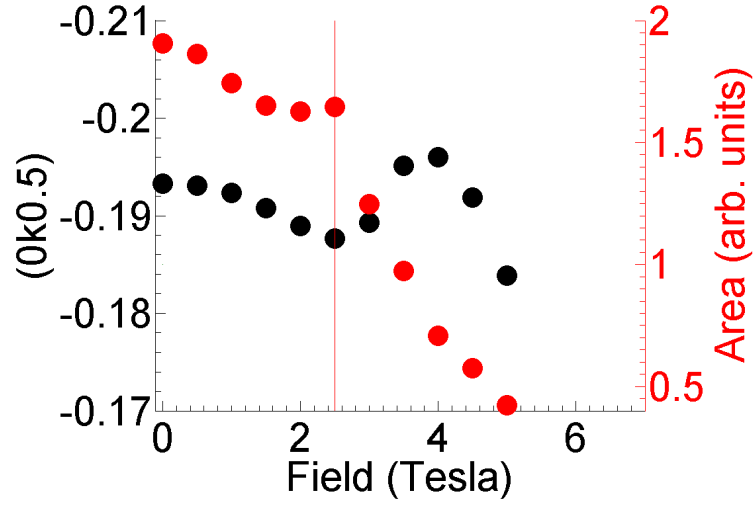
the Bragg peak area. The 6.29T phase transition is obtained by extrapolating the Bragg peak area to zero which occurs precisely at  $\mu_0 H_c = 6.29(1)\text{T}$ . In this figure the movement of  $k_{ic}$  can be seen in more detail. It can be seen that  $k_{ic} = -0.1935(3)$  remains fixed until 1.5T. Between 1.5T and 3.5T,  $k_{ic}$  moves until at 3.5T  $k_{ic}$  reaches  $-0.199(8)$  and remains fixed until 4.5T. There is then movement of  $k_{ic}$  until 5.75T. At 5.75  $k_{ic} = -0.133(2)$  and with increasing field  $|k_{ic}|$  increases slowly until at 6.25T  $k_{ic} = -0.135(1)$ . At higher fields the Bragg peak intensity becomes too small to be directly measured. The  $\mathbf{H} // \mathbf{a}$ , 1.6K dataset can also be seen in figure 4.59(b) in a similar manner. Here only one clear transition can be identified. That is the transition at 2.5T, where the area drops dramatically. It is possible that  $k_{ic}$  continues to  $\sim 0.13$  for 1.6K dataset as well; however, measurements did not extend that far. Therefore, it is not clear if there is another transition at higher temperatures.

The  $\mathbf{H} // \mathbf{a}$  50mK and 1.6K datasets are seen compared directly in figure 4.60 on page 244. Here the 50mK and 1.6K dataset is given in blue and red respectively. The area is normalised to the zero field area,  $A_0$ . In figure 4.60 it can be seen that  $k_{ic}$  and Bragg peak areas behave very similarly for both temperatures. There are a few differences which are worth noting. For 50mK,  $k_{ic}$  is constant up to 1.5T whilst for 1.6K it is constant up to 0.5T. When  $k_{ic}$  is constant the area seems to be roughly constant as well. For 1.6K data the  $|k_{ic}|$  at 2.5T is much smaller than for 50mK data. Also the 1.6K data does not extend to  $|k_{ic}| \sim 0.199$ .

For the  $\mathbf{H} // \mathbf{b}$  direction there is a slight increase in the position of the Bragg peak and a steady decrease of the intensity with increasing field. This can be seen in figure 4.61 on page 244, where the Bragg peak measurements above and below  $k=0$  can be seen in blue and red points respectively. Here  $k < 0$  measurements were close to a hard limit of the instrument and therefore its fitted position could be affected by this. It is for this reason that  $k < 0$  and  $k > 0$  are plotted separately. Note that the 8T measurement is where there is coexistence between the  $k=0$  and



(a)



(b)

**Figure 4.59: Field dependence of  $k_{ic}$  and area.** The  $k_{ic}$  and area field dependence is given in black and red respectively for (a)  $\mathbf{H} // \mathbf{a}$  50mK dataset and (b) 1.6K dataset. Phase transitions obtained from changes in Bragg peak area are given in red vertical lines.

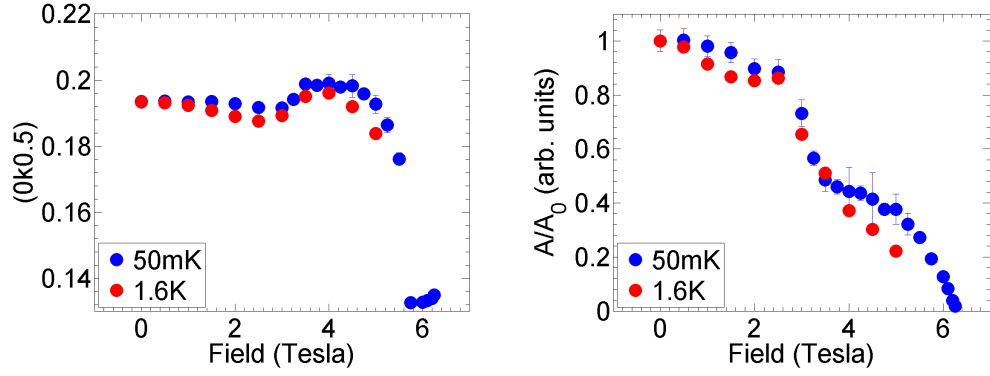


**Figure 4.60:** Field dependence for  $H//a$  with 50mK and 1.6K compared via (a)  $k_{ic}$  and (b) area of the Bragg peak normalised by the 0T Bragg peak area ( $A_0$ )

$k_{ic} \sim 0.1$  phases. The individual fits to the  $H//b$  data can be seen in figure 4.62 on page 245. Note that here the 8T, 8.5T, and 9T datasets have been scaled up by 100, 300, and 500 counts respectively for clarity.

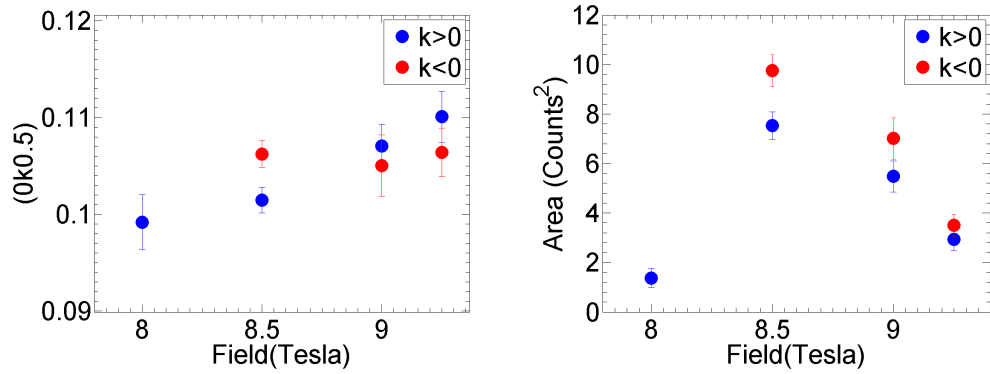


**Figure 4.61:** Field dependence for  $H//b$  at 50mK can be seen in (a)  $k_{ic}$  and (b) area of the Bragg peak. Here  $k < 0$  measurements (given in red) were close to a hard limit and therefore fits to this data may not be correct.

For the  $H//b$  dataset, it is possible to extrapolate where the Bragg peak intensity



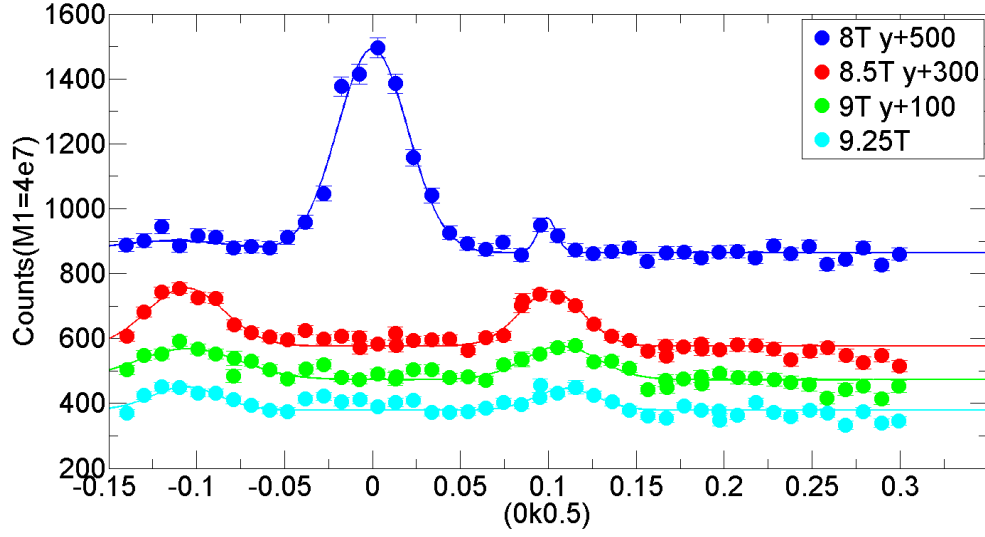


**Figure 4.62: Fits to  $\mathbf{H} // \mathbf{b}$ , 50mK,  $(0, k, 0.5)$  scans.** Note that 8T, 8.5T, and 9T datasets have been scaled up by 500, 300, and 100 counts respectively for clarity.

at  $k_{ic}$  will reach zero. This can be done by fitting a line to the last few points of the area. This gives a critical field of  $\mu_0 H_c = 9.74(8)\text{T}$ . Using the same method for  $\mathbf{H} // \mathbf{a}$  a critical field of  $\mu_0 H_c = 6.29(1)\text{T}$  was obtained. These values may correspond to the saturation field of the system. It is of interest that both of these values are higher than the estimated saturation field from (002) and (200) Bragg peak intensities as seen in figure 4.58 which provided  $\mu_0 H_c = 9.25(25)\text{T}$  and  $\mu_0 H_c = 6.05(5)\text{T}$  for  $\mathbf{H} // \mathbf{b}$  and  $\mathbf{H} // \mathbf{a}$ .

It is possible to check if the observed field dependence of  $k_{ic}$  is compatible with a  $\text{SDW}_{(p)}$  phase. The expected characteristic vector of such a  $\text{SDW}_{(p)}$  phase is  $q_{max} = \pi(1 - m/m_{sat})/p$ . This is defined for a one site per unit cell with the nearest neighbour distance  $d_{NN} = 1$ . In linarite there are two Cu sites along the  $\mathbf{b}$  axis. Therefore  $\tilde{k}_{ic} = k_{ic}/2$  is defined, which corresponds to the new  $\mathbf{b}$  axis with length  $d_{NN} = b/2$ . The expected dependence of the incommensurate Bragg peak becomes

$\tilde{k}_{ic} = (1 - m/m_{sat})/2p$ . The magnetisation,  $m$ , is obtained from interpolating and smoothing the  $m(H)$  curves presented in figure 4.58. For  $m_{sat}$  the 6.29T and 9.74T results are used for  $\mathbf{H} // \mathbf{a}$  and  $\mathbf{H} // \mathbf{b}$  respectively. These saturation fields were obtained by extrapolating the drop in incommensurate Bragg peak area to zero. The calculated and the measured  $\tilde{k}_{ic}(H)$  for  $\mathbf{H} // \mathbf{a}$  and  $\mathbf{H} // \mathbf{b}$  can be seen in figures 4.63(a) and (b) respectively. From these figures it is clear to see that the measured field dependence of  $\tilde{k}_{ic}$  does not follow the predictions of a  $\text{SDW}_{(p)}$  phase for any value of  $p$ . It is important to note that this prediction was made for a one-dimensional  $J_1$ - $J_2$  chain with isotropic exchange.

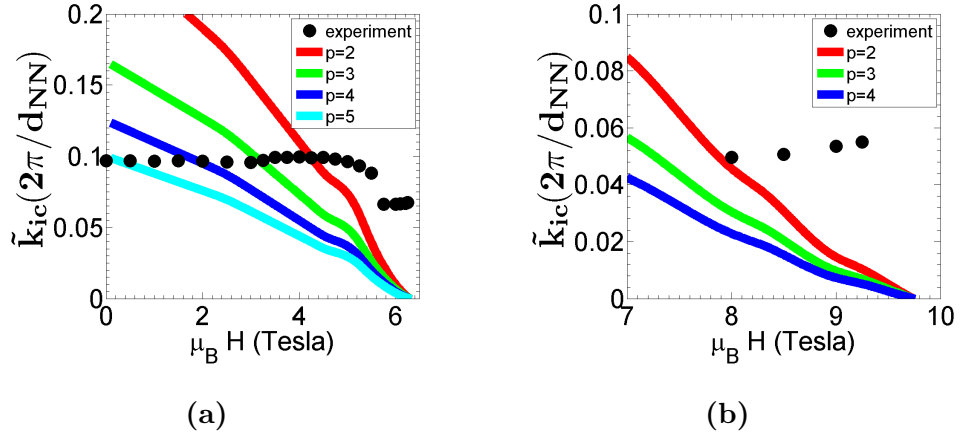


**Figure 4.63: The measured incommensurate Bragg peak position and the expected position from a  $\text{SDW}_{(p)}$  phase.** Here the theoretically predicted characteristic vector for a  $\text{SDW}_{(p)}$  phase is given in the coloured lines as obtained from the equation  $\tilde{k}_{ic} = (1 - m/m_{sat})/2p$ , where  $\tilde{k}_{ic}$  corresponds to  $d_{NN} = b/2$ . For no value of  $p$  is there agreement between the  $\text{SDW}_{(p)}$  prediction and the experimentally measured  $\tilde{k}_{ic}$  (black points). This is true for both (a)  $\mathbf{H} // \mathbf{a}$  and (b)  $\mathbf{H} // \mathbf{b}$  field directions.

## 4.6 Magnetisation Measurements

Magnetisation measurements on linarite were performed for two main reasons. The primary reason was to identify the position of the spin plane as there were two different proposed magnetic structures in the literature (see subsection 4.1.4). These two structures correspond to having the spin plane  $-27^\circ$  or  $74.5^\circ$  from  $\mathbf{a}$  axis. The latter corresponds to having the spins in the Cu-O plane. This disagreement in the orientation of the spin plane could originate from the confusion in literature regarding the crystal structure (see subsection 4.1.3). The aim of this part of the thesis work was to perform magnetisation measurements within the  $\mathbf{ac}$  plane for linarite. For the experiment, an untwinned crystal was used and its correct orientation was determined using neutron diffraction experiments. When the field is applied along the spin-plane, a spin-flop transition is expected which is easily identifiable by a “S” shaped curve in the magnetisation.

Magnetisation measurements were performed on a Quantum design MPMS at Max-Planck Institute, Stuttgart, Germany. A rotation stage was able to perform  $360^\circ$  rotations at a base temperature of 1.8K and at a maximum field strength of 7T. An untwinned crystal of mass  $\sim 21\text{mg}$  (crystal 3) was mounted on the copper rotation stage with the rotation axis along the  $\mathbf{b}$  axis, so that the magnetisation in the  $\mathbf{ac}$  plane could be explored. This set-up can be seen in figure 4.64 on page 248 where the  $\mathbf{c}^*$  crystal face and the positive rotation direction are shown. The direction of  $\mathbf{b}^*$  and the crystal faces were obtained on IN3 triple axis spectrometer at the ILL, Grenoble. By measuring the  $(-101)$  and  $(001)$  type reflections it is possible to distinguish between the  $\mathbf{b}^*$  and  $-\mathbf{b}^*$  directions.

The rotation mechanism was calibrated using a small piece of magnetised Ni wire. However, when changing between positive and negative rotation 10 to  $15^\circ$  of backlash was observed in the measurements. This made determining the exact angular position of the crystal inside of the MPMS challenging. Three different

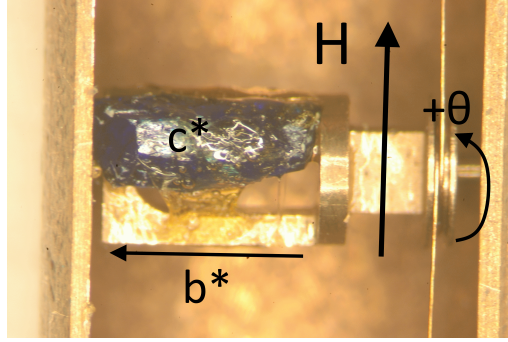


**Figure 4.64: Experimental set up for magnetisation measurements.** The crystal was mounted in the rotation stage as shown. The  $b^*$  direction and the  $c^*$  face were identified in prior neutron diffraction experiments.

methods were used to determine the orientation of the crystal within the MPMS, they were all within  $\sim 5^\circ$  agreement. The first method depends on measuring the magnetisation with rotation above  $T_N$ . Such a measurement can be seen in figure 4.65 on page 249, which was obtained by supplying a small field of  $\mu_0 H = 0.1 \text{ T}$ . Since Linarite has a Néel temperature of  $T_N \sim 2.8 \text{ K}$  [24], the 4K measurement (red) probes the paramagnetic phase whilst the 1.8K measurement (blue) probes the helical phase. In the paramagnetic phase of linarite, the largest moment should be perpendicular to the  $\text{CuO}_2$  planes. This is due to the Jahn-Teller distortion [175] on the Cu-O octahedron. An elongation of an octahedron along the  $z$  axis will cause the degeneracy between  $d_{z^2}$  and  $d_{x^2-y^2}$  to split and  $d_{z^2}$  to shift to a lower energy [176]. Therefore, the maximum long moment in 4K data corresponds to  $\mathbf{H}/\mathbf{n}_\perp$ , i.e. at the maximum of 4K curve the field is parallel to normal of the  $\text{CuO}_2$  planes,  $\mathbf{n}_\perp$  [177]. For now this method for determining the orientation will be assumed to be correct. At the end of this section it will be compared to the other two methods for determining the orientation. The 1.8K measurement shows a phase shift of  $-100^\circ$  compared to the 4K data. For a helical magnetic structure,

the smallest induced uniform magnetic moment is expected when the field is applied within the spin plane. Therefore, one can conclude that the spin-plane should be  $-10^\circ$  from  $\mathbf{n}_\perp$ . However, a more robust method of determining the position of the spin plane is to find the lowest field for which a spin-flop transition occurs. The spin plane position obtained using this method is different to the minimum of the 1.8K data and is denoted by SP in figure 4.65.

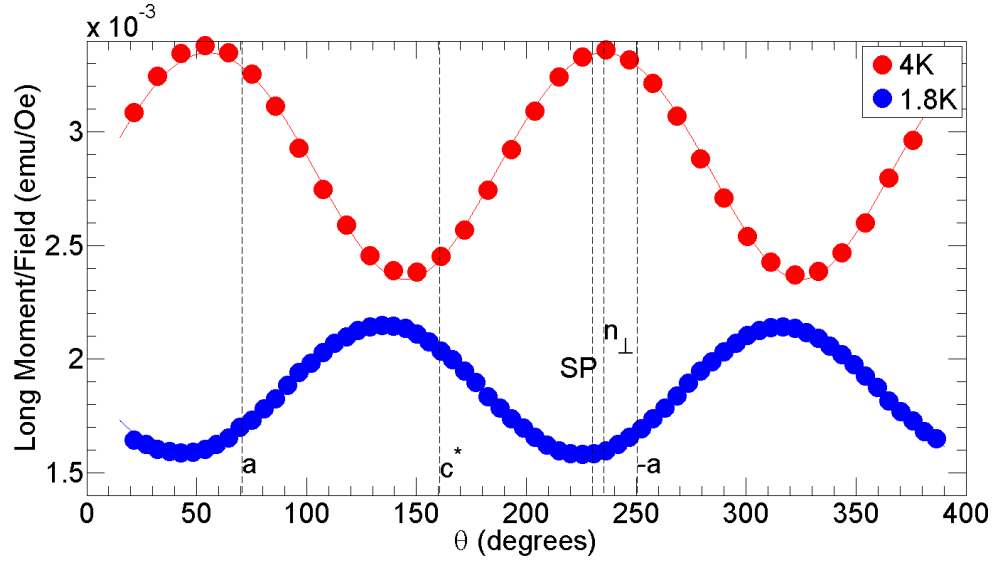


**Figure 4.65: Magnetisation vs rotations scans** at 4K (red) and 1.8K (blue) which are above and below the Néel temperature. The 4K maximum provides  $\mathbf{n}_\perp$ , the direction perpendicular to the Cu-O planes. The spin-plane is denoted as SP and does not correspond to the minimum of 1.8K data.

At a base temperature of 1.8K, magnetisation measurements were performed at various angles with field scans from 0T to 7T and back to 0T. For most of the directions two clear phase transitions were observed. The resulting phase diagram can be seen in figure 4.66 on page 250. Here the field angle  $\theta$  is the same as that in figure 4.65 and the orientation of the crystal was obtained in the same way. The

field-rotation phase diagram can be split into three main regions: the  $200^\circ$ - $250^\circ$  region where there are transitions at 3T and 4T,  $200^\circ$ - $150^\circ$  where there are two transitions with hysteresis, and  $150^\circ$ - $110^\circ$  where there is only one transition visible. There is potentially a fourth region at  $90^\circ$  which shows hysteresis and therefore might be similar to the  $200^\circ$ - $150^\circ$  region. Note that the location of saturation was not clear, therefore it is not shown in the phase diagram in figure 4.66.

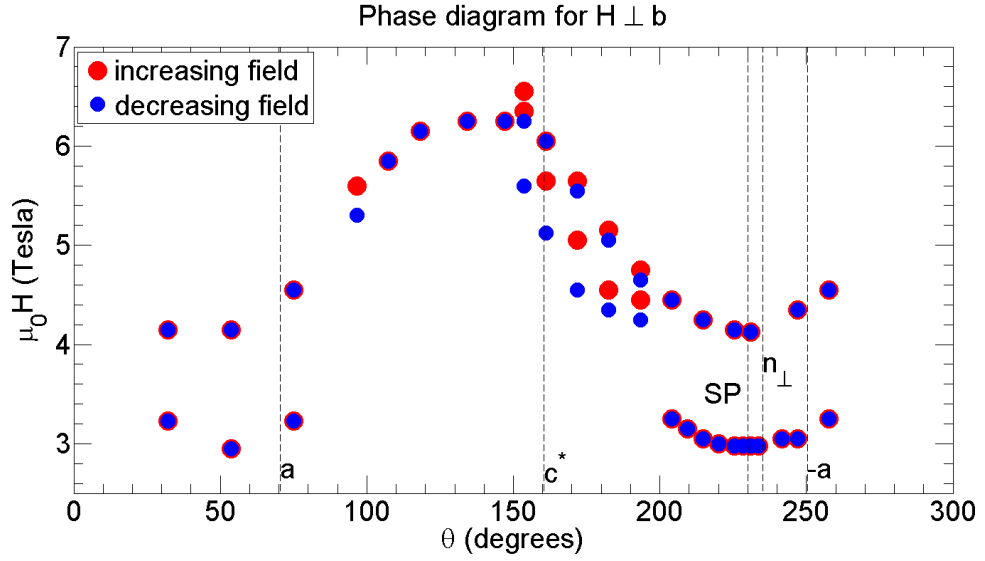


**Figure 4.66: Field-rotation phase diagram** as obtained for 1.8K and  $H \perp b$ . The  $\sim 3\text{T}$  transition in the region  $200^\circ$ - $250^\circ$  is most likely a spin-flop transition. The  $200^\circ$ - $150^\circ$  region show hysteresis. In the region  $150^\circ$ - $110^\circ$  only one transition was measured up to 7T.

In figure 4.67 on page 251, examples of each one of these three main regions can be seen. At  $225^\circ$  the first transition can be seen at 3T with a “S” shaped curve and the second, less pronounced, transition at 4T. At  $134^\circ$  only one transition can be seen; however, another transition could easily exist at higher field strengths. At  $172^\circ$  two transitions can be seen and at each transition hysteresis is observed. The “S” shaped curve is indicative of a spin-flop transition, all of the  $\sim 3\text{T}$  transitions in

the range  $200^\circ$ - $250^\circ$  show this kind of curve. The minimum field for a spin-flop was extrapolated using these points and was found to be at  $-5^\circ$  from  $\mathbf{n}_\perp$  at a field of  $2.96(1)$ T. Therefore, the spin plane is at  $-5^\circ$  from  $\mathbf{n}_\perp$  which corresponds to  $-20.35^\circ$  from the  $\mathbf{a}$  axis.

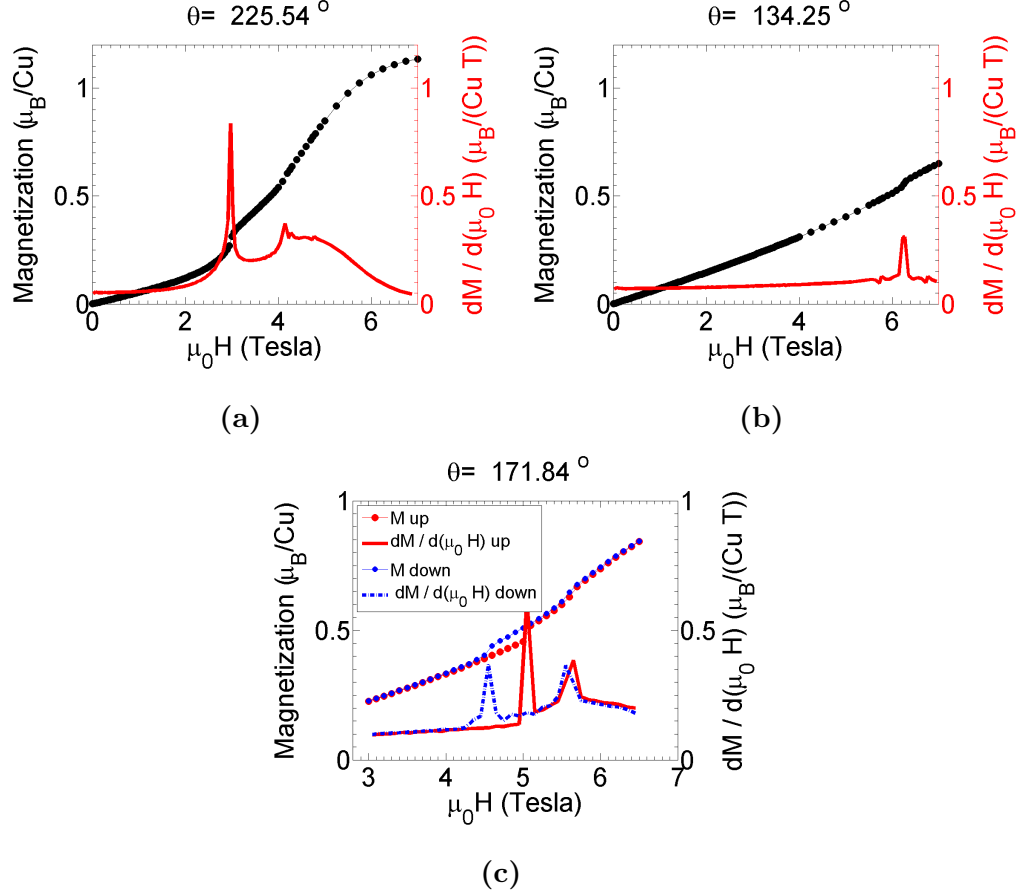


**Figure 4.67: Example magnetisation curves.** An example for each region of the phase diagram in figure 4.66 can be seen. (a) At  $225^\circ$  there is a “S” shaped transition at 3T which is indicative of a spin-flop. (b) At  $134^\circ$  there is a only one measured transition. (c) Measurements at  $171^\circ$  show two transitions and both of them have hysteresis.

Aside from various rotations, a detailed field and temperature dependence was

also measured for  $\mathbf{H}/\mathbf{n}_\perp$  which can be seen in figure 4.68. Both temperature and field scans were used to construct the phase diagram which are given in red and black respectively in the figure. The phase transitions going into the helical phase were very easy to identify; however, the others were usually a very small signal in the gradient of magnetisation. These smaller signatures are shown as squares in figure 4.68. Despite this uncertainty from the small signatures, a consistent phase diagram does appear where three different phases can be identified. In this phase diagram the saturation limit is not shown because it could not be reached. Using the  $\partial M/\partial H = 0$  definition for saturation, none of the measured angles showed saturation at 7T and 1.8K.

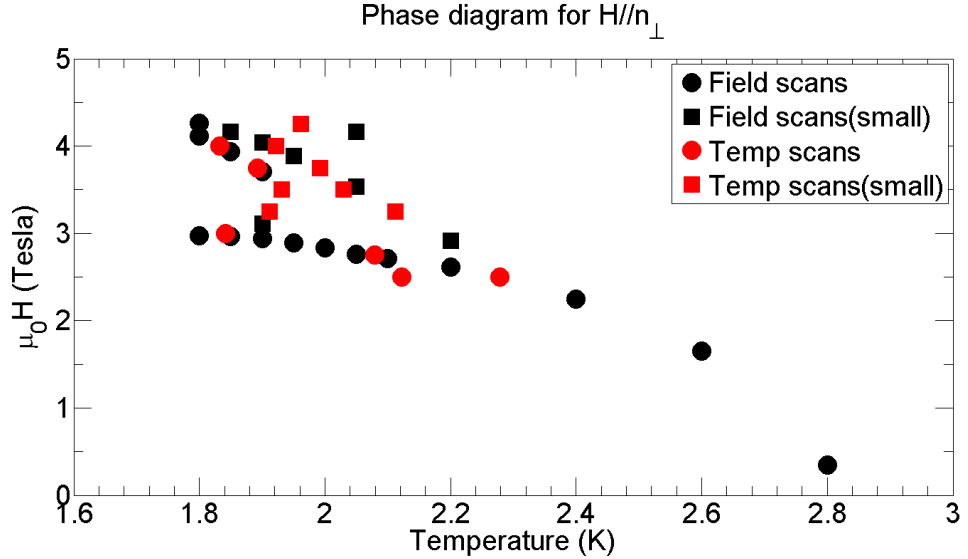


**Figure 4.68:** Field-temperature phase diagram for  $\mathbf{H}/\mathbf{n}_\perp$ .

There are three clear phases apart from the paramagnetic and FM phases.

Some of the  $M(H)$ ,  $M(T)$  curves which make up the  $\mathbf{H}/\mathbf{n}_\perp$  field-temperature phase diagram can be seen in figure 4.69 on page 254. In figure 4.69(a) the  $M(H)$  curve at 1.8K and its three clear transitions can be seen. In figure 4.69(b) a similar measurement at 2.05K can be seen. These two higher field transitions are much



weaker at 2.05K compared to 1.8K. Note that both the 1.8K and 2.05K  $M(H)$  curves were measured from 0T to 7T. The regions of interest were measured again with a much smaller step size. It is these smaller step sized  $M(H)$  curves which are shown in figures 4.69(a) and (b). The  $M(T)$  curves in figure 4.69(c-d) both show two clear transitions and an anomalous transition like signal at 2.2K. This 2.2K signal was present in all  $M(T)$  curves measured from 1T up to 7T. This makes it unlikely that it is caused by the sample. The most likely explanation is the superfluid transition of  $^4\text{He}$ , which is at 2.172K [178]. Note that all  $M(T)$  curves were measured up to 4K. The regions of interest were measured in smaller step size. It is these measurements which are presented in figures 4.69(c-d).

Note that the  $M(T)$  curves have been measured up to 4K but only in figures 4.66(c-d) only the measurements with small step sizes are shown.

The  $\mathbf{H}/\mathbf{n}_\perp$  phase diagram in figure 4.68 is mostly self-consistent despite some relatively small thermomagnetic signatures (which are given in black or red squares). There are two points which appear to be inconsistent, which are close to 4.25T, 2K. The first can be seen in figure 4.69(b) in the 2.05K  $M(H)$  curve at 4.16T. A very weak peak can be observed in the derivative here, because it is so weak this point might not be an actual transition but simply a fluctuation in the background. The second inconsistent point can be seen in figure 4.70(a,b), on page 255, in the 4.25T  $M(T)$  curve at 1.97K. Here there is a clear jump in magnetisation. The fact that one of the points is much higher than the others indicates that this point might be from a spurious signal. A similar peak is observed at 1.98K in the 7T  $M(T)$  curve. This can be seen in figure 4.70(c,d). This peak is not observed clearly in any other  $M(T)$  curve despite a measurement every 0.5T between 7T and 4.5T. Therefore, the small peak in magnetisation at  $\sim 1.97\text{K}$  for 4.25T and 7T must originate from a spurious signal. This could mean that the two inconsistent points in the  $\mathbf{H}/\mathbf{n}_\perp$  phase diagram in figure 4.68 could potentially be discarded.

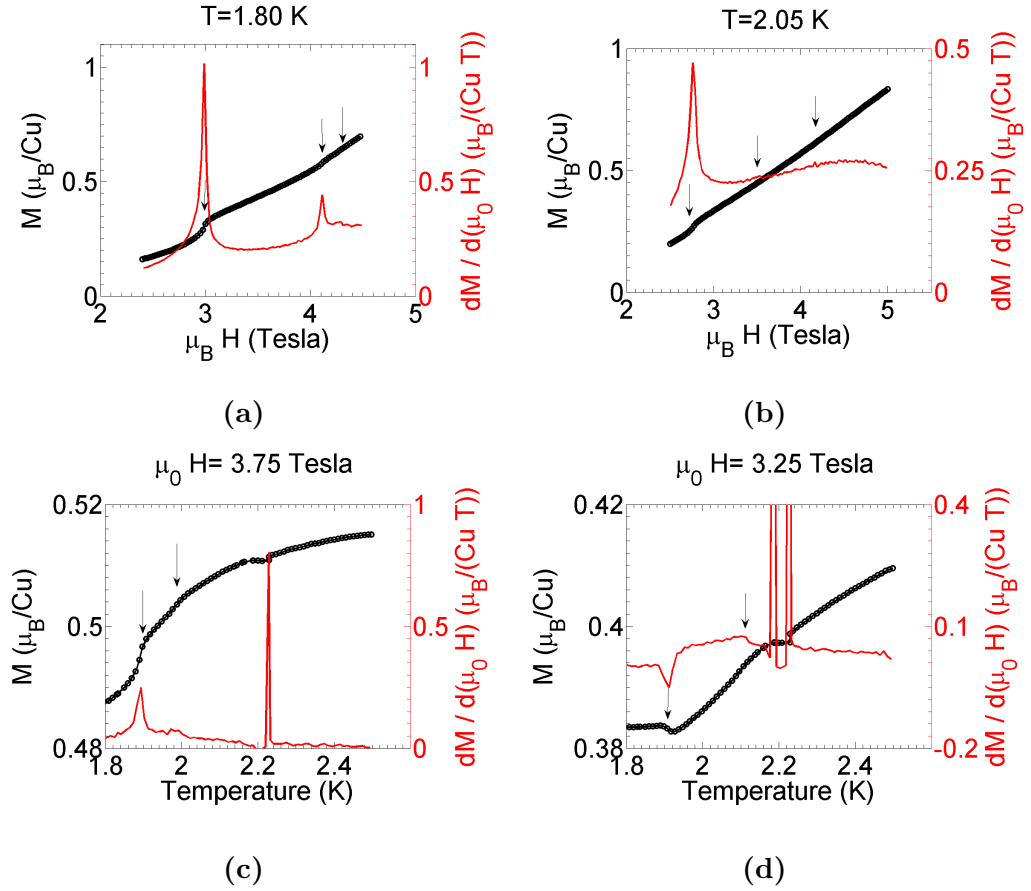


**Figure 4.69: Examples of  $H//n_\perp$   $M(H)$  and  $M(T)$  curves.** These curves have been used to construct the field-temperature phase diagram in figure 4.68. **(a,b)** In the  $M(H)$  curves the clearest signal is from the helical phase boundary. **(c,d)** The  $M(T)$  curves show some clear signals as well; however, they also show a spurious signal at 2.2K which is believed to originate from the superfluid transition of  $^4\text{He}$ .

The  $H//n_\perp$  phase diagram also sheds some light into the 1.8K  $H$ - $\theta$  phase diagram presented in figure 4.66. Note that in the angular range  $200$ - $250^\circ$  only two phase transitions are shown. However in the  $H//n_\perp$  phase diagram at 1.8K there is three clear transitions. This is because a much smaller step size was used for obtain-

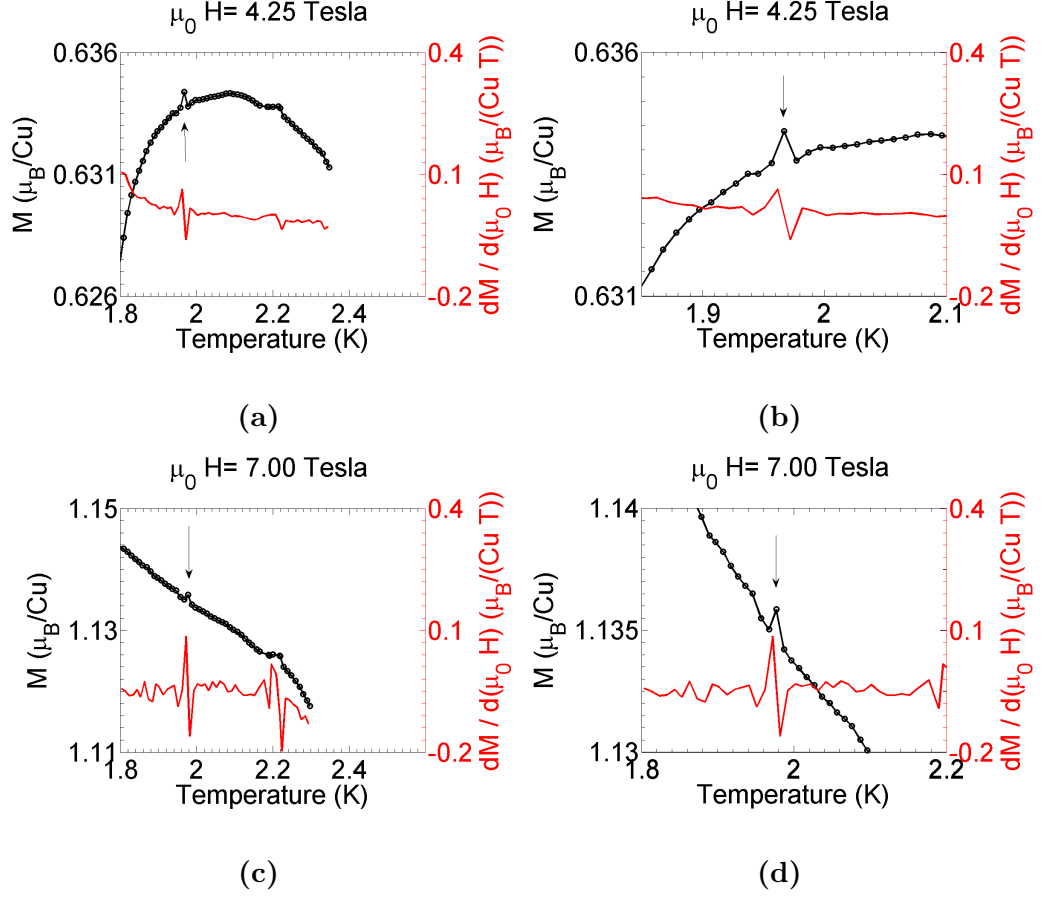


**Figure 4.70: Spurious signal in  $M(T)$  seen at (a,b) 4.25T and (c,d) 7T. The peaks in magnetisation appear at  $\sim 1.97\text{K}$  for both fields. None of the  $M(T)$  measurements between 7T and 4.25T has such a feature.**

ing  $\mathbf{H} // \mathbf{n}_\perp M(H)$  curves. It is possible that throughout the  $200\text{-}250^\circ$  region there is a third phase transition just above the  $\sim 4\text{T}$  transition. Further measurements with a smaller step size are necessary to confirm this.

So far it has been assumed that the maximum of the 4K curve in figure 4.65 corresponds to  $\mathbf{H} // \mathbf{n}_\perp$ . However, this is only the first of three different methods used to try to obtain the orientation. The second method for determining the orientation of the crystal within the cryostat was to remove the sample at various angles and to

take pictures of it. Using the knowledge of the crystal faces, it was possible to make some rough estimates of the orientation of the crystal. Ten different pictures were used in total. The average of this picture method is in  $-1(5)^\circ$  disagreement with the first method. This cannot be taken as a direct confirmation of the first method for determining the structure. The photograph method was simply not precise enough. However, it does suggest that the first method must be correct within roughly  $\sim 5^\circ$ . For the third method, the crystal was put in with  $\mathbf{H} // \mathbf{a}$  and no rotation operations were performed. The obtained  $M(H)$  curve for  $\mathbf{H} // \mathbf{a}$  was then compared to the  $53.65^\circ$  and  $75.11^\circ$  measurements which can be seen in figure 4.71(a-b) on page 257. The  $\mathbf{H} // \mathbf{a}$   $M(H)$  curve is very similar to that of the  $75.11^\circ$  measurement except for the higher field region where  $\mathbf{H} // \mathbf{a}$   $M(H)$  curve is a bit higher. However compared to the  $53.65^\circ$   $M(H)$  curve, the  $\mathbf{H} // \mathbf{a}$   $M(H)$  curve is lower at high fields. This guarantees that the  $\mathbf{H} // \mathbf{a}$  exists between  $53.65^\circ$  and  $75.11^\circ$ . By linear interpolation, it is possible to obtain an angle for  $\mathbf{H} // \mathbf{a}$  measurement. The low field part of  $\mathbf{H} // \mathbf{a}$  measurement results in an angle of  $\sim 72^\circ$  whilst the higher field part results in an angle of  $\sim 65^\circ$ . In the first method model, shown in figure 4.65, the  $\mathbf{a}$  axis belongs at  $70.5^\circ$ . Therefore, there is an overall agreement between the first and third methods as well. In the worst case scenario, the difference between the first and third methods is  $\sim 5^\circ$ .

There is another possible problem with assuming the first orientation model is correct. It has been assumed that at 4K, the temperature is high enough so that the magnetic response is only due to the anisotropy in the  $g$  tensor and not due to the anisotropy of the exchange interactions. In fact, ESR line widths indicate that short range correlations could start developing at  $\sim 50$ K. Therefore, one cannot simply assume that at 4K, the system is fully paramagnetic and only the  $g$  tensor anisotropy applies.

It would be useful to make similar magnetisation with rotation measurements at

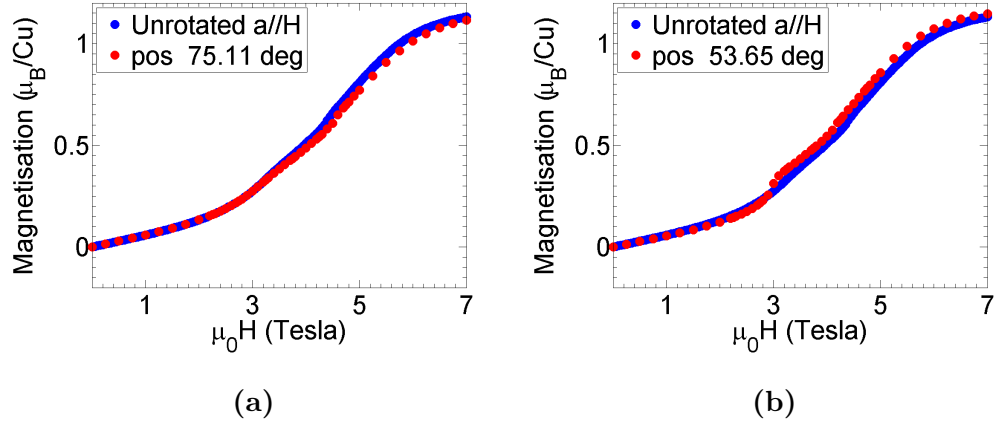


**Figure 4.71: Determining the orientation of the sample within the MPMS.** The sample is placed within the MPMS with  $\mathbf{H} // \mathbf{a}$  orientation. The  $M(H)$  curve obtained is compared to the (a)  $75.11^\circ$  and (b)  $53.65^\circ$  measurements of the previous dataset.

much higher temperatures. For linarite, the magnetisation with rotation was measured for temperatures up to 10K. In order to find the phase shift with temperature, the following function was fitted to the data:

$$f(\theta) = \sqrt{y_1^2 \sin^2(\theta + \theta_0) + y_2^2 \cos^2(\theta + \theta_0)} \quad (4.21)$$

Here  $\theta$  is the rotation angle  $\theta_0$  is the phase and  $y_1$  and  $y_2$  are arbitrary constants. The evolution of  $\theta_0$  with temperature can be seen in figure 4.72 on page 258. It is important to note that this data was obtained from a slightly different mounting of the crystal and therefore it does not share the same  $\theta$  offset as the rest of the results stated in this section. Two important observations can be made from the  $\theta_0$  temperature dependence in figure 4.72. The first is that the position of the magnetic transition is apparent at  $\sim 2.7\text{K}$ . The second important observation is that from 4K to 10K, there is a phase shift of  $1^\circ$ . This shows that at 4K the magnetisation signal is not only dependent on the  $g$  tensor. It might be necessary to go to temperatures

above 10K to obtain a magnetisation signal only dependent on the  $g$  tensor.

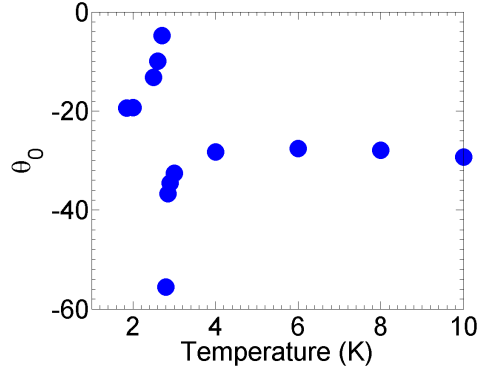


**Figure 4.72: Temperature dependence of phase  $\theta_0$ .** From 4K to 10K there is  $1^\circ$  difference.

## 4.7 Discussion

The main achievement of the thesis work is shedding light to the magnetic interaction scheme of linarite by performing INS experiments above saturation field. A total of four different spin-wave models are used to describe the data. All of the models point towards exchange interactions  $J_1 \sim 14\text{meV}$  (FM) and  $J_2 \sim -4\text{meV}$  (AFM). In most of the models the strongest inter-chain interaction appears to be an AFM skew interaction  $J_{c0} \sim -0.6\text{meV}$ . These values are much different from those reported in literature. The  $J$  parameters obtained from spin waves are larger than those reported from physical-property measurements. Similarly, the ratio  $\alpha = J_2/J_1 \sim -0.275$  obtained from INS data is much closer to  $\alpha = -0.25$  than any other reports in literature [24–26]. It is important to reiterate that even within the models which are based on physical-property measurements there is very little agreement.

It must be acknowledged that the spin-wave models used to describe the INS data above the saturation field were not perfect. Firstly, there is imperfect information

regarding the orientations of the crystals in the experiments. It is possible that these orientations may have changed for some of the crystals for different field strengths. At least in the D23 experiments it was observed that the torque on the crystal due to the magnetic field was large enough to break the crystal. Secondly, there appears to be a large energy difference observed between the (001) spin waves measured at 11T and 14.5T. If the observed energy change of  $\sim 0.6\text{meV}$  were only attributed to  $g_{avg}\mu_B H$ , one would expect an average  $g$  factor of  $g_{avg} = 2.79(2)$ , which is too large and incompatible with the rest of the dataset. For this reason a spin-wave model was tested which does not have a linear field energy dependence, instead, the relative energy shift for each field strength was left as a free parameter. The validity of such an approach is questionable; however, this model provided a much better fit to the data compared to the other models. A non-linear energy-field dependence is beyond the simple LSWT models which have been used in this thesis and therefore a different theoretical approach might be necessary. It would be beneficial to validate the non-linear energy-field dependence with another set of INS experiments. An experiment with a better orientation should be carried out and the (001) spin-wave dispersion should be measured for different field strengths. At every field strength, the orientation of the crystal should be checked. The third imperfection of the spin-wave models is their disagreement with the 10T high energy data. This problem might be related to the non-linear energy-field dependence of the spin-waves or it might be related to the imperfect orientations. Either way, to describe this part of the data a third nearest-neighbour interaction  $J_3$  was introduced. In the non-linear energy-field dependence spin-wave model a small AFM  $J_3 = -0.65(5)$  interaction was able to provide a more accurate fit to the high energy 10T data.

Putting aside the non-linear energy-field dependency concept, the average  $g$  factor  $g_{avg}=2.36(3)$  obtained from the isotropic  $J_1 - J_2$  spin-wave model is in agreement with  $g_a=2.34$  obtained by Wolter et al. via ESR measurements at  $\sim 50\text{K}$  [26].

Even though in their initial article they cite the Schofield article for structure, their later work (Ref. [153]) has the correct atomic positions which indicates that they are using the Effenberg-Araki structure as well.

In addition to the saturated phase, linarite's zero field excitations were measured. The excitations appear magnon-like and therefore a simple spin-wave model was used to obtain some  $J$  parameters. It is important to note that the zero field spin-wave model has no anisotropy and is treated classically. For frustrated quasi-one-dimensional spin-1/2 systems, quantum fluctuations can become strong which can stabilise complex ground states. A simple spin-wave model can still be used to parametrise the system; however, these parameters are now non-trivially related to the original  $J$  parameters of the system. The  $J$  parameters obtained at zero field,  $J^{zero}$ , can be compared to those obtained above saturation field,  $J^{sat}$ , in table 4.19 on page 260. Here the isotropic  $J_1$ - $J_2$  model has been used for  $J^{sat}$ . These two parameter sets are often compared through  $R_i J_i^{sat} = J_i^{zero}$ , where  $R$  is referred to as the normalisation for zero field [169]. Here it can be seen that  $R_i \sim 0.5$  for almost all interactions. This is different to the observations of  $\text{LiCuVO}_4$  where only the AFM  $J_2$  interaction was normalised by  $R_2 = \pi/2$ .

Parameter	$J_1$	$J_2$	$J_{c0}$	$J_{c1}$	$J_a$
$J_i^{sat}$	14.6(1)	-4.02(4)	-0.62(7)	0.05(4)	0.124(5)
$J_i^{zero}$	6.38(4)	-1.94(1)	-0.398(8)	0.0000(1)	0.05(1)
$R_i$	0.44(4)	0.48(1)	0.64(7)	-	0.40(2)

**Table 4.19: Comparison of  $J$  parameters obtained above saturation ( $J_i^{sat}$ ) and at zero field ( $J_i^{zero}$ ).** The normalisation due to quantum fluctuations are given by  $R_i = J_i^{zero}/J_i^{sat}$ . The  $J$  parameters are given in units of meV.

The zero field spin-wave model does manage to qualitatively explain many of



the INS features observed. There are a few features that it fails to explain. Firstly, one of the spin-wave branches observed between  $(0,0,0.5)$  and  $(0,0.2,0.5)$  is not reproduced in the calculations. Secondly, the intensity of the spin-waves drop rapidly and become hard to resolve above  $\sim 1\text{meV}$ . However, in the spin-wave calculations, there is no rapid decrease in intensity. It might be possible to explain some of these features by expanding upon the simple spin-wave model used. Ideally, a theoretical model which considers the quantum nature of the system would be used. However, by introducing anisotropy to the LSWT model one could improve the fit. It might be necessary to introduce an anisotropy which would result in an elliptical helical magnetic order.

The position of the magnetic Bragg peak was measured at  $\sim 50\text{mK}$  for  $\mathbf{H} // \mathbf{b}$ . The obtained results can be compared to the  $\mathbf{H} // \mathbf{b}$  phase diagram of Willenberg et al. [148], as seen in figure 4.11. Based on this phase diagram, for  $50\text{mK}$ , phase IV is expected from  $\sim 4\text{T}$  to  $8\text{T}$  and phase V is expected from  $8\text{T}$  to  $\sim 9.5\text{T}$ . Phase IV is known to be an AFM structure with a propagation vector of  $(0,0,0.5)$ , and phase V is estimated to be a SDW with an incommensurate propagation vector of  $(0, k_{ic}, 0.5)$  [148, 150]. In phase V, the value of  $k_{ic}$  first decreases then increases with increasing field, as seen in figure 4.13(a) [154]. The results presented in this thesis can expand upon the results of Willenberg et al. [154]. At  $\sim 50\text{mK}$  for  $\mathbf{H} // \mathbf{b}$ , Bragg peaks were measured at  $(0,0,0.5)$  and  $(0, k_{ic}, 0.5)$ , which can be taken as an indication of phase IV and phase V respectively. In agreement with Willenberg et al.'s phase diagram, the  $(0,0,0.5)$  Bragg peak was observed at  $7\text{T}$  and  $8\text{T}$ . However, at  $8\text{T}$  both  $(0,0,0.5)$  and  $(0, k_{ic}, 0.5)$  Bragg peaks are measured which would suggest a coexistence of phase IV and phase V. The  $(0, k_{ic}, 0.5)$  Bragg peaks continued from  $8\text{T}$  until  $9.25\text{T}$ . From a linear extrapolation of the Bragg peak area, the area is expected to reach zero at  $\mu_0 H_c = 9.74(8)\text{T}$ . This is slightly higher than the value of  $\sim 9.5\text{T}$  stated the phase diagram. From  $8\text{T}$  to  $9.25\text{T}$  the measured position of the

Bragg peak changes from  $k_{ic} \sim 0.1$  to  $k_{ic} \sim 0.11$  in a linear fashion. This is similar to the value of  $k_{ic} \sim 0.1$  which has been reported in literature for  $\sim 7\text{T}$ ,  $1.8\text{K}$  [154].

The position of the magnetic Bragg peak was also measured for  $\mathbf{H} // \mathbf{a}$  direction. In literature, this field direction has not been explored with diffraction experiments. Neutron diffraction measurements at  $\sim 50\text{mK}$  and  $\sim 1.6\text{K}$  can be compared to the magnetisation measurements carried out for this field direction. For  $\mathbf{H} // \mathbf{a}$ , there are two very clear transitions at  $\sim 50\text{mK}$ , as obtained from change in Bragg peak area. The first one is at  $2.5\text{T}$  and the second one is at  $\mu_0 H_c = 6.29(1)\text{T}$  which is obtained by extrapolating the Bragg peak area to zero. For  $1.6\text{K}$  diffraction data a clear transition at  $2.5\text{T}$  can also be seen. Another clear transition may exist at higher field strengths, but this was not adequately explored. From the magnetisation measurements, for  $\mathbf{H} // \mathbf{a}$  at  $1.8\text{K}$ , a spin-flop transition is expected at  $\sim 3\text{T}$  and a second transition is expected at  $\sim 4.4\text{T}$ . For  $\mathbf{H} // \mathbf{n}_\perp$ , which is only  $-15.35^\circ$  from the  $\mathbf{a}$  axis, at  $1.8\text{K}$  these two transitions are also observed but additionally a third transition can be observed at  $\sim 0.1\text{T}$  after the second transition. It is possible that such a weak third transition also exists for  $\mathbf{H} // \mathbf{a}$  magnetisation data as well. One would assume that the  $2.5\text{T}$  transition observed in neutron diffraction would also correspond to the spin-flop transition observed in magnetisation measurements at  $\sim 3\text{T}$ . The slight differences in spin-flop field might be attributed to the differences in the experiments. The diffraction measurements were carried out on twinned crystals at  $1.6\text{K}$  with a step size of  $0.5\text{T}$ . The magnetisation measurements were carried out on untwinned crystals at  $1.8\text{K}$ .

The saturation field has been estimated in a few different ways. It would be of interest to see how these different estimates compare to each other. Before the comparison, it is important to note that for  $\mathbf{H} // \mathbf{a}$  and  $\mathbf{H} // \mathbf{b}$  the incommensurate Bragg peaks are still visible at  $6.2\text{T}$  and  $9.25\text{T}$  respectively. These field strengths can be used as lower limits for the saturation field. Note that, in literature for

$\mathbf{H} // \mathbf{a}^*$  at 1.8K, magnetisation measurements have found  $\mu_0 H_{a^*}^{sat} \sim 7.6\text{T}$  [26]. This orientation is only  $12.65^\circ$  from  $\mathbf{H} // \mathbf{a}$ ; therefore, it is expected for the two field directions to have similar saturation fields. The different saturation limit estimates are tabulated in table 4.20 on page 264. Here the first method uses the areas of the (002) or (200) Bragg peaks to determine a critical field. It can already be seen that for  $\mathbf{H} // \mathbf{a}$  this method provides a value lower than the lower limit of 6.2T. Based on this, the estimate for  $\mathbf{H} // \mathbf{b}$  could be inaccurate as well. The second method is linearly extrapolating the area of the incommensurate Bragg peak area to zero field. The third and fourth methods use the isotropic and anisotropic LSWT fits to the data. Using LSWT, it is possible to obtain a lower limit to the saturation field. For the isotropic model, many different estimates for the lower limit were made, and here only the largest and smallest values are stated. It is not clear how accurate any of these estimates are considering the data is not compatible with a linear field-energy dependence for the spin-wave branches. In order to obtain an accurate estimate of the saturation, the issues with the field-energy dependence of the spin waves must be addressed. Regardless of these problems, it can be seen that these current isotropic LSWT estimates are similar to that of  $\mu_0 H_{a^*}^{sat} \sim 7.6\text{T}$  [26] as found for  $\mathbf{H} // \mathbf{a}^*$ . On the contrary, the anisotropic LSWT models give a larger saturation field. One could speculate that the true saturation field for  $\mathbf{H} // \mathbf{a}$  is in the region of  $\sim 7\text{T}$ , which could mean that there is another phase between 6.29(1)T and  $\sim 7\text{T}$ . In order to determine the saturation field reliably, and to search for any additional phases, a detailed magnetisation measurement at 50mK would be necessary. For the  $\mathbf{H} // \mathbf{b}$ , the end of phase V is stated at  $\sim 9.5\text{T}$  in the phase diagram in figure 4.11 for  $\sim 0.25\text{K}$ . This is in compatible with the 50mK results which states that the lower limit is 9.25T and that the  $(0k0.5)$  area extrapolated to zero reaches 9.74(8)T.

Method	$\mu_0 H_a^{sat}$ (Tesla)	$\mu_0 H_b^{sat}$ (Tesla)
(002) or (200) area	6.05(5)	9.3(3)
(0 $k$ 0.5) area reaches zero	6.29(1)	9.74(8)
LSWT isotropic models	7.3-8.2	-
LSWT anisotropic models	8.8,9.3	-

**Table 4.20: Estimating the saturation fields for  $\mathbf{H}/\mathbf{a}$  and  $\mathbf{H}/\mathbf{b}$ .** Note that first two methods were performed at 50mK, but for the LSWT models, measurements were made at  $\sim 1.6$ K.

The magnetisation measurements performed on linarite were able to help on three important points. Firstly, the orientation of the spin-plane was found at  $\sim -20^\circ$  from  $\mathbf{a}$  axis with an accuracy of  $\sim 5^\circ$ . Magnetic structure solutions based on neutron diffraction find the spin plane at  $-27(2)^\circ$  [150]. This result is in agreement with the findings in this thesis. On the contrary, the magnetic structure stated by Yasui et al. [25], which suggest that the spin-plane is in the Cu-O planes, is not compatible with the findings in this thesis. A strong part of the crystal orientation determination was the magnetisation measurements within the  $\mathbf{ab}$  plane performed above the Néel temperature. The structure determined from these measurements (figure 4.65) is in agreement with similar measurements made by Schäpers et al. [153] (figure 4.10(b)), but not in agreement with those of Szymczak et al. [152](figure 4.10(a)). Secondly, a preliminary magnetic phase diagram was established for rotation within the  $\mathbf{ab}$  plane for 1.8K. This phase diagram shows that a spin-flip type transition can be observed at  $\sim 3$ T, even at  $\sim 30^\circ$  from the spin plane. In this angular range another transition is observed at  $\sim 4$ T. Thirdly, a detailed field-temperature phase diagram was performed for  $\mathbf{H}/\mathbf{n}_\perp$  (figure 4.68). This field direction is only  $5^\circ$  from the spin plane. From this phase diagram it was seen that just above the  $\sim 4$ T transition there is a second, much smaller transition. It is possible that this second transition

exists for all angles where a spin-flop is observed. However, it is only at this field direction where the step size is small enough to successfully observe it. The lowest field phase must be the helical phase. The true nature of the second and third phases observed at 1.8K are unknown. However, it is known that from the helical to the second phase a spin-flop transition is observed. In the classical  $J_1 - J_2$  chain with easy-plane anisotropy suggested by Nagamiya et al. [131], two phase transitions are expected before saturation. The first one is a spin-flop into a conical structure and the second transition is into a fan phase (see figure 4.3). It is important to note that this is for a system with no inter-chain coupling. Additionally the anisotropy of linarite might be more complicated. This is apparent from the differences in the  $\mathbf{H} // \mathbf{b}$  and  $\mathbf{H} // \mathbf{n}_\perp$ , phase diagrams. The suggested ellipticity of the helical structure is another indication that the anisotropy could be more complicated than an easy-plane anisotropy. The  $\mathbf{H} // \mathbf{n}_\perp$  phase diagram can be compared to those of  $\text{LiCuVO}_4$  or  $\text{LiCu}_2\text{O}_2$  (figures 4.16, 4.17), where there is a spin-flop transition into a conical phase and a second transition into a SDW phase. Based on this comparison, the second phase transition observed for  $\mathbf{H} // \mathbf{n}_\perp$  could be into a SDW phase.

One of the most important results to be taken from this thesis work is that for the field directions  $\mathbf{H} // \mathbf{a}$  and  $\mathbf{H} // \mathbf{b}$ , the incommensurate propagation vectors observed at  $(0, k, 0.5)$  close to saturation do not show a simple  $\text{SDW}_{(p)}$  type behaviour. The comparison between theory and measurements can be seen in figure 4.63. For the field directions  $\mathbf{H} // \mathbf{a}$  and  $\mathbf{H} // \mathbf{b}$ , at high field close to saturation, the incommensurate Bragg peak is observed at  $|k| \sim 0.14$  and  $|k| \sim 0.1$  respectively. For both field directions,  $|k|$  increases slightly with increasing field strength. The fact that the measured incommensurate Bragg peaks do not match expected  $\text{SDW}_{(p)}$  type behaviour is not sufficient to disprove the existence of a spin multipolar phase within linarite. A spin multipolar phase could be at much smaller field range close to saturation. For one dimensional  $J_1 - J_2$  chains, the closer the ratio  $\alpha$  is to -0.25, the

smaller the spin-multipolar phases are (figure 4.4). For linarite this  $\alpha$  is much closer to -0.25 than it was for  $\text{LiCuVO}_4$ . Therefore, in linarite one would expect the spin-multipolar phases to appear much closer to saturation than it did for  $\text{LiCuVO}_4$ . It is possible that the characteristic vector of the  $\text{SDW}_{(p)}$  phase is too small in intensity, or it is located at another region in reciprocal space.

The  $\mathbf{H}/\mathbf{b}$  magnetic Bragg peak versus field dependence in phase V has been reported in detail by Willenberg et al. [154] (figure 4.13). These measurements were performed at different field strengths and temperatures. The observed magnetic Bragg peak did not follow a simple  $\text{SDW}_{(p)}$  type behaviour. To account for this, a field dependent  $\alpha$  model was used. There are a few problems with this approach. Firstly, the data is obtained at different temperatures. There could be some unknown temperature dependence which is coming into play. The constant temperature measurements in this thesis expand upon this issue. Secondly, the used interaction model is incompatible with the spin-waves observed above saturation. From the spin waves a much smaller  $|\alpha|$  is expected with  $\alpha \sim -0.275$ . In Willenberg et al.'s model a large  $J_{c1}$  is assumed, whereas from LSWT the largest inter-chain interaction is found to be  $J_{c0}$ , and a small  $J_{c1}$  is found in most models. It is only in the non-linear  $E(H)$  model where  $J_{c1}$  is larger than  $J_{c0}$ . Even in this model,  $J_{c1}$  is roughly nine times smaller than the  $J_{c1}$  assumed by Willenberg et al.

It is difficult to comment on the possibility of a spin multipolar phase of linarite. For the one-dimensional  $S=1/2$   $J_1 - J_2$  spin chain, many different spin-multipolar phases are predicted for different values of the parameter  $\alpha = J_2/J_1$ . At  $\alpha = -\infty$ , spin-quadrupolar ( $p=2$ ) phases can exist. As  $\alpha$  approaches  $\alpha = -0.25$ , phases with octupolar ( $p=3$ ) or hexadecapolar ( $p=4$ ) can exist [42]. For linarite,  $\alpha \sim -0.275$  and by comparing this to the phase diagram in figure 4.4, a four-magnon bound state with hexadecapolar order might be expected. However, unlike the theoretical model for which this phase diagram was calculated, linarite is subject to inter-chain

coupling and anisotropy. Nishimoto et al. has shown that an AFM inter-chain coupling can be detrimental to the stability of the spin-multipolar phases. If the field applied is along an easy-axis anisotropy, the stability can be enhanced; however, if the field is applied perpendicular to an easy-plane the stability is diminished [137]. It is not clear how the stability is affected if the field is applied within the easy-plane or for an arbitrary angle. In figure 4.7, the stability of the spin-multipolar phases can be seen. For linarite,  $1/\alpha \sim 3.64$  and  $J_0^{IC}/J_2 = J_{c0}/J_2 \sim 0.15$ . Comparing these values to figure 4.7, it could be determined that in linarite the spin-multipolar phase cannot be stabilised. However, this is a rather simple estimate. In order to be more rigorous, the full interaction scheme of linarite, including anisotropies, must be considered. This could be done with the parameters obtained in this thesis. However, it is important to note that these parameters do not provide the best description of spin-wave data. One possible way to check that the used anisotropy is correct is to calculate the spin-flop transition field and compare it to experimental observations. Nagamiya et al. has analytically calculated the spin-flop transition field for a model which does not have inter-chain interactions [131]. This model could be improved by including inter-chain interactions and used to establish the strength of the anisotropy. Once the anisotropy is established it would be of interest to know if there is any field direction for which a spin-multipolar phase can be stabilised.

## 4.8 Conclusion

The INS measurements of the spin waves above saturation field has shed important information with regards to its magnetic interaction scheme. The obtained  $J$  parameters from the spin-waves are much larger than those previously reported in literature [24–26]. With a value of  $\alpha \sim -0.275$ , linarite could sustain a four-magnon bound state with hexadecapolar order. Its ability to sustain such a phase depend

on the exact values of the anisotropies and inter-chain coupling. The strongest type of inter-chain interaction is a skew AFM interaction,  $J_{c0}$ . An easy-plane anisotropy was assumed on both nearest and second nearest interactions along the spin chain,  $J_1$  and  $J_2$  interactions. These anisotropic models were not able to explain some features of the data. In the INS data there is some indications that the spin-wave increases non-linearly with increasing field strength. The origin of this non-linear behaviour is not clear. In future INS experiments the non-linearity can be explored in greater detail. This would provide more confidence in the obtained  $J$  parameters from LSWT.

The anisotropy in linarite can also be established from the magnetisation measurements. At 1.8K, a spin-flop transition is observed in the **ac** plane for  $\sim 3$ T. Using this field strength it could be possible to calculate the strength of the easy-axis anisotropy by building upon the calculations of Nagamiya et al. [131].

The INS spectrum of linarite was also explored for zero field. The observed excitations do not appear to be spinons like observed in  $\text{LiCuVO}_4$  [127]. Instead, clear spin-wave branches were observed. Using the SpinW software [122], a fit was obtained to the spin-wave branches. The model considered the system classically and did not include any anisotropies. Such a model was capable of explaining most of the features; however there are still some discrepancies between the INS data and the model. It is not clear if these discrepancies can be resolved by simply introducing an anisotropy or if a more rigorous model, which considers the quantum mechanical nature of the system, is required. The obtained  $J$  parameters from zero field can be compared to those obtained above saturation field. The zero field  $J$  parameters are roughly half as small compared to those obtained above saturation field and the ratio  $\alpha = J_2/J_1$  also changes to  $\alpha \sim -0.3$ . It is important to note that the parameters obtained at zero field are non-trivially related to the true  $J$  parameters of the system. At zero field LSWT has been used because there is no clear alternative. Many of



the approximations used for LSWT could be invalid for zero field.

Diffraction measurements has been carried out at 50mK for  $\mathbf{H} // \mathbf{a}$  and  $\mathbf{H} // \mathbf{b}$  for untwinned crystals. For  $\mathbf{H} // \mathbf{b}$ , a coexistence of phase IV and phase V is observed (figure 4.11) which produce Bragg peaks at  $(0,0,0.5)$  and  $(0,\sim 0.1,0.5)$  respectively. The field dependence of incommensurate Bragg peak  $(0,k_{ic},0.5)$  of phase V is measured at constant temperature for high field strengths. A small increase in  $k_{ic}$  is observed with increasing field strength. The observed change in  $k_{ic}$  is not compatible with a p-type spin-density wave  $\text{SDW}_{(p)}$ . The previous measurements of  $k_{ic}$  in phase V had been interpreted as a  $\text{SDW}_{(p)}$  phase where  $p$  changes due to a field dependent  $\alpha_{eff}$ . The interaction model that has been used to calculate  $\alpha_{eff}$  is very different to the interaction model obtained by spin-waves at field strengths above saturation. Based on this discrepancy, it is possible to say that there is no direct evidence so far of a  $\text{SDW}_{(p)}$  phase for linarite for  $\mathbf{H} // \mathbf{b}$ . The  $\mathbf{H} // \mathbf{a}$  field direction has also been explored in detail. The magnetic Bragg peak remains incommensurate up to  $\sim 6.3\text{T}$  for this field direction. Between zero field and  $\sim 6.3\text{T}$ ,  $k_{ic}$  changes with field in a complicated manner, and none of its regions are directly compatible with a  $\text{SDW}_{(p)}$  phase. The only clear phase transitions observed by change in Bragg peak area are at  $\sim 2.5\text{T}$  and  $\sim 6.3\text{T}$ . This  $\sim 2.5\text{T}$  transition is also measured at  $\sim 1.6\text{K}$  as well as  $50\text{mK}$ . This transition could be the same as the  $\sim 3\text{T}$  spin-flop transition observed with magnetisation measurements at  $1.8\text{K}$ .

Magnetisation measurements were performed at  $1.8\text{K}$  on an untwinned linarite crystal. With the help of a rotation stage, the  $\mathbf{ac}$  plane of linarite was explored and a preliminary phase diagram was established. The spin plane was assumed to be at the angle which corresponds to the lowest spin-flop transition field. The spin-plane was found at  $-20(5)^\circ$  from the  $\mathbf{a}$  axis, in agreement with the  $-27(2)^\circ$  estimate of Willenberg et al. [150], as obtained from neutron diffraction. Two transitions are observed  $\sim 30^\circ$  either side of the spin plane. There is a spin-flop transition at  $\sim 3\text{T}$ ,

and a second transition at  $\sim 4\text{T}$ . For  $\mathbf{H}/\mathbf{n}_\perp$ , which is only  $5^\circ$  from the spin plane, a detailed field-temperature phase diagram was obtained. In this phase diagram, a third phase can be identified. At  $1.8\text{K}$ , three transitions are observed at  $\sim 3\text{T}$ ,  $\sim 4.1\text{T}$  and  $\sim 4.3\text{T}$ . The nature of the phases in this phase diagram is not known. Based on comparisons to the  $\mathbf{H}/\mathbf{b}$  phase diagram of linarite [148,150,155], it could be speculated that the phase between  $\sim 4.1\text{T}$  and  $\sim 4.3\text{T}$  is a SDW phase. Since the  $\sim 3\text{T}$  transition is a spin-flop transition the phase between  $\sim 3\text{T}$  and  $\sim 4.1\text{T}$  could be a conical phase, where the new spin-plane is perpendicular to the field direction.

# Chapter 5

## Summary and Outlook

### 5.1 $\text{Na}_{0.8}\text{CoO}_2$

#### 5.1.1 Summary

The aim of this thesis work for  $\text{Na}_x\text{CoO}_2$  was to study the effect of the Na superstructures on the magnetic exchange interactions. Previous inelastic neutron measurements on samples of unknown superstructure but with similar concentration ( $x=0.75$  [5] and  $x=0.82$  [4]), found a factor of two difference in the out of plane exchange constant  $J_c$ . In this concentration range there are three different Na superstructures: the square ( $x=0.8$ ), the stripe ( $x=0.8$ ), and the 1/13th ( $x \sim 0.77$ ) phases. It was already shown that the magnetic exchange constants of the 1/13th [69] were very similar to that of the  $x=0.75$  sample [5]. In this thesis work it was shown that exchange constants of the stripe and square phase are also very similar to that of the  $x=0.75$  sample. Therefore the origin of the smaller  $J_c$  observed for the  $x=0.82$  [4] sample remains unexplained.

In the spin-wave dispersion of the square phase  $\text{Na}_{0.8}\text{CoO}_2$ , an interesting anomaly was observed along the  $(hh3)$  and  $(h03)$  directions. Below  $\sim 14\text{meV}$  a typical

acoustic spin-wave branch is present. At  $\sim 14\text{meV}$  there is a dip in intensity and after this dip the spin-wave dispersion becomes infinitely dispersive, i.e. it does not move in  $\mathbf{q}$  with increasing energy. An infinitely dispersive excitation has been seen before in phonon spectra and is referred to as the “waterfall effect” [119]. In prior observations it was explained by coupling between an acoustic and an optic phonon branch. To the authors knowledge, the waterfall observed in  $\text{Na}_{0.8}\text{CoO}_2$  is the first ever observation of a magnetic version of the waterfall effect. The magnetic nature of the waterfall was confirmed with XYZ polarisation analysis on the triple-axis spectrometer IN20 at the ILL.

The origin of the magnetic waterfall effect is not clear. Two different possibilities are suggested in this thesis. The first is the coupling between acoustic magnons and optic phonons. Such a model might explain the dip in intensity at  $\sim 14\text{meV}$ . It is known that for the square phase  $\text{Na}_{0.8}\text{CoO}_2$ , there are many flat optic phonon modes at  $\sim 13\text{meV}$ . These are the rattling modes and are responsible for a factor of six drop in the thermal transport [21]. It might not be a coincidence that these flat optic modes are at the same energy where the spin-wave waterfall features start to appear. In future work, it might be possible to calculate the magnon-phonon coupling directly. However, before this can be done a better understanding of the magnetism in  $\text{Na}_x\text{CoO}_2$  must be established. Experiments suggest the need for a magnetic model more complicated than the currently adopted A-type AFM structure [19, 111]. In this thesis more complex magnetic structures were considered. The resulting spin-wave spectrums from these superstructures could account for some but not all of the features observed in  $\text{Na}_{0.8}\text{CoO}_2$ . The second model for explaining the waterfall is a magnetic cluster model. In this model, the position of the waterfall  $q_{wf}$  is related to the size of the magnetic clusters. From  $|q_{wf}| = 0.37(2)\text{\AA}^{-1}$  one would expect magnetic clusters of the size  $17(1)\text{\AA}$ . This is in agreement with nm-sized clusters as suggested from muon experiments [111]. There are some indications that

the spin-wave waterfall loses correlation with increasing energy. If this effect is real, it could corroborate the magnetic cluster model.

### 5.1.2 Outlook

There are at least two possible experiments one could carry out to expand upon the result of this thesis work. The first is to determine if the waterfall's decrease in correlation length at higher energies is a real effect. The experiments in this thesis work were not optimised for measuring correlation lengths therefore its results cannot be fully trusted. However, the measurements can be easily repeated on a TAS instrument after it has been optimised for  $Q$  resolution. The results from such an experiment might help understand the origin of the magnetic waterfall.

The second experiment would be to study the effect of a magnetic field on the spin-wave dispersion, in particular the effects it might have on the magnetic waterfall. If magnon-phonon coupling is responsible for the magnetic waterfall, a change to the waterfall should be observed with increasing magnetic field. For an applied magnetic field, the spin-wave dispersion should shift to a higher energy, however the phonon dispersion should remain unchanged. This would alter the position where phonon and magnon branches would cross each other in  $Q, \omega$  space and this could result in a shift of the position of the waterfall. This would apply to fields up to  $\sim 8\text{T}$ , as at this field a spin-flop transition is reported [92]. There is another important reason for studying the field dependence of the spin waves. It is believed that the high thermopower of  $\text{Na}_x\text{CoO}_2$  is of magnetic origin, since it can be suppressed with a magnetic field [16]. It would be of interest to see how the magnetic excitations of  $\text{Na}_x\text{CoO}_2$  would change with increasing field strength. At low temperatures, one would expect to suppress the thermopower almost completely at 10T [16]. A good comparison between 0T and 10T excitation spectrum might shed light to  $\text{Na}_x\text{CoO}_2$ 's large magnetic thermopower.

## 5.2 Linarite

### 5.2.1 Summary

For linarite, the main aim of the thesis work was to obtain the exchange interactions above saturation field strength and comment on the possibility of a multi-magnon spin-nematic phase. Of the tested interaction models, all of them indicated a ratio of  $\alpha = J_2/J_1 \sim -0.275$ . If linarite was a fully one-dimensional system without any anisotropies, this would mean linarite could support a four-magnon bound state with hexadecapolar order. However, it is not clear if linarite can sustain such an exotic quantum phase when inter-chain interactions and anisotropies are considered. More experimental and theoretical work is necessary in order to obtain a reliable prediction.

By looking at the spin-wave data obtained above saturation, it is possible to speculate that the spin-wave energy gain with increasing field is not linear. For an isotropic LWST model, the field dependence should be linear. Uncertainties over alignment perpendicular to the chain direction make it difficult to assess whether the non-linearity is a real effect. Further experiments are required to explore this phenomenon.

INS measurements were also performed at zero field for linarite. In a similar compound,  $\text{LiCuVO}_4$ , at zero field, a spinon continuum is present [127]. However, for linarite the zero-field excitations are relatively sharp and resemble spin waves instead. A spin-wave fit is performed to this dispersion using SpinW software [122], however, the model used is relatively simplistic. This model includes no anisotropies, even though anisotropy appears to be important for linarite. The obtained exchange parameters are roughly twice as small compared to the true exchange parameters as obtained above the saturation field. The theoretical spin-wave model used does manage to explain most of the observed features, but it fails to explain the existence

of a complete spin-wave branch. In order to explain all the observed features, a more detailed theoretical model might be necessary.

The magnetisation measurements indicate that the spin-plane is  $-20(5)^\circ$  away from the  $\mathbf{a}$  axis. This is in agreement with the magnetic structure solution of  $-27(2)^\circ$  as obtained by Willenberg et al. [150] using neutrons. The detailed measurements at  $\mathbf{H} // \mathbf{n}_\perp$  find that there are at least three phase transitions observable at 1.8K with a change in magnetic field. The first one is the spin-flop transition at  $\sim 3\text{T}$ . The second is a weaker transition at  $\sim 4.1\text{T}$  and the third one is a very weak signal at  $\sim 4.3\text{T}$ . These findings can be compared to the neutron diffraction results for  $\mathbf{H} // \mathbf{a}$ , since  $\mathbf{n}_\perp$  and  $\mathbf{a}$  are only  $-15.35^\circ$  apart. The magnetisation data shows that the spin-flop transition should occur at slightly larger field at  $\mathbf{H} // \mathbf{a}$  compared to  $\mathbf{H} // \mathbf{n}_\perp$ . However, in the  $\mathbf{H} // \mathbf{a}$ ,  $\sim 1.8\text{K}$  diffraction data the only clear transition is at  $\sim 2.5\text{T}$ . There may be other transitions but they cannot be resolved in this dataset. It is not clear why the first transition in diffraction data is at slightly lower fields compared to magnetisation data.

The magnetic Bragg peaks were measured at  $\sim 50\text{mK}$  for  $\mathbf{H} // \mathbf{a}$  or  $\mathbf{H} // \mathbf{b}$ . For  $\mathbf{H} // \mathbf{a}$ , the magnetic Bragg peak remained incommensurate up to  $\sim 6.3\text{T}$  where the intensity reached zero. For  $\mathbf{H} // \mathbf{b}$ , only the high field region was studied. A coexistence of commensurate and incommensurate phases was observed at  $8\text{T}$ . At higher fields, only the incommensurate field was present which disappeared at  $\sim 9.7\text{T}$ . From the diffraction dataset, the saturation fields could not be reliably obtained. Therefore it is not clear if  $\sim 6.3\text{T}$  and  $\sim 9.7\text{T}$  correspond to saturation for  $\mathbf{H} // \mathbf{a}$  or  $\mathbf{H} // \mathbf{b}$  respectively. This could be clarified by a series of magnetisation measurements at similar temperatures.

The field dependence of the  $\mathbf{H} // \mathbf{a}$  or  $\mathbf{H} // \mathbf{b}$  incommensurate Bragg peaks measured in this thesis do not follow the expected field dependence of a p-type SDW phase. However, this is not sufficient to disprove the existence of a p-type SDW

phase in linarite for these field directions. It is possible that the p-type SDW phase presents a Bragg peak at a different, unexplored region of reciprocal space. Alternatively, the intensity of the Bragg peak could be very small, or perhaps this phase only appears at a very narrow region of field strengths. Willenberg et al. [154] stated that their  $\mathbf{H} // \mathbf{b}$  field dependence at 1.8K is proof of p-type SDW phase. However, the interaction model they have used in their calculations is incompatible with the spin-wave measurements presented in this thesis. The spin-wave data indicate that  $\alpha = J_2/J_1 \sim -0.275$ , and that the diagonal inter-chain interaction is rather small. On the contrary, the Willenberg model assumes  $\alpha = -0.36$  and adopts a rather large diagonal inter-chain interaction.

The results from this thesis allow one to make some qualitative statements regarding the anisotropy in linarite. To first approximation, one might think that the helical structure ground state of linarite at zero field indicates an easy-axis anisotropy. The  $\mathbf{a}$  axis is only  $\sim 20^\circ$  away from the spin plane and magnetisation data at 1.8K show that these two directions should be relatively similar. The  $\mathbf{b}$  axis is in the spin plane as well, however, diffraction data show very different magnetic response for  $\mathbf{H} // \mathbf{a}$  or  $\mathbf{H} // \mathbf{b}$  field directions. Therefore the anisotropy in linarite must be more complicated than an easy-axis anisotropy. This results is in agreement with the proposed elliptical nature of the helical ground state [150].

### 5.2.2 Outlook

There are many different experiments one could perform to clarify or expand upon results stated in this thesis. One of the first to perform would be to clarify the issue with the apparent non-linear field dependence of the spin waves above saturation field. One possible explanation is the presence of imperfect crystal orientations throughout the experiments. An INS experiment in a cryomagnet at a cold triple axis instrument must be carried out to figure out if the non-linear beha-



viour is real. Perfect orientational information is necessary for all the crystals used in this experiment. The spin wave can be measured at  $(0,0,0.5)$  and  $(0,0,1)$  for many different field strengths, especially between 10T and 14.5T. For each field, nuclear Bragg peaks must be checked to ensure the sample has not moved.

The next task is to determine the shape and size of the anisotropy seen in linarite. This might not be possible with only the experimental measurements presented in this thesis. However, if one assumes an easy-axis anisotropy, it should be possible to extrapolate the strength of the anisotropy based on the spin-flop field. This can be done by expanding slightly on the theoretical work of Nagamiya et al. [131]. A more complex anisotropy model might be necessary, as indicated by some of the results of this thesis. In order to establish the values for a more complex model, more experimental data might be required.

Once the problems surrounding non-linearity and anisotropy have been solved, another fit can be performed to the spin-wave data obtained above saturation. This would give the final interaction parameters which can be used to determine the possibility of a spin-multipolar phase for linarite. The calculations for this would be similar to the work of Nishimoto et al. [137]. These calculations should be performed for as many different field directions as possible, especially if a complex anisotropy model is adopted.

Another task for linarite is to find a better model to explain the magnetic excitations at zero field. Perhaps an introduction of an easy-plane anisotropy into the LSWT model can account for some of the shortcomings of the isotropic model used in this thesis. It is possible that some of the features cannot be explained by LSWT at all and that a more complex excitation model is required.

In the  $\mathbf{H} // \mathbf{a}$  or  $\mathbf{H} // \mathbf{b}$ , 50mK neutron diffraction data, the incommensurate Bragg peaks disappeared at  $\sim 6.3\text{T}$  and  $\sim 9.7\text{T}$  respectively. However, from the diffraction data it is not clear if this corresponds to saturation. Magnetisation

measurements performed at these temperature and field directions would solve this discrepancy. This could provide valuable insight into the nature of the magnetic transitions close to saturation.

# Bibliography

- [1] I. Terasaki, Y. Sasago, and K. Uchinokura, Phys. Rev. B **56**, R12685 (1997).
- [2] R. Berthelot, D. Carlier, and C. Delmas, Nat. Mat. **10**, 74 (2011).
- [3] K. Takada *et al.*, Nature **422**, 53 (2003).
- [4] S. P. Bayrakci *et al.*, Phys. Rev. Lett. **94**, 157205 (2005).
- [5] L. M. Helme *et al.*, Phys. Rev. Lett. **94**, 157206 (2005).
- [6] J. R. Hook and H. E. Hall, Solid state physics. 1991.
- [7] C. Kittel, *Introduction to solid state* (John Wiley & Sons, 1966).
- [8] N. E. Bickers, D. J. Scalapino, and R. T. Scalettar, International Journal of Modern Physics B **1**, 687 (1987).
- [9] M. D. Johannes, I. I. Mazin, D. J. Singh, and D. A. Papaconstantopoulos, Physical review letters **93**, 097005 (2004).
- [10] I. I. Mazin and M. D. Johannes, Nature Physics **1**, 91 (2005).
- [11] G. Baskaran, Physical review letters **91**, 097003 (2003).
- [12] M. M. Doeff *et al.*, Electrochimica acta **40**, 2205 (1995).

- [13] A. Scott, Challenging lithium-ion batteries with new chemistry, <http://cen.acs.org/articles/93/i29/Challenging-Lithium-Ion-Batteries-New.html>, Accessed: 18/07/2016.
- [14] M. H. Han, E. Gonzalo, G. Singh, and T. Rojo, *Energy & Environmental Science* **8**, 81 (2015).
- [15] D. G. Porter, *Control of electrons through patterning of superstructures in sodium cobaltate* (PhD Thesis, 2012).
- [16] Y. Wang, N. S. Rogado, R. J. Cava, and N. P. Ong, *Nature* **423**, 425 (2003).
- [17] M. Roger *et al.*, *Nature* **445**, 631 (2007).
- [18] M. Gao, S. Zhou, and Z. Wang, *Phys. Rev. B* **76**, 180402 (2007).
- [19] I. R. Mukhamedshin and H. Alloul, *Physica B: Condensed Matter* **460**, 58 (2015).
- [20] D. J. P. Morris, *Sodium ordering and the control of properties in sodium cobaltate* (PhD Thesis, 2007).
- [21] D. J. Voneshen *et al.*, *Nat. Mat.* **12**, 1028 (2013).
- [22] R. S. W. Braithwaite and P. J. Dunn, *Mineralogical Magazine* **50**, 129 (1986).
- [23] H. Effenberger, *Mineralogy and Petrology* **36**, 3 (1987).
- [24] M. Baran *et al.*, *physica status solidi (c)* **3**, 220 (2006).
- [25] Y. Yasui, M. Sato, and I. Terasaki, *Journal of the Physical Society of Japan* **80**, 033707 (2011).
- [26] A. U. B. Wolter *et al.*, *Phys. Rev. B* **85**, 014407 (2012).

- [27] R. W. Robinett, *Quantum mechanics: classical results, modern systems, and visualized examples* (Oxford University Press, 2006).
- [28] T. Giamarchi, *Quantum physics in one dimension* (Oxford university press, 2004).
- [29] S.-i. Tomonaga, Progress of Theoretical Physics **5**, 544 (1950).
- [30] J. M. Luttinger, Journal of Mathematical Physics **4**, 1154 (1963).
- [31] C. Lacroix, P. Mendels, and F. Mila, *Introduction to Frustrated Magnetism: Materials, Experiments, Theory* Vol. 164 (Springer Science & Business Media, 2011).
- [32] J. Villain, R. Bidaux, J.-P. Carton, and R. Conte, Journal de Physique **41**, 1263 (1980).
- [33] S. T. Bramwell and M. J. P. Gingras, Science **294**, 1495 (2001).
- [34] C. Castelnovo, R. Moessner, and S. L. Sondhi, Nature **451**, 42 (2008).
- [35] M. Harris, Nature **456**, 886 (2008).
- [36] D. I. Khomskii, Journal of Magnetism and Magnetic Materials **306**, 1 (2006).
- [37] D. I. Khomskii, Physics **2**, 20 (2009).
- [38] F. Heidrich-Meisner, A. Honecker, and T. Vekua, Phys. Rev. B **74**, 020403 (2006).
- [39] T. Vekua, A. Honecker, H.-J. Mikeska, and F. Heidrich-Meisner, Phys. Rev. B **76**, 174420 (2007).
- [40] L. Kecke, T. Momoi, and A. Furusaki, Phys. Rev. B **76**, 060407 (2007).

- [41] T. Hikihara, L. Kecke, T. Momoi, and A. Furusaki, Phys. Rev. B **78**, 144404 (2008).
- [42] J. Sudan, A. Lüscher, and A. M. Läuchli, Phys. Rev. B **80**, 140402 (2009).
- [43] A. F. Andreev and I. A. Grishchuk, Sov. Phys. JETP **60**, 267 (1984).
- [44] L. E. Svistov *et al.*, JETP letters **93**, 21 (2011).
- [45] M. Mourigal *et al.*, Phys. Rev. Lett. **109**, 027203 (2012).
- [46] L. Brillouin, Comptes Rendus Hebdomadaires des Séances de l'Académie des Sciences **191**, 292 (1930).
- [47] M. I. Aroyo and H. Wondratschek, *International Tables for Crystallography Vol. B Chapter 1.5* (Kluwer Academic Publishers, 2006).
- [48] U. Shmueli and A. J. C. Wilson, *International Tables for Crystallography Vol. B Chapter 2.1* (Kluwer Academic Publishers, 2006).
- [49] W. L. Bragg, Nature **90**, 410 (1912).
- [50] W. Friedrich, P. Knipping, M. v. Laue, and I.-E. bei Röntgenstrahlen, Mathematische-Physische Klasse **42**, 303 (1912).
- [51] W. Heisenberg, Mehrkörperproblem und resonanz in der quantenmechanik, in *Original Scientific Papers Wissenschaftliche Originalarbeiten*, pp. 456–471, Springer, 1985.
- [52] P. A. M. Dirac, On the theory of quantum mechanics, in *Proceedings of the Royal Society of London A: Mathematical, Physical and Engineering Sciences* Vol. 112, pp. 661–677, The Royal Society, 1926.

- [53] B. D. Cullity and C. D. Graham, *Introduction to magnetic materials* (John Wiley & Sons, 2011).
- [54] H. A. Kramers, *Physica* **1**, 182 (1934).
- [55] J. B. Goodenough, *Phys. Rev.* **100**, 564 (1955).
- [56] P. W. Anderson, *Magnetism* **1**, 25 (1963).
- [57] J. Kanamori, *Journal of Physics and Chemistry of Solids* **10**, 87 (1959).
- [58] G. L. Squires, *Introduction to the theory of thermal neutron scattering* (Cambridge university press, 2012).
- [59] P. A. M. Dirac, The quantum theory of the emission and absorption of radiation, in *Proceedings of the Royal Society of London A: Mathematical, Physical and Engineering Sciences* Vol. 114, pp. 243–265, The Royal Society, 1927.
- [60] F. Bloch, *Zeitschrift für Physik* **74**, 295 (1932).
- [61] V. Petříček, M. Dušek, and L. Palatinus, *Zeitschrift für Kristallographie-Crystalline Materials* **229**, 345 (2014).
- [62] J. Rodriguez-Carvajal, Fullprof: a program for rietveld refinement and pattern matching analysis, in *satellite meeting on powder diffraction of the XV congress of the IUCr* Vol. 127, Toulouse, France, 1990.
- [63] A. Dianoux and G. Lander, *Neutron data booklet* (OCPscience, 2003).
- [64] S. J. Clark *et al.*, *Zeitschrift für Kristallographie-Crystalline Materials* **220**, 567 (2005).
- [65] L. H. Thomas, The calculation of atomic fields, in *Mathematical Proceedings of the Cambridge Philosophical Society* Vol. 23, pp. 542–548, Cambridge Univ Press, 1927.

- [66] E. Fermi, Zeitschrift für Physik **48**, 73 (1928).
- [67] E. Ressouche, École thématique de la Société Française de la Neutronique **13**, 02002 (2014).
- [68] M. Enderle, École thématique de la Société Française de la Neutronique **13**, 01002 (2014).
- [69] G. B. Pasquino, *Polarized neutron studies of spin dynamics of functional materials* (PhD Thesis, 2015).
- [70] M. Blume, Physical Review **130**, 1670 (1963).
- [71] S. V. Maleyev and V. G. Bar'yakhtar, Sov. Phys. Solid State **4**, 2533 (1963).
- [72] S. V. Maleev, Physics-Uspekhi **45**, 569 (2002).
- [73] M. Enderle, Private communications (2015).
- [74] W. E. Fischer, Physica B: Condensed Matter **234**, 1202 (1997).
- [75] J. C. Maxwell, The London, Edinburgh, and Dublin Philosophical Magazine and Journal of Science **19**, 19 (1860).
- [76] E. Fermi, Neutron velocity selector, 1950, US Patent 2,524,379.
- [77] M. J. Cooper and R. Nathans, Acta Crystallographica **23**, 357 (1967).
- [78] M. Popovici, Acta Crystallographica Section A: Crystal Physics, Diffraction, Theoretical and General Crystallography **31**, 507 (1975).
- [79] W. P. Farhi E, Debab Y, J. Neut. Res. **17** (2013).
- [80] J. Šaroun and J. Kulda, Physica B: Condensed Matter **234**, 1102 (1997).
- [81] J. B. Hayter, Zeitschrift für Physik B Condensed Matter **31**, 117 (1978).



- [82] M. Enderle, Hercules school lecture notes on triple-axis spectroscopy (2015).
- [83] H. G. Büttner, E. Lelievre-Berna, and F. Pinet, Institut Laue-Langevin, Grenoble (1997).
- [84] H. B. Callen, *Thermodynamics, an Intro. to Thermostatistics* (John Wiley & Sons, 2006).
- [85] J. Clarke and A. I. Braginski, *The SQUID handbook* (Wiley Online Library, 2004).
- [86] K. K. Likharev, *Dynamics of Josephson junctions and circuits* (Gordon and Breach science publishers, 1986).
- [87] M. McElfresh, Fundamentals of magnetism and magnetic measurements, <http://qdusa.com/sitedocs/appNotes/mpms/FundPrimer.pdf>, Accessed: 08/07/2016.
- [88] T. Motohashi *et al.*, Phys. Rev. B **67**, 064406 (2003).
- [89] D. Prabhakaran, A. T. Boothroyd, R. Coldea, L. M. Helme, and D. A. Tennant, arXiv preprint cond-mat/0312493 (2003).
- [90] B. C. Sales *et al.*, arXiv preprint cond-mat/0402379 (2004).
- [91] J. Sugiyama *et al.*, Phys. Rev. B **67**, 214420 (2003).
- [92] L. M. Helme *et al.*, Phys. Rev. B **73**, 054405 (2006).
- [93] M. L. Foo *et al.*, Phys. Rev. Lett. **92**, 247001 (2004).
- [94] T. Fujimoto *et al.*, Phys. Rev. Lett. **92**, 047004 (2004).
- [95] W. Higemoto *et al.*, Phys. Rev. B **70**, 134508 (2004).

- [96] M. Lee *et al.*, Nat. Mat. **5**, 537 (2006).
- [97] G. Lang *et al.*, Phys. Rev. B **72**, 094404 (2005).
- [98] A. Zorkovská *et al.*, physica status solidi (b) **247**, 665 (2010).
- [99] J. Sugiyama *et al.*, Phys. Rev. Lett. **92**, 017602 (2004).
- [100] F. C. Chou *et al.*, Phys. Rev. Lett. **101**, 127404 (2008).
- [101] H. W. Zandbergen, M. Foo, Q. Xu, V. Kumar, and R. J. Cava, Phys. Rev. B **70**, 024101 (2004).
- [102] D. J. P. Morris *et al.*, Phys. Rev. B **79**, 100103 (2009).
- [103] H. Alloul, I. R. Mukhamedshin, T. A. Platova, and A. V. Dooglav, Europhys. Lett. **85**, 47006 (2009).
- [104] Q. Huang *et al.*, Journal of physics: Condensed matter **16**, 5803 (2004).
- [105] M. S. Pandiyan, *Phase diagram and control of thermoelectric properties of sodium cobaltate* (PhD Thesis, 2013).
- [106] H. Alloul *et al.*, Phys. Rev. B **85**, 134433 (2012).
- [107] Y. Krockenberger *et al.*, arXiv preprint arXiv:0705.0517 (2007).
- [108] W. Koshibae, K. Tsutsui, and S. Maekawa, Phys. Rev. B **62**, 6869 (2000).
- [109] P. Mendels *et al.*, Phys. Rev. Lett. **94**, 136403 (2005).
- [110] C. Bernhard *et al.*, Phys. Rev. Lett. **93**, 167003 (2004).
- [111] C. Bernhard *et al.*, Europhys. Lett. **80**, 27005 (2007).
- [112] M. D. Johannes, I. I. Mazin, and D. J. Singh, Phys. Rev. B **71**, 214410 (2005).

- [113] A. T. Boothroyd *et al.*, Phys. Rev. Lett. **92**, 197201 (2004).
- [114] J. L. Gavilano *et al.*, Phys. Rev. B **69**, 100404 (2004).
- [115] R. Ray, A. Ghoshray, K. Ghoshray, and S. Nakamura, Phys. Rev. B **59**, 9454 (1999).
- [116] M. Z. Hasan *et al.*, Phys. Rev. Lett. **92**, 246402 (2004).
- [117] M. Daghofer, P. Horsch, and G. Khaliullin, Phys. Rev. Lett. **96**, 216404 (2006).
- [118] G. Khaliullin, Progress of Theoretical Physics Supplement **160**, 155 (2005).
- [119] J. Hlinka *et al.*, Phys. Rev. Lett. **91**, 107602 (2003).
- [120] F. James and M. Roos, Computer Physics Communications **10**, 343 (1975).
- [121] G. Allodi, Fminuit software package, <http://www.fis.unipr.it/~giuseppe.allodi/Fminuit/>, Accessed:09/2015.
- [122] S. Toth and B. Lake, Journal of Physics: Condensed Matter **27**, 166002 (2015).
- [123] D. J. Voneshen, *Lattice dynamics in materials for energy applications* (PhD Thesis, 2015).
- [124] O. Delaire *et al.*, Nat. Mat. **10**, 614 (2011).
- [125] J.-P. Rueff *et al.*, Phys. Rev. B **74**, 020504 (2006).
- [126] G. Sangiovanni, P. Wissgott, F. Assaad, A. Toschi, and K. Held, Phys. Rev. B **86**, 035123 (2012).
- [127] M. Enderle *et al.*, Phys. Rev. Lett. **104**, 237207 (2010).
- [128] A. Yoshimori, Journal of the Physical Society of Japan **14**, 807 (1959).

- [129] M. Mostovoy, Phys. Rev. Lett. **96**, 067601 (2006).
- [130] T.-h. Arima, Journal of the Physical Society of Japan **76**, 073702 (2007).
- [131] T. Nagamiya, K. Nagata, and Y. Kitano, Progress of Theoretical Physics **27**, 1253 (1962).
- [132] Y. Kitano and T. Nagamiya, Progress of Theoretical Physics **31**, 1 (1964).
- [133] H. Bethe, Zeitschrift für Physik **71**, 205 (1931).
- [134] D. C. Mattis, Luttinger Model: The First 50 Years and Some New Directions **20**, 255 (2013).
- [135] A. Smerald, H. T. Ueda, and N. Shannon, Physical Review B **91**, 174402 (2015).
- [136] S. Nishimoto, S.-L. Drechsler, R. Kuzian, J. Richter, and J. Brink, arXiv preprint arXiv:1005.5500 (2010).
- [137] S. Nishimoto, S.-L. Drechsler, R. Kuzian, J. Richter, and J. v. d. Brink, arXiv preprint arXiv:1303.1933 (2013).
- [138] F. Heidrich-Meisner, I. P. McCulloch, and A. K. Kolezhuk, Phys. Rev. B **80**, 144417 (2009).
- [139] O. A. Starykh and L. Balents, Physical Review B **89**, 104407 (2014).
- [140] S. Nishimoto *et al.*, Phys. Rev. Lett. **107**, 097201 (2011).
- [141] D. V. Dmitriev and V. Y. Krivnov, Phys. Rev. B **79**, 054421 (2009).
- [142] S. Furukawa, M. Sato, S. Onoda, and A. Furusaki, Phys. Rev. B **86**, 094417 (2012).

- [143] T. Araki, Mineralogical Journal **3**, 282 (1962).
- [144] H. G. Bachmann and J. Zemann, Acta Crystallographica **14**, 747 (1961).
- [145] M. Enderle, Private communications (2014).
- [146] P. F. Schofield, C. C. Wilson, K. S. Knight, and C. A. Kirk, The Canadian Mineralogist **47**, 649 (2009).
- [147] F. I. Z. Karlsruhe, Inorganic crystal structure database, <https://icsd.fiz-karlsruhe.de>, Accessed:07/2015.
- [148] A. U. B. Willenberg, *Ground state properties and field induced phases in quasi one-dimensional quantum magnets* (PhD Thesis, 2014).
- [149] Y. Mizuno *et al.*, Phys. Rev. B **57**, 5326 (1998).
- [150] B. Willenberg *et al.*, Phys. Rev. Lett. **108**, 117202 (2012).
- [151] M. Schäpers *et al.*, Phys. Rev. B **88**, 184410 (2013).
- [152] R. Szymczak *et al.*, Acta Physica Polonica-Series A General Physics **115**, 925 (2009).
- [153] M. Schäpers *et al.*, Phys. Rev. B **90**, 224417 (2014).
- [154] B. Willenberg *et al.*, Phys. Rev. Lett. **116**, 047202 (2016).
- [155] B. Willenberg *et al.*, arXiv preprint arXiv:1508.02207 (2015).
- [156] S.-L. Drechsler *et al.*, EPL (Europhysics Letters) **73**, 83 (2006).
- [157] M. Enderle *et al.*, EPL (Europhysics Letters) **70**, 237 (2005).
- [158] S.-L. Drechsler *et al.*, Phys. Rev. Lett. **98**, 077202 (2007).

- [159] S.-L. Drechsler *et al.*, Journal of Physics: Conference Series **200**, 012028 (2010).
- [160] S. E. Dutton *et al.*, Phys. Rev. Lett. **108**, 187206 (2012).
- [161] M. Hase *et al.*, Phys. Rev. B **70**, 104426 (2004).
- [162] M. Matsuda, K. Kakurai, M. Yethiraj, and K. Oka, Journal of the Physical Society of Japan **74**, 1578 (2005).
- [163] T. Masuda *et al.*, Phys. Rev. B **72**, 014405 (2005).
- [164] L. Capogna *et al.*, Phys. Rev. B **71**, 140402 (2005).
- [165] F. Sapina *et al.*, Solid State Communications **74**, 779 (1990).
- [166] H. J. Xiang, C. Lee, and M.-H. Whangbo, Phys. Rev. B **76**, 220411 (2007).
- [167] M. Hase *et al.*, Journal of applied physics **97** (2005).
- [168] M. Boehm *et al.*, EPL (Europhysics Letters) **43**, 77 (1998).
- [169] R. Coldea *et al.*, Phys. Rev. Lett. **88**, 137203 (2002).
- [170] A. Bush *et al.*, Phys. Rev. B **85**, 054421 (2012).
- [171] N. Büttgen *et al.*, Phys. Rev. B **76**, 014440 (2007).
- [172] N. Büttgen, W. Kraetschmer, L. E. Svistov, L. A. Prozorova, and A. Prokofiev, Phys. Rev. B **81**, 052403 (2010).
- [173] M. Nespolo and G. Ferraris, European Journal of Mineralogy **21**, 673 (2009).
- [174] H. R. Glyde *et al.*, Phys. Rev. B **61**, 1421 (2000).

- [175] H. A. Jahn and E. Teller, Stability of polyatomic molecules in degenerate electronic states. i. orbital degeneracy, in *Proceedings of the Royal Society of London A: Mathematical, Physical and Engineering Sciences* Vol. 161, pp. 220–235, The Royal Society, 1937.
- [176] S. A. G. Housecroft C., *Inorganic Chemistry* (Prentice Hall, 2008).
- [177] R. K. Kremer, Private communications (2015).
- [178] W. H. Keesom and A. P. Keesom, *Physica* **2**, 557 (1935).